frontiers | Research Topics

Additive manufacturing and biomaterials in regenerative dentistry

Edited by
Monireh Kouhi, Marziyeh Ranjbar-Mohammadi and Mohammad Khodaei

Published in
Frontiers in Bioengineering and Biotechnology
Frontiers in Materials

ISSN 1664-8714
ISBN 978-2-8325-2532-6
DOI 10.3389/978-2-8325-2532-6

About Frontiers

Frontiers is more than just an open access publisher of scholarly articles: it is a pioneering approach to the world of academia, radically improving the way scholarly research is managed. The grand vision of Frontiers is a world where all people have an equal opportunity to seek, share and generate knowledge. Frontiers provides immediate and permanent online open access to all its publications, but this alone is not enough to realize our grand goals.

Frontiers journal series

The Frontiers journal series is a multi-tier and interdisciplinary set of open-access, online journals, promising a paradigm shift from the current review, selection and dissemination processes in academic publishing. All Frontiers journals are driven by researchers for researchers; therefore, they constitute a service to the scholarly community. At the same time, the *Frontiers journal series* operates on a revolutionary invention, the tiered publishing system, initially addressing specific communities of scholars, and gradually climbing up to broader public understanding, thus serving the interests of the lay society, too.

Dedication to quality

Each Frontiers article is a landmark of the highest quality, thanks to genuinely collaborative interactions between authors and review editors, who include some of the world's best academicians. Research must be certified by peers before entering a stream of knowledge that may eventually reach the public - and shape society; therefore, Frontiers only applies the most rigorous and unbiased reviews. Frontiers revolutionizes research publishing by freely delivering the most outstanding research, evaluated with no bias from both the academic and social point of view. By applying the most advanced information technologies, Frontiers is catapulting scholarly publishing into a new generation.

What are Frontiers Research Topics?

Frontiers Research Topics are very popular trademarks of the *Frontiers journals series*: they are collections of at least ten articles, all centered on a particular subject. With their unique mix of varied contributions from Original Research to Review Articles, Frontiers Research Topics unify the most influential researchers, the latest key findings and historical advances in a hot research area.

Find out more on how to host your own Frontiers Research Topic or contribute to one as an author by contacting the Frontiers editorial office: frontiersin.org/about/contact

Additive manufacturing and biomaterials in regenerative dentistry

Topic editors

Monireh Kouhi — Isfahan University of Medical Sciences, Iran
Marziyeh Ranjbar-Mohammadi — University of Bonab, Iran
Mohammad Khodaei — Isfahan University of Technology, Iran

Citation

Kouhi, M., Ranjbar-Mohammadi, M., Khodaei, M., eds. (2023). *Additive manufacturing and biomaterials in regenerative dentistry*. Lausanne: Frontiers Media SA.
doi: 10.3389/978-2-8325-2532-6

Table of contents

frontiers | Frontiers in Bioengineering and Biotechnology

TYPE Editorial
PUBLISHED 10 May 2023
DOI 10.3389/fbioe.2023.1211009

OPEN ACCESS

EDITED AND REVIEWED BY
Hasan Uludag,
University of Alberta, Canada

*CORRESPONDENCE
Monireh Kouhi,
m.kouhi@dnt.mui.ac.ir

RECEIVED 24 April 2023
ACCEPTED 29 April 2023
PUBLISHED 10 May 2023

CITATION
Kouhi M and Khodaei M (2023), Editorial: Additive manufacturing and biomaterials in regenerative dentistry.
Front. Bioeng. Biotechnol. 11:1211009.
doi: 10.3389/fbioe.2023.1211009

Editorial: Additive manufacturing and biomaterials in regenerative dentistry

Monireh Kouhi[1]* and Mohammad Khodaei[2]

[1]Dental Materials Research Center, Dental Research Institute, School of Dentistry, Isfahan University of Medical Sciences, Isfahan, Iran, [2]Materials Engineering Group, Golpayegan College of Engineering, Isfahan University of Technology, Golpayegan, Isfahan, Iran

KEYWORDS

additive manucatruing, biomaterials, dentistry, tissue regeneration, titanium based bioimplants

Editorial on the Research Topic
Additive manufacturing and biomaterials in regenerative dentistry

Clinical approach to heal hard and soft tissue defects in dental and maxillofacial area sometimes rely upon biomaterials based mass products fabricated for a variety of surgical treatments, however, additive manufacturing and 3D printing express a paradigm shift in producing patient specific medical devices. Additive manufacturing or 3D printing are a collection of technologies allowing the fabrication of 3D structures via a computer and a computer aided design (CAD). Printing materials or ink can include metals, polymers, ceramics and cells. When cells are included in the printing ink, the technique is called 3D bioprinting which enables the precise deposition of cells, matrix, and signaling factors to produce sophisticated objects. It has the potential to revolutionize the dental treatments and to speed up transition from traditional restoration approach towards bioengineered solutions. Regarding this, Ostrovidov et al. (Frontiers in Bioengineering and Biotechnology, 2023, 11, 991821) reviewed the recent advances in different bioprinting techniques (such as extrusion based, stereolithography, inkjet, laser assisted) and bioinks for application in regeneration of different dental alveolar tissues including dentine, dental pulp, bone, periodontal ligament, etc. The bioprinting regulation for both 3D printed constructs, without cells (regulated as medical devices) and with cells (regulated as biologics and drugs), is also discussed in this review paper.

One of the challenges in the reconstruction of oral and maxillofacial defects is available biomaterials, which may not be appropriately able to perform true formation of new tissues. Optimization and fabrication of bioresorbable scaffolds with the capacity to reconstruct defects reliably and safely must be the major focuses of the future researches. Further, the potential functionalization of scaffolds for therapeutic purposes should be consider when designing regenerative bio constructs.

Most of the available bone grafting materials in clinics lack appropriate degradability and efficient osteoinductivity. In a study by Xu et al., a novel biomimetic nanocrystalline calcium phosphate containing bone morphogenetic protein-2 (BMP-2) was developed to prepare degradable and highly osteoinductive granules to heal critical sized bone defects. The results of cytotoxicity and cytocompatibility assessment of MC3T3-E1 pre-osteoblasts showed no obvious cytotoxicity and improved pre-osteoblast cells adhesion. *In-vivo* histomorphometric

analysis revealed that the new bone volume induced by the developed granules showed a BMP-2 amount-dependent increasing behavior.

Titanium and its alloys are being widely used for bone repair purposes, due to their high biocompatibility and strength/weight ratio. (Su et al.), compared the properties of titanium with other dental implant materials such as zirconia and polyetheretherketone (PEEK). They stated that titanium had lowest water contact angle and better wettability, higher cell viability and improved alkaline phosphatase activity compared to other studied materials. The most interesting matter is that, the anti-adhesion effect against bacteria of titanium was significantly better than zirconia and PEEK.

Besides lots of benefits, titanium is inherently bioinert and cannot bond to surrounding tissue after implantation. To alleviate this restriction of titanium, many different surface treatment techniques have been used by researchers to improve titanium bioactivity and osteoconductivity. Regarding this, in a review paper by Nansi López-Valverde et al., chitosan coating on the surface of titanium implant was mentioned to enhance antibacterial ability, osteoinductivity and osseointegration capability of titanium. The superior biological properties of chitosan and also its excellent ability to bond on the surface of titanium, can lead to applying chitosan coating on the surface of titanium dental implants in future. Different techniques can be used for chitosan coating on the surface of titanium implants.

Besides the coating technique, acid etching can be used to improve the surface properties of titanium. Yan et al. 3D printed Cu-bearing titanium alloys and applied acid etching on the surface of 3D printed titanium alloys, they concluded that biological properties of the Cu-bearing titanium alloys could be significantly improved upon etching treatment with acid. Acid etching treatment could enhance cell adhesion, activate macrophage polarization, and reduce ROS levels on the surface of titanium.

Superior properties of titanium and also lots of surface treatment techniques resulted in widely implantation for dental and bone repair. However, not only titanium and its alloys, but also titanium oxide (TiO_2) in the forms of anatase and rutile are biocompatible and also are bioactive. So, titanium oxide nano particles are widely used as reinforcement (filler) of nano-biocomposites and also as coating on the surface of implants. Yu Ma et al. used titanium oxide nano particles to reinforce glass ionomer cement, it was reported that titanium oxide addition to the glass ionomer cement resulted in mechanical properties improvement, significantly. The strength, hardness and antibacterial properties and also bioactivity of anatase and rutile (two different forms of titanium oxide) lead to clinical wide application of titanium oxide nano particles.

Beside the treatment of hard tissue defects, the soft tissue regeneration and wound healing strategies are of great importance in oral and maxillofacial area and remains a significant clinical problem due to inflammation, infection, and dysangiogenesis. A variety of biocompatible materials in the form of hydrogels, membrane and lubricants have been investigated to enhance wound healing rate. Regarding this, Lu et al., developed a novel injectable hydrogel based on catechol modified chitosan and aldehyde modified cellulose modified nanocrystal containing Ag. The developed hydrogels showed *in situ* forming properties, suitable mechanical properties, biocompatibility, controlled release of Ag, and antibacterial performance, as well as promoted neovascularization and tissue regeneration. Additionally, the obtained hydrogel was able to completely cover and firmly attach wounds with irregular shapes, so eliminates the re-injury process. In another study, a water-based polyethylene glycole (PEG)/chitosan (CS) composite lubricant was successfully developed for wound healing (Gao et al.). The L929 cells viability test indicated the good biocompatibility of the PEG/CS lubricant, and the results of tribological test revealed that it had a good lubrication effect. In addition, the developed PEG/CS lubricant has been proved to possess a good wound-healing effect as resulted from the animal study.

Biocompatible materials are also applied in dentistry field as desensitization materials to effectively alleviate dentin hypersensitivity (by occluding exposed dentinal tubules), and inhibit S. mutans to prevent caries simultaneously. For instance, in a study by Yan et al. an approach for the development of IgY-loaded amorphous calcium phosphate (ACP) (IgY@ACP) has been proposed, which have synergetic advantages of IgY and ACP in enabling the dentin surface to resist dentin hypersensitivity and caries. Their results showed that IgY@ACP could stably occlude dentinal tubules with acid challenge and effectively inhibit the formation and growth of biofilm of S. mutans and could be a promising desensitization material for dentin hypersensitivity therapy.

Author contributions

All authors listed have made a substantial, direct, and intellectual contribution to the work and approved it for publication.

Acknowledgments

We would like to express our thanks to all the authors who presented their work and all the researchers who reviewed the submissions to this Research Topic.

Conflict of interest

The authors declare that the research was conducted in the absence of any commercial or financial relationships that could be construed as a potential conflict of interest.

Publisher's note

frontiers | Frontiers in Bioengineering and Biotechnology

ORIGINAL RESEARCH
published: 26 April 2022
doi: 10.3389/fbioe.2022.876936

Antibacterial Cellulose Nanocrystal-Incorporated Hydrogels With Satisfactory Vascularization for Enhancing Skin Regeneration

Haibin Lu[1,2], *Xiaoling Li*[1], *Mu Zhang*[1], *Changpeng Xu*[3], *Wenqiang Li*[4]* *and Lei Wan*[1]*

[1]Stomatological Hospital, Southern Medical University, Guangzhou, China, [2]Shunde Hospital, Southern Medical University (The First People's Hospital of Shunde), Foshan, China, [3]Department of Orthopaedics, Guangdong Second Provincial General Hospital, Guangzhou, China, [4]Engineering Technology Research Center for Sports Assistive Devices of Guangdong, Guangzhou Sport University, Guangzhou, China

Wound healing of skin defects remains a significant clinical problem due to inflammation, infection, and dysangiogenesis; especially, the promotion of microvasculature formation in healing of chronic wound or deep skin defects is critical as it supplies oxygen and nutrients to the impaired tissue, relieving uncontrolled inflammatory responses. The cellulose nanocrystals (CNCs) in the liquid crystalline phase, which facilitates cell proliferation and migration, has been shown to improve vascularization effectively. Therefore, we developed a novel injectable hydrogel based on Schiff base and coordination of catechol and Ag. The obtained hydrogels (CCS/CCHO-Ag) exhibited *in situ* forming properties, satisfactory mechanical performance, controlled release of Ag, antibacterial capacity, and biocompatibility. In addition, the hydrogels could also entirely cover and firmly attach wounds with irregular shapes, so as to reduce the re-injury rate. More importantly, experiments *in vitro* and *in vivo* demonstrated that CCS/CCHO-Ag hydrogels can promote neovascularization and tissue regeneration, thanks to their anti-inflammatory and antibacterial effects. In conclusion, these multifunctional hydrogels are well on the way to becoming competitive biomedical dressings, which show tremendous potential application in the field of tissue engineering.

Keywords: hydrogel, cellulose nanocrystals, angiogenesis, antibacterial activity, skin regeneration

OPEN ACCESS

Edited by:
Mohammad Khodaei,
Isfahan University of Technology, Iran

Reviewed by:
Anuj Kumar,
Yeungnam University, South Korea
Elena F. Krivoshapkina,
ITMO University, Russia
Hamed Nosrati,
Shahrekord University of Medical Sciences, Iran

***Correspondence:**
Wenqiang Li
gztylwq@foxmail.com
Lei Wan
wanleilucky@126.com

Specialty section:
This article was submitted to Biomaterials, a section of the journal Frontiers in Bioengineering and Biotechnology

Received: *16 February 2022*
Accepted: *21 March 2022*
Published: *26 April 2022*

Citation:
Lu H, Li X, Zhang M, Xu C, Li W and Wan L (2022) Antibacterial Cellulose Nanocrystal-Incorporated Hydrogels With Satisfactory Vascularization for Enhancing Skin Regeneration. Front. Bioeng. Biotechnol. 10:876936. doi: 10.3389/fbioe.2022.876936

INTRODUCTION

In severe cases, skin wounds can cause disability and even be life-threatening, which is a notable issue that deserves immediate attention (Lei et al., 2020; Li et al., 2020; Sheng et al., 2021). Currently, the treatment of chronic skin wounds is still a clinical challenge, and more than 50% of chronic wounds are refractory to current therapies (Li et al., 2020). Wound dressing, particularly hydrogel, plays an important part in skin repair and structure remodeling (Khan et al., 2020; Peng et al., 2020). Backed by hydrophilic three-dimensional networks, hydrogels create a breathable and moist environment in which wounds can heal more rapidly, suggesting that they are one of the most effective wound dressings (Majumder et al., 2020; Mao et al., 2020; Tamahkar et al., 2020). Due to excellent biocompatibility and biodegradability, polysaccharides such as hyaluronic acid and chitosan are the most commonly used natural biopolymers in the wound dressing field (Nosrati et al., 2021). For example, Cao et al. (2021) prepared a novel carboxymethyl chitosan hydrogel used for wound

healing, which exhibited thermoresponsive capacity to accelerate wound closure and surrounding tissues regeneration. Yang et al. (2016) proposed a facile approach to produce a polyacrylamide–chitosan (PAM-CS) composite hydrogel with dramatically improved tensile strength and toughness, which can efficiently accelerate skin repair at different wound healing periods. Unfortunately, these preparation of hydrogel dressings show poor antibacterial performance and weak biological adhesion, thus greatly limiting their further application in the wound dressing market.

Generally, silver (Ag) nanoparticles have attracted much attention owing to distinctive chemical and physical performance, low toxicity, and broad-spectrum antibacterial ability (Xie et al., 2018; Basha et al., 2020). It was reported that Ag-loaded nanocomposite hydrogel can be used as a controlled release carrier of the bacteria-killing activity for accelerating wound healing (Yang et al., 2021), but the reported hydrogel system based on UV polymerization of the polymer matrix restricts their application in irregular skin wounds, thanks to their inherent traits that do not completely avoid infection. Recently, the development of injectable hydrogels with unique shape adaptability and self-healing ability contribute to complete fit and adequate contact between the wound and hydrogel dressing and thereby promote the therapeutic efficacy on the injuries, which has aroused considerable interest. Through non-covalent cross-links such as coordination bonds, hydrogen bonds, ionic bonds, and Schiff bases to form injectable self-healing hydrogels can be endowed with good adhesion behavior, mechanical strength, and biological activity (Guo et al., 2015; Huang et al., 2019; Liu et al., 2019). Moreover, the injectable self-healing hydrogel fabricated by dynamic cross-link show favorable potential for 3D bioprinting, which can also provide a 3D microenvironment for complex tissue regeneration (Kumar et al., 2020; Guyot et al., 2021). Nevertheless, long gelation time and low mechanical strength of hydrogel remain an important challenge to develop injectable self-healing hydrogels as 3D bioink. In wound dressing, another critical issue of the chronic wound or full-thickness skin defect is impaired angiogenesis that supplies oxygen and nutrients for cells and tissues (Balagangadharan et al., 2018; Chen et al., 2019a; Chen et al., 2019b). Exogenous angiogenic growth factors (GFs), such as vascular endothelial growth factor (VEGF), are usually exploited to facilitate wound closure and angiogenesis (Huang et al., 2019). Unfortunately, the instability of VEGF in a highly proteolytic and oxidative environment of the wound leads to large limitation of its clinical application.

Important biomolecules such as polypeptides, proteins, nucleic acids, lipids, and polysaccharides in organisms have liquid crystal states (Chen et al., 2019b). Previous studies have proved that the cell membrane has special conformation similar to the liquid crystalline (LC) state, and its surface, which is always in contact with blood, is in a flowing lipid LC condition (Jewell, 2011; Wu et al., 2017). Since this viscoelastic material can be seen as a soft elastic solid, LC has the potential to design the cellular surface and to study cell adhesion (Lockwood et al., 2006). The alignment structure of LC not only facilitates the ring formation of endothelial cells but also has positive effects on cell migration, leading to promote angiogenesis due to LC stimulation *via* tunable physical properties and anisotropic viscoelastic behavior (Zhan et al., 2021). Cellulose nanocrystals (CNCs) (from cellulose with a rod-like structure) have the ability to self-assemble from the liquid phase to the cholesteric LC phase (Lin et al., 2017; Chen et al., 2021). It is important to note that surface chemical modification makes the formation of injectable hydrogels available while ensuring high-water and biocompatible properties to apply to biomedicine. For example, Kumar et al. (2019) prepared carboxylated CNC-reinforced and ionically cross-linked polysaccharide hydrogels and further designed 3D printable carboxylated CNC-reinforced hydrogel inks for tissue engineering (Kumar et al., 2020). To date, there is almost no report on CNCs with the LC state and the promotion of vascularization during wound healing, which are expected to be promising LC biomaterials for regeneration of blood vessels as cells can sense and respond to the microenvironment constructed by the LC state and upregulated angiogenic factors (Zhan et al., 2021).

Inspired by the mussels' high adhesion to various substrates, catechol has been introduced into the polymer matrix, which usually displays strong and long-term adhesiveness to soft tissues. More importantly, the catechol group can be coordinated with metal ions (including Mg^{2+}, Fe^{3+}, and Ag^{+}) by facile mixing to enhance gelation of the hydrogel (Yuan et al., 2021). Here, we designed a newly multifunctional hydrogel with double cross-linking for wound healing. First, hydrocaffeic acid was used to graft the CS by the amidation reaction to prepare catechol-modified CS (CCS), which acts as the backbone of hydrogel, and aldehyde-modified cellulose nanocrystals (CCHOs) play roles as both physical fillers and cross-linkers in the fabrication of hydrogels. Then double cross-linking of Ag-catechol and Schiff base bonds are used as part of the gel-forming mechanism, and a bio-multifunctional hydrogel (CCS/CCHO-Ag) is produced by introducing Ag to catechol-modified chitosan (CCS) and aldehyde-modified cellulose nanocrystals (CCHOs). As a result, the obtained hydrogel system show enhanced mechanical behavior, good injectable properties, tissue adhesion, long-term antibacterial, and cytocompatibility. Based on these unique properties, a full-thickness skin wound model was created for investigating the wound healing efficiency of hydrogel dressings *in vivo*.

EXPERIMENTAL SECTION

Materials

Cellulose was supplied by Fujian Qingshan Paper Industry Co., Ltd., China. Chitosan (degree of deacetylation ≈95%, 100–200 mps), 3,4-dihydroxyhydrocinnamic acid, 1-ethyl-3-(3-dimethylaminopropyl)-carbodiimide hydrochloride (EDC), silver nitrate ($AgNO_3$), and sodium borohydride ($NaBH_4$) were all purchased from Aladdin Biochemical Technology Co., Ltd. (China). In terms of other analytical reagents, they were obtained from the Tianjin Damao Chemical Reagent Factory.

Cellulose Nanocrystals

A certain amount of cellulose was pretreated with 5 wt% NaOH solutions at 70°C three times. The resultant specimen was further washed with DI water and dried. A measure of 10 g of dried cellulose was immersed in 100 ml of 64 wt% H_2SO_4 solution and heated to 65°C for 90 min A volume of 2L DI water was used to stop the reaction. The acid was removed by centrifugation, and the final suspension was dialyzed in a dialysis tube (MW 8000–14000) for a week. The concentration of the CNC was set at 2.5 wt%.

Synthesis of Modified CNCs (CCHOs)

A measure of 50 g of CNC suspension was heated to 35°C and 2 g $NaIO_4$ was added to it under vigorous stirring. The reaction was carried out in a dark room for 12 h and quenched with the addition of 15 ml glycol. The product was dialyzed in a dialysis tube (M_W 7500–14000) for 3 days to remove excess glycol and impure ions. The aldehyde group content of CCHOs was determined using a NaOH titration method, according to previous studies (Yin et al., 2016). The morphology and distribution of the CNCs and CCHOs were studied *via* a field emission scanning electron microscope (FE-SEM, ULTRA 55, Carl Zeiss, Germany) and transmission electron microscopy (TEM, Philips CM-120, Eindhoven, Netherlands). A polarizing optical microscope (POM, BX53M, Olympus, Tokyo, Japan) equipped with a digital camera (DP200) was used to study the optical phenomenon of the CNCs or CCHOs whisker aqueous suspensions with 0.5, 1, and 2% (w/v).

Synthesis of Catechol-Modified Chitosan (CCS)

Based on the EDC activation reaction, CCS was produced by the esterification between the NH_2 group (chitosan) and the carboxyl group (hydrocinnamic acid). In brief, chitosan was poured into 1 N HCl (aq) solution, and its pH was regulated by 1 N NaOH (aq) to pH of 5 under vigorous stirring. Then hydrocaffeic acid dissolved in DI water was added to the above solution. Subsequently, EDC dissolved in DI water and equal volume of ethanol solution (1:1, v/v) were also added. The pH of the mixed solution was adjusted to 5 and stirred constantly for 5 h. Finally, the obtained solution required dialysis to remove residual reagents after completion of all reaction steps, including 3 days in acidified DI water (pH = 5.0) and 8 h in DI water. CCS was obtained after lyophilization and observed under FTIR spectroscopy (Fts6000, Bio-Rad, United States). In addition, the resulting freeze-dried samples characterized by ^{1}H NMR and UV-vis spectroscopy. The catechol substitute ratio of CCS was determined by ^{1}H NMR (Bruker Biospin GmbH, Germany).

Formation of CCS/CCHO-Ag Hydrogels

The resultant CCS (0.25 g) dissolved in 10 ml CCHO suspensions with a molar ratio of 0.5, 1.0, and 2.0 for -CHO/-NH_2, respectively. Then 0.2 mM $AgNO_3$ was added to the abovementioned solution, and the pH of the solution was adjusted above nine by NaOH after stirring for 30 s. Next, the pregel solution was incubated at 37°C for 5 min to trigger the transformation to a hydrogel through the Schiff base and the coordination bond. The gelation of CCS/CCHO-Ag was evaluated by the tube inverted test. Finally, the obtained hydrogels were washed with PBS solution three times for purification. The functional groups of the prepared hydrogels were tested by FTIR spectroscopy (Fts6000, Bio-Rad, United States).

Characterization of Hydrogels

Rheological Measurements

The rheological behavior of the hydrogels was investigated using a rotational rheometer (DHR, TA Instruments, United States) at 37°C. The viscosity of the whisker aqueous suspensions was measured in the shear rate range from 0.1 to 10 s^{-1}. Then the gelation time of the mixtures was investigated by time sweeps at a constant oscillatory strain of 1% and frequency of 6.28 rad/s. Also, the frequency sweep oscillatory tests were carried out by varying amplitude-frequency of 0.1–100 rad/s (a strain of 1%). At last, the strain sweep was performed with the oscillatory strain from 0.1 to 100% to make sure this modulus value was within the linear elastic range (a frequency of 6.28 rad/s).

Scanning Electron Microscope Observation

The morphology of resulting hydrogel specimens were detected using a scanning electron microscope (SEM, LEO1530 VP, Philips, Netherlands). First, the prepared hydrogels were transferred to a freezer with −80°C and dried by using a freeze dryer. After that, the freeze-dried samples were cryogenically fractured in liquid nitrogen condition. Then the cross sections of the hydrogel samples were treated by gold spraying (Sputter Coater, Ted Pella, LJ-16) for SEM observation, and the pore diameter was determined by ImageJ analysis.

Mechanical Behavior

All hydrogels were made cylindrical in shape with a diameter of 10 mm and a thickness of 8 mm for the following compression tests, which were conducted by a dynamometer machine (AGI-1, Shimadzu, 1 kN load, Japan), and the Young's modulus values were calculated from the compression stress–strain curves of hydrogel between 40 and 60% strain. In addition, cycling compression tests were also performed with a speed of 2 mm/min and in the 0–70% range. In particular, the experiment was repeated 20 times to test the compression and recovery features.

Swelling Property

The swelling ratio (SR) was measured by a previously reported approach (Huang et al., 2019). The resulting CCS/CHOs, CCS/CNC-Ag, and CCS/CHO-Ag hydrogels (n = 3) were soaked in PBS solution (pH = 7.4) for 24 h to swell completely.

Adhesion Performance

Tensile adhesion tests were conducted to investigate the adhesive capacities of the hydrogels (Huang et al., 2019). In brief, the samples (25 mm × 20 mm × 2.5 mm) were pulled to fracture at a rate of 5 mm/min by the mechanical testing machine equipped

with a 50 N load. The adhesion strength was calculated as the maximum load divided by contact area. All experiments were repeated at least three times.

Ag^+ Release Analysis and Antibacterial Activity *In Vitro*

To evaluate the release of Ag^+ and Ag loading efficiency calculated from the mass percentage of the loaded Ag to the feeding Ag, atomic absorption spectroscopy (AAS; PE, AA700, United States) was performed. Before the examination, the release profiles of silver from the hydrogels were characterized *in vitro* by the all-change method in the PBS solution (pH 7.4). Here, at 37°C, CCS/CNC-Ag and CCS/CCHO-Ag (25 μg/sample) hydrogels were immersed in the PBS solution (5 ml) and shaken (100 rpm). At predetermined intervals, the released PBS was collected and replaced by fresh PBS. The amount of released Ag was determined using an AAS instrument, and the release profiles were obtained. The tests were repeated three times.

The germ-killing ability of the hydrogels was evaluated by turbidimetry measurements using *Staphylococcus epidermidis* (*S. epidermidis*, ATCC6538, Gram-positive organism) and *Escherichia coli* (*E. coli*, ATCC8739, Gram-negative organism) (Huang et al., 2019). By extension, the sterilized samples were placed into tubes, and then 5 ml of a bacterial suspension (1×10^4 CFU/ml) was added to completely immerse the hydrogels, which were served as the experimental groups. However, the control group only contained the same volume of bacterial suspension in the test tube. Subsequently, all groups were incubated in the bacterial incubator at 37°C and 5% CO_2. After incubating for 1, 4, 7, and 10 days, respectively, 500 μl of the bacterial suspension was taken to measure through turbidimetry at 570 nm. In addition, the antibacterial rate (AR) can be calculated using the following formula (Annabi et al., 2017):

$$AR = \frac{I_1 - I_2}{I_1} \times 100\%,$$

where I_1 represents the OD value of the control group, while I_2 for the experimental groups.

In Vitro Cell Experiment

Human umbilical vein endothelial cells (HUVECs) were used to evaluate the biocompatibility of different hydrogels. Specifically, sterilized cylindrical hydrogels about 7 mm in diameter and 1 mm in deep were immersed in HUVECs with a density of 2×10^4 cells/well. The cells were cultured in RPMI 1640 medium (Gibco) containing 10% FBS and 1% penicillin/streptomycin (P/S, Gibco). On days 1, 3, and 5, the cell proliferation and survival were assessed by using the CCK-8 assay and LIVE/DEAD® Viability/Cytotoxicity Kit. In brief, the hydrogel films of 1.5 mm thickness were fabricated and cut into 5-mm-diameter disks, and then these hydrogel samples were sterilized by alcohol immersion and UV irradiation process. The HUVECs were seeded into the 96-well plate (10,000 cells per well) and cultured for overnight. The hydrogel disks were introduced into the wells, then incubated at 37°C for 1, 3, and 5 days. At each time point, 10 μl Cell counting Kit-8 (CCK-8, Jiancheng, Nanjing, China) was added into each well, followed by incubation at 37°C for 2 h, then the absorbance value at 590 nm was measured by using a microplate reader. Meanwhile, the cells after co-cultured with hydrogel films for 5 days were washed with PBS twice before Live/Dead staining. After that, 200 μl of acridine orange/ethidium bromide (AO/EB, Beyotime, Shanghai, China) was added into each well and incubated in the dark at room temperature for 5 min, then observed by an inverted fluorescence microscope. And then, the living and dead cells were counted using the ImageJ software (V1.8.0.112).

To evaluate the migration ability, the cell transwell experiments of HUVECs were conducted on the surface of hydrogels samples. In brief, the treated cells with a density of 5×10^5 cells/well were collected and resuspended in the surface of a transwell insert with the addition of 200 μl of culture medium with 1% FBS. After 48-h incubation with the addition of a full culture medium in the lower chamber, the resultant cells were fixed with 4% polyoxymethylene and stained with 0.5% crystal violet. Then five fields were chosen to photograph and count. In addition, the neovascularization capacity of the extracellular proteins was evaluated by immunofluorescence staining. In brief, the hydrogel samples were washed three times with PBS and then fixed with 4% polyformaldehyde for another 15 min. After incubating with anti-ANG (ab2831, Abcam) antibodies for 12 h, the cells were stained by DAPI solution for 15 min. The hydrogels were rinsed with PBS four times at 5 min per wash and were observed and photographed *via* CLSM.

In Vivo Animal Experiments

The whole animal experiments were approved by the Animal Ethical Committee of Guangzhou Sport University SD rats. Before preparing the hydrogel, all precursors sterilized by filtration (0.22-μm filter, Millipore), and the hydrogel dressings were fabricated as described before in the section of hydrogel preparation. To establish the full-thickness skin defect model, streptozotocin (STZ, 60 μg/g) solution was injected into Sprague Dawley rats (male, 180–200 g) through their tail vein. The criteria for successful establishment were defined as fasting blood glucose above 16.7 mmol/L. Then the full thickness skin round wounds with 8 mm diameter were created by a needle biopsy. After the removal of wound skin, the obtained CCS/CCHOs and CCS/CCHO-Ag hydrogels were injected into the wound area until they completely covered the entire wound, and then the petrolatum gauze and elastic bandage with surgical suture were used to strongly fix the dressing in the wound area. For the control group, the control wounds were added to 40 μL of PBS and were additionally covered with a 4-cm × 10-cm piece of Tegaderm TM dressing (3M, St. Paul, MN, United States). Wound conditions of rats were observed and recorded on 0, 5, 10, and 15 days, respectively. At the same time, the wound area was measured *via* ImageJ software. Wound contraction (%) was calculated using the formula below: Wound contraction= [area (0 day)-area (n day))/(area (0 day)] ×100%, where "n" represents the day, such as 5th, 10th, and 15th days. All results were analyzed by using the one-way ANOVA test.

Histological Analysis

Wound tissues were collected and fixed with 4% paraformaldehyde solution on days 5, 10, and 15. The

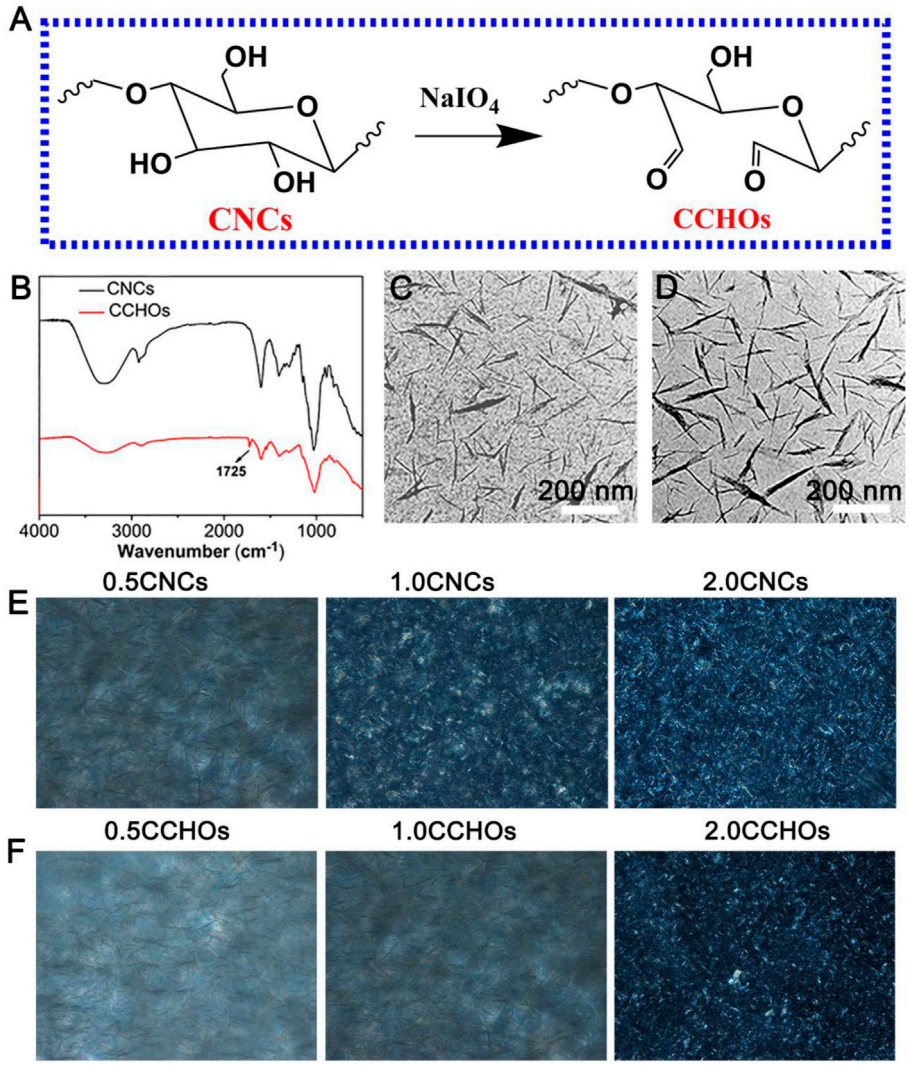

FIGURE 1 | (A) Schematic of synthesis of CCHOs. **(B)** FTIR spectra of the CNCs and CCHOs. TEM image of CNCs **(C)** and CCHOs **(D)**. The corresponding POM images of CNC **(E)** and **(F)** CCHO whisker aqueous suspensions with 0.5, 1, and 2% concentrations.

harvested samples were stained with hematoxylin and eosin (H&E), and immunohistochemical staining of IL-1β and IL-6 was performed using a standard protocol on adjacent sections for confirming the pro-inflammatory cytokine levels after the hydrogels treatment *in vivo*. In addition, the immunofluorescence staining of CD31 was conducted according to standard protocol (Zhang et al., 2019). All the slices were observed under a microscope (IX53, Olympus, Japan).

Statistical Analysis

All experiments were repeated three times, and data were shown as mean ± SD. One-way ANOVA, following Tukey's test, was carried out for statistical analysis by GraphPad Prism software. In particular, we defined $p < 0.05$ as statistically significant ($^{*}p < 0.05$, $^{**}p < 0.01$, and $^{***}p < 0.001$).

RESULTS AND DISCUSSION

Synthesis and Characterization of CCHOs

As a specific marker of biofilms, CNC liquid crystal (LC) has been known for its positive effects on cell affinity, migration, and proliferation (Zhang et al., 2020; Xie et al., 2020). Here, the CNCs were modified with $NaIO_4$ (**Figure 1A**). In order to validate the successful surface-modified aldehyde groups of CNCs, we carried out the attenuated total reflection Fourier transform infrared (ATR-FTIR) (**Figure 1B**). When compared with the spectrum of CNCs, CCHOs showed a new peak that appeared at 1725 cm^{-1}, which can be explained as the stretching vibration of C=O of the aldehyde group on its surface after oxidation (Chen et al., 2021). The content of aldehyde groups of the CCHOs was evaluated to be 7.30 mmol/g using a NaOH titration approach. The

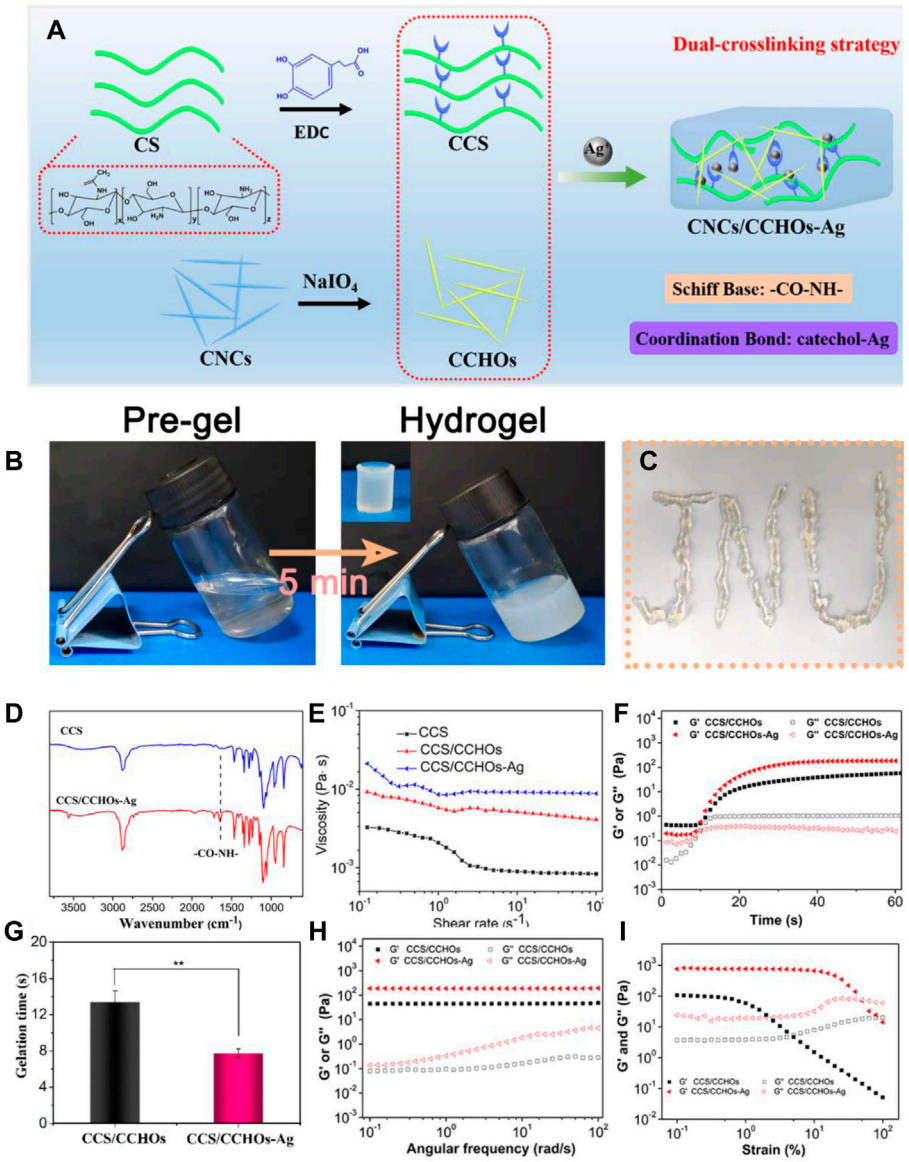

FIGURE 2 | (A) Scheme of CCS/CHO-Ag hydrogel synthesis by a dual-cross-linking strategy. **(B)** Optical images of hydrogels *via* a tube inverted test. **(C)** Injection process of the resultant hydrogel. **(D)** FTIR spectra showed the formation of the CCS/CHO-Ag hydrogel. The rheological results of obtained hydrogels: **(E)** Viscosity and viscoelasticity of CCS, CCS/CCHOs, and CCS/CCHO-Ag whisker aqueous suspensions; **(F)** time sweeping of storage modulus (G') and loss modulus (G''); **(G)** gelation time obtained by time sweeping test; **(H)** frequency-dependent (at a strain of 1%) and **(I)** strain-dependent (ω = 6.28 rad/s) oscillatory shear.

morphology of the CCHOs was observed by TEM. It can be seen that the CNCs and CCHOs exhibited a needle-like morphology without noticeable change after modification (**Figures 1C,D**). The results suggested that aldehyde modification did not play a significant role in the average length and diameter of the whiskers. According to the POM observation results, both the CNC and CCHO aqueous suspensions showed the typical cholesteric texture at 37°C from anisotropic materials. As the content increased, the domains of the LC phase gradually increased, and the field of view under POM gradually became brighter (**Figures 1E,F**), confirming that the modification of CNCs did not influence on its LC property.

Fabrication of the CCS/CCHO-Ag Hydrogels

Figure 2A shows the synthesis pathways of CCS/CCHO-Ag nanocomposite hydrogel and its application to wound healing. In this study, the modified CS with 3, 4-dihydroxy hydrocinnamic acid (CCS) is the matrix material of the

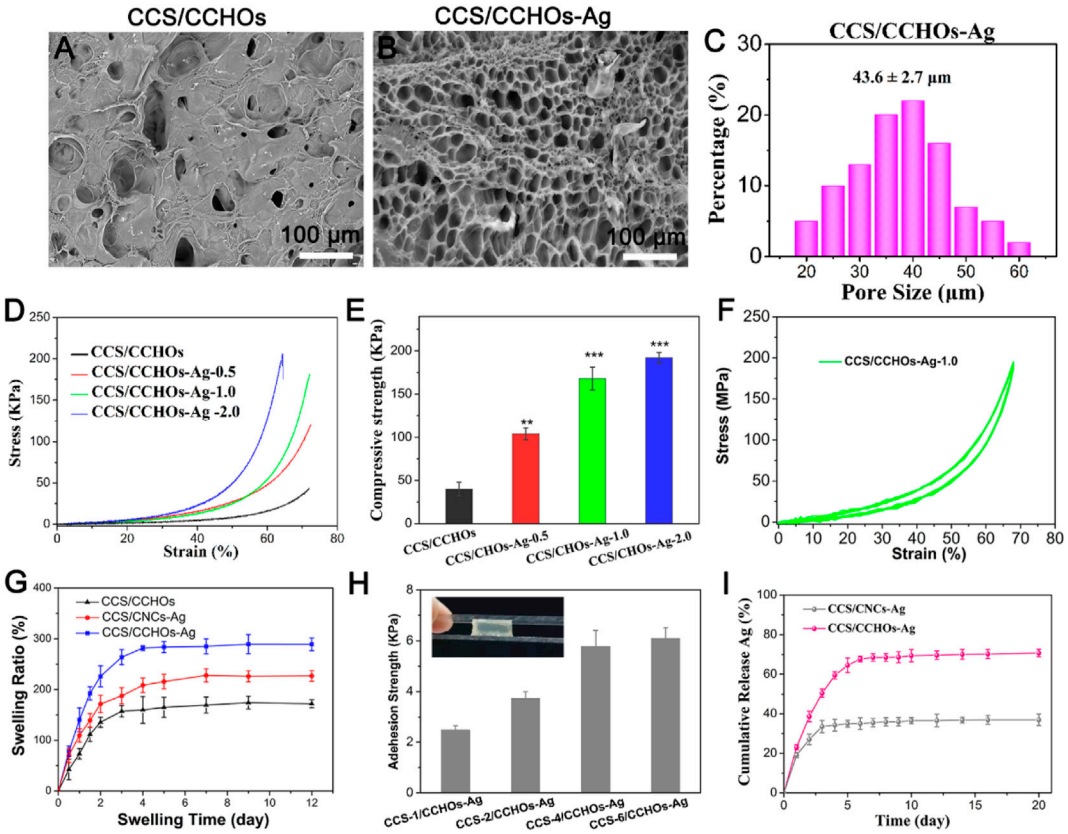

FIGURE 3 | SEM images of CCS/CHOs **(A)** and CCS/CHOs–Ag **(B)**, and statistical pore size of CCS/CHO-Ag hydrogel **(C)**. **(D)** Compressive stress–strain curves of Gel-DA/DOHA/DMON@Fe hydrogels with a molar ratio of 0.5, 1.0, and 2.0 for -CHO/-NH_2 and **(E)** its corresponding results of mechanical strength and Yong's modulus. **(F)** In total, 20 successive compressive loading-unloading cycles for hydrogel with a strain of 70%. **(G)** Swelling rate. **(H)** Adhesion strength of hydrogels with different CCS content adhered to porcine skin. **(I)** *In vitro* release profiles of Ag^+ from the hydrogel scaffolds.

hydrogel system. Based on the activation of EDC, the carboxylic group of hydrocaffeic acid was reacted with an amino group in CS to produce an amide bond. The efficiency of catechol grafting onto the CS was about 23.1%, which was verified by ^{1}H NMR and UV-vis analysis (**Supplementary Figure S1**, Supporting Information). Then CS was mixed with CCHOs, followed by incorporation of Ag^+ to form CCS/CCHO-Ag hydrogel based on Schiff base bonds (amino group of CCS and aldehyde group of CCHOs) and coordinate bonds (Ag and catechol group of CCS). The tube inverted test ensured the successful formation of the dual-cross-linking hydrogel. Since the hydrogel is composed of the dynamically cross-linked network, the resulting hydrogel showed good injectability (**Figure 1C**). Also, its chemical structure was further studied using FTIR. According to the FTIR spectra (**Figure 2D**), a strong peak at 1637 cm^{-1} was observed, indicating the formation of imine bonds (Tang et al., 2021). Meanwhile, the CCS/CHO-Ag hydrogel specimen showed a new band at 1350 cm^{-1}, which may be seen as the interaction between Ag and catechol group. These results demonstrated the successful formation of dual-cross-linking hydrogel based on Schiff base bonds and coordinate bonds between the Ag and catechol groups.

In order to further reveal the gelation mechanism of CCS/CCHO-Ag, a series of rheological tests of composite hydrogels were conducted. First, the shear viscosity of the different pre-gel solutions was measured by a rotating rheometer. As shown in **Figure 2E**, the shear viscosity of CCS/CCHO solution exhibited an obvious increase compared with pure CCS solution with a shear rate of 0.1 s^{-1}, with the addition of Ag, the viscosity continues to increase. This may result from a loose network formed *via* the interaction between the catechol group and Ag, which can be destroyed as the improvement of shear rate (Huang et al., 2017). Next, rheological measurements were conducted using different sweeps (time, frequency, and strain) during the gelation process. The G' value gradually increased from 0 to 60 s and then intersected the G'' value, indicating the transition point of sol-gelation (**Figure 2F**). Due to the dual-cross-linking mechanism, the gelatin time of the CCS/CCHO-Ag hydrogel group was shorter than the pure CCS/CCHOs hydrogel group (**Figure 2G**) and possessed higher equilibrium modulus (G_e'). **Figure 2H** demonstrates the frequency sweep of hydrogels samples. The G' value maintained constant during the whole frequency sweep process, which meant the characteristics of a well-developed cross-linked network (Huang et al., 2019). In addition, strain-dependent oscillatory rheology of the CCS/

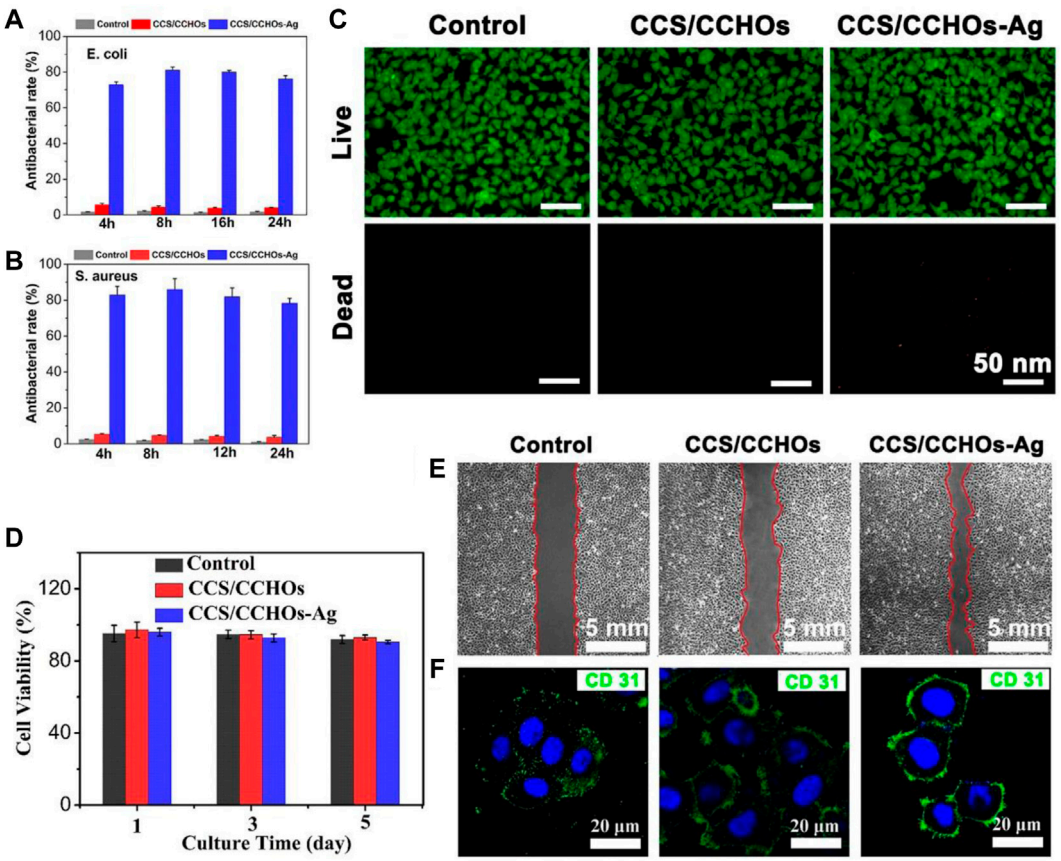

FIGURE 4 | Antibacterial rate of corresponding samples against *E. coli* **(A)** and **(B)** *S. aureus* after co-culturing for 4, 8, 16, and 24 h. **(C)** Live/Dead staining of HUVECs cultured on hydrogel scaffolds for 5 days. **(D)** CCK-8 assay of the proliferation of cells. **(E)** Transwell migration assays of HUVECs. **(F)** Fluorescence staining for CD 31 (green) and nucleus (blue) in HUVECs cultured with hydrogel sample.

CCHO-Ag hydrogels showed a stress relaxation when the strain exceeded 50%, which suggested that the processing range was wide because of their shear thinning property (**Figure 2I**).

Scanning Electron Microscope Observation, Mechanical Performance, Swelling Behaviors, Adhesive Properties, and Morphology of the Hydrogels

As can be seen from **Figure 3A**, scanning electron microscope (SEM) images demonstrated that the collapsed hole structure was observed in CCS/CHOs hydrogel owing to unstable cross-linked structure easy to change through rapid lyophilization, while the CCS/CHO-Ag displayed open porous structure, with the average diameter around 30–50 μm (**Figures 3C,D**). The introduction of Ag^{+} promoted the formation of uniform networks *via* a dual-cross-linking strategy. The interconnected porous structure is beneficial to the transmission of nutrients for cells (Jin et al., 2020). A typical compressive test was conducted to assess the mechanical behavior of the CCS/CHO-Ag scaffold, and the mechanical properties of the above hydrogels were illustrated (**Figures 3D,E**). The compressive strength and Young's modulus of the CCS/CCHO-Ag hydrogels were significantly higher than those of the CCS/CCHOs hydrogel because of the formation of Ag-catechol coordination that strengthened the microfibrils and improved the overall strength of the composite scaffolds. The compressive stress of CCS/CHOs dual-cross-linking hydrogel containing 0.5, 1.0, and 2.0 wt% of Ag increased to 107, 163, and 183 KPa, respectively, and its corresponding modulus values increased to 275, 432, 258.6, and 603 KPa, respectively, which showed significant improvement compared with the CCS/CHOs sample. It is noted that CCS/CCHO-Ag-2.0 samples showed reduced ductility, which might be possible that in the presence of excessively high concentration CCHOs, the dual-cross-linking hydrogel may lead to weak energy dissipation and small stress tolerance of nanoparticles to deformation (Han et al., 2017). The mechanical performance of obtained CCS/CCHO-Ag system is superior to previously reported histatin 1-modified thiolated chitosan dressings (Lin et al., 2020). In addition, the CCS/CCHO-Ag-1.0 was chosen as the sample for the following experiments. As expected, 20 cycles of loading–unloading compression tests were operated using a strain of 70%

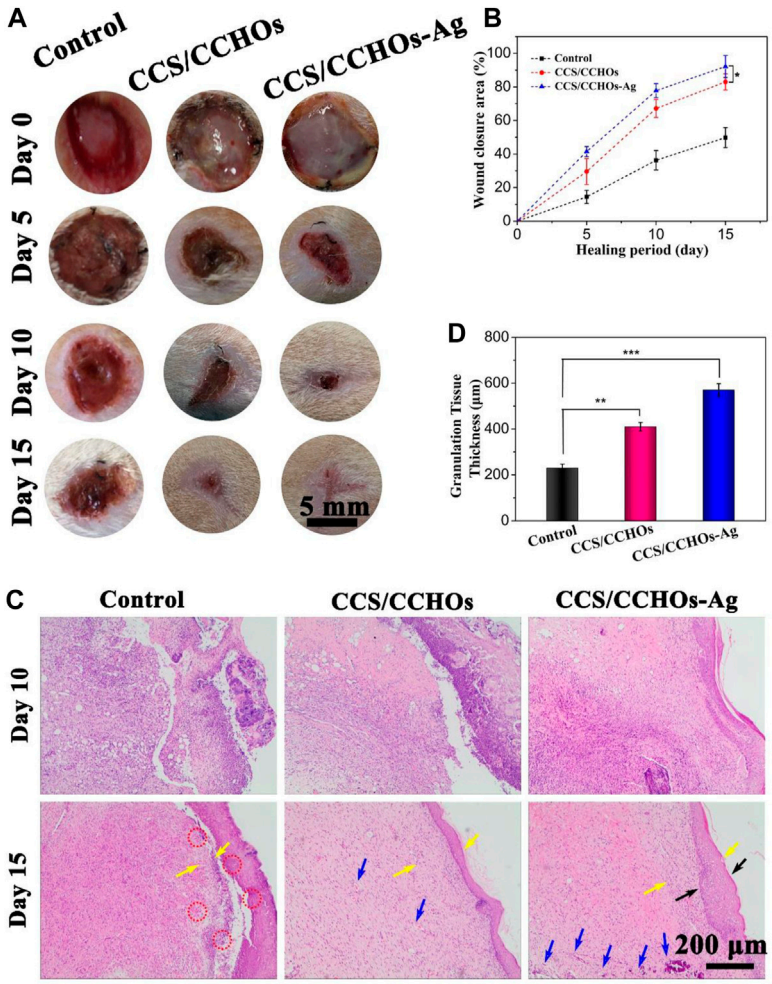

FIGURE 5 | (A) Optical images of wounds untreated or treated with CSS/CCHO and CCS/CCHO-Ag dressings on days 0, 5,10, and 15. **(B)** Corresponding healing rate of wounds. **(C)** Tissue slices stained with hemotoxylin and eosin (H&E) from different groups on days 10 and 15. **(D)** Quantitative analysis of the granulation tissue thicknesses (as pointed by the yellow arrows) using ImageJ.

(**Figure 3F**). The formed CCS/CCHO-Ag hydrogel could withstand 70% of the strain, indicating that the hydrogel showed excellent resilience and toughness properties.

Considering that hydrogel wound dressings should have a certain degree of water absorption capacity for the clearance of exudates during the process of wound healing, swelling behaviors of the hydrogel are needed to be evaluated (Lin et al., 2020). The swelling ratio of the hydrogels was also consistent with the above SEM results. **Figure 3G** shows that the dual-cross-linking CCS/CCHO-Ag hydrogels possessed a higher swelling rate than pure CCS/CCHOs sample, and CCS/CCHO-Ag-1.0 reached 274.6% after 12 h, indicating the dual cross-linking hydrogel possess desirable water absorption capacity owing to formation of large interpenetrating pores for absorbing more water molecule, which is almost 2 times that of previously reported CS double network hydrogel (Huang et al., 2019). A good wound dressing required not only to accelerate skin regeneration but also firmly attach to surrounding tissues, so we evaluated the adherence of hydrogels *via* the lap shear test using pigskin (**Figure 3H**). The adhesion abilities improved with the increase of the amount of CCS incorporated, and the long-term adhesion ability of CCS-6/CCHO-Ag was further reached to 5.8 KPa surprisingly, most likely from the enhancement of catechol chemistry–based hydrogel with long-term adhesiveness (Gan et al., 2019).

Antibacterial Activities of Ag-Loaded Hydrogels

The sustained antibacterial activity to fight infection has a significant meaning in wound healing (Garakani et al., 2020). Silver has potential biosafety risks despite its broad-spectrum antibacterial activity (Yang et al., 2021). Thus, the Ag-loaded hydrogels possess controlled release property. As shown in **Figure 3I**, the CCS/CCHO-Ag specimen presented a faster release rate during the first three days and slower subsequent release of Ag within 7 days. The denser coordination between Ag and CCS of hydrogels structure can be regarded as a barrier to

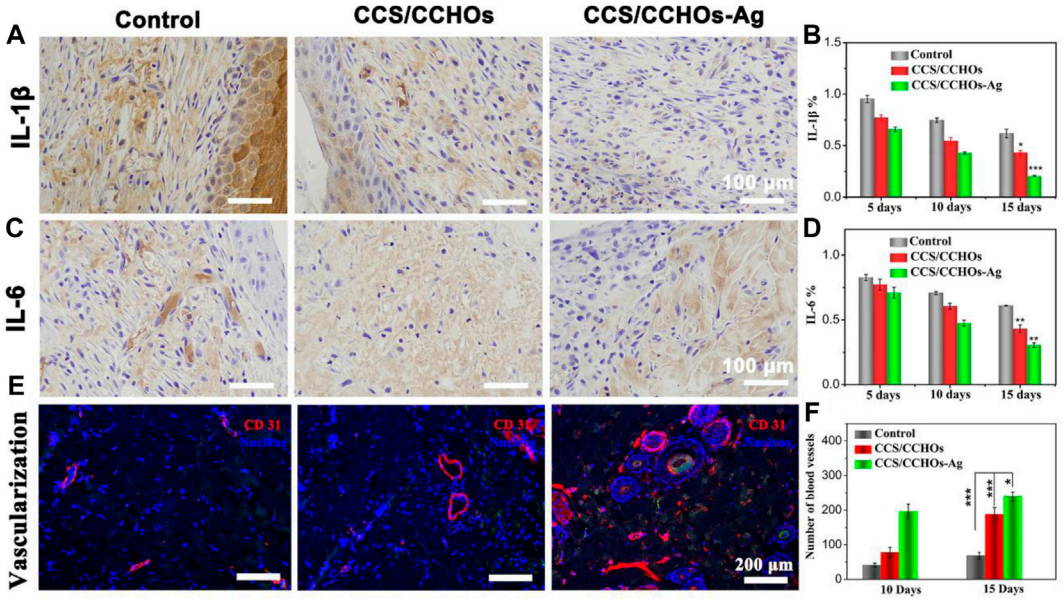

FIGURE 6 | Immunohistochemical staining of pro-inflammatory factors: **(A)** IL-1β and **(C)** IL-6 after different treatments for 15 days, and **(B,D)** its corresponding results of semi-quantitative analysis of immunohistochemical staining. **(E)** Immunofluorescence staining of CD31 for blood vessel formation *in vivo*, and **(C)** quantitative counts of newly formed blood vessels per mm^2 at 15 days.

prevent the Ag release rate and lead to more stability and sustained release in 10 days compared to CCS/CNC-Ag group. It is note that the amounts of Ag release from CCS/CCHO-Ag was much higher than that from CCS/CNC-Ag group because of the higher Ag loading efficiency (83.6 ± 3.7 vs. 39.8% ± 4.1%) after incubated for 21 days. In addition, the amounts of Ag^+ released from the CCS/CCHO-Ag hydrogels were 0.4877 mg/L after 7 days of release. This low concentration of Ag^+ ions is safe for cells and tissues (Basha et al., 2020). These results suggests that the CCS/CCHO-Ag hydrogels are capable of providing sustained release of active substances and contributing to protect the wounds from infection for a long time. Subsequently, the evaluation of the antimicrobial activity of hydrogels was based on the turbidimetry method, and the Ag-loaded hydrogels exhibited more remarkably enhanced antimicrobial features against both *E. coli* and *S. aureus* when compared with CCS/CCHOs samples (**Figures 4A,B**). More importantly, the antibacterial rate was consistently above 80% during incubation at 4, 8, 16, and 24 h, which is ascribed to the sustained release of Ag. All the results suggested that the hydrogel had the ability to minimize the growth of both G– and G+ bacteria.

Cytocompatibility and Angiogenesis Assay *In Vitro*

Furthermore, the biocompatibility of the fabricated scaffolds was tested *via* cytotoxicity test, including the examination of cell counting and Live/Dead staining. The HUVECs were co-cultured with CCS/CCHOs and CCS/CCHO-Ag, and the survival rate of cells in both groups was over 90% at 5 days (**Figure 4D**), which was consistent with the results of Live/Dead staining (**Figure 4C**), suggesting that the addition of Ag exhibited good biocompatibility without obvious detrimental effects on cell growth. Apart from that, angiogenic activity plays another important role in accelerating wound healing (Li et al., 2019; Zhang et al., 2017). Also, the transwell migration behavior of HUVECs cultivated on the surface of various hydrogels was conducted. As shown in **Figure 4E**, no significant increase in migration was shown in the control group. The significant cell migration appeared in CCS/CCHOs and CCS/CCHO-Ag, and the maximal rate of migration was observed in the dual-cross-linking scaffold. Meanwhile, CD 31 (green) immunofluorescence staining was further performed to study the revascularization ability of the endothelial cells (**Figure 4F**). According to the highest expression of CD 31 displayed in the CCS/CCHO-Ag hydrogel group, undoubtedly it had the best revascularization ability. Firstly, previous studies have revealed that CNCs LC state is an important basis for the induction of angiogenesis, thanks to its oriented structure, thus leading to the promotion of cell adhesion and proliferation (Zhai et al., 2012; Liu et al., 2020). Secondly, dual-cross-linking scaffolds co-regulate the cell–matrix relationship by stimulating anisotropic viscoelastic and biochemical interactions between receptors and ligands, providing an appropriate substrate for three-dimensional (3D) cell growth (Lin et al., 2019). Taken together, the composite

system containing CNCs LC exhibited synergistic effects on promoting the formation of vascularization, which could be seen as an excellent skin dressing.

In Vivo Evaluation of Wound Healing

Inspiring the excellent angiogenesis and antibacterial activity of resulting hydrogel *in vitro*, a full-thickness skin defect model was created to evaluate the effect of different hydrogels on promoting wound healing. All mice were divided into three groups totally: no treatment group (the control group), CCS/CCHOs hydrogel treatment group, and Ag-incorporated CCS/CCHOs treatment group. In view of capable of sustained Ag release from CCS/CCHO-Ag, we reasonably speculate that the our hydrogel dressing has a long-lasting therapeutic effect on wound healing, therefore the full thickness skin round wounds covered by hydrogels without additional dressing treatment. As shown in **Figure 5A**, on days 5 and 10, yellow pus was observed on the bright red wound surface in the control group, suggesting that the injured site was going through inflammation. However, hydrogel dressings groups showed more tidy wound areas with faster contraction rates, perhaps because of a moist environment maintained by the wound dressing (Huang et al., 2019). In particular, the CCS/CCHO-Ag hydrogel group covered the wound completely with the newly-formed epidermis, showing the fastest wound healing rate. On day 15, the wound closure area of CCS/CCHOs and CCS/CCHO-Ag group were 92.5 ± 6.5% and 77.5 ± 4.1%, respectively, which clearly superior than control group (41.7 ± 3.1%). It is noted that the efficiency of wound healing between CCS/CCHOs and CCS/CCHO-Ag displayed statistical significance ($^*p < 0.05$) by one-way ANOVA tests with a Tukey model, indicating wound healing got better results from the incorporated Ag composite system by inhibiting infection to reduce inflammation.

To evaluate the quality of wound healing, histological analysis was conducted on days 10 and 15. On the 10th day, there were fewer inflammatory cells (as pointed by the red circle) but more fibroblast cells in the CCS/CCHOs and CCS/CCHO-Ag hydrogel groups than the control group (**Figure 5C**), thanks to the sustained release of Ag^+ from CCS/CCHO-Ag system, which could significantly control inflammation. In addition, more blood vessels (as pointed by the blue circle) in these two groups could be attributed to the LC component that enhanced angiogenesis and accelerated wound regeneration as well (Xie et al., 2020; Zhan et al., 2021). After 15 days, a large area of immature granulation tissues were observed in the control and CCS/CCHOs hydrogel groups, while normal epithelium and almost completely regenerated dermal tissue were shown in the CCS/CCHO-Ag group. In addition, the dual-cross-linking hydrogel treated group showed the thickest granulation tissue and formed normal epidermal–dermal layer structure (as pointed by the black arrows), indicating this hydrogel achieved the best results concerning wound healing among these three groups (**Figure 5D**). In brief, the prepared CCS/CCHO-Ag hydrogel was the optimal wound dressing because it could promote skin regeneration.

Anti-inflammatory and Vascularization Effect of Hydrogels *In Vivo*

The inflammatory reaction is so severe in some infections that the wound repair can be delayed (Barkhordari et al., 2014; Zhao et al., 2017). IL-1β and IL-6, two typical inflammatory cytokines, are usually used to assess the early and middle stages of inflammatory response in the process of wound healing, respectively (Liu et al., 2018). **Figures 6A–D** show the lower expression of IL-1β and IL-6 in CCS/CCHO-Ag and CCS/CCHOs hydrogels rather than the control group, which represented less inflammatory response. Specifically, the highest level of inflammatory response among the three groups was the control group, while the lowest was the CCS/CCHO-Ag group. On the 15th day, the expressions of IL-1β and IL-6 presented a relatively higher level in the CCS/CCHOs groups, while the inflammatory responses of the CCS/CCHO-Ag group almost disappear, implying that the Ag-loaded hydrogels were able to effectively prevent infection and to promote wound repair.

Next, we explored the influence of CCS/CCHO-Ag on the formation of blood vessels *in vivo*. The blood vessel density was evaluated by immunofluorescence staining of CD31 that is mainly used to demonstrate the presence of vascular endothelium. CCS/CCHOs and CCS/CCHO-Ag group showed the property of increasing vessel numbers because the introduction of CNCs LC triggered the angiogenic process *in vivo* (**Figure 6E**). Also, quantification analysis reveals a significantly higher number of blood vessels in the CCS/CCHO-Ag than the control group (**Figure 6F**), suggesting the good anti-inflammatory ability in Ag-loaded hydrogels could also promote the formation of blood supply (Eming et al., 2007). Therefore, the prepared dual-cross-linking hydrogel system plays a combined role in regulating the inflammatory microenvironment and promoting angiogenesis, showing synergistic effects triggered skin repair.

CONCLUSION

To sum up, a multifunctional skin wound dressing with self-remodeling and biocompatible property was prepared, and its repairing potential in the full-thickness wound was also well-demonstrated. The fabrication of CCS/CCHO-Ag hydrogel was based on the double cross-linking strategy using the dynamic Schiff base and catechol–Ag coordination, which endowed the hydrogel with superior mechanical strength, strong tissue adhesion, perfect antibacterial activity, and good biocompatibility property. The LC-mimetic hydrogel showed a strong synergistic effect by the paracrine mechanism to significantly improve the migration and to stimulate angiogenesis of HUVECs *in vitro*. Also, the animal experiments demonstrated that CCS/CCHO-Ag scaffold had remarkable antibacterial activity and anti-inflammatory effects due to the one-demand release of the Ag. At the same time, the scaffold provided an anisotropic viscoelastic microenvironment that could promote neovascularization, jointly accelerating the wound healing process. In conclusion, the aforementioned satisfactory results proved that the multifunctional hydrogel is

expected to be used for wound healing and provoke more interest in stimulus-responsive wound dressings.

DATA AVAILABILITY STATEMENT

The original contributions presented in the study are included in the article/**Supplementary Material**, further inquiries can be directed to the corresponding authors.

ETHICS STATEMENT

The animal study was reviewed and approved by the Animal Ethics Committee of Southern Medical University.

AUTHOR CONTRIBUTIONS

WL contributed to research concept and design, LW provided project design and adequate experimental funding support, HL contributed to the operation of the experiment and the completion of the article, XL and MZ contributed to data analysis and interpretation, and CX completed data collection and/or assembly of data.

FUNDING

The present study was supported in part by the National Natural Science Foundation of China (No. 81972083); Science and Technology Planning Project of Guangzhou (Nos. 202102080052 and 202102010057); Science Foundation of Guangdong Second Provincial General Hospital (No. 3D-A2020004 and 3D-A2020002); National Natural Science Foundation of China (81600900); Science Foundation of Stomatological Hospital, Southern Medical University (PY2019013, PY2020013); and Postdoctoral sustentation fund of Shunde district, Foshan city.

SUPPLEMENTARY MATERIAL

The Supplementary Material for this article can be found online at: https://www.frontiersin.org/articles/10.3389/fbioe.2022.876936/full#supplementary-material

REFERENCES

Annabi, N., Rana, D., Shirzaei Sani, E., Portillo-Lara, R., Gifford, J. L., Fares, M. M., et al. (2017). Engineering a Sprayable and Elastic Hydrogel Adhesive with Antimicrobial Properties for Wound Healing. *Biomaterials* 139, 229–243. doi:10.1016/j.biomaterials.2017.05.011

Balagangadharan, K., Viji Chandran, S., Arumugam, B., Saravanan, S., Devanand Venkatasubbu, G., and Selvamurugan, N. (2018). Chitosan/Nano-Hydroxyapatite/Nano-Zirconium Dioxide Scaffolds with miR-590-5p for Bone Regeneration. *Int. J. Biol. Macromolecules* 111, 953–958. doi:10.1016/j.ijbiomac.2018.01.122

Barkhordari, S., Yadollahi, M., and Namazi, H. (2014). pH Sensitive Nanocomposite Hydrogel Beads Based on Carboxymethyl Cellulose/Layered Double Hydroxide as Drug Delivery Systems. *J. Polym. Res.* 21 (6), 454. doi:10.1007/s10965-014-0454-z

Basha, S. I., Ghosh, S., Vinothkumar, K., Ramesh, B., kumari, P. H. p., Mohan, K. V. M., et al. (2020). Fumaric Acid Incorporated Ag/agar-agar Hybrid Hydrogel: A Multifunctional Avenue to Tackle Wound Healing. *Mater. Sci. Eng. C* 111, 110743. doi:10.1016/j.msec.2020.110743

Cao, J., Wu, P., Cheng, Q., He, C., Chen, Y., and Zhou, J. (2021). Ultrafast Fabrication of Self-Healing and Injectable Carboxymethyl Chitosan Hydrogel Dressing for Wound Healing. *ACS Appl. Mater. Inter.* 13 (20), 24095–24105. doi:10.1021/acsami.1c02089

Chen, H., Cheng, R., Zhao, X., Zhang, Y., Tam, A., Yan, Y., et al. (2019). An Injectable Self-Healing Coordinative Hydrogel with Antibacterial and Angiogenic Properties for Diabetic Skin Wound Repair. *NPG Asia Mater.* 11 (1), 3. doi:10.1038/s41427-018-0103-9

Chen, H., Cheng, R., Zhao, X., Zhang, Y., Tam, A., Yan, Y., et al. (2019). An Injectable Self-Healing Coordinative Hydrogel with Antibacterial and Angiogenic Properties for Diabetic Skin Wound Repair. *NPG Asia Mater.* 11 (1), 3. doi:10.1038/s41427-018-0103-9

Chen, T., Yao, T., Peng, H., Whittaker, A. K., Li, Y., Zhu, S., et al. (2021). An Injectable Hydrogel for Simultaneous Photothermal Therapy and Photodynamic Therapy with Ultrahigh Efficiency Based on Carbon Dots and Modified Cellulose Nanocrystals. *Adv. Funct. Mater.* 31 (45), 2106079. doi:10.1002/adfm.202106079

Eming, S., Brachvogel, B., Odorisio, T., and Koch, M. (2007). Regulation of Angiogenesis: Wound Healing as a Model. *Prog. Histochem. Cytochem.* 42 (3), 115–170. doi:10.1016/j.proghi.2007.06.001

Gan, D., Xing, W., Jiang, L., Fang, J., Zhao, C., Ren, F., et al. (2019). Plant-Inspired Adhesive and Tough Hydrogel Based on Ag-Lignin Nanoparticles-Triggered Dynamic Redox Catechol Chemistry. *Nat. Commun.* 10 (1), 1487. doi:10.1038/s41467-019-09351-2

Garakani, S. S., Davachi, S. M., Bagher, Z., Esfahani, A. H., Jenabi, N., Atoufi, Z., et al. (2020). Fabrication of Chitosan/Polyvinylpyrrolidone Hydrogel Scaffolds Containing PLGA Microparticles Loaded with Dexamethasone for Biomedical Applications. *Int. J. Biol. Macromolecules* 164, 356–370. doi:10.1016/j.ijbiomac.2020.07.138

Guo, Z., Ni, K., Wei, D., and Ren, Y. (2015). Fe3+-induced Oxidation and Coordination Cross-Linking in Catechol-Chitosan Hydrogels under Acidic pH Conditions. *RSC Adv.* 5 (47), 37377–37384. doi:10.1039/c5ra03851k

Guyot, C., Cerruti, M., and Lerouge, S. (2021). Injectable, Strong and Bioadhesive Catechol-Chitosan Hydrogels Physically Crosslinked Using Sodium Bicarbonate. *Mater. Sci. Eng. C* 118, 111529. doi:10.1016/j.msec.2020.111529

Han, L., Xu, J., Lu, X., Gan, D., Wang, Z., Wang, K., et al. (2017). Biohybrid Methacrylated Gelatin/Polyacrylamide Hydrogels for Cartilage Repair. *J. Mater. Chem. B* 5 (4), 731–741. doi:10.1039/c6tb02348g

Huang, B., Liu, M., and Zhou, C. (2017). Chitosan Composite Hydrogels Reinforced with Natural Clay Nanotubes. *Carbohydr. Polym.* 175, 689–698. doi:10.1016/j.carbpol.2017.08.039

Huang, L., Zhu, Z., Wu, D., Gan, W., Zhu, S., Li, W., et al. (2019). Antibacterial Poly (Ethylene Glycol) Diacrylate/Chitosan Hydrogels Enhance Mechanical Adhesiveness and Promote Skin Regeneration. *Carbohydr. Polym.* 225, 115110. doi:10.1016/j.carbpol.2019.115110

Jewell, S. A. (2011). Living Systems and Liquid Crystals. *Liquid Crystals* 38 (11-12), 1699–1714. doi:10.1080/02678292.2011.603846

Jin, Y., Koh, R. H., Kim, S.-H., Kim, K. M., Park, G. K., and Hwang, N. S. (2020). Injectable Anti-Inflammatory Hyaluronic Acid Hydrogel for Osteoarthritic Cartilage Repair. *Mater. Sci. Eng. C* 115, 111096. doi:10.1016/j.msec.2020.111096

Khan, M. U. A., Raza, M. A., Razak, S. I. A., Abdul Kadir, M. R., Haider, A., Shah, S. A., et al. (2020). Novel Functional Antimicrobial and Biocompatible Arabinoxylan/Guar Gum Hydrogel for Skin Wound Dressing Applications. *J. Tissue Eng. Regen. Med.* 14, 1488–1501. doi:10.1002/term.3115

Kumar, A., I Matari, I. A., and Han, S. S. (2020). 3D Printable Carboxylated Cellulose Nanocrystal-Reinforced Hydrogel Inks for Tissue Engineering. *Biofabrication* 12 (2), 025029. doi:10.1088/1758-5090/ab736e

Kumar, A., Matari, I. A. I., Choi, H., Kim, A., Suk, Y. J., Kim, J. Y., et al. (2019). Development of Halloysite Nanotube/Carboxylated-Cellulose Nanocrystal-

Reinforced and Ionically-Crosslinked Polysaccharide Hydrogels. *Mater. Sci. Eng. C* 104, 109983. doi:10.1016/j.msec.2019.109983

Lei, H., Zhu, C., and Fan, D. (2020). Optimization of Human-Like Collagen Composite Polysaccharide Hydrogel Dressing Preparation Using Response Surface for Burn Repair. *Carbohydr. Polym.* 239, 116249. doi:10.1016/j.carbpol.2020.116249

Li, M., Liang, Y., He, J., Zhang, H., and Guo, B. (2020). Two-Pronged Strategy of Biomechanically Active and Biochemically Multifunctional Hydrogel Wound Dressing to Accelerate Wound Closure and Wound Healing. *Chem. Mater.* 32, 9937–9953. doi:10.1021/acs.chemmater.0c02823

Li, W., Wu, D., Zhu, S., Liu, Z., Luo, B., Lu, L., et al. (2019). Sustained Release of Plasmid DNA from PLLA/POSS Nanofibers for Angiogenic Therapy. *Chem. Eng. J.* 365, 270–281. doi:10.1016/j.cej.2019.02.043

Lin, S.-P., Kung, H.-N., Tsai, Y.-S., Tseng, T.-N., Hsu, K.-D., and Cheng, K.-C. (2017). Novel Dextran Modified Bacterial Cellulose Hydrogel Accelerating Cutaneous Wound Healing. *Cellulose* 24 (11), 4927–4937. doi:10.1007/s10570-017-1448-x

Lin, S., Yang, G., Jiang, F., Zhou, M., Yin, S., Tang, Y., et al. (2019). A Magnesium-Enriched 3D Culture System that Mimics the Bone Development Microenvironment for Vascularized Bone Regeneration. *Adv. Sci.* 6 (12), 1900209. doi:10.1002/advs.201900209

Lin, Z., Li, R., Liu, Y., Zhao, Y., Ao, N., Wang, J., et al. (2020). Histatin1-Modified Thiolated Chitosan Hydrogels Enhance Wound Healing by Accelerating Cell Adhesion, Migration and Angiogenesis. *Carbohydr. Polym.* 230, 115710. doi:10.1016/j.carbpol.2019.115710

Liu, L., Xiang, Y., Wang, Z., Yang, X., Yu, X., Lu, Y., et al. (2019). Adhesive Liposomes Loaded onto an Injectable, Self-Healing and Antibacterial Hydrogel for Promoting Bone Reconstruction. *NPG Asia Mater.* 11 (1), 81. doi:10.1038/s41427-019-0185-z

Liu, W., Liu, K., Zhu, L.-H., Li, W., Liu, K., Wen, W., et al. (2020). Liquid Crystalline and Rheological Properties of Chitin Whiskers with Different Chemical Structures and Chargeability. *Int. J. Biol. Macromolecules* 157, 24–35. doi:10.1016/j.ijbiomac.2020.04.158

Liu, Z., Hu, D., Huang, L., Li, W., Tian, J., Lu, L., et al. (2018). Simultaneous Improvement in Toughness, Strength and Biocompatibility of Poly(Lactic Acid) with Polyhedral Oligomeric Silsesquioxane. *Chem. Eng. J.* 346, 649–661. doi:10.1016/j.cej.2018.03.077

Lockwood, N. A., Mohr, J. C., Ji, L., Murphy, C. J., Palecek, S. P., de Pablo, J. J., et al. (2006). Thermotropic Liquid Crystals as Substrates for Imaging the Reorganization of Matrigel by Human Embryonic Stem Cells. *Adv. Funct. Mater.* 16 (5), 618–624. doi:10.1002/adfm.200500768

Majumder, S., Ranjan Dahiya, U., Yadav, S., Sharma, P., Ghosh, D., Rao, G. K., et al. (2020). Zinc Oxide Nanoparticles Functionalized on Hydrogel Grafted Silk Fibroin Fabrics as Efficient Composite Dressing. *Biomolecules* 10 (5), 710. doi:10.3390/biom10050710

Mao, L., Hu, S., Gao, Y., Wang, L.-Q., Zhao, W.-W., Fu, L., et al. (2020). Biodegradable and Electroactive Regenerated Bacterial Cellulose/MXene (Ti3 C2 Tx) Composite Hydrogel as Wound Dressing for Accelerating Skin Wound Healing under Electrical Stimulation. *Adv. Healthc. Mater.* 9 (19), e2000872. doi:10.1002/adhm.202000872

Nosrati, H., Khodaei, M., Alizadeh, Z., and Banitalebi-Dehkordi, M. (2021). Cationic, Anionic and Neutral Polysaccharides for Skin Tissue Engineering and Wound Healing Applications. *Int. J. Biol. Macromolecules* 192, 298–322. doi:10.1016/j.ijbiomac.2021.10.013

Peng, J., Zhao, H., Tu, C., Xu, Z., Ye, L., Zhao, L., et al. (2020). *In Situ* hydrogel Dressing Loaded with Heparin and Basic Fibroblast Growth Factor for Accelerating Wound Healing in Rat. *Mater. Sci. Eng. C* 116, 111169. doi:10.1016/j.msec.2020.111169

Sheng, L., Zhang, Z., Zhang, Y., Wang, E., Ma, B., Xu, Q., et al. (2021). A Novel "Hot Spring"-Mimetic Hydrogel with Excellent Angiogenic Properties for Chronic Wound Healing. *Biomaterials* 264, 120414. doi:10.1016/j.biomaterials.2020.120414

Tamahkar, E., Özkahraman, B., Süloğlu, A. K., İdil, N., and Perçin, I. (2020). A Novel Multilayer Hydrogel Wound Dressing for Antibiotic Release. *J. Drug Deliv. Sci. Technol.* 58, 101536. doi:10.1016/j.jddst.2020.101536

Tang, X., Wang, X., Sun, Y., Zhao, L., Li, D., Zhang, J., et al. (2021). Magnesium Oxide-Assisted Dual-Cross-Linking Bio-Multifunctional Hydrogels for Wound Repair during Full-Thickness Skin Injuries. *Adv. Funct. Mater.* 31 (43), 2105718. doi:10.1002/adfm.202105718

Wu, S., Yang, X., Li, W., Du, L., Zeng, R., and Tu, M. (2017). Enhancing Osteogenic Differentiation of MC3T3-E1 Cells by Immobilizing RGD onto Liquid Crystal Substrate. *Mater. Sci. Eng. C* 71, 973–981. doi:10.1016/j.msec.2016.11.003

Xie, W., Ouyang, R., Wang, H., Li, N., and Zhou, C. (2020). Synthesis and Cytotoxicity of Novel Elastomers Based on Cholesteric Liquid Crystals. *Liquid Crystals* 47 (3), 449–464. doi:10.1080/02678292.2019.1657594

Xie, Y., Liao, X., Zhang, J., Yang, F., and Fan, Z. (2018). Novel Chitosan Hydrogels Reinforced by Silver Nanoparticles with Ultrahigh Mechanical and High Antibacterial Properties for Accelerating Wound Healing. *Int. J. Biol. Macromolecules* 119, 402–412. doi:10.1016/j.ijbiomac.2018.07.060

Yang, C., Huang, H., Fan, S., Yang, C., Chen, Y., Yu, B., et al. (2021). A Novel Dual-Crosslinked Functional Hydrogel Activated by POSS for Accelerating Wound Healing. *Adv. Mater. Technol.* 6 (4), 2001012. doi:10.1002/admt.202001012

Yang, Y., Wang, X., Yang, F., Shen, H., and Wu, D. (2016). A Universal Soaking Strategy to Convert Composite Hydrogels into Extremely Tough and Rapidly Recoverable Double-Network Hydrogels. *Adv. Mater.* 28 (33), 7178–7184. doi:10.1002/adma.201601742

Yin, Y., Tian, X., Jiang, X., Wang, H., and Gao, W. (2016). Modification of Cellulose Nanocrystal via SI-ATRP of Styrene and the Mechanism of its Reinforcement of Polymethylmethacrylate. *Carbohydr. Polym.* 142, 206–212. doi:10.1016/j.carbpol.2016.01.014

Yuan, Y., Shen, S., and Fan, D. (2021). A Physicochemical Double Cross-Linked Multifunctional Hydrogel for Dynamic Burn Wound Healing: Shape Adaptability, Injectable Self-Healing Property and Enhanced Adhesion. *Biomaterials* 276, 120838. doi:10.1016/j.biomaterials.2021.120838

Zhai, W., Lu, H., Chen, L., Lin, X., Huang, Y., Dai, K., et al. (2012). Silicate Bioceramics Induce Angiogenesis during Bone Regeneration. *Acta Biomater.* 8 (1), 341–349. doi:10.1016/j.actbio.2011.09.008

Zhan, Y., Deng, B., Wu, H., Xu, C., Wang, R., Li, W., et al. (2021). Biomineralized Composite Liquid Crystal Fiber Scaffold Promotes Bone Regeneration by Enhancement of Osteogenesis and Angiogenesis. *Front. Pharmacol.* 12, 736301. doi:10.3389/fphar.2021.736301

Zhang, K., Lin, S., Feng, Q., Dong, C., Yang, Y., Li, G., et al. (2017). Nanocomposite Hydrogels Stabilized by Self-Assembled Multivalent Bisphosphonate-Magnesium Nanoparticles Mediate Sustained Release of Magnesium Ion and Promote *In-Situ* Bone Regeneration. *Acta Biomater.* 64, 389–400. doi:10.1016/j.actbio.2017.09.039

Zhang, Y., Chen, M., Tian, J., Gu, P., Cao, H., Fan, X., et al. (2019). *In Situ* bone Regeneration Enabled by a Biodegradable Hybrid Double-Network Hydrogel. *Biomater. Sci.* 7 (8), 3266–3276. doi:10.1039/c9bm00561g

Zhang, Z., Chen, Z., Wang, Y., and Zhao, Y. (2020). Bioinspired Conductive Cellulose Liquid-Crystal Hydrogels as Multifunctional Electrical Skins. *Proc. Natl. Acad. Sci. U.S.A.* 117, 18310–18316. doi:10.1073/pnas.2007032117

Zhao, L., Niu, L., Liang, H., Tan, H., Liu, C., and Zhu, F. (2017). pH and Glucose Dual-Responsive Injectable Hydrogels with Insulin and Fibroblasts as Bioactive Dressings for Diabetic Wound Healing. *ACS Appl. Mater. Inter.* 9 (43), 37563–37574. doi:10.1021/acsami.7b09395

Conflict of Interest: The authors declare that the research was conducted in the absence of any commercial or financial relationships that could be construed as a potential conflict of interest.

Publisher's Note: All claims expressed in this article are solely those of the authors and do not necessarily represent those of their affiliated organizations, or those of the publisher, the editors, and the reviewers. Any product that may be evaluated in this article, or claim that may be made by its manufacturer, is not guaranteed or endorsed by the publisher.

frontiers | Frontiers in Materials

ORIGINAL RESEARCH
published: 05 May 2022
doi: 10.3389/fmats.2022.883027

Mechanical and Antibacterial Properties of h-BN-TiO_2 Nanocomposite-Modified Glass Ionomer Cement

Yu Ma[1,2,3†], Yan-Zhu Guo[1†], Yan Liu[1], Yu-Rui Wang[1], Jiang-Chuan Yang[1], Xin-Zi Kong[1], Hong-Lin Jia[1], Rui-Zhi Li[1], Qi-Ze Han[1], Cheng-Dong Zheng[4], Xin-Jun Hu[5*] and Bin Liu[1,2*]*

[1]School and Hospital of Stomatology, Lanzhou University, Lanzhou, China, [2]Key Laboratory of Dental Maxillofacial Reconstruction and Biological Intelligence Manufacturing, Lanzhou University, Lanzhou, China, [3]Biointerfaces Institute, University of Michigan, Ann Arbor, MI, United States, [4]Clinical Research Center of Shanxi Province for Dental and Maxillofacial Diseases, College of Stomatology, Xi'an Jiaotong University, Xi'an, China, [5]School of Mechanical Engineering, Sichuan University of Science and Engineering, Zigong, China

This study investigated the mechanical properties and antibacterial properties of hexagonal boron nitride and titanium dioxide (h-BN-TiO_2) nanocomposite modified traditional glass ionomer cement. The mechanism of formation of the h-BN-TiO_2 nanocomposite was elucidated by conducting molecular dynamics (MD) simulations using the Material Studio (MS) software. Furthermore, synthesis of h-BN-TiO_2 nanocomposite by the original growth method using hexagonal boron nitride nanosheets (h-BNNs) and titanium dioxide nanoparticles (TiO_2 Nps) and characterization using TEM and AFM to determine their particle sizes, morphologies, and structures. The mechanical properties and antibacterial efficacies of the glass ionomer cement composites were analyzed based on the different mass fractions (0, 0.3, 0.7, 1.1, and 1.5 wt%) of the h-BN-TiO_2 nanocomposite. The results showed when the concentration of the h-BN-TiO_2 nanocomposite was 1.1 wt%, the Compressive strength (CS) and Vicker hardness (VHN) were 80.2% and 149.65% higher, respectively, compared to the glass ionomer cement without any h-BN-TiO_2 nanocomposite. Also, the increase in the concentration of the h-BN-TiO_2 nanocomposite led to a decrease in both the coefficient of friction (COF) and solubility, but a 93.4% increase in the antibacterial properties of the glass ionomer cement composites. The cell survival rate of each group was more than 70% after 48 h, but the difference was not statistically significant ($p > 0.05$). Therefore, the h-BN-TiO_2 nanocomposite served as a reinforcing material for glass ionomer cement, which can be useful in clinical dentistry and provide a new strategy for improving the clinical utility of glass ionomer cement.

Keywords: glass ionomer cement, h-BN-TiO2 nanocomposite, mechanical properties, antibacterial properties, molecular dynamics analysis

OPEN ACCESS

Edited by:
Marziyeh Ranjbar-Mohammadi, University of Bonab, Iran

Reviewed by:
Kawaljit Randhawa, Charotar University of Science and Technology, India
Sara Banijamali, Materials and Energy Research Center, Iran

***Correspondence:**
Yu Ma
mayu@lzu.edu.cn
Xin-Jun Hu
xjhu@suse.edu.cn
Bin Liu
liubkq@lzu.edu.cn

†These authors have contributed equally to this work and share first authorship

Specialty section:
This article was submitted to Biomaterials, a section of the journal Frontiers in Materials

Received: *24 February 2022*
Accepted: *07 April 2022*
Published: *05 May 2022*

Citation:
Ma Y, Guo Y-Z, Liu Y, Wang Y-R, Yang J-C, Kong X-Z, Jia H-L, Li R-Z, Han Q-Z, Zheng C-D, Hu X-J and Liu B (2022) Mechanical and Antibacterial Properties of h-BN-TiO_2 Nanocomposite-Modified Glass Ionomer Cement. Front. Mater. 9:883027. doi: 10.3389/fmats.2022.883027

1 INTRODUCTION

Since the 1970s, glass ionomer cement (GIC) has received significant attention as a dental restorative material in clinical practice due to its anti-caries effect, biocompatibility (Nicholson et al., 1991), excellent bonding with dentin (Nicholson, 2016; Yamakami et al., 2018), and simplicity of handling (Nicholson et al., 2020). However, GIC undergoes initial dehydration and has a high swelling rate, both of which are disadvantages that have significantly limit the mechanical and antibacterial properties of GIC (Moshaverinia et al., 2009a; Brito et al., 2010; Sun et al., 2018). To overcome these shortcomings, researchers have experimented with various methods to improve the mechanical properties of GIC. One effective method entailed incorporating organic additives, such as methacryloyl, N-vinylcaprolactam, N-vinylpyrrolidone-modified acrylic acid copolymer, and fluorapatite, into GIC to increase the mechanical strength of GIC through chemical bonding (Simmons, 1990; Moshaverinia et al., 2008a; Moshaverinia et al., 2008b; Moshaverinia et al., 2008c; Moshaverinia et al., 2009b; Moshaverinia et al., 2019; Randhawa and Patel, 2020b; Randhawa and Patel, 2020c). However, these methods are finite, and there is still significant room for improving the mechanical properties of the GIC.

In recent years, nanoflake or nanoparticle rigid materials, such as fluorapatite (FAp) nanoparticles (NPs) (Ching et al., 2018), calcium fluoride (CaF_2) (Xu et al., 2010), titanium dioxide (Zhang and Gao, 2001), and hydroxyapatite (Moheet et al., 2018), have demonstrated to be ideal candidates as nanoscale fillers, as their incorporation into dental materials has led to the effective reinforcement of dental substrates. While one study reported that adding CaF_2 nanoparticles to resin-modified GIC (RMGIC) improved the mechanical properties of the RMGIC (Moreau and Xu, 2010), the insolubility of CaF_2 reduces the ability of GIC to release fluoride. Hexagonal boron nitride (h-BN) is a 2D material like graphite, has excellent thermal, mechanical, and tribological properties (Randhawa and Patel, 2020c). Kawaljit Singh Randhawa et al. report that with the increase of content of h-BN, the COF and wear rate of composites decreased up to 4 wt% due to transfer film formation and lubricious effects of h-BN fillers (Randhawa and Patel, 2020a). Surprisingly, h-BN in nanoscale usually exhibit some unique properties in physical and chemical aspects compared with bulk h-BN materials. Some studies reported that hexagonal boron nitrides nanaosheets (h-BNNs) have received significant attention as a two-dimensional nanomaterial because of their excellent mechanical properties and biological safety (Czarniewska et al., 2019; Yue et al., 2019). In addition, h-BNNs are white powders, which enable them to be an ideal filler for medical materials, especially dental materials, with aesthetic requirements. Lee B et al. prepared boron nitride nanoplatelets/alumina (BNNP/ATZP) ceramic composites by spark plasma sintering (SPS) technology after mixing alumina powder with BNNs prepared by ball milling (Lee et al., 2020), after which a 27% increase in the bending strength of the composites, as well as a 37.5% increase in the fracture toughness, were achieved. Farooq et al. prepared a composite by functionalized hexagonal boron nitride nanosheets (h-BNNSs-OH) with polymethyl methacrylate (PMMA), which led to a 70% increase in the ultimate tensile strength (UTS) of the functionalized BN/PMMA (Farooq et al., 2020). Despite these advancements, only a few studies have investigated the addition of rigid nanomaterials to improve the mechanical properties of GIC.

Since traditional GIC are capable of releasing fluoride into the surrounding tissue, they have inherent antibacterial and anti-caries properties (Wiegand et al., 2007; Hasan et al., 2019). However, the release of fluoride would also be accompanied by the depletion of fluoride on the surface of the filling to form insoluble particles in the interior of the filling, making it inadequate to achieve long-term antibacterial effects. Recently, GIC composites have been prepared by the addition of antimicrobial agents or materials, such as dimethylamine lauryl methacrylate (DMADDM) (Zhang et al., 2015; Wang et al., 2016), chlorhexidine, and antibiotics (Abdallah et al., 2020), to increase the antibacterial and anticaries properties of the GIC (Yesilyurt et al., 2009). However, achieving a controlled rate release and the terminal depletion of drug represent the bottlenecks that limit the utility of GIC composites in clinical application. In addition, the clinical application of these materials is further restricted by the risk of drug resistance and the potential to produce superbugs (Varela et al., 2021). Thus, the development of emerging antibacterial nanomaterials would be highly advantageous to improve the antibacterial properties of GIC. Elsaka et al. reported that the addition of 2, 3, 5, and 7 wt% TiO_2 NPs to GIC was effective for inhibiting bacterial growth, and the compressive strength and microhardness of the GIC composites increased by 17% and 4%, respectively, over the unmodified GIC (Elsaka et al., 2011). Nida Hamid et al. reported that GIC containing 3 wt% TiO_2 NPs caused an increase in the inhibition rate of *Streptococcus mutans* (S.mutans) by 30% (Hamid et al., 2019). Chen B. et al. prepared ZnO/Ag hybrid microspheres that demonstrated excellent antibacterial activities, with a minimum inhibition concentration (MIC) and a minimum biotic concentration (MBC) of *Staphylococcus aureus* of 40 and 80 μg/ml, respectively (Chen et al., 2020). Since the antibacterial properties of these nanomaterials were dependent on their surface characteristics, such as the mechanical damage to bacteria caused by electrostatic forces (Hajipour et al., 2012), they exhibit long-term and non-fading antibacterial properties while eliminating the risk of bacterial resistance. While the aforementioned methods were effective for improving the antibacterial performance of GIC, there remains a lack of effective methods for synergistically improving both the antibacterial and the mechanical properties of GIC.

Given the outstanding mechanical effect of h-BNNs and the inherent antibacterial properties of TiO_2 NPs, this study investigated the combination of h-BN and TiO_2 by first-principles calculations of density functional theory. The ball-milling and the thermal hydrolysis of Titanium oxysulfate were used to prepare h-BN-TiO_2 nanocomposite to construct a two-dimensional and zero-dimensional nanocomposite system. Subsequently, the synthesized h-BN-TiO_2 nanocomposite was added to GIC in a certain proportion, aiming not only to enhance GIC effectively achieved a substantial improvement in the

mechanical and antibacterial properties of traditional GIC (**Figure 1**), but also to provide a novel insight into the development of more GIC enhancement methods.

2 MATERIALS AND METHODS

2.1 Molecular Dynamics Analysis of Hexagonal Boron Nitride and Titanium Dioxide

We utilized molecular dynamic (MD) simulations to analyze the changes in the molecular structure and reaction system energy during the recombination of h-BN and TiO_2 to better understand the reaction mechanism. Based on the first principles of density functional theory (DFT), we calculated the adsorption energy of TiO_2 (anatase type, 101 face) onto the h-BN using the Forcite$^+$ module in MS package. Three systems were constructed: 1) the anatase-TiO_2 model, 2) the monolayer h-BN model, and 3) the h-BN-TiO_2 composite model. The structural and size parameters of TiO_2 and h-BN inputted into the software program were derived from the literature and were used to optimize the geometric structures of TiO_2 (**Supplementary Figure S1, S2**) and h-BN (**Supplementary Figure S3, S4**). The initial h-BN-TiO_2 composite structure was the (101) TiO_2 surface adsorbed onto the h-BN. Simulations were carried out under the NVT ensemble, and each system was simulated for 100 ns. The adsorption energy of anatase-TiO_2 on h-BN was calculated after the reaction reached equilibrium using the following equation:

$$E = E_{h-BN-TiO_2} - \left(E_{h-BN} + E_{TiO_2}\right)$$

The adsorption energy of the TiO_2 onto the h-BN was calculated by selecting the final XML schema definition (XSD) structure of the TiO_2 and the h-BN from the MD simulations and subtracting the TiO_2 energy from the total energy of the h-BN-TiO_2 system and then subtracting the h-BN energy.

2.2 Preparation of Hexagonal Boron Nitride and Titanium Dioxide Nanocomposite

2.2.1 Preparation and Exfoliation of Hexagonal Boron Nitride Nanosheets

The h-BNNs were prepared by a widely used physical method with controlled numbers of the layer. The 0.2 g h-BN (Sigma-Aldrich, American) powder was dispersed in a mixture of 100 ml of ethanol (Damao Chemical Reagent Factory, Tianjin, China) and 100 ml of deionized water, to prepare a large amount of stripped h-BNNs by mechanical ball milling.

2.2.2 Preparation of Hexagonal Boron Nitride and Titanium Dioxide Nanocomposite

The precursor of amorphous hydrate was prepared through the aqueous phase reaction of titanyl sulfate ($TiOSO_4$, Sigma-Aldrich, American) and 10% ammonium hydroxide solution ($NH_3{\cdot}H_2O$, Damao Chemical Reagent Factory, Tianjin, China) in an ice bath until a pH value of 6 is attained. The white precipitate was separated by centrifugation and washed with deionized water in three cycles to remove the sulfate ions. The fresh precipitate was mixed with a predefined volume of exfoliated h-BNNs suspension in water and subsequently refluxed at 80°C for 5 h to produce white precipitates. Using the method, samples of h-BN-TiO_2 nanocomposite were prepared.

2.3 Characterization of Hexagonal Boron Nitride and Titanium Dioxide Nanocomposite

The particle size and the morphology of the h-BN-TiO_2 nanocomposite were inspected using the transmission electron microscope (TEM, Tecnai F30, FEI, Hillsboro, American) and the atomic force microscope (AFM, Multimode 8-HR, BRUKER, American). The crystal structure of the h-BN-TiO_2 nanocomposite was characterized by X-Ray diffraction (XRD, Smart APEX Ⅱ, BRUKER, German) patterns and the Raman spectra were measured using the micro confocal Raman spectrometer (LabRAM HR Evolution, HORIBA Jobin Yvon S.A.S, Paris, France) with 532 nm laser excitation.

2.4 Preparation of Hexagonal Boron Nitride and Titanium Dioxide/Glass Ionomer Cement Composite

Commercial GIC (Chang Shu Shang Chi Dental Materials, Chang Shu, China) was selected for this study. The powder are composed of silica (SiO_2), CaF_2, sodium fluorosilicate (Na_2SiF_6), aluminum oxide (Al_2O_3), and aluminium phosphate ($AlPO_4$); the liquid are composed of polyacrylic acid, tartaric acid, and deionized water. The prepared h-BN-TiO_2 and GIC powders were weighed when the ratio of h-BN-TiO_2 to the GIC powder was 0, 0.3, 0.7, 1.1, 1.5 wt%, respectively. The quantitative h-BN-TiO_2/GIC powder and GIC liquid were mixed on a ratio of 2:1. The mixture was thoroughly shaken and quickly transferred to the mold for compression, after it was formed and the sample was stored at 100% relative humidity at 37°C for 24 h.

2.5 Characterization of Hexagonal Boron Nitride and Titanium Dioxide/Glass Ionomer Cement Composites

2.5.1 Mechanical Performance Test of Hexagonal Boron Nitride and Titanium Dioxide/Glass Ionomer Cement Composites

2.5.1.1 Vicker Hardness Test

The VHN test was conducted on each group of 5 specimens with a diameter and thickness of 10 mm and about 5 mm, respectively using a Vicker Hardness Tester (HV-1000IS, SIOMN, Shanghai, China) with a load of 100 g and a dwelling time of 10 s, and the average results were analyzed. The diagonal length of each indentation was measured directly using a graduated eyeglass Lens. The VHN was obtained using the following Formula 5:

$$VHN = \frac{0.1891F}{d^2}$$

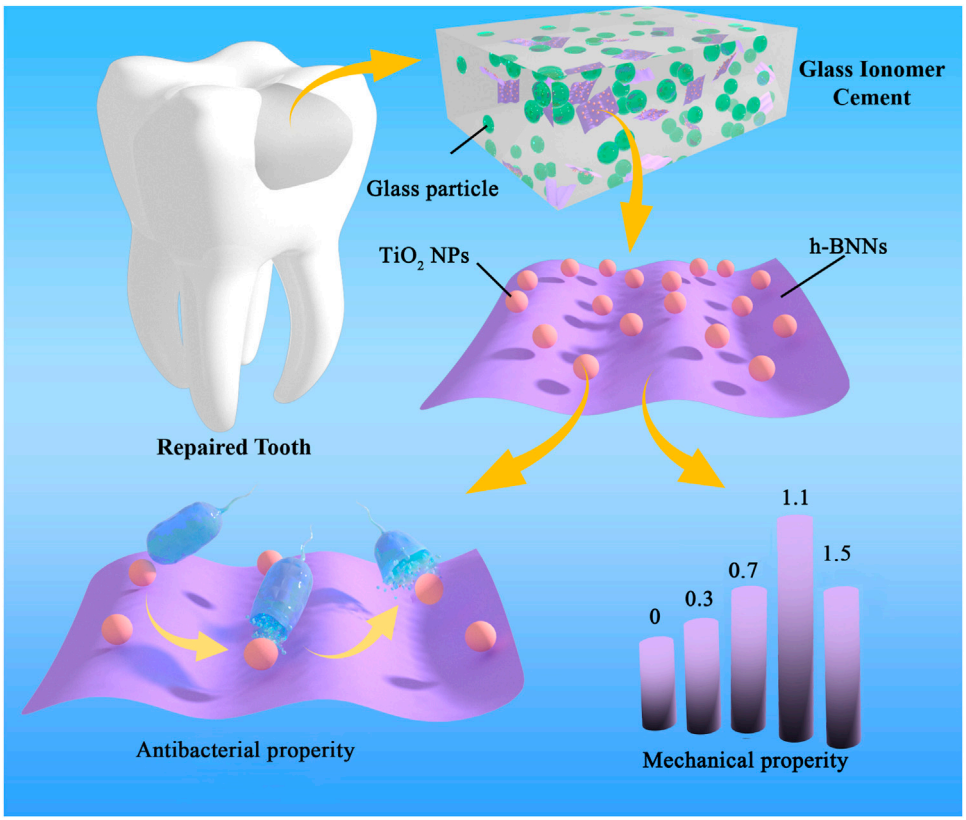

FIGURE 1 | Schematic diagram of synthesis and performance evaluation h-BN-TiO_2/GIC composites.

Where d is the length of the diagonals (mm) and F denotes the load (N).

2.5.1.2 Cs Test

A cylinder (4 mm in diameter, 6 mm in high) made from quartz glass molds was the compression specimen. The CS test was performed on a universal testing machine (312 Frame, Test Resources, United States) at a rate of 0.5 mm/min (Sun et al., 2018). The CS was calculated based on the following formula:

$$CS = \frac{F}{r^2}$$

where F is the load at the fracture point (N) and r denotes the radius of the cylindrical specimen (mm).

2.5.1.3 Friction Experiment

Three samples of each ratio (10 × 4 × 6 mm) were prepared and cured for 24 h. Zirconia ceramic balls with a diameter of 6 mm were selected for testing on the UMT-2 friction testing machine (UMT-2, CETR, American). The experimental parameters are set as follows: the loading force, speed, frequency, test time, and the running distance of the sample were 5 N, 10 mm/s, 2 Hz, 20 min, and 5 mm, respectively (Sun et al., 2018). The COF was automatically calculated by computer software.

2.5.2 Scanning Electron Microscope Observation

To evaluate the morphology of the materials, the scanning electron microscope (SEM, Nova200 NanoLab, FEI, Eindhoven, Nederlanden) was used to analyze the fractured surfaces of pure GIC and h-BN-TiO_2/GIC composites.

2.5.3 Evaluation of Solubility

Five specimens were prepared for each group and immersed in artificial saliva at 37°C. The samples were taken out after 1, 7, 14, 28, and 35 days, respectively, and the surface was rinsed with deionized water. After drying, the comparison of the weights before and after immersing in artificial saliva were done to calculate solubility of per sample weight. The associated calculations were presented in the following equation:

$$S = \frac{M_0 - M_1}{M_0}$$

where M_1 denotes the weight of the soaked sample after x days (1 = 1, 7, 14, 28, 35), M_0 is the row weight of the specimen.

2.5.4 Evaluation of Biological Performance

2.5.4.1 Direct Contact Test

The DCT method (Sun et al., 2018) was used to evaluate the h-BN-TiO_2/GIC composites against *Streptococcus mutans* (*S. mutans*, ATCC®700610). Round samples and glass slides with a diameter

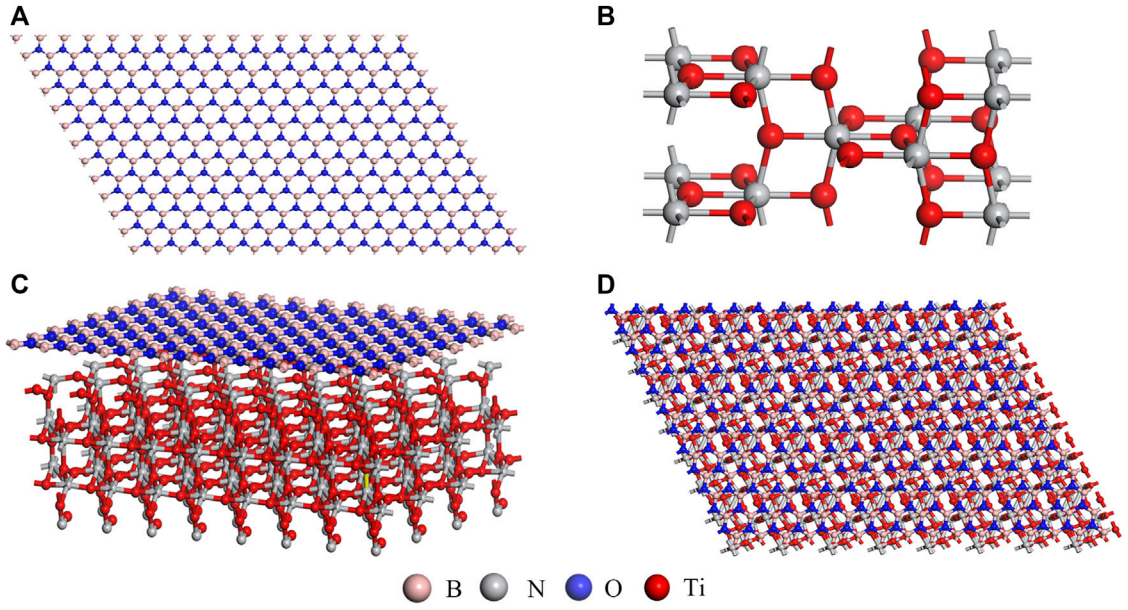

FIGURE 2 | Heterostructures of h-BN and TiO_2 **(A,B)**, h-BN-TiO_2 side views **(C)** and top views **(D)**.

of 10 mm were prepared, cleaned and disinfected with 75% alcohol. Then 100 μL bacterial suspension with a concentration of 10^6 CFU/ml was drawn and dropped onto the sample surface until the glass slide was covered. After incubation in a biochemical incubator (SHP-150PY, Jing hong, Shanghai) for 24 h, the sample and the surface of the slides were washed with PBS; Subsequently, the washing solution was diluted 100 times for the plating test and the analysis of the data. The measurement was replicated thrice in each group, and the loss of viability (VL) in the S.mutans was calculated as follows:

$$V_L = \frac{N_m - N_x}{N_x} 100\%$$

where N_m denotes the numbers of colonies corresponding to the blank group and N_x (x = 0, 0.3, 0.7, 1.1, 1.5) corresponds to the h-BN-TiO_2/GIC (0 wt%), h-BN-TiO_2/GIC (0.3 wt%), h-BN-TiO_2/GIC (0.7 wt%), h-BN-TiO_2/GIC (1.1 wt%) and h-BN-TiO_2/GIC (1.5 wt%) composites, respectively.

2.5.4.2 Scanning Electron Microscope Observation

The sample preparation method was the same as above. The disinfected h-BN-TiO_2/GIC specimen was placed in the pore cell culture plate, *S.mutans* suspension was added and subsequently incubated in a biochemical incubator for 4 h. After fixing in 2.5% glutaraldehyde (Sigma-Aldrich, American) and dehydrated in graded ethanol, the sample was observed using SEM after spraying with gold.

2.5.4.3 Cytotoxicity Testing

The cytotoxicity of the sample was detected through the evaluation of the effect of the sample on the viability and morphology of mouse fibroblasts (L-929, Shanghai Cell Bank, Chinese Academy of Sciences) *in vitro*. The sample preparation and sterilization methods were the same as before. Based on ISO standard, the extract was prepared with DMEM serum-free (Sigma-Aldrich, American) cell culture medium with a specific surface area/volume ratio of 3 cm^2/ml, and the eluate was prepared by incubating for 24 h in a biochemical incubator. The cells were seeded in a 96-well cell culture plate at a cell culture medium concentration of 5×10^3/(100 μl) per well and adhered to the wall after 24 h of culture. Subsequently, the medium is replaced with 100 μl of sample eluate and with the addition of 10 μl of tetramethylammonium salt (MTT tetrazolium salt; Sigma-Aldrich, American) to each well. The incubation period is continued for 24, 48, and 72 h in a biochemical incubator, and absorbance was measured at 490 nm using the enzyme-labeled method. The experiment was replicated thrice.

2.6 Statistical Analysis

All statistical analysis were conducted using GraphPad Prism (V6.01, GraphPad Software, San Diego, CA, United States) and Origin (2019, Origin Lab, Northampton, Massachusetts, United States) Windows version. Tukey's test was used in the subsequent multiple comparisons, the difference was considered significant when $p < 0.05$, and the difference was very significant when $p < 0.001$. All determinations were independently replicated thrice to ensure reproducibility.

3 RESULTS

3.1 Characterization of Hexagonal Boron Nitride and Titanium Dioxide Nanocomposite

The MD simulations of the adsorption of TiO_2 onto the h-BN are shown in **Figure 2**. There refer to the molecular models of h-BN (**Figure 2A**) and TiO_2 (**Figure 2B**) after structural optimization.

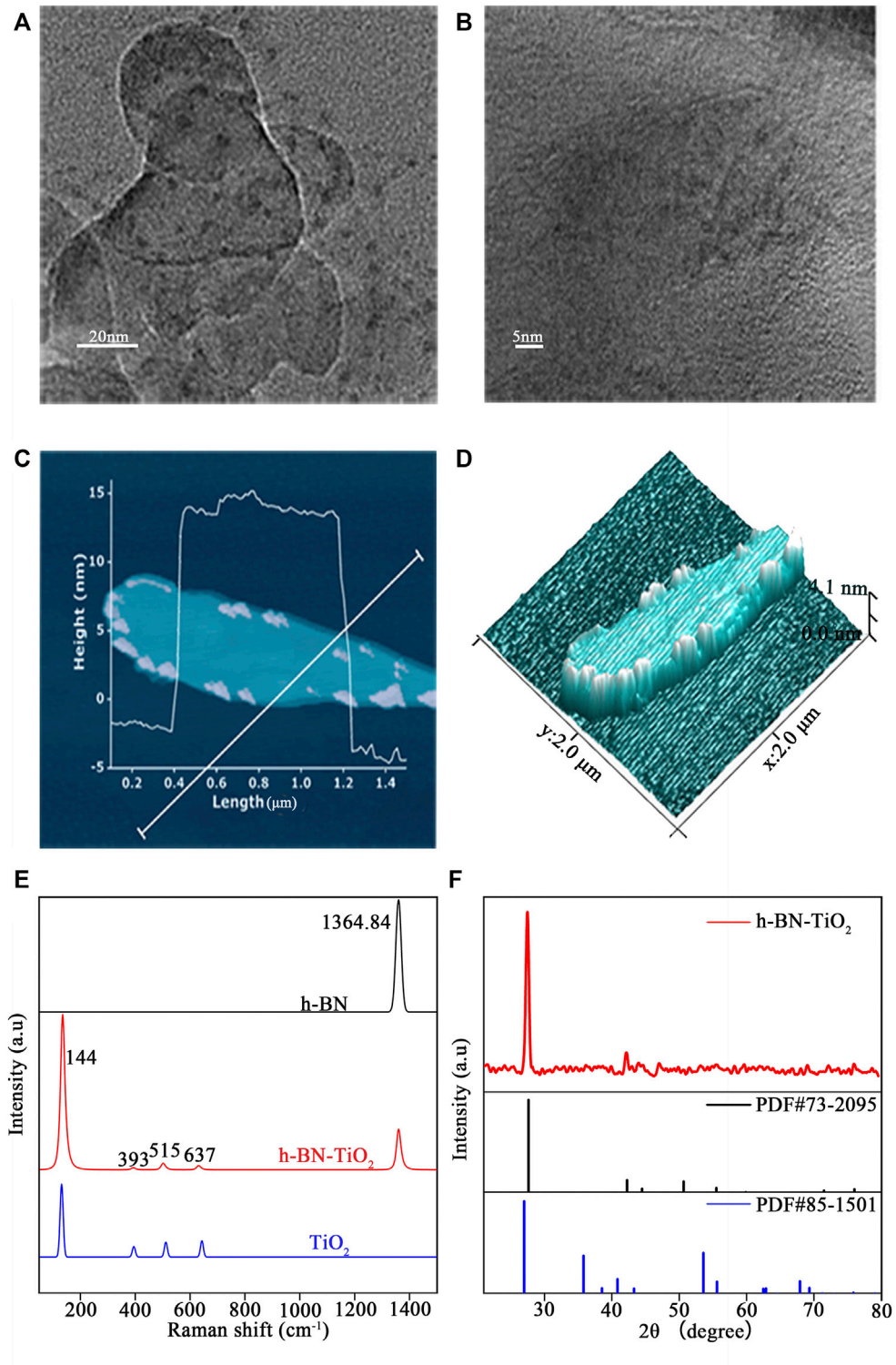

FIGURE 3 | TEM analysis of h-BN-TiO_2 by low **(A)** and high **(B)** magnification images. And the prepared h-BN-TiO_2 **(C,D)** were observed by AFM. Raman spectrometry **(E)** and XRD patterns **(F)** of prepared h-BN-TiO_2.

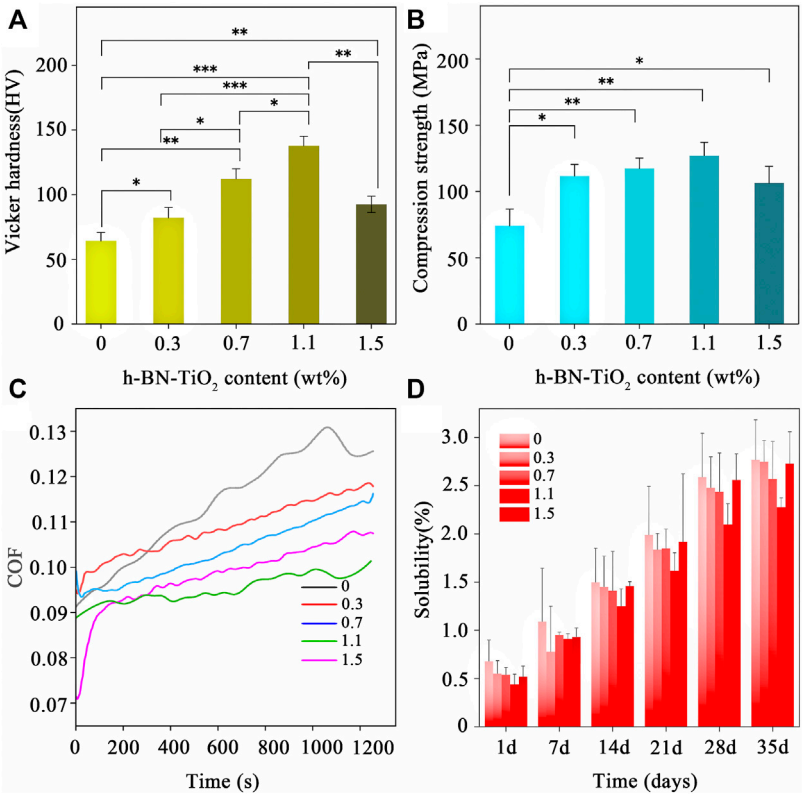

FIGURE 4 | Mechanical properties and solubility of h-BN-TiO_2/GIC composite (0, 0.3, 0.7, 1.1, 1.5 wt%). **(A)** Vicker hardness (in HV); **(B)** Compression stress (in MPa); **(C)** the real-time COF; and **(D)** solubility (%).

Figures 2C,D show the final XSD structure of the TiO_2 and the h-BN from the MD simulations. It was found by calculation that the adsorption energy of TiO_2 onto the surface of h-BN was −235 kcal/mol, indicating that the adsorption process was exothermic.

The morphologies of the h-BNNs and TiO_2 NPs were observed by TEM. **Figure 3A** shows that the h-BN featured a thin and transparent two-dimensional nanostructure with a lateral dimension ranging from 200 nm to 1 μm, while the TiO_2 NPs exhibited diameters ranging from ranging from 20 to 200 nm after growing *in situ* on the surface of the h-BNNs. The lattice fringes of the TiO_2 NPs were observed under high magnification (**Figure 3B**). To further investigate the unique structure of the h-BN-TiO_2 nanocomposite, AFM was used to observe the three-dimensional morphology. **Figure 3C** shows that the h-BNNs and TiO_2 NPs form a rivet structure with a minimum thickness of 4.0 nm (**Figure 3D**). In addition, the Raman spectrum confirmed the existence of an h-BN-TiO_2 nanocomposite (**Figure 3E**). In previous studies, the Raman spectra of h-BNNs featured peaks near 1,364.84 cm^{-1} (Czarniewska et al., 2019), and anatase TiO_2 NPs peaks were located at 144 cm^{-1} (Eg1), 197 cm^{-1} (Eg2), 393 cm^{-1} (B1g), 512 cm^{-1} (B1g + A1g), and 635 cm^{-1} (Eg3) (Choi et al., 2005), all of which were consistent with the peaks in the Raman spectrum of the h-BN-TiO_2 nanocomposite in this study. In addition, the XRD patterns of h-BN-TiO_2 nanocomposite are shown in **Figure 3F**. All these diffraction peaks match well with the standard values of h-BN (PDF#73-2095) and TiO_2 (PDF#85-1501) and were highly consistent with the Raman spectroscopy results.

3.2 Mechanical Properties of the Hexagonal Boron Nitride and Titanium Dioxide/Glass Ionomer Cement Composites

Figures 4A,B show the VHN and CS results of the h-BN-TiO_2/GIC with 0, 0.3, 0.7, 1.1, and 1.5 wt% loading of the h-BN-TiO_2 nanocomposite. Compared to the 0 wt% h-BN-TiO_2/GIC composite, the CS of the h-BN-TiO_2/GIC composite (0.3, 0.7, 1.1, 1.5 wt%) increased by 32.8%, 64.5%, 80.2%, and 52.6%, respectively, while the VHN increased by 25.6%, 77.9%, 149.65%, and 56.5%, respectively. The VHN and CS of the 1.1 wt% h-BN-TiO_2 were the highest of all the nanocomposites, while the values began to decline from 1.5 wt%. The VHN and CS of the 1.1 wt% h-BN-TiO_2/GIC were 149.65% and 80.2% higher than the 0 wt% h-BN-TiO_2/GIC ($p < 0.001$).

Next, the friction performance of the nanocomposites were assessed. The changes in the coefficient of friction (COF) of the h-BN-TiO_2/GIC composites over time were shown in **Figure 4C**. The COF of the h-BN-TiO_2/GIC composites were more stable throughout the friction tests, and the friction curves generated from the data were smooth without fluctuations. The COF of the h-BN-TiO_2/GIC composite (0.3, 0.7, 1.1, 1.5 wt%) were lower

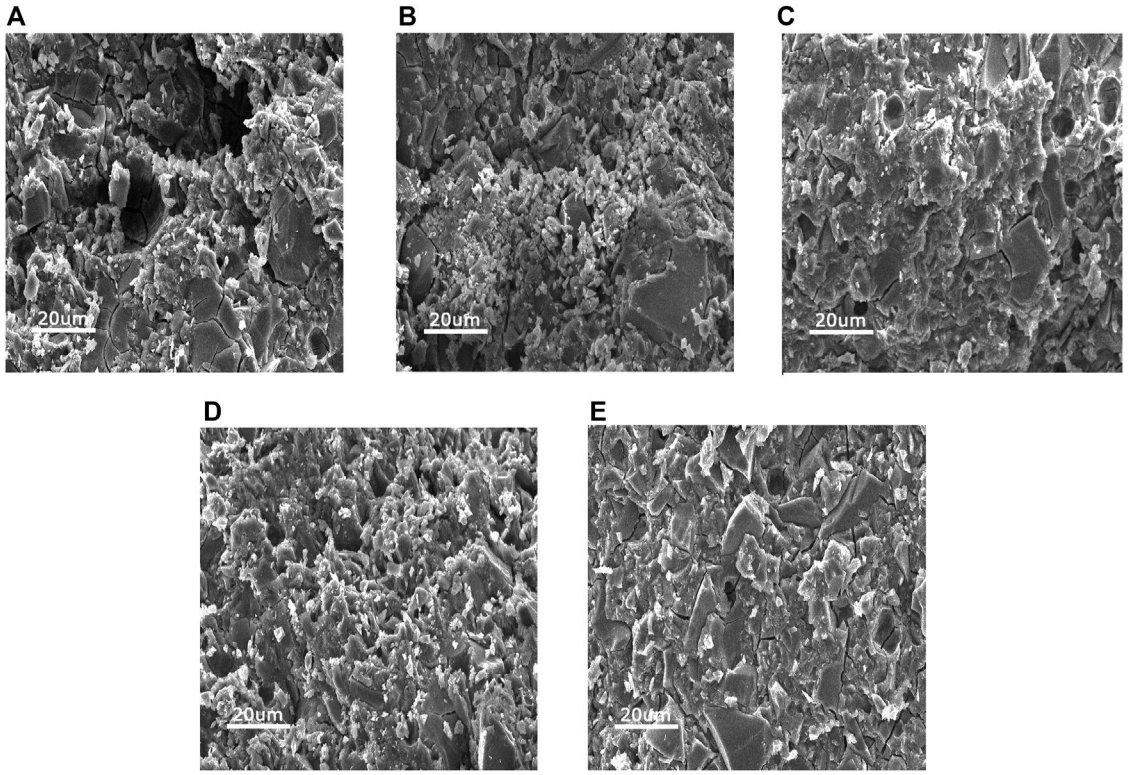

FIGURE 5 | The SEM images of the fractured surfaces of h-BN-TiO_2/GIC composites after the compression test with h-BN-TiO_2 nanocomposite concentration of **(A)** 0 wt%, **(B)** 0.3 wt%, **(C)** 0.7 wt%, **(D)** 1.1 wt%, **(E)** 1.5 wt%.

than the 0 wt% h-BN-TiO_2/GIC starting from 380 s, with the 1.1 wt% h-BN-TiO_2/GIC exhibiting the highest friction resistance.

3.3 Solubility of Hexagonal Boron Nitride and Titanium Dioxide/Glass Ionomer Cement Composites

Figure 4D shows the average solubilities of the h-BN-TiO_2/GIC (0, 0.3, 0.7, 1.1, 1.5 wt%) composites on days 1, 7, 14, 21, 28, and 35. The figures showed that the solubility of pure GIC was higher than the solubilities of the GIC composites on each day. During the first day of the solubility experiments, there were no significant differences among the h-BN-TiO_2/GIC composite groups. However, lower solubilities of the nanocomposite were manifested after extending the soaking duration and increasing the amount of h-BN-TiO_2. The 0.7 wt% and 1.1 wt% h-BN-TiO_2/GIC composites exhibited the lowest solubilities after day 14.

3.4 Characterization of the Prepared Hexagonal Boron Nitride and Titanium Dioxide/Glass Ionomer Cement Composites

SEM images of the h-BN-TiO_2/GIC (0, 0.3, 0.7, 1.1, 1.5 wt%) composites were acquired after undergoing compressive strength tests at low magnification (×500, **Figure 5**). The h-BN-TiO_2 nanocomposite was found to be uniformly dispersed throughout the GIC but could easily be distinguished from the GIC material. Some cracks and pores were observed on the fracture surfaces of all samples, but only a few of these structures were observed in the pure GIC without h-BN-TiO_2 nanocomposite.

3.5 Evaluation of Biological Performance

Figure 6(A–F) displays the antibacterial efficacy of the h-BN-TiO_2/GIC composites (0, 0.3, 0.7, 1.1, 1.5 wt%). Although the GIC had a certain degree of antibacterial effect, the h-BN-TiO_2/GIC composites (0.3, 0.7, 1.1, 1.5 wt%) showed a stronger antibacterial effect. Compared with the blank non-bacterial samples, the antibacterial rates of h-BN-TiO_2/GIC composites (0.3, 0.7, 1.1, 1.5 wt%) were 14.5%, 38.4%, 67.2%, 93.4%, and 76.9%, respectively (**Figure 7C**). Based on the loss of viability of *S.mutans* in the GIC composites containing different concentrations of the h-BN-TiO_2 nanocomposite, we find the nanocomposites had a better antibacterial effect than pure GIC without h-BN-TiO_2 nanocomposite.

The *S. mutans* adhered to and aggregated on the surface of the GIC after 4 h of incubation and SEM images were obtained. **Figures 7A,D** (magnification ×3,000) and **Figures 7B,E** (magnification ×5,000) represented the 0 wt% and 1.1 wt% h-BN-TiO_2/GIC composites, respectively. 1.1 wt% the h-BN-TiO_2/GIC composite

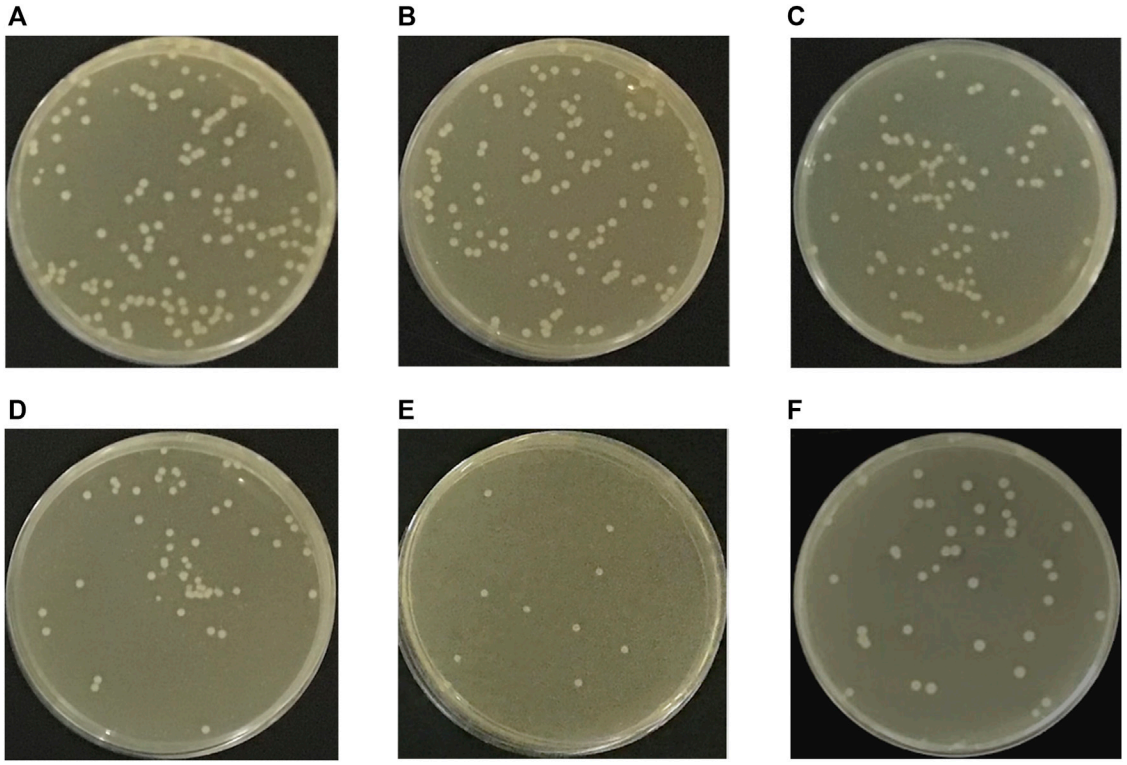

FIGURE 6 | *S. mutans* colonies on agar of blank group **(A)**, h-BN-TiO_2/GIC (0 wt%) and h-BN-TiO_2/GIC (0.3 wt%), h-BN-TiO_2/GIC (0.7 wt%), h-BN-TiO_2/GIC (1.1 wt%), h-BN-TiO_2/GIC (1.5 wt%) composites **(B–F)**, respectively.

shows that the number of viable bacteria substantially decreased and the morphologies of bacteria damaged compared with 0 wt% h-BN-TiO_2/GIC composite.

The extent of cell damage by the nanocomposite was evaluated using MTT assays at while culturing the bacteria for 24, 48, and 72 h (**Figure 7F**). After co-culturing the cell strain L929 and the extracts of h-BN-TiO_2/GIC composite, the cell viability of 0 wt% h-BN-TiO_2/GIC reached up to 70% at 24 h. Although the h-BN-TiO_2/GIC composites (0.3, 0.7, 1.1, 1.5 wt%) had lower viability at 24 h, the cell viability also increased after 48 and 72 h. The nanocomposites did not significant affect the viability of the L929 cells ($p > 0.5$), indicating that the h-BN-TiO_2/GIC composites were biologically compatible.

4 DISCUSSION

The poor mechanical and antibacterial properties of traditional GIC limit the utility of this restorative material in clinical applications. However, the addition of nanomaterials into the GIC matrix as dispersion enhancers have the potential to significantly improve the respective performances of traditional GIC.

In this study, h-BNNs were combined with TiO_2 NPs to obtain a zero-dimensional-two-dimensional nanocomposite system, after which we theoretically studied the mechanism of formation of the GIC composites comprising the h-BNNs and TiO_2 nanocomposite, with emphasis on the impact of the h-BN-TiO_2 nanocomposite on the performance of the GIC. The theoretical and experimental results both established that, although a two-dimensional structure similar to graphene was formed, the delocalization of the electrons throughout the h-BN were completely different compared to graphene. The h-BN prepared by the ball-milling was negatively charged (Fu et al., 2013), and the surface charge of the TiO_2 NPs depended on the pH value of the solution. In an acidic medium, the surface of the TiO_2 NPs is positively charged (Hoffmann et al., 1995); therefore, the positive charge of the surface of the TiO_2 NPs enabled the stable formation of a h-BN-TiO_2 nanocomposite structure with the negatively charged h-BN monolayer through electrostatic interactions in this work. In addition, mechanical cutting forces caused the thin, multilayered h-BNNs to separate into single h-BN layers, creating a structural basis for the cohesiveness between the TiO_2 NPs and h-BNNs, which is also important for enhancing the electrostatic attraction. The adsorption energy of the TiO_2 NPs onto the h-BNNs in the h-BN-TiO_2 composite was calculated to be −235 kcal/mol through MD simulations. This negative adsorption energy indicated that the two-dimensional-zero-dimensional heterostructure had a lower energy and a more stable configuration, implying that the experimental preparation of the nanocomposite resulted in a reduction in entropy. Therefore, this method could be used for the effective preparation of the h-BN-TiO_2 nanocomposite.

The h-BN-TiO_2 nanocomposite was prepared using ball-milling and thermal hydrolysis methods. TEM and AFM images showed that the h-BN-TiO_2 nanocomposite exhibited a rivet-like

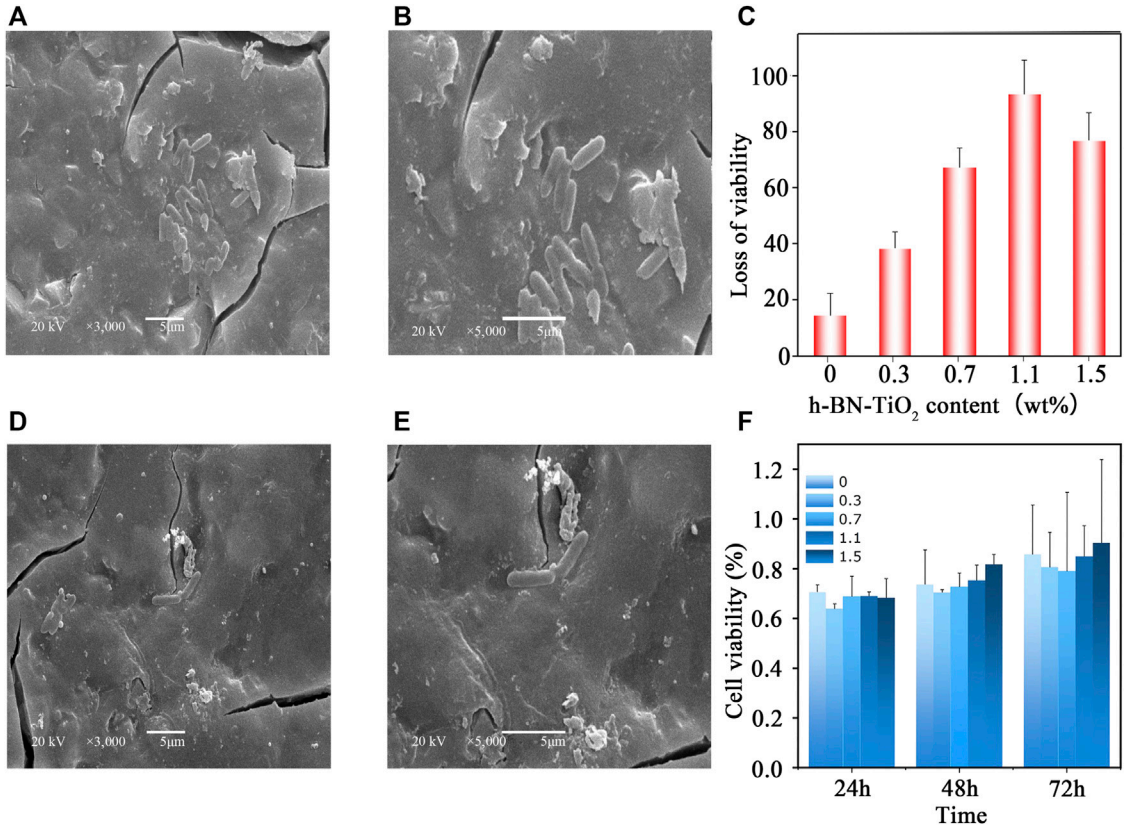

FIGURE 7 | The SEM micrograph of the colony of representative samples from the groups of h-BN-TiO_2/GIC: 0 wt% h-BN-TiO_2/GIC **(A)** magnification ×3,000; 0 wt.%h-BN-TiO_2/GIC **(B)**, magnification ×5,000; 1.1 wt.%h-BN-TiO_2/GIC **(D)**, magnification ×3,000; 1.1 wt.%h-BN-TiO_2/GIC **(E)**, magnification ×5,000; The influence of different concentrations of the h-BN-TiO_2/GIC composites on the loss of viability in *S. mutans* **(C)** and the cell viability of the L-929 cells cultured in h-BN-TiO_2/GIC extract **(F)**.

structure composed of two-dimensional nanosheets with thicknesses of 200 nm–1 μm and zero-dimensional nanoparticles with diameters of 20–200 nm. In addition to the prevention of the agglomeration of the h-BNNs, SEM confirmed not only the rivet-like structure of the h-BN-TiO_2 nanocomposite but also that the h-BN-TiO_2 nanocomposite were uniformly dispersed throughout the GIC matrix. Furthermore, significant improvements in the CS and VHN of the h-BN-TiO_2/GIC composite compared to the traditional GIC were observed, which indicated that the h-BN-TiO_2 nanocomposite had a significant impact on the mechanical properties of GIC. Compared to the GIC without the h-BN-TiO_2 nanocomposite (0 wt% h-BN-TiO_2/GIC), the VHN and CS of the 1.1 wt% h-BN-TiO_2/GIC increased by 149.65% and 80.2%, respectively, which were the highest of all of the h-BN-TiO_2/GIC composites; furthermore, the CS and VHN values decreased as the concentration of the h-BN-TiO_2 in the composite increased to 1.5 wt%.

There were three potential mechanisms by which h-BN-TiO_2 nanocomposite enhanced the performance of the GIC substrate. First, because the ultra-thin h-BN-TiO_2 nanocomposite was evenly dispersed in the GIC matrix, when the composite was subjected to external stress, the rigid nanosheets effectively functioned as conductors for the external stress, resulting in the reinforcement of the composite. Second, the discrete rivet-like structures of the TiO_2 NPs were tightly embedded within the thin layer of the h-BNNs by adsorption manifested by electrostatic interactions; when subjected to external stress, the TiO_2 NPs distributed throughout the surface of the h-BNNs not only effectively dissipated the stress but also prevented excessive external stress from removing the h-BNNs from the substrate, thereby enhancing the mechanical strength of the GIC substrate. Third, there was a good combination between TiO_2 NPs as additional polyacrylic polymer attachment sites and the GIC matrix; therefore, when the TiO_2 NPs were removed from the GIC matrix by external stress, a large amount of local stress needed to be dissipated to effectively strengthen the GIC. However, when the concentration of the h-BN-TiO_2 nanocomposite was higher than 1.1 wt%, the nanomaterials tended to have lower surface energies, making it easier for them to combine *via* van der Waals forces. The agglomeration of the materials decreased their surface energy until reaching a stable energy, making it impossible to effectively achieve uniform dispersion throughout the GIC. The agglomerated nanocomposites became a significant source of defects that manifested concentrated local stresses in the GIC. When subjected to external stress, the GIC first broke from the stress concentration; therefore, the defects caused by the agglomeration reduced the mechanical strength of the GIC.

This study also evaluated the effects of the concentration of the h-BN-TiO_2 nanocomposite on the friction coefficient of the GIC. As the amount of h-BN-TiO_2 nanocomposite was increased, the COF of GIC composites became decrease. The nanomaterial containing 1.1 wt% of the h-BN-TiO_2/GIC composite had the lowest wear coefficient, confirming that the h-BN-TiO_2 nanocomposite improved the wear resistance of GIC. Also, the addition of the h-BNNs into simultaneously enhanced the stiffness and toughness of the GIC matrix, thereby preventing the GIC matrix from propagating along cracks caused by friction. Furthermore, the addition of the h-BN-TiO_2 nanocomposite into the GIC matrix reduced the distance between the particles and effectively protected the matrix, thereby reducing the incidence of peeling and improving the overall wear resistance of the material. Since the friction experiments were mainly performed on the surfaces of the samples, and the results obtained were consistent with the surface hardness trends, we speculated that the increase in surface hardness might potentially be the cause of the increased friction performance.

Solubility is an important factor affecting the mechanical and antibacterial properties of dental materials. The GIC surface gradually erodes after being in contact with various liquids, resulting in the dissolution of the chemical components of the matrix. Importantly, GIC has a high dissolution rate during the initial curing period (Brito et al., 2010). The main reason for this is that, during the curing process, the anions within the GIC matrix can interact with sodium ions to form soluble compounds, resulting in continuous dissolution. However, we found that the solubility of GIC composites gradually decreased as the concentration of the h-BN-TiO_2 nanocomposite increased, likely because the addition of the h-BN-TiO_2 nanocomposite reduced the internal pores of the GIC, and they acted as a micro-separator, causing the material to form a porous structure, which subsequently increased the stability of the GIC matrix and reduced its dissolution rate. As we all know, environmental humidity and water absorption have a significant impact on the mechanical properties of materials (Randhawa and Patel, 2021), especially in the oral environment for dental materials. However, due to the limitations of experimental conditions in this study, the water absorption and ambient humidity are not discussed, which is also one of the limitations of in the paper. It is well-known that traditional GIC has fluoride-releasing properties, but the fluoride-releasing capacity of GIC in the oral cavity is the highest within the first two months of implantation, after which it gradually decreases (Sidhu and Nicholson, 2016). Although, GIC can absorb free fluoride ions in the oral cavity and store them for later release (Hasan et al., 2019). However, these trace amounts of fluoride ions are not enough to inhibit the formation of biofilms. In addition to being highly biocompatible, the 1.1 wt% h-BN-TiO_2/GIC composite we developed effectively killed 93.4% of the total S.mutans bacteria. SEM observation of the bacteria morphology after conducting the antibacterial efficacy experiments revealed that the GIC composites compromised the integrity of the bacteria cell membranes, which was evident because the bacteria exhibited a pronounced ruffled appearance. This result was mainly attributed to the synergistic antibacterial effect of the h-BN-TiO_2 nanocomposite. The antibacterial properties of the nanocomposite were derived from two different mechanisms. First, the sharp edges of the boron nitride nanosheets caused mechanical damage to the bacterial cell membrane, causing cell deformation and lysis. Second, the electrostatic effect between the positively charged TiO_2 NPs and the negatively charged cell membrane disrupted the inherent functions of the bacterial cell membrane (Sondi and Salopek-Sondi, 2004; Devanesan and AlSalhi, 2021), leading to the eventual death of the bacteria. In this study, we only tested the antibacterial effects of the h-BN-TiO_2/GIC composites over 24 h; thus, the long-term antibacterial effects of the composites and its effect on the occurrence of secondary caries need to be further studied. Another limitation of this study involves the lack of understanding of the long-term aging performance of the h-BN-TiO_2/GIC composite. Therefore, it is necessary to further explore the long-term effects of the h-BN-TiO_2/GIC composites to ensure the viability of its clinical application.

5 CONCLUSION

In this study, we successfully prepared a two-dimensional-zero-position nanocomposite system composed of h-BNNs and TiO_2 NPs and simulated the formation of the composite from the h-BN and TiO_2 components at the atomic scale using MD simulations. The combination of the h-BN-TiO_2 nanocomposite with the GIC was enabled through electrostatic forces, and the nanocomposite particles were uniformly dispersed throughout the GIC matrix. Moreover, the addition of 1.1 wt% of the Compressive strength (CS), Vicker hardness (VHN) and antibacterial properties were 80.2%, 149.65%, and 93.4% higher, respectively. The increase in the concentration of the h-BN-TiO_2 nanocomposite led to a decrease in both the frictional coefficient and solubility. In addition, the material exhibited excellent biocompatibility and satisfied the biomedical requirements. Thus, this study provided a novel method for enhancing the performance of GIC.

Further studies are required to investigate the long-term aging performance of the h-BN-TiO_2/GIC composites and water absorption. Also, different test conditions can be selected to test the effect of environmental conditions on the properties of h-BN-TiO_2/GIC composite.

DATA AVAILABILITY STATEMENT

The original contributions presented in the study are included in the article/**Supplementary Material**, further inquiries can be directed to the corresponding authors.

AUTHOR CONTRIBUTIONS

YM, BL, and X-JH conceived this study; Y-ZG, J-CY, and H-LJ conducted sample preparation and testing of all samples; Y-RW performed the theoretical calculations; YL conducted cell experiments and analyzed the data; X-ZK, R-ZL, Q-ZH, and C-DZ analyzed part data; YM and Y-ZG wrote the manuscript.

FUNDING

This work also supported by the Fundamental Research Funds for the Central Universities (lzujbky-2020-52) and the Research Fund of Lanzhou University School/Hospital of Stomatology (lzukqky-2021-q02). The authors are grateful to Lanzhou Hand and Foot Surgery Hospital for financial support.

ACKNOWLEDGMENTS

The authors thank the National Natural Science Foundation of China (No. 81970976), the Natural Science Foundation of Gansu Province (20JR10RA593) and Science and Technology Planning Project of Chengguan District, Lanzhou City (2021-2-1) for support. All the authors thank the Clinical Research Center of Shanxi Province for Dental and Maxillofacial Diseases (2020YHJB04), College of Stomatology, Xi'an Jiaotong University. The authors are grateful to the Michigan Center for Materials Characterization (MC)2 for its assistance with electron microscopy used in this work.

SUPPLEMENTARY MATERIAL

The Supplementary Material for this article can be found online at: https://www.frontiersin.org/articles/10.3389/fmats.2022.883027/full#supplementary-material

REFERENCES

Abdallah, R. M., Abdelghany, A. M., and Aref, N. S. (2020). Does Modification of Amalgomer with Propolis Alter its Physicomechanical Properties? an *In Vitro* Study. *Int. J. Biomater.* 2020, 1–10. doi:10.1155/2020/3180879

Brito, C. R., Velasco, L. G., Bonini, G. A. V. C., Imparato, J. C. P., and Raggio, D. P. (2010). Glass Ionomer Cement Hardness after Different Materials for Surface Protection. *J. Biomed. Mater. Res.* 93 (1), 243-246. doi:10.1002/jbm.a.32524

Chen, B., Jiang, Y., Zhao, M., Wang, W., Chu, Z., Huo, R., et al. (2020). Ag Nanoparticles Decorated Hybrid Microspheres for Superior Antibacterial Properties. *Mater. Lett.* 262, 127057. doi:10.1016/j.matlet.2019.127057

Ching, H. S., Luddin, N., Kannan, T. P., Ab Rahman, I., and Abdul Ghani, N. R. N. (2018). Modification of Glass Ionomer Cements on Their Physical-Mechanical and Antimicrobial Properties. *J. Esthet Restor Dent* 30 (6), 557–571. doi:10.1111/jerd.12413

Choi, H. C., Jung, Y. M., and Kim, S. B. (2005). Size Effects in the Raman Spectra of TiO2 Nanoparticles. *Vibrational Spectrosc.* 37 (1), 33–38. doi:10.1016/j.vibspec.2004.05.006

Czarniewska, E., Mrówczyńska, L., Jędrzejczak-Silicka, M., Nowicki, P., Trukawka, M., and Mijowska, E. (2019). Non-Cytotoxic Hydroxyl-Functionalized Exfoliated Boron Nitride Nanoflakes Impair the Immunological Function of Insect Haemocytes *In Vivo*. *Sci. Rep.* 9 (1), 14027. doi:10.1038/s41598-019-50097-0

Devanesan, S., and AlSalhi, M. S. (2021). Green Synthesis of Silver Nanoparticles Using the Flower Extract of Abelmoschus Esculentus for Cytotoxicity and Antimicrobial Studies. *Int. J. Nanomedicine* 16, 3343–3356. doi:10.2147/IJN.S307676

Elsaka, S. E., Hamouda, I. M., and Swain, M. V. (2011). Titanium Dioxide Nanoparticles Addition to a Conventional Glass-Ionomer Restorative: Influence on Physical and Antibacterial Properties. *J. Dent* 39 (9), 589–598. doi:10.1016/j.jdent.2011.05.006

Farooq, M. U., Jan, R., Azeem, M., Umer, M. A., Akram, M. A., Khan, A. N., et al. (2020). Enhanced Mechanical Properties of Functionalized BN Nanosheets-Polymer Composites. *J. Polym. Res.* 27 (10), 310. doi:10.1007/s10965-020-02286-z

Fu, X., Hu, Y., Yang, Y., Liu, W., and Chen, S. (2013). Ball Milled H-BN: An Efficient Holes Transfer Promoter to Enhance the Photocatalytic Performance of TiO2. *J. Hazard. Mater.* 244-245, 102–110. doi:10.1016/j.jhazmat.2012.11.033

Hajipour, M. J., Fromm, K. M., Akbar Ashkarran, A., Jimenez de Aberasturi, D., Larramendi, I. R. d., Rojo, T., et al. (2012). Antibacterial Properties of Nanoparticles. *Trends Biotechnol.* 30 (10), 499–511. doi:10.1016/j.tibtech.2012.06.004

Hamid, N., Telgi, R. L., Tirth, A., Tandon, V., Chandra, S., and Chaturvedi, R. K. (2019). Titanium Dioxide Nanoparticles and Cetylpyridinium Chloride Enriched Glass-Ionomer Restorative Cement: A Comparative Study Assessing Compressive Strength and Antibacterial Activity. *J. Clin. Pediatr. Dent* 43 (1), 42–45. doi:10.17796/1053-4625-43.1.8

Hasan, A. M. H. R., Sidhu, S. K., and Nicholson, J. W. (2019). Fluoride Release and Uptake in Enhanced Bioactivity Glass Ionomer Cement ("Glass Carbomer") Compared with Conventional and Resin-Modified Glass Ionomer Cements. *J. Appl. Oral Sci.* 27, e20180230. doi:10.1590/1678-7757-2018-0230

Hoffmann, M. R., Martin, S. T., Choi, W., and Bahnemann, D. W. (1995). Environmental Applications of Semiconductor Photocatalysis. *Chem. Rev.* 95 (1), 69–96. doi:10.1021/cr00033a004

Lee, B., Kwon, J.-S., Khalid, M. W., Kim, K.-M., Kim, J., Lim, K. M., et al. (2020). Boron Nitride Nanoplatelets as Reinforcement Material for Dental Ceramics. *Dental Mater.* 36 (6), 744–754. doi:10.1016/j.dental.2020.03.002

Moheet, I. A., Luddin, N., Ab Rahman, I., Masudi, S. a. M., Kannan, T. P., and Abd Ghani, N. R. N. (2018). Evaluation of Mechanical Properties and Bond Strength of Nano-Hydroxyapatite-Silica Added Glass Ionomer Cement. *Ceramics Int.* 44 (8), 9899–9906. doi:10.1016/j.ceramint.2018.03.010

Moreau, J. L., and Xu, H. H. K. (2010). Fluoride Releasing Restorative Materials: Effects of pH on Mechanical Properties and Ion Release. *Dental Mater.* 26 (11), e227–e235. doi:10.1016/j.dental.2010.07.004

Moshaverinia, A., Ansari, S., Moshaverinia, M., Roohpour, N., Darr, J. A., and Rehman, I. (2008a). Effects of Incorporation of Hydroxyapatite and Fluoroapatite Nanobioceramics into Conventional Glass Ionomer Cements (GIC). *Acta Biomater.* 4 (2), 432–440. doi:10.1016/j.actbio.2007.07.011

Moshaverinia, A., Ansari, S., Movasaghi, Z., Billington, R. W., Darr, J. A., and Rehman, I. U. (2008b). Modification of Conventional Glass-Ionomer Cements with N-Vinylpyrrolidone Containing Polyacids, Nano-Hydroxy and Fluoroapatite to Improve Mechanical Properties. *Dental Mater.* 24 (10), 1381–1390. doi:10.1016/j.dental.2008.03.008

Moshaverinia, A., Roohpour, N., Billington, R. W., Darr, J. A., and Rehman, I. U. (2008c). Synthesis of N-Vinylpyrrolidone Modified Acrylic Acid Copolymer in Supercritical Fluids and its Application in Dental Glass-Ionomer Cements. *J. Mater. Sci. Mater. Med.* 19 (7), 2705–2711. doi:10.1007/s10856-008-3399-0

Moshaverinia, A., Roohpour, N., Darr, J. A., and Rehman, I. U. (2009a). Synthesis and Characterization of a Novel N-Vinylcaprolactam-Containing Acrylic Acid Terpolymer for Applications in Glass-Ionomer Dental Cements. *Acta Biomater.* 5 (6), 2101–2108. doi:10.1016/j.actbio.2009.02.015

Moshaverinia, A., Roohpour, N., and Rehman, I. (2009b). Synthesis and Characterization of a Novel Fast-Set Proline-Derivative-Containing Glass Ionomer Cement with Enhanced Mechanical Properties. *Acta Biomater.* 5 (1), 498–507. doi:10.1016/j.actbio.2008.06.011

Moshaverinia, M., Navas, A., Jahedmanesh, N., Shah, K. C., Moshaverinia, A., and Ansari, S. (2019). Comparative Evaluation of the Physical Properties of a Reinforced Glass Ionomer Dental Restorative Material. *The J. Prosthetic Dentistry* 122 (2), 154–159. doi:10.1016/j.prosdent.2019.03.012

Nicholson, J. W. (2016). Adhesion of Glass-Ionomer Cements to Teeth: A Review. *Int. J. Adhes. Adhesives* 69, 33–38. doi:10.1016/j.ijadhadh.2016.03.012

Nicholson, J. W., Braybrook, J. H., and Wasson, E. A. (1991). The Biocompatibility of Glass-Poly(alkenoate) (Glass-Ionomer) Cements: A Review. *J. Biomater. Sci. Polym. Edition* 2 (4), 277–285. doi:10.1163/156856291x00179

Nicholson, J. W., Sidhu, S. K., and Czarnecka, B. (2020). Enhancing the Mechanical Properties of Glass-Ionomer Dental Cements: A Review. *Materials* 13 (11), 2510. doi:10.3390/ma13112510

Randhawa, K. S., and Patel, A. D. (2020a). Enhancing Tribo-Mechanical Properties and thermal Stability of Nylon 6 by Hexagonal boron Nitride Fillers. *E-Polymers* 20 (1), 733–745. doi:10.1515/epoly-2020-0069

Randhawa, K. S., and Patel, A. D. (2020b). Influence of Boric Anhydride Reinforcement on Mechanical Properties and Abrasive Wear of Nylon 6. *Mater. Res. Express* 7 (5), 055303. doi:10.1088/2053-1591/ab8ee4

Randhawa, K. S., and Patel, A. D. (2020c). Tribological Behaviour of PA6/diborontrioxide Composites. *J. Phys. Conf. Ser.* 1706 (1), 012124. doi:10.1088/1742-6596/1706/1/012124

Randhawa, K. S., and Patel, A. (2021). The Effect of Environmental Humidity/Water Absorption on Tribo-Mechanical Performance of Polymers and Polymer Composites - a Review. *Ind. Lubrication Tribology* 73 (9), 1146–1158. doi:10.1108/ilt-02-2021-0045

Sidhu, S., and Nicholson, J. (2016). A Review of Glass-Ionomer Cements for Clinical Dentistry. *J. Funct. Biomater.* 7 (3), 16. doi:10.3390/jfb7030016

Simmons, J. J. (1990). Silver-Alloy Powder and Glass Ionomer Cement. *J. Am. Dent Assoc.* 120 (1), 49–52. doi:10.14219/jada.archive.1990.0018

Sondi, I., and Salopek-Sondi, B. (2004). Silver Nanoparticles as Antimicrobial Agent: A Case Study on *E. coli* as a Model for Gram-Negative Bacteria. *J. Colloid Interf. Sci* 275 (1), 177–182. doi:10.1016/j.jcis.2004.02.012

Sun, L., Yan, Z., Duan, Y., Zhang, J., and Liu, B. (2018). Improvement of the Mechanical, Tribological and Antibacterial Properties of Glass Ionomer Cements by Fluorinated Graphene. *Dental Mater.* 34 (6), e115–e127. doi:10.1016/j.dental.2018.02.006

Varela, M. F., Stephen, J., Lekshmi, M., Ojha, M., Wenzel, N., Sanford, L. M., et al. (2021). Bacterial Resistance to Antimicrobial Agents. *Antibiotics* 10 (5), 593. doi:10.3390/antibiotics10050593

Wang, S.-P., Ge, Y., Zhou, X.-D., Xu, H. H., Weir, M. D., Zhang, K.-K., et al. (2016). Effect of Anti-Biofilm Glass-Ionomer Cement on Streptococcus Mutans Biofilms. *Int. J. Oral Sci.* 8 (2), 76–83. doi:10.1038/ijos.2015.55

Wiegand, A., Buchalla, W., and Attin, T. (2007). Review on Fluoride-Releasing Restorative Materials-Fluoride Release and Uptake Characteristics, Antibacterial Activity and Influence on Caries Formation. *Dental Mater.* 23 (3), 343–362. doi:10.1016/j.dental.2006.01.022

Xu, H. H. K., Moreau, J. L., Sun, L., and Chow, L. C. (2010). Novel CaF(2) Nanocomposite with High Strength and Fluoride Ion Release. *J. Dent Res.* 89 (7), 739–745. doi:10.1177/0022034510364490

Yamakami, S. A., Ubaldini, A. L. M., Sato, F., Medina Neto, A., Pascotto, R. C., and Baesso, M. L. (2018). Study of the Chemical Interaction between a High-Viscosity Glass Ionomer Cement and Dentin. *J. Appl. Oral Sci.* 26, e20170384. doi:10.1590/1678-7757-2017-0384

Yesilyurt, C., Er, K., Tasdemir, T., Buruk, K., and Celik, D. (2009). Antibacterial Activity and Physical Properties of Glass-Ionomer Cements Containing Antibiotics. *Oper. Dent* 34 (1), 18–23. doi:10.2341/08-30

Yue, Y., Zeng, L., Wang, X., Su, L., Sun, M., Wu, B., et al. (2019). Loading of AgNPs onto the Surface of boron Nitride Nanosheets for Determination of Scopoletin in Atractylodes Macrocephala. *Sci. Rep.* 9 (1), 3864. doi:10.1038/s41598-019-40511-y

Zhang, K., Wang, S., Zhou, X., Xu, H. H. K., Weir, M. D., Ge, Y., et al. (2015). Effect of Antibacterial Dental Adhesive on Multispecies Biofilms Formation. *J. Dent Res.* 94 (4), 622–629. doi:10.1177/0022034515571416

Zhang, R., and Gao, L. (2001). Effect of Peptization on Phase Transformation of TiO2 Nanoparticles. *Mater. Res. Bull.* 36 (11), 1957–1965. doi:10.1016/S0025-5408(01)00674-2

Conflict of Interest: The authors declare that the research was conducted in the absence of any commercial or financial relationships that could be construed as a potential conflict of interest.

Publisher's Note: All claims expressed in this article are solely those of the authors and do not necessarily represent those of their affiliated organizations, or those of the publisher, the editors and the reviewers. Any product that may be evaluated in this article, or claim that may be made by its manufacturer, is not guaranteed or endorsed by the publisher.

frontiers | Frontiers in Bioengineering and Biotechnology

TYPE Review
PUBLISHED 22 July 2022
DOI 10.3389/fbioe.2022.907589

OPEN ACCESS

EDITED BY
Monireh Kouhi,
Isfahan University of Medical Sciences, Iran

REVIEWED BY
Cristian Covarrubias,
University of Chile, Chile
Sara Ferraris,
Politecnico di Torino, Italy
Silvia Spriano,
Politecnico di Torino, Italy

*CORRESPONDENCE
Antonio López-Valverde,
alopezvalverde@usal.es

†These authors have contributed equally to this work

SPECIALTY SECTION
This article was submitted to Biomaterials, a section of the journal Frontiers in Bioengineering and Biotechnology

RECEIVED 29 March 2022
ACCEPTED 04 July 2022
PUBLISHED 22 July 2022

CITATION
López-Valverde N, Aragoneses J, López-Valverde A, Rodríguez C, Macedo de Sousa B and Aragoneses JM (2022), Role of chitosan in titanium coatings. trends and new generations of coatings.
Front. Bioeng. Biotechnol. 10:907589.
doi: 10.3389/fbioe.2022.907589

Role of chitosan in titanium coatings. trends and new generations of coatings

Nansi López-Valverde[1†], Javier Aragoneses[1†], Antonio López-Valverde[2*], Cinthia Rodríguez[3], Bruno Macedo de Sousa[4] and Juan Manuel Aragoneses[5]

[1]Department of Medicine and Medical Specialties, Faculty of Health Sciences, Universidad Alcalá de Henares, Madrid, Spain, [2]Department of Surgery, University of Salamanca, Instituto de Investigación Biomédica de Salamanca (IBSAL), Salamanca, Spain, [3]Department of Dentistry, Universidad Federico Henríquez y Carvajal, Santo Domingo, Dominican Republic, [4]Institute for Occlusion and Orofacial Pain, Faculty of Medicine, University of Coimbra, Polo I-Edifício Central Rua Larga, Coimbra, Portugal, [5]Faculty of Dentistry, Universidad Alfonso X El Sabio, Madrid, Spain

Survival studies of dental implants currently reach high figures. However, considering that the recipients are middle-aged individuals with associated pathologies, research is focused on achieving bioactive surfaces that ensure osseointegration. Chitosan is a biocompatible, degradable polysaccharide with antimicrobial and anti-inflammatory properties, capable of inducing increased growth and fixation of osteoblasts around chitosan-coated titanium. Certain chemical modifications to its structure have been shown to enhance its antibacterial activity and osteoinductive properties and it is generally believed that chitosan-coated dental implants may have enhanced osseointegration capabilities and are likely to become a commercial option in the future. Our review provided an overview of the current concepts and theories of osseointegration and current titanium dental implant surfaces and coatings, with a special focus on the *in vivo* investigation of chitosan-coated implants and a current perspective on the future of titanium dental implant coatings.

KEYWORDS

titanium dental implants1, osteointegration2, bioactive surfaces3, chitosan coating4, future direction5

Introduction

In the last 50 years, dental implants have become a predictable treatment option for the replacement of missing teeth, improving the quality of life and masticatory function of patients rehabilitated using them (Jofre et al., 2013; Hartlev et al., 2014; Tarnow, 2014; Buser et al., 2017).

There are currently about 1,500 different implant systems in terms of topography, wettability, chemistry, and surface modification (Le Guéhennec et al., 2007; Junker et al., 20092009). These characteristics contribute to the biological processes occurring during osseointegration by direct interaction with host osteoblasts in bone formation (Le

Guéhennec et al., 2007; Dohan Ehrenfest et al., 2010; Pattanaik et al., 2012; Ogle, 2015; Hotchkiss et al., 2016; Wennerberg et al., 2018).

In general, long-term studies report excellent results in terms of the survival rate of dental implants. After 20 years in operation, the overall cumulative survival rate ranges from 89.5 to 99%, according to different studies (Horikawa et al., 2017; Chrcanovic et al., 2018). However, considering that most patients who undergo dental implant treatment are of a certain age (50–60 years) (Guillaume, 2016) in which coexisting pathologies (diabetes mellitus, osteoporosis, bisphosphonate treatments) can affect bone quality and quantity, making it necessary to modify the bioactive surface to accelerate and ensure osseointegration after implant insertion (Gil et al., 2021). On the other hand, surface modification becomes necessary to accelerate osseointegration and to achieve more comfortable and faster prosthetic loading protocols. For all these reasons, biomedical research on surface modifications of dental implants is focused on achieving bioactive surfaces that guarantee long-term bone-implant contact (Bosshardt et al., 2017).

Today's rigorous manufacturing processes in modern dental implantology have brought about a true technological revolution. The breakthrough in the treatment of edentulism, although it has not been given the deserved relevance as other novel surgical procedures, greatly influences the physiological and psychological state of patients and improves their quality of life (Guillaume, 2016; Fonteyne et al., 2021).

Chitosan (Cht) is an FDA-approved copolymer that has demonstrated properties such as bioactivity, biocompatibility, biodegradability, non-toxicity and broad-spectrum antimicrobial activity against both gram-positive and gram-negative bacteria. On the other hand, it is important to highlight the prominent role of chitosan-based scaffolds in combination with natural biomolecules and drugs in bone regeneration (Fakhri et al., 2020).

Our review provided an overview of the current concepts and theories of osseointegration and current titanium dental implant surfaces and coatings, with a special focus on the *in vivo* investigation of chitosan coatings and a future perspective on coatings.

Titanium

The history of titanium (Ti) as a biomedical material began in the 1940s. Bothe et al. implanted titanium together with other metallic materials in laboratory animals, re-porting its good tolerance due to its excellent resistance to corrosion in biological fluids; Beder et al. proposed the use of Ti for intraoral implants, using a canine model (Clarke and Hickman, 1953; Beder and Ploger, 1959; Nakajima and Okabe, 1996).

Currently for the manufacture of orthopedic and dental implants, four grades of pure Ti are used depending on their oxygen and iron content. Apart from pure Ti, Titanium-Aluminum-Vanadium alloy (Ti-6Al-4V, Ti6-4) and Ti-grade 5 are the most commonly used for biomedical applications. Ti6Al4V ELI (Grade 23) is an alloy of titanium with aluminum and vanadium. It is a purer version of Ti6Al4V (Grade 5). The content of interstitial elements (iron, oxygen and carbon) in this alloy are strictly controlled and limited during the melting process. This purity gives it superior mechanical properties and increased fatigue strength. It has excellent biocompatibility with the human body and is one of the most widely used dental implants to restore function (Jujur et al., 2020).

The concept of osseointegration

The pioneer of modern implant dentistry, Professor Brånemark of the University of Gothenburg (Sweden), performed the first preclinical studies in the 1960s, describing the phenomenon of osseointegration. The 'Brånemark team' (Tomas Albrektsson, Ragnar Adell, Ulf Lekholm and Torsten Jemt) was the first to propose the concept of osseointegration of a metallic biomaterial implanted in bone, demonstrating that biocompatibility and bone-Ti bonding were the main biological properties of this metal. This aspect led them to define the concept of osseointegration of titanium as 'the direct structural and functional connection between the ordered living bone and the surface of a load-bearing implant' (Brånemark et al., 1977; Adell et al., 1981; Albrektsson et al., 1981). However, the biological bone-Ti interaction can be found in the scientific literature under different terminologies such as 'bone ankylosis', 'bone union', 'osteotolerance' etc. that define more precisely the bone-implant relationship (Lang, 2019).

Cornell & Lane defined osteoconduction a three-dimensional process of ingrowth of capillaries sprouting from a bone bed, perivascular tissue and osteoprogenitor cells into the three-dimensional structure of a porous implant, which is used as a guide to cover a defect with bone tissue (Cornell and Lane, 1998). Osteoinduction is defined by Barradas et al. as the induction of undifferentiated mesenchymal stem cells, which are not yet committed to the osteogenic lineage, to form osteoprogenitor cells and produce bone in heterotopic sites (Barradas et al., 2011; Weber, 2019). However, the actual mechanism of the osseointegration process remains unknown (López-Valverde et al., 2020) although, in recent years, different novel theories have been proposed to explain it:

Osteosufficiency/osteoseparation theory

Kota and Zarb (Koka and Zarb, 2012) have proposed a rational theory in which host biology and implant

characteristics are considered two distinct entities that are expected to interact and coexist for decades and caution that although short-term studies, animal models and *in vitro* work may provide clues, long-term human observation is the definitive reason. Some factors predisposing to a state of osteoinsufficiency create little controversy, e.g., uncontrolled diabetic; others, such as parafunctional habits, occlusal overload, certain drugs, or bacterial aggression are controversial.

Brain-bone axis theory

The central nervous system, and more specifically the hypothalamus, has an important regulatory role in the functions of peripheral tissues and in the processes of bone healing and remodeling (Ruan et al., 2014; Kim et al., 2015). Recent studies have also demonstrated important links between the central nervous system and the immune system, which in turn plays a key role in peri-implant bone healing (Elefteriou et al., 2014). Other studies have suggested that impaired osseointegration and dental implant failures may be associated with the use of antidepressant drugs (Abu Nada et al., 2018). Some researchers have even gone so far as to propose the gut-brain-bone axis, in which the gut would drive bone physiology through the regulation of key hormones that are originally synthesized in the brain. And in this aspect, the oral microbiota would play an important role (Quach and Britton, 2017).

Foreign body reaction theory

Any type of implant is considered a foreign body, to which the organism reacts by activating the immune and inflammatory systems, whereby the defense cells (neutrophils, lymphocytes, proinflammatory reactive macrophages and osteoclasts) react by engulfing the foreign body. In this situation, reparative cells (fibroblasts and osteoblasts) are activated and help repair and remodel tissues and protect them from further destruction, however, when a foreign body is too bulky to be engulfed by immune cells, a fibrous or osseous encapsulation process develops around it (Carcuac et al., 2013; Miron et al., 2016; Naveau et al., 2019). Trindade et al. and Albrektsson et al. defined osseointegration as a foreign body reaction, an immunomodulated, multifactorial and complex healing process involving various cells and mediators, hypothesizing that the primary etiology of crestal bone loss around osseointegrated implants would be a change in the inflammatory equilibrium (foreign body equilibrium). Such an inflammatory response would be caused by sudden changes in the loading situation, or by alterations of the foreign body itself, in the form of accidental tissue dispersion, and that bacterial colonization, now classically considered as a triggering factor for peri-implant bone loss, could be secondary to such alterations (Trindade et al., 2016; Trindade et al., 2018).

Titanium surface modifications

After implantation, titanium comes into contact with biological fluids and tissues, and two types of response may occur: either the formation of a fibrous soft tissue capsule around the implant that does not guarantee adequate biomechanical fixation and leads to clinical failure, or direct bone-to-implant contact without an intermediate connective tissue layer, which is known as osseointegration (Brånemark et al., 1977) (Figure 1).

Most dental implants are manufactured with grade 4 Ti, as it is stronger than other grades, however, titanium alloys are mainly composed of Ti6Al4V (Titanium grade 5-Aluminum-Vanadium), with higher elastic modulus and better fatigue properties than pure titanium (Glied and Mundiya, 2021).

The implant surface is now considered to play a key role in clinical success. The surface roughness of Ti implants affects the osseointegration rate and biomechanical fixation (Ferraris et al., 2011). Ti implants with SLA (Sandblasted, Large-grit, Acid-etched) etched surfaces show superior bone-to-implant contact (50–60%) compared to other surface modifications, and the suitability of this type of etching in terms of overall osteogenic performance has been demonstrated *in vivo* (Ogle, 2015; Ren et al., 2021) (Figure 2).

The degree of surface wettability (range 0° hydrophilic to 140° hydrophobic) is a matter of controversy among different researchers; Buser et al. (Buser et al., 2004) proposed that hydrophilic SLA surfaces generate greater bone-to-implant contact than normal SLA. However, earlier *in vivo* studies by Carlsson et al. and Wennerberg et al. found no difference (Carlsson et al., 1989; Wennerberg et al., 1991). Nevertheless, new findings on wetting and nanoroughness are driving current research in this exciting field (Rupp et al., 2018).

Currently, surface roughening is the most commonly used technique in practice, however, titanium implants with microscale and/or nanoscale surface topographical features have moved from novelty to commodity and are advancing in the field of the implant industry. Certain researchers have reported that the failure resistance of dental implants is influenced by the acid-etched surface; furthermore, it is known that Ti etched, SLA-type surfaces have a mean value, after 6 weeks, of 50–60% bone-to-implant contact, compared to the Ti plasma sprayed titanium surface, which had only a mean value of 30–40% (Ong and Chan, 2000; Socorro-Perdomo et al., 2022).

To ensure a high quality of coatings, the importance of surface pretreatment prior to the deposition work has to be taken into account. Despite the high number of studies performed to date on the plasma spraying method, the literature results demonstrate the difficulties in deciding the

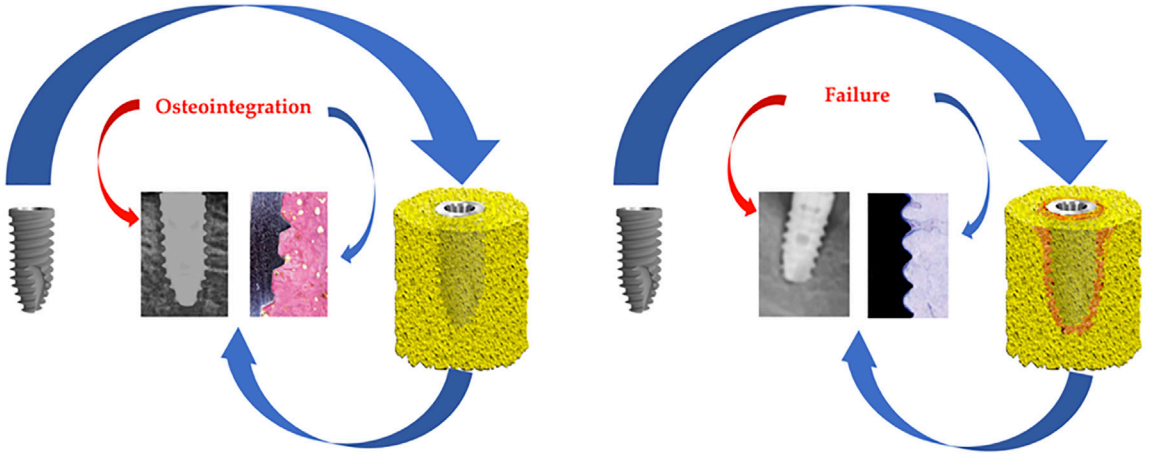

FIGURE 1
Osseointegration and failure.

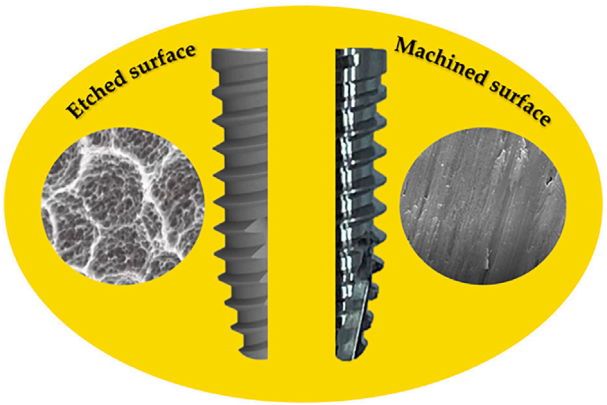

FIGURE 2
Engraved and machined surface of Ti implants.

optimal value of surface roughness to improve osseointegration and decrease bacterial adhesion (Jemat et al., 2015).

Implant surface modifications by methods based on the immobilization of biologically active organic molecules on Ti and Ti6Al4V surfaces have attracted much interest recently (Panayotov et al., 2015).

Human defensins are normally produced by neutrophil granulocytes and epithelial cells. The alpha defensins, were originally identified as small antibiotic peptides, termed human neutrophil peptides (HNP-1, HNP-2, HNP-3) (Jarczak et al., 2013). Notably, HNP-1 has been detected in saliva samples from patients with oral cancer and patients with other oral pathologies. Human beta-defensins are synthesized by epithelial cells lining the oral mucosal surfaces. Beta-defensin is secreted in saliva and it has been found that certain inflammatory stimuli could significantly increase beta-defensin expression in gingival keratinocyte cultures (Cunliffe, 2003). Pfeufer et al. (Pfeufer et al., 2011) observed that coating Ti surfaces with human beta-defensin was effective against Escherichia coli, a gram-negative bacterium associated with implant failure (Alshammari et al., 2021).

Histatins are antimicrobial peptides secreted in human parotid saliva, which have been attributed an important role in wound healing *in vitro* (Pal et al., 2014). Certain studies have highlighted the role of these peptides in the osseointegration of Ti dental implants. Van Dijk et al. immobilized histatin peptide on the surface of Ti and found that it enhanced osteoblast cell adhesion (Van Dijk et al., 2017). Makihira et al. tested the performance of Ti implants coated with a histatin-derived peptide on edentulous ridges of dogs; histological analysis and microcomputed tomography showed increased trabecular bone formation around the coated implants versus untreated implants (Makihira et al., 2011). Siwakul et al. (Siwakul et al., 2021) evaluated cell adhesion, proliferation, osteogenesis-related genes and alkaline phosphatase activity on histatin-coated Ti surfaces; the results showed that the adhesion of cells to the histatin-coated group achieved cell proliferation significantly histatin achieved significantly higher cell proliferation.

Sugawara et al. (Sugawara et al., 2016) described a method that allowed adhesion of human gingival epithelial cells to a smooth Ti surface by a protease receptor 4 activating peptide, based on the idea that peri-implantitis could result from a lack of epithelial seal at the peri-implant collar; the coating produced a rapid aggregation of platelets on the Ti surface. Other studies have demonstrated the induced epithelial barrier function to prevent bacterial adhesion, penetration, and invasion on Ti (Maeno et al., 2017). Local production of antimicrobial

TABLE 1 Innovative surfaces based on organic components.

Surface coating	Sustrate	Outcome	Study
Human beta-defensin	Ti	Effective against Escherichia coli	Pfeufer et al. (Pfeufer et al., 2011)
Histatins	Ti	Enhance osteoblast cell adhesion	Van Dijk et al. (Van Dijk et al., 2017)
	Ti	Increased trabecular bone formation around coated implants	Makihira et al. (Makihira et al., 2011)
	Ti	Promote cellular activities around dental implants	Siwakul et al. (Siwakul et al., 2021)
Peptides	Ti	Adhesion of human gingival epithelial cells to a smooth titanium surface. Epithelial sealing at the implant neck. Platelet aggregation on the titanium surface	Sugawara et al. (Sugawara et al., 2016)
	Ti	Induced epithelial barrier to prevent bacterial adhesion, penetration and invasion on titanium. Prevent adhesion, penetration and invasion of Escherichia coli bacteria	Maeno et al. (Maeno et al., 2017)
	Ti	Certain oral pathogens associated with periodontitis induce the production of beta-defensin-2 in human gingival epithelial cells	Krisanaprakornkit et al. (Krisanaprakornkit et al., 2000)

peptides may contribute to the barrier function of the epithelial seal formed around the transmucosal part of dental implants; in this regard it is noteworthy that certain bacteria such as *Fusobacterium nucleatum*, an anaerobic member of the oral pathogens associated with periodontitis, induced the production of beta-defensin-2 in human gingival epithelial cells (Krisanaprakornkit et al., 2000). This type of research on the immobilization of peptides on Ti surfaces could prevent bacterial colonization of implants and facilitate the initial phase of osseointegration (Table 1).

Chitin and chitosan

Chitin is a carbohydrate found mainly in the exoskeleton of crustaceans and some fungi. Albert Hofmann first described its structure, although as early as 1859, Rouget treated chitin with a hot potassium hydroxide solution, leading to the discovery of chitosan (Cht) and laying the foundations for its production (Crini, 2019; Mohan et al., 2022). The deacetylation process increases the interaction between Cht and cells by increasing the number of positive charges, thus improving its biocompatibility (Hamed et al., 2016). It does not produce antigenic response and possesses anti-inflammatory properties. Its hemostatic power is an important feature, as it can induce platelet adhesion and aggregation and activate blood coagulation. Thus, Cht can control bleeding by adsorbing plasma and coagulating red blood cells (Keast DH Janmohammad, 2021; Ferraris S et al., 2022).

Chitosan titanium dental implants coatings

Surface treatments and coatings of dental implants are of great importance in the osseointegration process. Cht has excellent ability to bind to metal, which could improve the mechanical strength and increase the durability of titanium implants. However, solubility in aqueous solutions depends on pH. At neutral pH, most chitosan molecules will lose their charge and precipit from solution. Certain researchers have highlighted the adhesion strength of Cht coatings to Ti surfaces as unsuitable for clinical applications. Ferraris et al. (Ferraris S et al., 2022) has recently proposed a chemical pretreatment of the Ti substrate, by three methods: in the first one ("direct coating") he immerses the Ti6Al4V samples in the solution; in the second one, he activates the surface by tresyl chloride and in the third one he performs a treatment with polidopamine, concluding that the best result is obtained with the direct coating at acid pH on a pretreated Ti substrate, due to the nanometric porosity of the substrate and to the strong electrostatic attraction between the chitosan and the hydroxyl groups. In this way, mechanically and chemically stable coatings are obtained.

Natural or biopolymer-based composites containing chitin or chitosan have advantages such as biocompatibility and biodegradability, which are essential for bone tissue engineering. Carboxymethylation, quaternization, sulfonation and phosphorylation are the most common methods to overcome the insolubility of Cht and to enhance its antimicrobial effect (Qin and Li, 2020).

Cht is produced by the N-deacetylation of chitin. The application of high-power ultrasound significantly intensifies the deacetylation process (removal of an acetyl group) of chitin, resulting in low molecular weight, high quality Cht by rapid treatment at low temperature (Figure 3).

It has been shown that, deacetylated Cht chemically binds to titanium surfaces, although the bond strength is lower than that of calcium phosphate coating; however, enhanced osteoblast growth and attachment has been reported on Cht-coated titanium (Bumgardner et al., 2003a). Despite this, *in vitro* and *in vivo* studies disagree as *in vitro* studies show that osteoblasts do not adhere to chitosan in normal cell cultures, requiring some

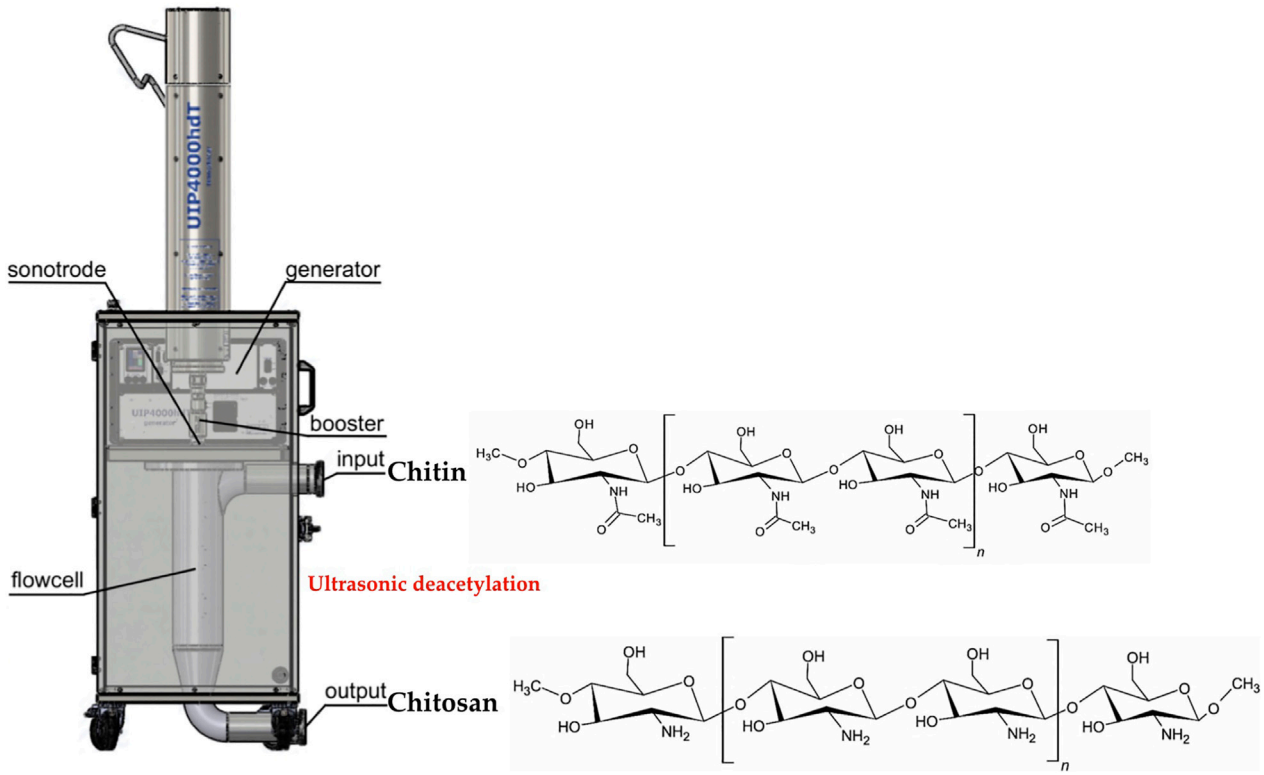

FIGURE 3
Chitin deacetylation process.

pretreatments such as serum soaking or fibronectin coating (Saccani et al., 2019).

Preparation of the different types of chitosan coating

The characteristic features of Cht, such as being cationic, hemostatic and insoluble at high pH, can be completely reversed by a sulfation process that can make the molecule anionic and water soluble, and also add anticoagulant properties (Suh and Matthew, 2000). On the other hand, due to its high molecular weight and linear structure, it has excellent viscosity. The higher viscosity of the Cht solution depends on the concentration, the decrease in temperature and the increase in the degree of deacetylation; this influences the elongation at fracture and tensile strength, all of which is of great importance in Cht coatings of dental implants by immersion, which would be more resistant to the forces provoked during the insertion phase in the bone tissue bed (Barton et al., 2014); however, studies investigating the influence of the degree of deacetylation on the properties of chitosan are contradictory. Foster et al. observed that variation in the degree of deacetylation could be responsible for the contrasting trends in chitosan properties. (Foster et al., 2015). At the same time, viscosity would enhance biological and healing properties, as well as biodegradation and osteogenic capacity (Gérentes et al., 2002). Other modifications of Cht, with the aim of reducing the drawbacks it presents (mechanical properties and antibacterial activity for biomedical applications), have involved chemical modification. Modifications of Cht, such as the incorporation of carboxymethyl, imizadolyl or methyl pyrrolidone, have been shown to improve osteoinductive properties and result in increased antibacterial activity (Alves and Mano, 2008; Jayakumar et al., 2010). Other strategies to compensate for its limitations have consisted of combining it with other natural polymers such as alginate, silk, or chitin (Mohire and Yadav, 2010; Rahmani et al., 2018; Quesada et al., 2020; Moenne and González, 2021).

Cht as a titanium coating has been studied in depth by different researchers (Bumgardner et al., 2003a; Abarrategi et al., 2008), however, few *in vivo* studies have been published (Bumgardner et al., 2007; Kung et al., 2011; Takanche et al., 2018; Zhang et al., 2020; López-Valverde et al., 2021a; López-Valverde et al., 2022). On the other hand, when preparing Cht coatings for silanization and attachment to the Ti substrate, toxic

reagents such as 3 isocyanatopropyltriethoxysilane and glutaraldehyde are used; moreover, these techniques involve complex processing that hinders the deposition of the coating and limits its clinical applicability. Grosso described an immersion coating method for preparing films on substrates from liquid solutions. This method facilitates the possibility of fine-tuning the amount of material that can be deposited, and thus the thickness of the final film; moreover, dip coating is an inexpensive way to deposit thin layers from chemical solutions with relatively fair control of the layer thickness (Grosso, 2011). The kinetics of dip coating is based on a continuous flow condition and the coating thickness is determined by the competition between viscous force, surface tension, gravity and substrate withdrawal rate (Nguyen du et al., 2014). Zhang et al. (Zhang et al., 2020) demonstrated that porous Ti with a Cht/hydroxyapatite coating could promote osteoblast-like cell proliferation and differentiation and osseointegration in a rabbit femur model. For the coating process, they resorted to a dilution of Cht/hydroxyapatite composite by dissolving 1.98 g of Ca(NO3)2–4H2O and 0.66 g of KH2PO4 in distilled water, along with 1 g of Cht powder in 100 ml of 2% acetic acid. The 2 solutions were mixed to prepare a composite Cht/hydroxyapatite coating on the porous titanium surface using an electrochemical deposition method described by Pang et al. (Pang and Zhitomirsky, 2007). Takanche et al. (Takanche et al., 2018) used a rat mandible osteoporotic model, where they implanted Ti devices coated with Cht-gold nanoparticles, obtaining an increase in osteogenesis and inhibition of osteoclastogenesis. Bumgardner et al. (Bumgardner et al., 2007) on a rabbit tibia model, implanted Ti devices coated with deacetylated Cht (1wt% deacetylated chitosan 92.3% in 1% acetic acid) melted in solution and adhered to rough Ti pins by their own method (Bumgardner et al., 2003a; Bumgardner et al., 2003b), using calcium phosphate-coated Ti pins and uncoated Ti pins as controls. The coating with Cht was performed by solution casting and silane reactions under acidic conditions. They used a 1% Cht solution in 1% acetic acid, poured over the samples and allowed to air dry for 7 days. The resulting layers, 10–15 μm thick, were neutralized with a weak base and rinsed with plenty of deionized water. Histological evaluations of the tissues in contact with the Cht-coated pins indicated a minimal inflammatory response and a healing sequence with bone tissue formation, followed by the development of laminar bone. Kung et al. (Kung et al., 2011) resorted to subcutaneous implants in a rat model, using two types of Cht with a degree of deacetylation >90%. The solution used consisted of 15 mg of Cht powder in 10 ml of vitamin C solution to obtain a 0.15% Cht solution with which they soaked type I collagen membranes that they then wrapped around Ti mini-implants, obtaining ectopic new bone formation in the area of the Cht-coated implants. The method, used by us in previous studies (Pang and Zhitomirsky, 2007; Nguyen du et al., 2014), resorted to a film-forming solution of Cht dissolved in an acid medium, on a dog jaw model; they compared implants with surfaces coated with Cht, by means of a procedure of immersion in acid solution and film-forming solution, with uncoated implants, type SLA. In our opinion, this is a suitable procedure for the coating of dental implants with Cht. The procedure, described by Vakili et al. (Vakili and Asefnejad, 2020), complemented with the procedure described by Zhang et al. (Zhang et al., 2019) for the film-forming solution, is performed by dissolving 0.5% (w/v) Cht in a 0.5% (v/v) acid solution and stirring the solution for 12 h on a magnetic stirrer. The film-forming solution is prepared following the procedure described by Zhang et al.; glycerol (0.4 g) is dispersed in 80 ml acetic acid (1%, w/v) by stirring for at least 12 h (4°C). The prepared Cht solution is added to the film-forming solution using a syringe pump (Infusomat® Space, Braun, Barcelona, Spain), at a rate of 50 ml/h, stirring by means of a mechanical stirrer at 800 rpm. Functionalization of the Cht-coated implants was performed by immersion in the prepared solution. The functionalized implants were then dried at 25°C with a relative humidity of 50% for the formation of a uniform film. (Figure 4).

Four of the *in vivo* studies reviewed (Bumgardner et al., 2007; Kung et al., 2011; Takanche et al., 2018; Zhang et al., 2020; López-Valverde et al., 2021a; López-Valverde et al., 2022) used coating formulations, in our opinion, of a certain complexity in terms of clinical applicability. The fifth study and sixth studies (López-Valverde et al., 2021a; López-Valverde et al., 2022) used a coating process described by Vakili et al. (Vakili and Asefnejad, 2020) and Zhang et al. (Zhang et al., 2019), with slight modifications, of easy applicability (Table 2). Grosso (Grosso, 2011) recommends immersion methods as a simple and inexpensive coating strategy, easily applicable in preclinical studies applicable in humans. The CAMARADES Research Group (University of Edinburgh) reported that simple strategies for preclinical studies in general, save more than 30% of in-research expenditure ($5.8 billion) (CAMARADES, 2022).

In any case, we have not found defined in the literature the optimal amount of Cht for coating Ti dental implants, although some research has hypothesized that it may not be important for the Cht coating to persist in the long term once a good bone-implant interface has been established. It also seems to be unclear whether it would be necessary for the chitosan polymeric material to possess high bond strength (Bumgardner et al., 2007).

Cht coatings on Ti-6Al-4V substrates *in vitro*, which showed improved mechanics, better cell adhesion and viability of human osteoblastic cells, were obtained by homogeneous coatings of 770–800 nanomicrons es-thickness, crack-free and well adhered (Gopi et al., 2014; Moskalewicz et al., 2015).

The layer-by-layer technique has many advantages over other multilayer fabrication methods, as no complicated instruments are needed for the process, which makes it affordable in practice; moreover, deposition by layer-by-layer is independent of the shape and size of the substrate. Song et al. (Song et al., 2020) used the layer-by-layer approach to modify the

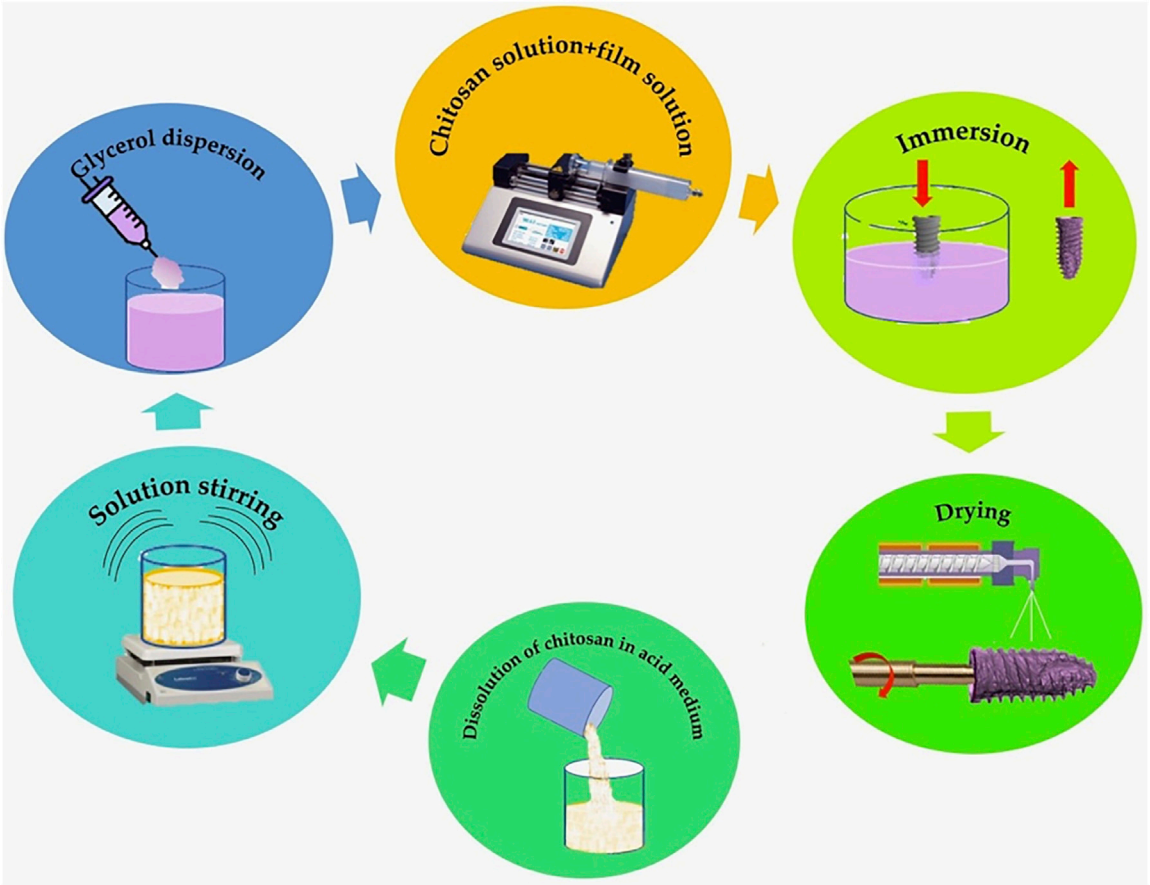

FIGURE 4
Modified Vakili and Zhang coating scheme for the immersion procedure.

titanium substrate, obtaining smooth multilayer coatings that promoted osteogenic differentiation of MG63 osteoblast-like cells.

Casting is another simple method of depositing Cht on the surface of a substrate. The technique involves preparing a polymer solution using a suitable solvent; subsequently, the solution is poured onto the substrate to create a thin film deposition. This is followed by heat treatment of the substrate at a given temperature for an extended period of time to increase the adhesion strength between the substrate and the coating. Wang et al. (Wang et al., 2021) demonstrated that, through the heat-alkali treatment, an ultrathin Ti dioxide layer, upon contacting the titanium surface with air, could react with sodium hydroxide to form an amorphous sodium titanate layer, considered as the stable structure with high corrosion resistance of Ti upon contact with body fluids, precisely, a phenomenon closely related to dental implant failures.

Nevertheless, some authors have highlighted the poor cytocompatibility of Cht, which is a key factor in osteoconductivity for bone regeneration, possibly due to the lack of cell binding sites (Albrektsson and Johansson, 2001). To solve these drawbacks, the incorporation of materials such as graphene or the enrichment with bioactive materials of the extracellular matrix has been proposed (Hansson et al., 2012; Wong et al., 2020; Brun et al., 2021; Schierano et al., 2021). Saccari et al. and Fernandez et al. proposed the modification of Cht with a fibronectin-DNA complex to enhance the activity of osteoblastic cells (Fernández et al., 2012; Saccani et al., 2019).

Other studies have highlighted the degree of deacetylation and molecular weight of Cht as determinants for osteoblast adhesion, growth, and differentiation. Sukul et al. (Sukul et al., 2021), found *in vitro* that high deacetylation chitosan favored osteoblast adhesion, secretion of bone markers and extracellular matrix production, while low deacetylation induced secretion of osteoclastogenesis-promoting factors. Similarly, high molecular weight Cht induced the secretion of factors facilitating angiogenesis and bone remodeling.

These new technologies are in the research phase, and in general, although it is accepted that Cht-coated dental implants may have a higher osseointegration capacity, they are not

TABLE 2 Characteristics of *in vivo* studies.

In vivo studies	Aplicability	Cost	Difficulty of coating preparation	Substrate	Coating and method	Outcomes
Zhang et al. (Zhang et al., 2020)	+ +	+ + +	+ + +	Porous Ti	Cht/HA composite coating Electrochemical deposition	Osteoblast-like cell proliferation and differentiation
Takanche et al. (Takanche et al., 2018)	+	+ + +	+ + +	Ti	Chitosan-gold nanoparticles Graft-on technique	Increased osteogenesis and inhibition of osteoclastogenesis
Bumgardner et al. (Bumgardner et al., 2007)	+ +	+ +	+ +	Ti	1 wt% of 92.3% deacetylated chitosan in 1% acetic acid Solution casting	Minimal inflammatory response and development of lamellar bone
Kung et al. (Kung et al., 2011)	+	+ +	+ +	Ti	Two types of chitosan with molecular weights of 450 and 750 kDa and with deacetylation degree > 90% Enveloped membranes	New bone formed ectopically
López-Valverde et al. (López-Valverde et al., (2021a); López-Valverde et al., (2022))	+ + +	+	+	Porous Ti6Al4V	Pure chitosan acid solution Immersion	Higher bone density compared to the conventional etched surface group

+ low; + + moderate; + + + high; HA, hydroxyapatite.

commercially available, but are likely to become a commercial option in the future. (Bumgardner et al., 2007; Civantos et al., 2017; Palla-Rubio et al., 2019; Alnufaiy et al., 2020; López-Valverde et al., 2021b; Eftekhar Ashtiani et al., 2021; Lin et al., 2021).

Trends; next generation coatings

Over the past 2 decades, several surface coatings approaches have been proposed and studied to improve implant osseointegration. The development of future generations of dental implants, both under normal and tissue compromised conditions, will involve "tailored modifications" of substrate surfaces that enhance their biological performance and locally release bone regeneration stimulating molecules, especially at the bone-implant interface.

The most important problems related to insufficient compatibility of material surfaces could be summarized in four types:

- Topographical or mechanical incompatibility. The implant microdesign or surface condition has a great impact on the dynamics of osseointegration, especially, in low-density bone (Steigenga et al., 2003). Although surgical integration depends mainly on the implant macrodesign, the microdesign or microsurface topography may also play an important role in this phase. Salabi et al. in an animal model demonstrated that rough surfaces presented higher removal torque values than machined surfaces (Shalabi et al., 2006). A consensus report published in 2009 concluded that "the highest level of bone-to-implant contact was associated with moderately rough surfaces" (Lang et al., 2009). Regarding macrodesign, different implant thread designs have been proposed with the aim of improving and optimizing the osseointegration process, and implant geometry has been reported to affect bone-to-implant ratio and mechanical pull-out test values (Abuhussein et al., 2010).
- Biofouling. Any artificial material introduced into the body environment is at risk of biofouling, causing infections and leading to implant failure. Numerous studies have investigated non-biofouling with the aim of increasing the bioactivity of titanium for its broader applications in biomedical areas; Kang et al. (Kang et al., 2010) used biologically active molecules on Ti surfaces coated with polyethylene glycol methacrylate to enhance the non-biofouling property. Jesmer and Wylie and Manivasagam et al. (Jesmer and Wylie, 2020; Manivasagam et al., 2021) in recent reviews highlighted that biofouling is crucial for the optimization of biomaterials and devices interacting with complex biological environments composed of macromolecules, fluids and cells.
- The reaction of the immune system to the implant material may be the cause of a number of problems. Trindade et al. and Albrektsson et al. (Trindade et al., 2016; Trindade et al., 2018) interpreted osseointegration as a foreign body reaction to a biomaterial. Macrophages, which are the main effector cells in biological reactions to biomaterials, could contribute to some extent to the success or failure of

TABLE 3 Suitability of models and implantation sites of *in vivo* studies.

Studies	Suitability of experimental model	Model	Implantation sites
Zhang et al. (Zhang et al., 2020)	Low suitability	Rabbit	Femur
Takanche et al. (Takanche et al., 2018)	Moderate suitability	Rat	Jaw
Bumgardner et al. (Bumgardner et al., 2007)	Low suitability	Rabbit	Tibia
Kung et al. (Kung et al., 2011)	Low suitability	Rat	Subcutaneous
López-Valverde et al. (López-Valverde et al., (2021a); López-Valverde et al., (2022))	Suitable	Dog	Jaw

Likewise, imaging assessment methods will gain more and more importance as diagnostic methods for bone quantification around implant surfaces.

implants (Chen et al., 2016). Macrophages have also been shown to directly contribute to bone formation during the healing process (Pajarinen et al., 2019). However, some studies have reported that macrophage infiltration triggered by implant insertion promotes bone formation around implants in the first 2 weeks, whereas macrophage depletion impairs new bone formation (Wang et al., 2020). After the implantation procedure, it seems that the bone regeneration capacity is strongly activated, which would indicate that Ti implants complement the bone healing process and that innate and acquired immune mechanisms would be required in these biological events. Inflammation is the main mechanism of innate immunity; therefore, an initial and well-controlled inflammatory immune response is essential for bone formation and osseointegration (Trindade et al., 2018). Amengual-Peñafiel et al. reported in a recent review article that immunomodulatory strategies focused on host osteoimmunology are a promising approach and that osteoimmunology will allow a better understanding and integration of the concept of osseointegration in the future (Amengual-Peñafiel et al., 2021).

Biodegradable coatings

This type of research is focused on the true biological character of osseointegration and the innovative approaches proposed are intended to mimic the biochemical environment and nanostructural architecture of human bone. Biodegradable polymers are polymers which are decomposed in a living body but whose degradation products remain in tissues for long-term. Coatings by different molecules, such as Cht, collagen, polysaccharides, peptides and biodegradable polymers, are being thoroughly investigated for their interesting results on implant surfaces (Song et al., 2020). Natural polymers possess highly organized structures and can contain an extracellular substance, called ligand, which is of great interest for binding to cell receptors; moreover, these types of structures can guide cell growth at different stages of development and stimulate an immune response (Coletta et al., 2018). It has been suggested that bioactive ions affect small molecules involved in intra- and intercellular signaling pathways and that these osteoinductive effects could be induced by bioactive small molecules that modulate bone morphogenic protein expression (Aravamudhan et al., 2013; Han et al., 2013; Kalinichenko et al., 2019).

However, although the underlying mechanism remains unexplored, the bone healing process at the bone/implant interface is hampered by oxidative stress induced by the overproduction of reactive oxygen species. In order to endow Ti substrates with antioxidant activity to enhance bone formation, Chen et al. (Chen et al., 2017) in a study on rabbit femur constructed on Ti substrates a multilayer structure composed of Cht-catechin, gelatin and HA nanofibers, obtaining excellent antioxidant and cell healing-promoting efficacy, osteogenesis differentiation and osteogenesis-related genes expression of osteoblasts.

Laser surface treatments

Moderately rough surfaces (1–2 μm) have been reported to have benefits in osteoblast differentiation and migration (Andrukhov et al., 2016). The application of laser treatment on Ti surfaces can create identical and constant morphologies, which provides better cell adhesion and proliferation, therefore, some researchers have proposed this type of treatment on dental implants; in addition, has demonstrated its efficacy as a pre-coating with certain ceramics (Veiko et al., 2021). It has even been proposed as an alternative technology for transforming hydrophobic implant surfaces to hydrophilic (Rupp et al., 2018). When a laser is used to modify the surface properties of titanium, surface modification occurs through melting and vaporization. Different surface patterns with enhanced biological responses can be provided, and the deposition of contaminants on the surface is minimized compared to traditional modification methods (Menci et al., 2019). A systematic review by Simões et al. (Simões et al., 2021) demonstrated the ability of the laser to modify the surface properties of titanium; however, a large variation in results was observed depending on the parameters used, such as number and speed of scans, energy density, power,

pulse repetition rate, fluence and focal plane variation, suggesting the need for specific protocols for the high-power laser to optimize results.

Some commercial firms have included this type of surface treatments in dental implants and prosthetic abutments. Blazquez-Hinarejos et al. (Blázquez-Hinarejos et al., 2017) in a systematic review carried out in preclinical and clinical studies, showed that different types of surface modifications of implant abutments can provide a benefit for the attachment of connective tissue to the abutment, although they recommended further human studies to obtain more evidence of the results.

Nanotechnology

It is well established that osteogenic cells respond better to microrough Ti surfaces compared to machined surfaces, however, research is needed to find the ideal surface topography that enhances bioactivity and osteogenesis (Yeo, 2019). Nanoengineering is emerging as a field of engineering aimed at further improving the bioactivity of dental implants. It has been demonstrated, *in vitro* and *in vivo*, that surface modification of titanium implants at the nanoscale offers enhanced bioactivity, surpassing clinical microroughness, employing various strategies such as plasma treatment, micromachining, polishing/grinding, particle blasting, chemical etching, and electrochemical anodization (Chopra et al., 2021).

The American Academy of Orthopaedic Surgeons (AAOS) indicates that infection (20.4%) was the most common etiology of failure in knee arthroplasty in the United States (Veerachamy et al., 2014), so certain studies focus their research on minimizing the immediate infection of the implant during surgery, investigating on coatings and metals with antibacterial properties, since the release of some of these coatings is prolonged during the first days after implantation, however, there is still no conclusive research on these aspects. (Kunrath et al., 2020; Kunrath and Campos, 2021).

DNA methylation

Epigenetics is the study of molecular processes that affect the flow of genetic information between DNA sequences and gene expression patterns, such as DNA methylation (Goldberg et al., 2007). The combined use of scaffolds with small molecules, such as novel epigenetic drugs (epi-drugs), can enhance cell differentiation (Cheng et al., 2016). In this regard, some studies on implant surfaces and osteoblast differentiation have focused on differences in the osteogenic potential of surfaces as a function of gene expression levels, and some have reported that implant surface topography can alter cellular activity (Zheng et al., 2020; Ichioka et al., 2021). A study by Cho et al. concluded that the surface topography of Ti implants affects their osteogenic potential through epigenetic changes, raising the possibility of using epidrugs to enhance osteogenesis on implant surfaces (Cho et al., 2021).

Considerations

The current approach to dental implant bioengineering involves the development of functionalized surfaces and bioactive coatings, together with strategies for *in situ* drug delivery, with the aim of reducing infection rates and improving clinical outcomes. Methods have to be developed to improve osseointegration of implants, both in normal and deficient bone conditions, especially through new macroscopic designs and surface modification.

In vitro methods are particularly fruitful for studying biological activity mechanistically, although their clinical application remains poor, mainly due to the absence of *in vivo* biokinetics; therefore, complete replacement of animals, at least in the near future, will not be possible (Saeidnia et al., 2015).

On the other hand, orthopedic and dental implant research will require specific animal models (Table 3), which reproduce the human condition and help to understand the complex process of osseointegration, and multiple preclinical and clinical trials will be necessary before new biomedical implant designs can enter the market, focusing, above all, on long-term functional studies.

Conclusion

Titanium and its alloys are the materials of choice for the manufacture of orthopedic and dental implants because of their excellent corrosion resistance and proven biocompatibility. However, there are still limitations caused by post-surgical infections or lack of biointegration.

In this review, different relevant methods of Cht coatings on Ti substrates for dental implant applications as well as next generation coatings have been addressed.

As a natural polysaccharide, it has been demonstrated in the different studies that Cht coatings provide biocompatibility, excellent adhesion and anti-corrosion properties in different coatings. In addition, it has been shown that Cht coatings offer mechanical stability during the first weeks after implantation, good degradability and optimal osseointegration. Better mineralization, cell proliferation and bioactivity have also been demonstrated around these coatings. However, despite the extensive literature, much research is needed to improve the performance of Cht-based coatings, especially by improving the bond strength and the interface between the coating and the substrate. Likewise, new coating strategies with Cht and other similar biopolymers should be implemented to improve bioactivity and adhesion without impairing the properties of

the substrates, with particular attention to reducing toxicity in coating preparations.

Nevertheless, Cht-based coatings are promising candidates for improving orthopedic and dental implants, although more research is needed to develop coatings customized to each patient's bone circumstances by establishing surfaces with a standardized topography to ensure long-term success.

Author contributions

Conceptualization, NL-V and JA. Methodology, AL-V. Validation, BM, NL-V and JA. Data curation, CR. Writing—original draft preparation, NL-V and JA. Writing—review and editing, AL-V. Supervision, JA. All authors have read and agreed to the published version of the manuscript.

Conflict of interest

The authors declare that the research was conducted in the absence of any commercial or financial relationships that could be construed as a potential conflict of interest.

Publisher's note

All claims expressed in this article are solely those of the authors and do not necessarily represent those of their affiliated organizations, or those of the publisher, the editors and the reviewers. Any product that may be evaluated in this article, or claim that may be made by its manufacturer, is not guaranteed or endorsed by the publisher.

References

Abarrategi, A., Civantos, A., Ramos, V., Sanz Casado, J. V., and Lopez-Lacomba, J. L. (2008). Chitosan film as rhBMP2 carrier: Delivery properties for bone tissue application. *Biomacromolecules* 9, 711–718. doi:10.1021/bm701049g

Abu Nada, L., Al Subaie, A., Mansour, A., Wu, X., Abdallah, M. N., Al-Waeli, H., et al. (2018). The antidepressant drug, sertraline, hinders bone healing and osseointegration in rats' tibiae. *J. Clin. Periodontol.* 45, 1485–1497. doi:10.1111/jcpe.13015

Abuhussein, H., Pagni, G., Rebaudi, A., and Wang, H. L. (2010). The effect of thread pattern upon implant osseointegration. *Clin. Oral Implants Res.* 21, 129–136. doi:10.1111/j.1600-0501.2009.01800.x

Adell, R., Lekholm, U., Rockler, B., and Brånemark, P. I. (1981). A 15-year study of osseointegrated implants in the treatment of the edentulous jaw. *Int. J. Oral Surg.* 10, 387–416. doi:10.1016/s0300-9785(81)80077-4

Albrektsson, T., Brånemark, P. I., Hansson, H. A., and Lindström, J. (1981). Osseointegrated titanium implants. Requirements for ensuring a long-lasting, direct bone-to-implant anchorage in man. *Acta Orthop. Scand.* 52, 155–170. doi:10.3109/17453678108991776

Albrektsson, T., and Johansson, C. (2001). Osteoinduction, osteoconduction and osseointegration. *Eur. Spine J.* 10 (2), S96–S101. doi:10.1007/s005860100282

Alnufaiy, B. M., Lambarte, R. N. A., and Al-Hamdan, K. S. (2020). The osteogenetic potential of chitosan coated implant: An *in vitro* study. *J. Stem Cells Regen. Med.* 16, 44–49. doi:10.46582/jsrm.1602008

Alshammari, H., Neilands, J., Svensäter, G., and Stavropoulos, A. (2021). Antimicrobial potential of strontium hydroxide on bacteria associated with peri-implantitis. *Antibiot. (Basel)* 10, 150. doi:10.3390/antibiotics10020150

Alves, N., and Mano, J. (2008). Chitosan derivatives obtained by chemical modifications for biomedical and environmental applications. *Int. J. Biol. Macromol.* 43, 401–414. doi:10.1016/j.ijbiomac.2008.09.007

Amengual-Peñafiel, L., Córdova, L. A., Constanza Jara-Sepúlveda, M., Brañes-Aroca, M., Marchesani-Carrasco, F., Cartes-Velásquez, R., et al. (2021). Osteoimmunology drives dental implant osseointegration: A new paradigm for implant dentistry. *Jpn. Dent. Sci. Rev.* 57, 12–19. doi:10.1016/j.jdsr.2021.01.001

Andrukhov, O., Huber, R., Shi, B., Berner, S., Rausch-Fan, X., Moritz, A., et al. (2016). Proliferation, behavior, and differentiation of osteoblasts on surfaces of different microroughness. *Dent. Mat.* 32, 1374–1384. doi:10.1016/j.dental.2016.08.217

Aravamudhan, A., Ramos, D. M., Nip, J., Subramanian, A., James, R., Harmon, M. D., et al. (2013). Osteoinductive small molecules: Growth factor alternatives for bone tissue engineering. *Curr. Pharm. Des.* 19, 3420–3428. doi:10.2174/1381612811319190008

Barradas, A. M., Yuan, H., van Blitterswijk, C. A., and Habibovic, P. (2011). Osteoinductive biomaterials: Current knowledge of properties, experimental models and biological mechanisms. *Eur. Cell. Mat.* 21: 407–429doi:10.22203/ecm.v021a31

Barton, M. J., Morley, J. W., Mahns, D. A., Mawad, D., Wuhrer, R., Fania, D., et al. (2014) Tissue repair strength using chitosan adhesives with different physical-chemical characteristics. *J. Biophot.* 11-12, 948–955. doi:10.1002/jbio.201300148

Beder, O. W., and Ploger, W. J. (1959). Intraoral titanium implants. *Oral Surg. Oral Med. Oral Pathol.* 12, 787–799. doi:10.1016/0030-4220(59)90028-3

Blázquez-Hinarejos, M., Ayuso-Montero, R., Jané-Salas, E., and López-López, J. (2017). Influence of surface modified dental implant abutments on connective tissue attachment: A systematic review. *Arch. Oral Biol.* 80, 185–192. doi:10.1016/j.archoralbio.2017.04.020

Bosshardt, D. D., Chappuis, V., and Buser, D. (2017). Osseointegration of titanium, titanium alloy and zirconia dental implants: Current knowledge and open questions. *Periodontol. 2000* 73, 22–40. doi:10.1111/prd.12179

Brånemark, P. I., Hansson, B. O., Adell, R., Breine, U., Lindstrom, J., Hallen, O., et al. (1977). Osseointegrated implants in the treatment of the edentulous jaw. Experience from a 10- year period. *Scand. J. Plast. Reconstr. Surg. Suppl.* 16, 1–132.

Brun, P., Zamuner, A., Battocchio, C., Cassari, L., Todesco, M., Graziani, V., et al. (2021). Bio-functionalized chitosan for bone tissue engineering. *Int. J. Mol. Sci.* 22 (11), 5916. doi:10.3390/ijms22115916

Bumgardner, J. D., Chesnutt, B. M., Yuan, Y., Yang, Y., Appleford, M., Oh, S., et al. (2007). The integration of chitosan-coated titanium in bone: An *in vivo* study in rabbits. *Implant Dent.* 16, 66–79. doi:10.1097/ID.0b013e3180312011

Bumgardner, J. D., Wiser, R., Elder, S. H., Jouett, R., Yang, Y., Ong, J. L., et al. (2003). Contact angle, protein adsorption and osteoblast pre-cursor cell attachment to chitosan coatings bonded to titanium. *J. Biomaterials Sci. Polym. Ed.* 14, 1401–1409. doi:10.1163/156856203322599734

Bumgardner, J. D., Wiser, R., Gerard, P. D., Bergin, P., Chestnutt, B., Marin, M., et al. (2003). Chitosan: Potential use as a bioactive coating for orthopaedic and craniofacial/dental implants. *J. Biomaterials Sci. Polym. Ed.* 14, 423–438. doi:10.1163/156856203766652048

Buser, D., Broggini, N., Wieland, M., Schenk, R. K., Denzer, A. J., Cochran, D. L., et al. (2004). Enhanced bone apposition to a chemically modified SLA titanium surface. *J. Dent. Res.* 83, 529–533. doi:10.1177/154405910408300704

Buser, D., Sennerby, L., and De Bruyn, H. (2017). Modern implant dentistry based on osseointegration: 50 years of progress, current trends and open questions. *Periodontol. 2000* 73, 7–21. doi:10.1111/prd.12185

CAMARADES CAMARADESResearch group. Available at: http://www.camarades.info/[Accessed March 2022].

Carcuac, O., Abrahamsson, I., Albouy, J. P., Linder, E., Larsson, L., Berglundh, T., et al. (2013). Experimental periodontitis and peri-implantitis in dogs. *Clin. Oral Implants Res.* 24, 363–371. doi:10.1111/clr.12067

Carlsson, L. V., Alberktsson, T., and Berman, C. (1989). Bone response to plasma-cleaned titanium implants. *Int. J. Oral Maxillofac. Implants* 4, 199–204.

Chen, W., Shen, X., Hu, Y., Xu, K., Ran, Q., Yu, Y., et al. (2017). Surface functionalization of titanium implants with chitosan-catechol conjugate for

suppression of ROS-induced cells damage and improvement of osteogenesis. *Biomaterials* 114, 82–96. doi:10.1016/j.biomaterials.2016.10.055

Chen, Z., Klein, T., Murray, R. Z., Crawford, R., Chang, J., Wu, C., et al. (2016). Osteoimmunomodulation for the development of advanced bone biomaterials. *Mater. Today* 6, 304–321. doi:10.1016/j.mattod.2015.11.004

Cheng, J., Ding, Q., Wang, J., Deng, L., Yang, L., Tao, L., et al. (2016). 5-Azacytidine delivered by mesoporous silica nanoparticles regulates the differentiation of P19 cells into cardiomyocytes. *Nanoscale* 8, 2011–2021. doi:10.1039/c5nr08560h

Cho, Y. D., Kim, W. J., Kim, S., Ku, Y., and Ryoo, H. M. (2021). Surface topography of titanium affects their osteogenic potential through DNA methylation. *Int. J. Mol. Sci.* 22, 2406. doi:10.3390/ijms22052406

Chopra, D., Gulati, K., and Ivanovski, S. (2021). Understanding and optimizing the antibacterial functions of anodized nano-engineered titanium implants. *Acta Biomater.* 127, 80–101. doi:10.1016/j.actbio.2021.03.027

Chrcanovic, B. R., Kisch, J., Albrektsson, T., and Wennerberg, A. (2018). A retrospective study on clinical and radiological outcomes of oral implants in patients followed up for a minimum of 20 years. *Clin. Implant Dent. Relat. Res.* 20, 199–207. doi:10.1111/cid.12571

Civantos, A., Martinez-Campos, E., Ramos, V., Elvira, C., Gallardo, A., Abarrategi, A., et al. (2017). Titanium coatings and surface modifications: Toward clinically useful bioactive implants. *ACS Biomater. Sci. Eng.* 3, 1245–1261. doi:10.1021/acsbiomaterials.6b00604

Clarke, E. G., and Hickman, J. (1953). An investigation into the correlation between the electrical potentials of metals and their behaviour in biological fluids. *J. Bone Jt. Surg. Br. volume* 35-B, 467–473. doi:10.1302/0301-620X.35B3.467

Coletta, D. J., Missana, L. R., Martins, T., Jammal, M. V., García, L. A., Farez, N., et al. (2018). Synthetic three-dimensional scaffold for application in the regeneration of bone tissue. *J. Biomater. Nanobiotechnol.* 9, 277–289. doi:10.4236/jbnb.2018.94016

Cornell, C. N., and Lane, J. M. (1998). Current understanding of osteoconduction in bone regeneration. *Clin. Orthop. Relat. Res.* 355S, S267–S273. doi:10.1097/00003086-199810001-00027

Crini, G. (2019). Historical review on chitin and chitosan biopolymers. *Environ. Chem. Lett.* 17, 1623–1643. doi:10.1007/s10311-019-00901-0

Cunliffe, R. N. (2003). α-Defensins in the gastrointestinal tract. *Mol. Immunol.* 40, 463–467. doi:10.1016/s0161-5890(03)00157-3

Dohan Ehrenfest, D. M., Coelho, P. G., Kang, B. S., Sul, Y. T., and Albrektsson, T. (2010). Classification of osseointegrated implant surfaces: Mate-rials, chemistry and topography. *Trends Biotechnol.* 28, 198–206. doi:10.1016/j.tibtech.2009.12.003

Eftekhar Ashtiani, R., Alam, M., Tavakolizadeh, S., and Abbasi, K. (2021). The role of biomaterials and biocompatible materials in implant-supported dental prosthesis. *Evidence-Based Complementary Altern. Med.* 2021, 1–9. doi:10.1155/2021/3349433

Elefteriou, F., Campbell, P., and Ma, Y. (2014). Control of bone remodeling by the peripheral sympathetic nervous system. *Calcif. Tissue Int.* 94, 140–151. doi:10.1007/s00223-013-9752-4

Fakhri, E., Eslami, H., Maroufi, P., Pakdel, F., Taghizadeh, S., Ganbarov, K., et al. (2020). Chitosan biomaterials application in dentistry. *Int. J. Biol. Macromol.* 162, 956–974. doi:10.1016/j.ijbiomac.2020.06.211

Fernández, M. S., Arias, J. I., Martínez, M. J., Saenz, L., Neira-Carrillo, A., Yazdani-Pedram, M., et al. (2012). Evaluation of a multilayered chitosan-hydroxy-apatite porous composite enriched with fibronectin or an *in vitro*-generated bone-like extracellular matrix on proliferation and diferentiation of osteoblasts. *J. Tissue Eng. Regen. Med.* 6, 497–504. doi:10.1002/term.455

Ferraris S, S., Örlygsson, G., Ng, C. H., Riccucci, G., and Spriano, S. (2022). Chemical, physical, and mechanical characterization of chitosan coatings on a chemically pre-treated Ti6Al4V alloy. *Surf. Coatings Technol.* 441, 128571. doi:10.1016/j.surfcoat.2022.128571

Ferraris, S., Spriano, S., Pan, G., Venturello, A., Bianchi, C. L., Chiesa, R., et al. (2011). Surface modification of Ti-6Al-4V alloy for biomineralization and specific biological response: Part I, inorganic modification. *J. Mat. Sci. Mat. Med.* 22, 533–545. doi:10.1007/s10856-011-4246-2

Fonteyne, E., Matthys, C., Bruneel, L., Becue, L., De Bruyn, H., Van Lierde, K., et al. (2021). Articulation, oral function, and quality of life in patients treated with implant overdentures in the mandible: A prospective study. *Clin. Implant Dent. Relat. Res.* 23, 388–399. doi:10.1111/cid.12989

Foster, L. J., Ho, S., Hook, J., Basuki, M., and Marçal, H. (2015). Chitosan as a biomaterial: Influence of degree of deacetylation on its physiochemical, material and biological properties. *PLoS One* 10, e0135153. doi:10.1371/journal.pone.0135153

Gérentes, P., Vachoud, L., Doury, J., and Domard, A. (2002). Study of a chitin-based gel as injectable material in periodontal surgery. *Biomaterials* 23, 1295–1302. doi:10.1016/s0142-9612(01)00247-2

Gil, J., Manero, J. M., Ruperez, E., Velasco-Ortega, E., Jiménez-Guerra, A., Ortiz-García, I., et al. (2021). Mineralization of titanium surfaces: Biomimetic implants. *Mater. (Basel)* 14, 2879. doi:10.3390/ma14112879

Glied, A., and Mundiya, J. (2021). Implant material Sciences. *Dent. Clin. North Am.* 65, 81–88. doi:10.1016/j.cden.2020.09.006

Goldberg, A. D., Allis, C. D., and Bernstein, E. (2007). Epigenetics: A landscape takes shape. *Cell* 128, 635–638. doi:10.1016/j.cell.2007.02.006

Gopi, D., Nithiya, S., Shinyjoy, E., Rajeswari, D., and Kavitha, L. (2014). Carbon nanotubes/carboxymethyl chitosan/mineralized hydroxyapatite composite coating on Ti-6Al-4V alloy for improved mechanical and biological properties. *Ind. Eng. Chem. Res.* 53, 7660–7669. doi:10.1021/ie403903q

Grosso, D. (2011). How to exploit the full potential of the dip-coating process to better control film formation. *J. Mat. Chem.* 21, 17033. doi:10.1039/C1JM12837J

Guillaume, B. (2016). Dental implants: A review. *Morphologie* 100, 189–198. doi:10.1016/j.morpho.2016.02.002

Hamed, I., Özogul, F., and Regenstein, J. M. (2016). Industrial applications of crustacean by-products (chitin, chitosan, and chitooligosaccharides): A review. *Trends Food Sci. Technol.* 40, 40–50. doi:10.1016/j.tifs.2015.11.007

Han, Q. Q., Du, Y., and Yang, P. S. (2013). The role of small molecules in bone regeneration. *Future Med. Chem.* 5, 1671–1684. doi:10.4155/fmc.13.133

Hansson, A., Hashom, N., Falson, F., Rousselle, P., Jordan, O., Borchard, G., et al. (2012). *In vitro* evaluation of an RGD-functionalized chitosan derivative for enhanced cell adhesion. *Carbohydr. Polym.* 90, 1494–1500. doi:10.1016/j.carbpol.2012.07.020

Hartlev, J., Kohberg, P., Ahlmann, S., Andersen, N. T., Schou, S., Isidor, F., et al. (2014). Patient satisfaction and esthetic outcome after immediate placement and provisionalization of single-tooth implants involving a definitive individual abutment. *Clin. Oral Implants Res.* 25, 1245–1250. doi:10.1111/clr.12260

Horikawa, T., Odatsu, T., Itoh, T., Soejima, Y., Morinaga, H., Abe, N., et al. (2017). Retrospective cohort study of rough- surface titanium implants with at least 25 years' function. *Int. J. Implant Dent.* 3, 42. doi:10.1186/s40729-017-0101-7

Hotchkiss, K. M., Reddy, G. B., Hyzy, S. L., Schwartz, Z., Boyan, B. D., Olivares-Navarrete, R., et al. (2016). Titanium surface characteristics, including topography and wettability, alter macrophage activation. *Acta Biomater.* 31, 425–434. doi:10.1016/j.actbio.2015.12.003

Ichioka, Y., Asa'ad, F., Malekzadeh, B. Ö., Westerlund, A., and Larsson, L. (2021). Epigenetic changes of osteoblasts in response to titanium surface characteristics. *J. Biomed. Mat. Res. A* 109, 170–180. doi:10.1002/jbm.a.37014

Jarczak, J., Kościuczuk, E. M., Lisowski, P., Strzałkowska, N., Jóźwik, A., Horbańczuk, J., et al. (2013). Defensins: Natural component of human innate immunity. *Hum. Immunol.* 74, 1069–1079. doi:10.1016/j.humimm.2013.05.008

Jayakumar, R., Prabaharan, M., Nair, S., Tokura, S., Tamura, H., Selvamurugan, N., et al. (2010). Novel carboxymethyl derivatives of chitin and chitosan materials and their biomedical applications. *Prog. Mat. Sci.* 55, 675–709. doi:10.1016/j.pmatsci.2010.03.001

Jemat, A., Ghazali, M. J., Razali, M., and Otsuka, Y. (2015). Surface modifications and their effects on titanium dental implants. *Biomed. Res. Int.* 2015, 1–11. doi:10.1155/2015/791725

Jesmer, A. H., and Wylie, R. G. (2020). Controlling experimental parameters to improve characterization of biomaterial fouling. *Front. Chem.* 8, 604236. doi:10.3389/fchem.2020.604236

Jofre, J., Castiglioni, X., and Lobos, C. A. (2013). Influence of minimally invasive implant-retained overdenture on patients' quality of life: A randomized clinical trial. *Clin. Oral Implants Res.* 24, 1173–1177. doi:10.1111/j.1600-0501.2012.02529.x

Jujur, I. N., Damisih, Devy K., Suha, S., Bachtiar, B. M., and Bachtiar, E. W. (2020). Effect of Implantation Ti-6Al-4V ELI in femoral bone defect regeneration of Sprague Dawley rat. *J. Adv. Pharm. Technol. Res.* 11, 202. doi:10.4103/japtr.JAPTR_74_20

Junker, R., Dimakis, A., Thoneick, M., and Jansen, J. A. (20092009). Effects of implant surface coatings and composition on bone integration: A systematic review. *Clin. Oral Implants Res.* 20 (4), 185–206. doi:10.1111/j.1600-0501.2009.01777.x

Kalinichenko, S. G., Matveeva, N. Y., Kostiv, R. Y., and Edranov, S. S. (2019). The topography and proliferative activity of cells immunoreactive to various growth factors in rat femoral bone tissues after experimental fracture and implantation of titanium implants with bioactive biodegradable coatings. *Biomed. Mat. Eng.* 30, 85–95. doi:10.3233/BME-181035

Kang, S. M., Kong, B., Oh, E., Choi, J. S., and Choi, I. S. (2010). Osteoconductive conjugation of bone morphogenetic protein-2 onto titanium/titanium oxide

surfaces coated with non-biofouling poly (poly (ethylene glycol) methacrylate). *Colloids Surfaces B Biointerfaces* 75, 385–389. doi:10.1016/j.colsurfb.2009.08.039

Keast Dh Janmohammad, A. (2021). The hemostatic and wound healing effect of chitosan following debridement of chronic ulcers. *Wounds* 33, 263–270. doi:10.25270/wnds/082421.01

Kim, J. G., Sun, B. H., Dietrich, M. O., Koch, M., Yao, G. Q., Diano, S., et al. (2015). AGRP neurons regulate bone mass. *Cell Rep.* 13, 8–14. doi:10.1016/j.celrep.2015.08.070

Koka, S., and Zarb, G. A. (2012). On osseointegration: The healing adaptation principle in the context of osseosufficiency, osseoseparation, and dental implant failure. *Int. J. Prosthodont.* 25, 48–52.

Krisanaprakornkit, S., Kimball, J. R., Weinberg, A., Darveau, R. P., Bainbridge, B. W., Dale, B. A., et al. (2000). Inducible expression of human beta-defensin 2 by Fusobacterium nucleatum in oral epithelial cells: Multiple signaling pathways and role of commensal bacteria in innate immunity and the epithelial barrier. *Infect. Immun.* 68, 2907–2915. doi:10.1128/IAI.68.5.2907-2915.2000

Kung, S., Devlin, H., Fu, E., Ho, K. Y., Liang, S. Y., Hsieh, Y. D., et al. (2011). The osteoinductive effect of chitosan-collagen composites around pure titanium implant surfaces in rats. *J. Periodontal Res.* 46, 126–133. doi:10.1111/j.1600-0765.2010.01322.x

Kunrath, M., Diz, F. M., Magini, R., and Galárraga-Vinueza, M. E. (2020). Nanointeraction: The profound influence of nanostructured and nano-drug delivery biomedical implant surfaces on cell behavior. *Adv. Colloid Interface Sci.* 284, 102265. doi:10.1016/j.cis.2020.102265

Kunrath, M. F., and Campos, M. M. (2021). Metallic-nanoparticle release systems for biomedical implant surfaces: Effectiveness and safety. *Nanotoxicology* 15, 721–739. doi:10.1080/17435390.2021.1915401

Lang, N. P., Jepsen, S., and Group 4, Working (2009). Implant surfaces and design (working group 4). *Clin. Oral Implants Res.* 20 (4), 228–231. doi:10.1111/j.1600-0501.2009.01771.x

Lang, N. P. (2019). Oral implants: The paradigm shift in restorative dentistry. *J. Dent. Res.* 98, 1287–1293. doi:10.1177/0022034519853574

Le Guéhennec, L., Soueidan, A., Layrolle, P., and Amouriq, Y. (2007). Surface treatments of titanium dental implants for rapid osseointegration. *Dent. Mat.* 23, 844–854. doi:10.1016/j.dental.2006.06.025

Lin, M. H., Wang, Y. H., Kuo, C. H., Ou, S. F., Huang, P. Z., Song, T. Y., et al. (2021). Hybrid ZnO/chitosan antimicrobial coatings with enhanced mechanical and bioactive properties for titanium implants. *Carbohydr. Polym.* 257, 117639. doi:10.1016/j.carbpol.2021.117639

López-Valverde, N., Flores-Fraile, J., and López-Valverde, A. (2020). The unknown process osseointegration. *Biol. (Basel)* 9, 168. doi:10.3390/biology9070168

López-Valverde, N., López-Valverde, A., Aragoneses, J. M., Martínez-Martínez, F., González-Escudero, M. C., Ramírez, J. M., et al. (2021). Bone density around titanium dental implants coating tested/coated with chitosan or melatonin: An evaluation via microtomography in jaws of beagle dogs. *Coatings* 11, 777. doi:10.3390/coatings11070777

López-Valverde, N., López-Valverde, A., Cortés, M. P., Rodríguez, C., Macedo De Sousa, B., Aragoneses, J. M., et al. (2022). Bone quantification around chitosan-coated titanium dental implants: A preliminary study by micro-CT analysis in jaw of a canine model. *Front. Bioeng. Biotechnol.* 10, 858786. doi:10.3389/fbioe.2022.858786

López-Valverde, N., López-Valverde, A., and Ramírez, J. M. (2021). Systematic review of effectiveness of chitosan as a biofunctionalizer of titanium implants. *Biology* 10, 102. doi:10.3390/biology10020102

Maeno, M., Lee, C., Kim, D. M., Da Silva, J., Nagai, S., Sugawara, S., et al. (2017). Function of platelet-induced epithelial attachment at titanium surfaces inhibits microbial colonization. *J. Dent. Res.* 96, 633–639. doi:10.1177/0022034516688888

Makihira, S., Nikawa, H., Shuto, T., Nishimura, M., Mine, Y., Tsuji, K., et al. (2011). Evaluation of trabecular bone formation in a canine model surrounding a dental implant fixture immobilized with an antimicrobial peptide derived from histatin. *J. Mat. Sci. Mat. Med.* 22, 2765–2772. doi:10.1007/s10856-011-4440-2

Manivasagam, V. K., Sabino, R. M., Kantam, P., and Popat, K. C. (2021). Surface modification strategies to improve titanium hemocompatibility: A comprehensive review. *Mat. Adv.* 2, 5824–5842. doi:10.1039/d1ma00367d

Menci, G., Demir, A. G., Waugh, D. G., Lawrence, J., and Previtali, B. (2019). Laser surface texturing of β-Ti alloy for orthopaedics: Effect of different wavelengths and pulse durations. *Appl. Surf. Sci.* 489, 175–186. doi:10.1016/j.apsusc.2019.05.111

Miron, R. J., Zohdi, H., Fujioka-Kobayashi, M., and Bosshardt, D. D. (2016). Giant cells around bone biomaterials: Osteoclasts or multi-nucleated giant cells? *Acta Biomater.* 46, 15–28. doi:10.1016/j.actbio.2016.09.029

Moenne, A., and González, A. (2021). Chitosan-alginate- carrageenan-derived oligosaccharides stimulate defense against biotic and abiotic stresses, and growth in plants: A historical perspective. *Carbohydr. Res.* 503, 108298. doi:10.1016/j.carres.2021.108298

Mohan, K., Ganesan, A. R., Ezhilarasi, P. N., Kondamareddy, K. K., Rajan, D. K., Sathishkumar, P., et al. (2022). Green and eco-friendly approaches for the extraction of chitin and chitosan: A review. *Carbohydr. Polym.* 287, 119349. doi:10.1016/j.carbpol.2022.119349

Mohire, N. C., and Yadav, A. V. (2010). Chitosan-based polyherbal toothpaste: As novel oral hygiene product. *Indian J. Dent. Res.* 21, 380. doi:10.4103/0970-9290.70808

Moskalewicz, T., Kot, M., Seuss, S., Kędzierska, A., Czyrska-Filemonowicz, A., Boccaccini, A. R., et al. (2015). Electrophoretic deposition and characterization of HA/chitosan nanocomposite coatings on Ti6Al7Nb alloy. *Mater. Mat. Int.* 21, 96–103. doi:10.1007/s12540-015-1011-y

Nakajima, H., and Okabe, T. (1996). Titanium in dentistry: Development and research in the. *Dent. Mat. J.* 15, 77–90. doi:10.4012/dmj.15.77

Naveau, A., Shinmyouzu, K., Moore, C., Avivi-Arber, L., Jokerst, J., Koka, S., et al. (2019). Etiology and measurement of peri-implant crestal bone loss (CBL). *J. Clin. Med.* 8, 166. doi:10.3390/jcm8020166

Nguyen du, T., Kleiman, M., Ryu, K. A., Hiew, S., Brubaker, K., Mughnetsyan, R., et al. (2014). Three-dimensional conformal coatings through the entrapment of polymer membrane precursors. *ACS Appl. Mat. Interfaces* 6, 2830–2835. doi:10.1021/am4053943

Ogle, O. E. (2015). Implant surface material, design, and osseointegration. *Dent. Clin. North Am.* 59, 505–520. doi:10.1016/j.cden.2014.12.003

Ong, J. L., and Chan, D. C. (2000). Hydroxyapatite and their use as coatings in dental implants: A review. *Crit. Rev. Biomed. Eng.* 28, 667–707. doi:10.1615/critrevbiomedeng.v28.i56.10

Pajarinen, J., Lin, T., Gibon, E., Kohno, Y., Maruyama, M., Nathan, K., et al. (2019). Mesenchymal stem cell-macrophage crosstalk and bone healing. *Biomaterials* 196, 80–89. doi:10.1016/j.biomaterials.2017.12.025

Pal, S., Tak, Y. K., Han, E., Rangasamy, S., and Song, J. M. (2014). A multifunctional composite of an antibacterial higher-valent silver metallopharmaceutical and a potent wound healing polypeptide: A combined killing and healing approach to wound care. *New J. Chem.* 38, 3889–3898. doi:10.1039/c4nj00160e

Palla-Rubio, B., Araújo-Gomes, N., Fernández-Gutiérrez, M., Rojo, L., Suay, J., Gurruchaga, M., et al. (2019). Synthesis and characterization of silica-chitosan hybrid materials as antibacterial coatings for titanium implants. *Carbohydr. Polym.* 203, 331–341. doi:10.1016/j.carbpol.2018.09.064

Panayotov, I. V., Vladimirov, B. S., Dutilleul, P. Y., Levallois, B., and Cuisinier, F. (2015). Strategies for immobilization of bioactive organic molecules on titanium implant surfaces - a review. *Folia Med. Plovdiv.* 57 (1), 11–18. doi:10.1515/folmed-2015-0014

Pang, X., and Zhitomirsky, I. (2007). Electrophoretic deposition of composite hydroxyapatite-chitosan coatings. *Mat. Charact.* 58, 339–348. doi:10.1016/j.matchar.2006.05.011

Pattanaik, B., Pawar, S., and Pattanaik, S. (2012). Biocompatible implant surface treatments. *Indian J. Dent. Res.* 23, 398. doi:10.4103/0970-9290.102240

Pfeufer, N. Y., Hofmann-Peiker, K., Mühle, M., Warnke, P. H., Weigel, M. C., Kleine, M., et al. (2011). Bioactive coating of titanium surfaces with recombinant human β-defensin-2 (rHuβD2) may prevent bacterial colonization in orthopaedic surgery. *J. Bone Jt. Surg.* 93, 840–846. doi:10.2106/JBJS.I.01738

Qin, Y., and Li, P. (2020). Antimicrobial chitosan conjugates: Current synthetic strategies and potential applications. *Int. J. Mol. Sci.* 21, 499. doi:10.3390/ijms21020499

Quach, D., and Britton, R. A. (2017). Gut microbiota and bone health. *Adv. Exp. Med. Biol.* 1033, 47–58. doi:10.1007/978-3-319-66653-2_4

Quesada, H. B., de Araújo, T. P., Vareschini, D. T., de Barros, M. A. S. D., Gomes, R. G., Bergamasco, R., et al. (2020). Chitosan, alginate and other macromolecules as activated carbon immobilizing agents: A review on composite adsorbents for the removal of water contaminants. *Int. J. Biol. Macromol.* 164, 2535–2549. doi:10.1016/j.ijbiomac.2020.08.118

Rahmani, F., Moghadamnia, A. A., Kazemi, S., Shirzad, A., and Motallebnejad, M. (2018). Effect of 0.5% chitosan mouthwash on recurrent aphthous stomatitis: A randomized double-blind crossover clinical trial. *Electron. Physician* 10, 6912–6919. doi:10.19082/6912

Ren, B., Wan, Y., Liu, C., Wang, H., Yu, M., Zhang, X., et al. (2021). Improved osseointegration of 3D printed Ti-6Al-4V implant with a hierarchical micro/nano surface topography: An *in vitro* and *in vivo* study. *Mater. Sci. Eng. C* 118, 111505. doi:10.1016/j.msec.2020.111505

Ruan, H. B., Dietrich, M. O., Liu, Z. W., Zimmer, M. R., Li, M. D., Singh, J. P., et al. (2014). O-GlcNAc transferase enables AgRP neurons to suppress browning of white fat. *Cell* 159, 306–317. doi:10.1016/j.cell.2014.09.010

Rupp, F., Liang, L., Geis-Gerstorfer, J., Scheideler, L., and Hüttig, F. (2018). Surface characteristics of dental implants: A review. *Dent. Mat.* 34, 40–57. doi:10.1016/j.dental.2017.09.007

Saccani, M., Parisi, L., Bergonzi, C., Bianchera, A., Galli, C., Macaluso, G. M., et al. (2019). Surface modification of chitosan films with a fibronectin fragment-DNA aptamer complex to enhance osteoblastic cell activity: A mass spectrometry approach probing evidence on protein behavior. *Rapid Commun. Mass Spectrom.* 33, 336–342. doi:10.1002/rcm.8335

Saeidnia, S., Manayi, A., and Abdollahi, M. (2015). From *in vitro* experiments to *in vivo* and clinical studies; pros and cons. *Curr. Drug Discov. Technol.* 12, 218–224. doi:10.2174/1570163813666160114093140

Schierano, G., Canuto, R. A., Mauthe von Degerfeld, M., Navone, R., Peirone, B., Preti, G., et al. (2021). Role of rhBMP-7, fibronectin, and type I collagen in dental implant osseointegration process: An initial pilot study on minipig animals. *Mater. (Basel)* 14 (9), 2185. doi:10.3390/ma14092185

Shalabi, M. M., Wolke, J. G., and Jansen, J. A. (2006). The effects of implant surface roughness and surgical technique on implant fixation in an *in vitro* model. *Clin. Oral Implants Res.* 17, 172–178. doi:10.1111/j.1600-0501.2005.01202.x

Simões, I. G., Dos Reis, A. C., and da Costa Valente, M. L. (2021). Analysis of the influence of surface treatment by high-power laser irradiation on the surface properties of titanium dental implants: A systematic review. *J. Prosthet. Dent.* 2S0022-3913, 00421–00422. doi:10.1016/j.prosdent.2021.07.026

Siwakul, P., Sirinnaphakorn, L., Suwanprateep, J., Hayakawa, T., and Pugdee, K. (2021). Cellular responses of histatin-derived peptides im-mobilized titanium surface using a tresyl chloride-activated method. *Dent. Mat. J.* 40, 934–941. doi:10.4012/dmj.2020-307

Socorro-Perdomo, P. P., Florido-Suárez, N. R., Mirza-Rosca, J. C., and Saceleanu, M. V. (2022). EIS characterization of Ti alloys in rela-tion to alloying additions of Ta. *Mater. (Basel)* 15, 476. doi:10.3390/ma15020476

Song, J., Winkeljann, B., and Lieleg, O. (2020). Biopolymer-based coatings: Promising strategies to improve the biocompatibility and functionality of materials used in biomedical engineering. *Adv. Mat. Interfaces* 7, 2000850. doi:10.1002/admi.202000850

Steigenga, J. T., al-Shammari, K. F., Nociti, F. H., Misch, C. E., and Wang, H. L. (2003). Dental implant design and its relationship to long-term implant success. *Implant Dent.* 12, 306–317. doi:10.1097/01.id.0000091140.76130.a1

Sugawara, S., Maeno, M., Lee, C., Nagai, S., Kim, D. M., Da Silva, J., et al. (2016). Establishment of epithelial attachment on titanium surface coated with platelet activating peptide. *PLoS One* 11, e0164693. doi:10.1371/journal.pone.0164693

Suh, J. K., and Matthew, H. W. (2000). Application of chitosan-based polysaccharide biomaterials in cartilage tissue engineering: A review. *Biomaterials* 21, 2589–2598. doi:10.1016/s0142-9612(00)00126-5

Sukul, M., Sahariah, P., Lauzon, H. L., Borges, J., Másson, M., Mano, J. F., et al. (2021). *In vitro* biological response of human osteoblasts in 3D chitosan sponges with controlled degree of deacetylation and molecular weight. *Carbohydr. Polym.* 254, 117434. doi:10.1016/j.carbpol.2020.117434

Takanche, J. S., Kim, J. E., Kim, J. S., Lee, M. H., Jeon, J. G., Park, I. S., et al. (2018). Chitosan-gold nanoparticles mediated gene delivery of c-myb facilitates osseointegration of dental implants in ovariectomized rat. *Artif. Cells Nanomed. Biotechnol.* 46, S807–S817. doi:10.1080/21691401.2018.1513940

Tarnow, D. P. (2014). Commentary: Replacing missing teeth with dental implants. A century of progress. *J. Periodontol.* 85, 1475–1477. doi:10.1902/jop.2014.140327

Trindade, R., Albrektsson, T., Galli, S., Prgomet, Z., Tengvall, P., Wennerberg, A., et al. (2018). Osseointegration and foreign body reaction: Titanium implants activate the immune system and suppress bone resorption during the first 4 weeks after implantation. *Clin. Implant Dent. Relat. Res.* 20, 82–91. doi:10.1111/cid.12578

Trindade, R., Albrektsson, T., Tengvall, P., and Wennerberg, A. (2016). Foreign body reaction to biomaterials: On mechanisms for buildup and breakdown of osseointegration. *Clin. Implant Dent. Relat. Res.* 18, 192–203. doi:10.1111/cid.12274

Vakili, N., and Asefnejad, A. (2020). Titanium coating: Introducing an antibacterial and bioactive chitosan-alginate film on titanium by spin coating. *Biomed. Tech.* 65, 621–630. doi:10.1515/bmt-2018-0108

Van Dijk, I., Beker, A., Jellema, W., Nazmi, K., Wu, G., Wismeijer, D., et al. (2017). Histatin 1 enhances cell adhesion to titanium in an implant integration model. *J. Dent. Res.* 96, 430–436. doi:10.1177/0022034516681761

Veerachamy, S., Yarlagadda, T., Manivasagam, G., and Yarlagadda, P. K. (2014). Bacterial adherence and biofilm formation on medical implants: A review. *Proc. Inst. Mech. Eng. H.* 228, 1083–1099. doi:10.1177/0954411914556137

Veiko, V., Karlagina, Y., Itina, T., Kuznetsova, D., Elagin, V., Zagaynova, E., et al. (2021). Laser-assisted fabrication and *in vitro* verification of functionalized surface for cells biointegration. *Opt. Laser Technol.* 138, 106871. doi:10.1016/j.optlastec.2020.106871

Wang, X., Li, Y., Feng, Y., Cheng, H., and Li, D. (2020). The role of macrophages in osseointegration of dental implants: An experimental study *in vivo*. *J. Biomed. Mat. Res. A* 108, 2206–2216. doi:10.1002/jbm.a.36978

Wang, Z., Mei, L., Liu, X., and Zhou, Q. (2021). Hierarchically hybrid biocoatings on Ti implants for enhanced antibacterial activity and osteogenesis. *Colloids Surfaces B Biointerfaces* 204, 111802. doi:10.1016/j.colsurfb.2021.111802

Weber, F. E. (2019). Reconsidering osteoconduction in the era of additive manufacturing. *Tissue Eng. Part B Rev.* 25, 375–386. doi:10.1089/ten.TEB.2019.0047

Wennerberg, A., Albrektsson, T., and Chrcanovic, B. (2018). Long-term clinical outcome of implants with different surface modifications. *Eur. J. Oral Implantol.* 11, S123–S136.

Wennerberg, A., Bolind, P., and Albrektsson, T. (1991). Glow-discharge pretreated implants combined with temporary bone tissue ischemia. *Swed. Dent. J.* 15, 95–101.

Wong, S. H. M., Lim, S. S., Tiong, T. J., Show, P. L., Zaid, H. F. M., Loh, H. S., et al. (2020). Preliminary *in vitro* evaluation of chitosan-graphene oxide scaffolds on osteoblastic adhesion, proliferation, and early differentiation. *Int. J. Mol. Sci.* 21 (15), 5202. doi:10.3390/ijms21155202

Yeo, I. L. (2019). Modifications of dental implant surfaces at the micro- and nano-level for enhanced osseointegration. *Mater. (Basel)* 13, 89. doi:10.3390/ma13010089

Zhang, C., Wang, Z., Li, Y., Yang, Y., Ju, X., He, R., et al. (2019). The preparation and physiochemical characterization of rapeseed protein hydrolysate-chitosan composite films. *Food Chem. x.* 272, 694–701. doi:10.1016/j.foodchem.2018.08.097

Zhang, T., Zhang, X., Mao, M., Li, J., Wei, T., Sun, H., et al. (2020). Chitosan/hydroxyapatite composite coatings on porous Ti6Al4V titanium implants: *In vitro* and *in vivo* studies. *J. Periodontal Implant Sci.* 50, 392. doi:10.5051/jpis.1905680284

Zheng, Y., Zheng, Y. F., Jia, L. F., Zhang, Y., and Lin, Y. (2020). Integrated analysis of lncRNA-mRNA networks associated with an SLA titanium surface reveals the potential role of HIF1A-AS1 in bone remodeling. *RSC Adv.* 10, 20972–20990. doi:10.1039/d0ra01242d

frontiers | Frontiers in Bioengineering and Biotechnology

ORIGINAL RESEARCH
published: 22 July 2022
doi: 10.3389/fbioe.2022.920696

Development, *In-Vitro* Characterization and *In-Vivo* Osteoinductive Efficacy of a Novel Biomimetically-Precipitated Nanocrystalline Calcium Phosphate With Internally-Incorporated Bone Morphogenetic Protein-2

Gaoli Xu[1,2†], Chenxi Shen[1,3†], Haiyan Lin[4,5†], Jian Zhou[4], Ting Wang[6], Ben Wan[1,3], Munerah Binshabaib[7], Tymour Forouzanfar[1], Guochao Xu[2], Nawal Alharbi[8] and Gang Wu[1,9]**

[1]Department of Oral and Maxillofacial Surgery/Pathology, Amsterdam UMC and Academic Center for Dentistry Amsterdam (ACTA), Vrije Universiteit Amsterdam (VU), Amsterdam Movement Science (AMS), Amsterdam, Netherlands, [2]Department of Stomatology, Zhejiang Hospital, Hangzhou, China, [3]Hangzhou Huibo Science and Technology Co. Ltd., Xinjie Science Park, Hangzhou, China, [4]Department of Implantology, Hangzhou Stomatology Hospital, Hangzhou, China, [5]Savid School of Stomatology, Hangzhou Medical College, Hangzhou, China, [6]Department of Stomatology, Zhejiang Chinese Medical University, Hangzhou, China, [7]Department of Preventive Dental Sciences, College of Dentistry, Princess Nourah Bint Abdulrahman University, Riyadh, Saudi Arabia, [8]Department of Prosthetic Dental Sciences, King Saud University, Riyadh, Saudi Arabia, [9]Department of Oral Cell Biology, Academic Centre for Dentistry Amsterdam (ACTA), University of Amsterdam (UvA) and Vrije Universiteit Amsterdam (VU), Amsterdam, Netherlands

The repair of large-volume bone defects (LVBDs) remains a great challenge in the fields of orthopedics and maxillofacial surgery. Most clinically available bone-defect-filling materials lack proper degradability and efficient osteoinductivity. In this study, we synthesized a novel biomimetically-precipitated nanocrystalline calcium phosphate (BpNcCaP) with internally incorporated bone morphogenetic protein-2 (BpNcCaP + BMP-2) with an aim to develop properly degradable and highly osteoinductive granules to repair LVBDs. We first characterized the physicochemical properties of the granules with different incorporation amounts of BMP-2 using scanning electron microscopy, X-ray diffraction, Fourier transform infrared spectroscopy and X-ray photoelectron spectroscopy. We evaluated the cytotoxicity and cytocompatibility of BpNcCaP by assessing the viability and adhesion of MC3T3-E1 pre-osteoblasts using PrestoBlue assay, Rhodamine-Phalloidin and DAPI staining, respectively. We further assessed the *in-vivo* osteoinductive efficacy in a subcutaneous bone induction model in rats. *In-vitro* characterization data showed that the BpNcCaP + BMP-2 granules were comprised of hexagonal hydroxyapatite with an average crystallite size ranging from 19.7 to 25.1 nm and a grain size at 84.13 ± 28.46 nm. The vickers hardness of BpNcCaP was 32.50 ± 3.58 HV 0.025. BpNcCaP showed no obvious cytotoxicity and was favorable for the adhesion of pre-osteoblasts. BMP-2 incorporation rate could be as high as 65.04 ± 6.01%. *In-vivo* histomorphometric analysis showed that the volume of new bone induced by BpNcCaP

OPEN ACCESS

Edited by:
Mohammad Khodaei, Isfahan University of Technology, Iran

Reviewed by:
Arun Prabhu Rameshbabu, Harvard Medical School, United States
Anuj Kumar, Yeungnam University, South Korea

***Correspondence:**
Nawal Alharbi
nalharbi@ksu.edu.sa
Gang Wu
g.wu@acta.nl

†These authors have contributed equally to this work and share first authorship.

Specialty section:
This article was submitted to Biomaterials, a section of the journal Frontiers in Bioengineering and Biotechnology

Received: *14 April 2022*
Accepted: *30 May 2022*
Published: *22 July 2022*

Citation:
Xu G, Shen C, Lin H, Zhou J, Wang T, Wan B, Binshabaib M, Forouzanfar T, Xu G, Alharbi N and Wu G (2022) Development, In-Vitro Characterization and In-Vivo Osteoinductive Efficacy of a Novel Biomimetically-Precipitated Nanocrystalline Calcium Phosphate With Internally-Incorporated Bone Morphogenetic Protein-2. Front. Bioeng. Biotechnol. 10:920696. doi: 10.3389/fbioe.2022.920696

exhibited a BMP-2 amount-dependent increasing manner. The BpNcCaP+50 μg BMP-2 exhibited significantly more degradation and fewer foreign body giant cells in comparison with BpNcCaP. These data suggested a promising application potential of BpNcCaP + BMP-2 in repairing LVBDs.

Keywords: nanocrystalline, hydroxyapatite, bone morphogenetic protein-2, biomimetic, bone regeneration

1 INTRODUCTION

Large-volume bone defects (LVBDs) can be resulted from congenital bone malformations, tumors, inflammation and trauma, severely compromising the aesthetics and functions of patients (Mansour et al., 2020; Migliorini et al., 2021). LVBDs override the self-healing capacity of bone tissue and thus do not heal spontaneously (Ma et al., 2021). Autologous bone grafts are still considered the gold standard to repair LVBDs in clinical practice since they contain osteoconductive scaffolds, osteoinductive growth factors and osteogenic cells (Kowalczewski and Saul, 2018). However, their application is associated with a series of drawbacks, such as limited availability, donor-site pain and morbidity as well as uncontrollable resorption rate (Baldwin et al., 2019). As alternatives, allogeneic and xenogeneic bone grafts are widely adopted as they bear bone-like structures and compositions (de Melo Pereira and Habibovic, 2018). Whereas, these materials are also associated with a series of concerns, such as disease transmission and severe immune reaction (Sohn and Oh, 2019). In this situation, synthetic calcium phosphate (CaP)-based bone grafts, such as tri-calcium phosphate (TCP) and hydroxyapatite (HA) show a promising application potential as they are available in unlimited quantities, free of pyrogens or antigens and also bear bone-like compositions (Piccinini et al., 2013). However, most of these materials do not bear intrinsic osteoinductivity so that they must be mixed with autologous bone grafts to heal LVBDs, in which the drawbacks of autologous bone grafts pursue (Vidal et al., 2020).

One viable method to confer osteoinductivity is to adopt an osteoinductive agent - bone morphogenetic protein-2 (BMP-2), a growth factor from the superfamily of transforming growth factor-β (TGF-β) (Wang et al., 2014). BMP-2 can induce *de novo* bone formation in ectopic sites, which proves its potent osteoinductivity. BMP-2 combined with collagen membrane has been approved for clinical applications to perform spine fusion, open fracture, anterior interbody fusion, and posterolateral lumbar fusion (Lo et al., 2012). Furthermore, BMP-2 may also be applied clinically to functionalize CaP-based bone grafts to promote bone regeneration. However, in order to achieve certain forms and mechanical stiffness, the production of most synthetic CaP bone grafts needs to be sintered at unphysiologically high temperatures (900–1,300°C) (de Groot, 1984; Layrolle and Daculsi, 2009; Diez-Escudero et al., 2020). Therefore, BMP-2 can only be absorbed superficially onto these bone grafts, for which BMP-2 will be burst released right after *in-vivo* implantation (Liu et al., 2018). The thereby-generated high concentration of BMP-2 may cause a series of side effects, such as osteolysis due to over-stimulated osteoclastic activity and bone formation in unintended sites (James et al., 2016).

One promising method to establish a CaP-based slow delivery system is biomimetic coating procedure, which is prepared in a physiological-like condition, such as 37°C and simulated body fluid (SBF) (Liu and Hunziker, 2009). BMP-2 may be co-precipitated into a thin layer of latticework of crystalline CaP on various substrates (Liu et al., 2010). In our previous study, we have shown that BMP-2-incorporated biomimetic CaP coating bore significantly higher osteoinductivity than the superficially adsorbed BMP-2 on various biomedical materials (Liu et al., 2006; Liu et al., 2007; Liu and Hunziker, 2009), such as titanium (Liu et al., 2007), polymers (Wu et al., 2010b) and deproteinized bovine bone (DBB) (Wu et al., 2011; Liu et al., 2013). Thereafter, we modified this protocol and realized a transition from a 2D coating to 3D granules. In our previous study, we have prepared a layer-by-layer (alternate amorphous CaP and crystalline CaP with about 3 cycles) assembled BioCaP-BMP-2 granules, which provides a slow-release carrier for BMP-2 (Zheng et al., 2014). In a recent study with a periodontitis model in beagle dogs, the co-administration of these granules with DBB was associated with significantly more connective tissue height, new cementum height, new bone height and area, as well as less down-growth of junctional epithelium than DBB alone (Wei et al., 2019). However, this type of granules bore insufficient mechanical strength and thus cannot be used alone as bone-defect-filling materials but only as an osteopromoter to enhance bone regeneration surrounding other bone-defect-filling materials, such as DBB.

To provide a viable option, in our previous studies, we have already presented a new type of CaP granules (Liu et al., 2017) that are fabricated using a modified protocol from our well-establish biomimetic coating technique (Liu et al., 2003; Liu et al., 2004; Wu et al., 2010a; Liu et al., 2018). CaP precipitates are achieved at 37°C in a Tris-HCL buffered five-fold supersaturated calcium phosphate solution and then subjected to overnight drying at room temperature. Such a fabrication in physiological temperature allows a co-precipitation of BMP-2 with CaP and a characteristic internal incorporation pattern of BMP-2 within the CaP granules, which enables a slow release of BMP-2 (Liu et al., 2005; Wu et al., 2010a; Liu et al., 2014; Liu et al., 2018). However, the thereby produced CaP granules are still suboptimal due to the simultaneous incorporation of chemicals, such as Tris base and sodium chloride, which may compromise the biocompatibility of the granules and the osteoinductive efficacy of BMP-2.

In this study, we further developed the protocol and fabricated a novel type of biomimetically-precipitated nanocrystalline calcium phosphate (BpNcCaP) granules with a minimized content of the unintended chemicals. We first characterized the physicochemical properties using scanning electron

TABLE 1 | The group set-up with the target dosage, actual dosage and corresponding loading efficiency of BMP-2 in the BpNcCaPs.

Groups (0.08 g/Sample)	Target Dosage of BMP-2/Sample (μg)	Actual Dosage of BMP-2/Sample (μg)	Loading Efficiency (%)
BpNcCaP	0	0	0
BpNcCaP+5 μg BMP-2	5	4.31 ± 0.17	43.08 ± 1.67
BpNcCaP+10 μg BMP-2	10	9.39 ± 0.14	46.97 ± 0.68
BpNcCaP+25 μg BMP-2	25	23.06 ± 2.19	57.65 ± 5.47
BpNcCaP+50 μg BMP-2	50	52.03 ± 4.81	65.04 ± 6.01

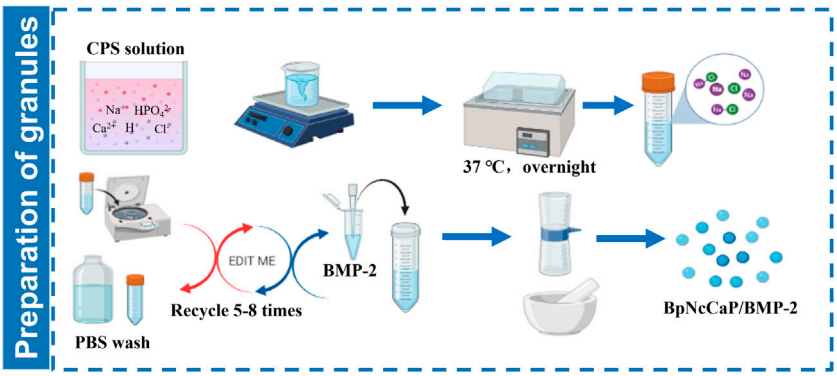

FIGURE 1 | Schematic illustration of preparation of BpNcCaP granules with internally incorporated BMP-2.

microscopy (SEM), X-ray diffraction (XRD), Fourier transform infrared spectroscopy (FTIR), X-ray photoelectron spectroscopy (XPS), and Vickers hardness (HV). We evaluated the cytotoxicity and cytocompatibility of BpNcCaP by assessing the viability and adhesion of MC3T3-E1 pre-osteoblasts using PrestoBlue assay, Rhodamine-Phalloidin and DAPI staining, respectively. We further assessed the *in-vivo* osteoinductive efficacy of the granules with different incorporation amounts of BMP-2 using micro-computed tomography (Micro-CT) and histomorphometric analysis.

2 MATERIALS AND METHODS

2.1 Preparation of Granules

Five-fold supersaturated CaP solution (200 mM HCl, 20 mM $CaCl_2{\cdot}2H_2O$, 680 mM NaCl, 10 mM Na_2HPO_4, and 250 mM Tris [PH 7.4]) was incubated in a shaking water bath (50 agitations/min) at 37°C. After 24 h of incubation, the precipitation was retrieved by maximally removing the supernatant. Then the precipitates were subjected to centrifugation at a speed of 10,000 rpm/min for 10 min. The highly condensed precipitates were thoroughly washed by phosphate buffer saline (PBS) with an 8-fold volume of precipitates. Then the centrifugation/washing cycle was repeated so as to minimize the content of unintended chemicals. After the last centrifugation, BMP-2 solution (1.5 mg/ml, INFUSE® Bone Graft, Medtronic, Minneapolis, MN, United States) at certain volumes was added to the precipitates to facilitate the incorporation of the target amount of BMP-2 as shown in **Table 1**. Then the BMP-2-containing precipitates were filtered using a top filter (0.22-μm pore, Corning, NY, United States) using a vacuum pump (−700 kPa) for 20 min to maximally remove the water content from the precipitates. Thereafter, the precipitates were dried overnight at room temperature in a safety cabinet until they were totally dry and hardened. Thereby achieved CaP blocks were carefully ground into small granules. Two sieves with pore diameters of 0.25 and 1 mm were used to retrieve the granules, whose sizes were ranging from 0.25 to 1 mm. All these fabrication procedures were performed in sterile conditions. The schematic illustration of preparation of BpNcCaP granules with internally incorporated BMP-2 was shown in **Figure 1**.

2.2 Determination of the Amount of the Incorporated BMP-2

The amount of incorporated BMP-2 was determined using an enzyme-linked immunosorbent assay (ELISA) kit (PeproTech, London, United Kingdom) as previously described (Zheng et al., 2014). 0.05 g of BpNcCaPs were dissolved in 1 ml 0.5 M Ethylenediaminetetraacetic acid (EDTA) (pH 8.0). The ELISA was performed according to the manufacturer's instructions. Six samples were used for this purpose.

2.3 *In-vitro* Characterization

2.3.1 Physical and Chemical Properties of BpNcCaP and BpNcCaP/BMP-2

The morphology of BpNcCaP without and with BMP-2 incorporations was examined by scanning electron microscopy

(SEM) (Zeiss Sigma 300), the accelerating voltage was 3 kV, and the magnifications were ×5,000 and 50,000×. The grain size distributions of BpNcCaP and BpNcCaP+50 μg BMP-2 were analyzed using a software of Image-pro plus 6.0. The crystal structure of the synthesized BpNcCaPs was analyzed using X-ray diffraction (XRD) with a Siemens D5000 X-ray diffractometer (CuKα radiation, 40 kV and 30 mA). The XRD patterns were collected in the range of $2\theta = 10–80^{\circ}$ using 0.05° step and 2 s/step scan speed. The achieved experimental patterns were analyzed using Inorganic Crystal Structure Database (ICSD). Rietveld refinement was adopted to analyze the approximation of the XRD patterns of BpNcCaPs to the structural model of the Crystallographic Information File (CIF) available in crystallographic databases. VESTA (Visualization for Electronic and Structural Analysis) program was also used to simulate the unit cell structure of BpNcCaPs. The vibrational molecular spectra of BpNcCaPs were obtained from a Fourier transformed infrared (FTIR) spectrometer (Nicolet iS20, Thermo Scientific, United States) with a Diamond ATR accessory (Termo Scientific Instruments) in the spectral range from 4000 to 400 cm^{-1} wavenumbers. The elemental composition and chemical bonding of BpNcCaPs were obtained by X-ray photoelectron spectroscopy (XPS) using a spectrometer (K-alpha, Thermo Scientific, United States), a monochromatic Al Kα source was used as an X-ray source (hv = 1,486.6 eV), and high-resolution [O1s], [Ca2p] and [P2p] spectra were collected. The hardness was measured by a Vickers hardness tester (Falcon 507, Innovatest, Netherlands). During Vickers indentation, the load applied and holding time on the polished surface of BpNcCaP were 25 g and 10 s, respectively.

2.3.2 Cytocompatibility of BpNcCaP

MC3T3-E1 pre-osteoblasts were obtained from the American Type Culture Collection (ATCC, Manassas, VA, United States) and cultured in alpha-modified Eagle's medium (α-MEM; Welgene, Deagu, Korea) supplemented with 10% fetal bovine serum (FBS; Gibco, Carlsbad, United States), 100 U/mL penicillin, and 100 μg/ml streptomycin (GibcoTM, Thermo Fisher Scientific, United States), at 37°C in a 5% CO_2 atmosphere. The medium was changed every 2 days.

Preparation of extracts of BpNcCaP and cell viability assay: Liquid extraction method has been recommended as a standard procedure to test cytotoxicity of biomedical materials in the ISO 10993. We mixed 250 mg of BpNcCaP with 5 ml of medium and incubated the suspensions at 37°C for 72 h. Control medium was prepared in the same manner without BpNcCaP. Suspensions were centrifuged at 1,500 rpm for 5 min and filtered through 0.22 μm membranes. Thereafter, the experimental concentrations (5, 10, 15, and 20 mg/ml) of BpNcCaP extracts were prepared with the medium using 50 mg/ml of the BpNcCaP extracts. MC3T3-E1 cells were seeded into 48-well plates at a density of 10^4 cells/well in 5, 10, 15, and 20 mg/ml of BpNcCaP extracts and cultured for 0, 3, and 5 days 200 μl cell culture medium containing 10% PrestoBlue (Thermo Fisher Scientific, United States) solution was added to each well and the plates were incubated at 37°C for 1 h according to the manufacturer's instruction. After incubation, 100 μl of PrestoBlue solution from each well of the assay plates (48-well plates) was transferred to a new well in 96-well plates and measured using a SpectraMax fluorescence multi-well plate reader with the excitation/emission wavelengths set at 560/590 nm.

Preparation of BpNcCaP discs and cell adhesion assay: We made the BpNcCaP round discs (diameter: 4 mm; height: 2 mm) using the same way as we made BpNcCaP granules in **Section 2.1**. BpNcCaP discs were put into 48-well plates (1 disc/well), then MC3T3-E1 cells were seeded on the discs at a density of 3×10^4 cells/disc and cultured for 3 days. Cell/BpNcCaP samples were rinsed twice with PBS and fixed with PBS-buffered 4% paraformaldehyde for 30 min at room temperature. After washing three times with PBS, cell/BpNcCaP were incubated with 0.3% Triton-X 100 in PBS for 5 min. Then, actin filaments were stained by rhodamine-phalloidin (Actin-Tracker Red-555, Beyotime, China) and the cell nucleus was stained using DAPI (Beyotime, China). The cell/BpNcCaP samples were observed under a confocal laser scanning microscope (FV3000, Olympus, Japan).

2.4 *In vivo* Experiments

2.4.1 Experimental Groups

In order to screen the optimal dosage of BMP-2, we set up BMP-2 at 5 μg, 10 μg, 25 μg and 50 μg per sample (0.08 g) of BpNcCaP granules as the target dosage. This dosage range of BMP-2 was set up according to our previous studies, in which tens micrograms of BMP-2 per sample is already sufficient to induce new bone formation (Hunziker et al., 2016; Wei et al., 2020). The experimental groups according to the target dosage of BMP-2 were defined as shown in **Table 1**. Five groups ($n = 6$ per group) were established: G1: BpNcCaP; G2: BpNcCaP+5 μg BMP-2; G3: BpNcCaP+10 μg BMP-2; G4: BpNcCaP+25 μg BMP-2; G5: BpNcCaP+50 μg BMP-2.

2.4.2 Animal Surgery for Ectopic Subcutaneous Bone Formation

The animal experiment was approved by the Ethical Committee of Zhejiang Chinese Medical University (No. IACUC-20210104-02). Throughout the study, the SD rats were treated following the guidelines of animal care established by Zhejiang Chinese Medical University. Fifteen eight-week-old male SD rats were used as an animal model for ectopic subcutaneous bone formation (Wu et al., 2010b). For induction of a general anesthesia, 1% pentobarbital was intraperitoneally injected. The iliac crest was used as the landmark for determining the location of the skin incision, and a 25 mm posterior longitudinal incision was made bilaterally, 5–10 mm laterally from the midline. BpNcCaP groups were implanted into the subcutaneous space of the lumbar back according to a randomization protocol as used in our previous study (Wu et al., 2011). Right after implantation, the soft tissues were repositioned, and the wound was closed using standard non-resorbable suture materials. The wound was then disinfected with 10% povidone-iodine. Rats were kept at ambient temperature conditions until awakened.

2.5 Micro-Computed Tomography

All rats were sacrificed 5 weeks after surgery by intramuscular injection of excessive Sumianxin II. The implanted samples and surrounding tissues were harvested and immediately fixed in 10%

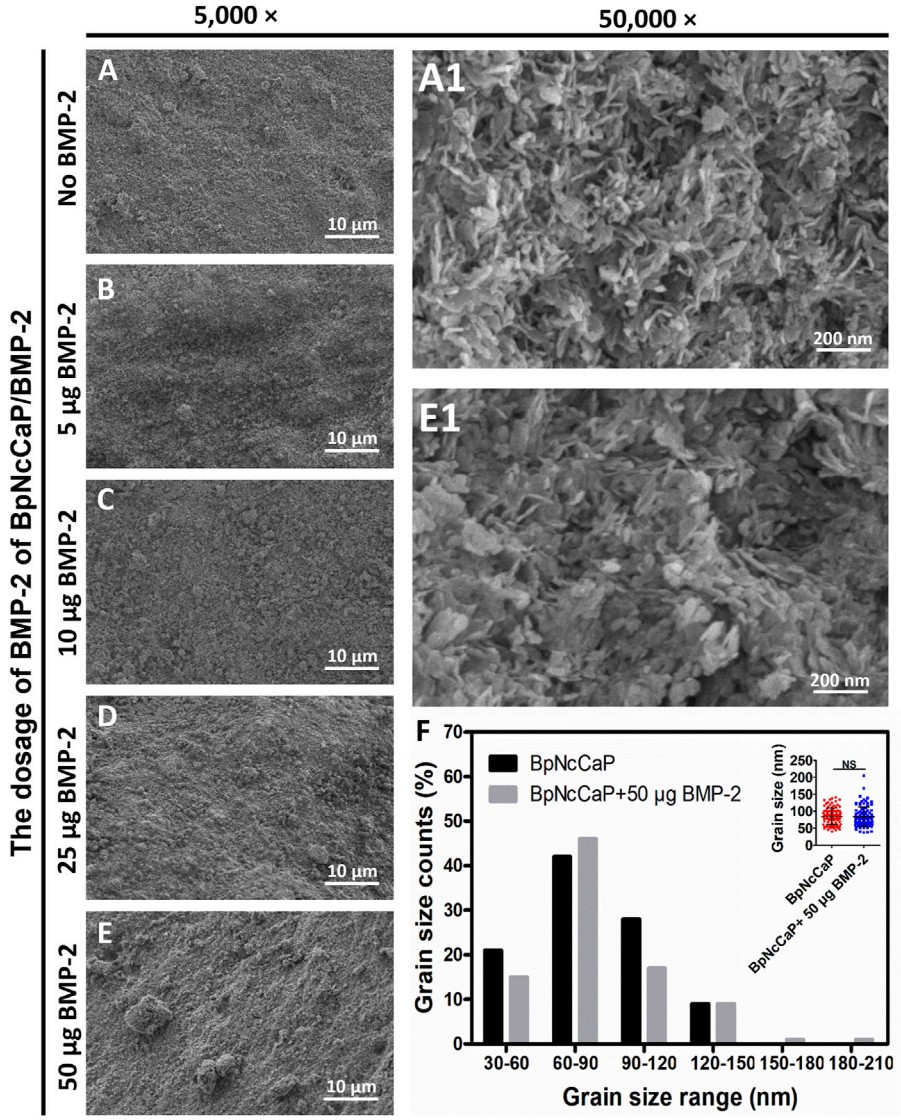

FIGURE 2 | Scanning electron microscopy (SEM) observations of surface characteristic and morphology of BpNcCaP without or with different amounts (5/10/25/50 μg) of BMP-2. Representative SEM images of BpNcCaP without **(A)** or with different amounts (5/10/25/50 μg) of BMP-2 **(B–E)** in a lower magnification (×5,000). Bar = 10 μm. Higher-magnification (50,000×) SEM images of BpNcCaP **(A1)** and BpNcCaP+50 μg BMP-2 **(E1)**. Bar = 200 nm. **(F)** Graph depicting the grain size distribution of BpNcCaP and BpNcCaP+50 μg BMP-2.

neutral-buffered formalin for 2 days. The samples were then scanned using Micro-CT (μCT 100, Scanco Medical AG, Switzerland) at a resolution of 10 μm (80 kV, 100 μA) and then subjected to offline reconstruction. We evaluated the micro-architectures of bone using the following parameters: 1) Bone volume (BV, mm^3); 2) Bone Mineral Density (BMD; mg HA/ccm); 3) Bone surface (BS, mm^2) and 4) Structure model index (SMI).

2.6 Histology Procedures

After micro-CT analysis, the samples were rinsed in tap water, dehydrated in ethanol and embedded in methylmethacrylate as reported previously (Wu et al., 2010b; Wu et al., 2011). Samples were cut using a Leica diamond saw fitted in a Leica SP1600 slicing machine (Leica Microsystems, Wetzlar, Germany), the tissue blocks were cut into 5-7 slices, 300-μm-thick and 500 μm apart, according to a systematic random sampling protocol. All slices were glued to plastic specimen holders and ground down to a final thickness of 80–100 μm. They were surface-polished and surface-stained with McNeal's Tetrachrome, basic Fuchsine and Toluidine blue as previously described (Wu et al., 2010b; Wu et al., 2011). The volume of the newly formed bone, blood vessels, undegraded particles and foreign body giant cells (FBGCs) were measured using the point-counting technique according to our previous publications (Liu et al., 2017; Teng et al., 2020).

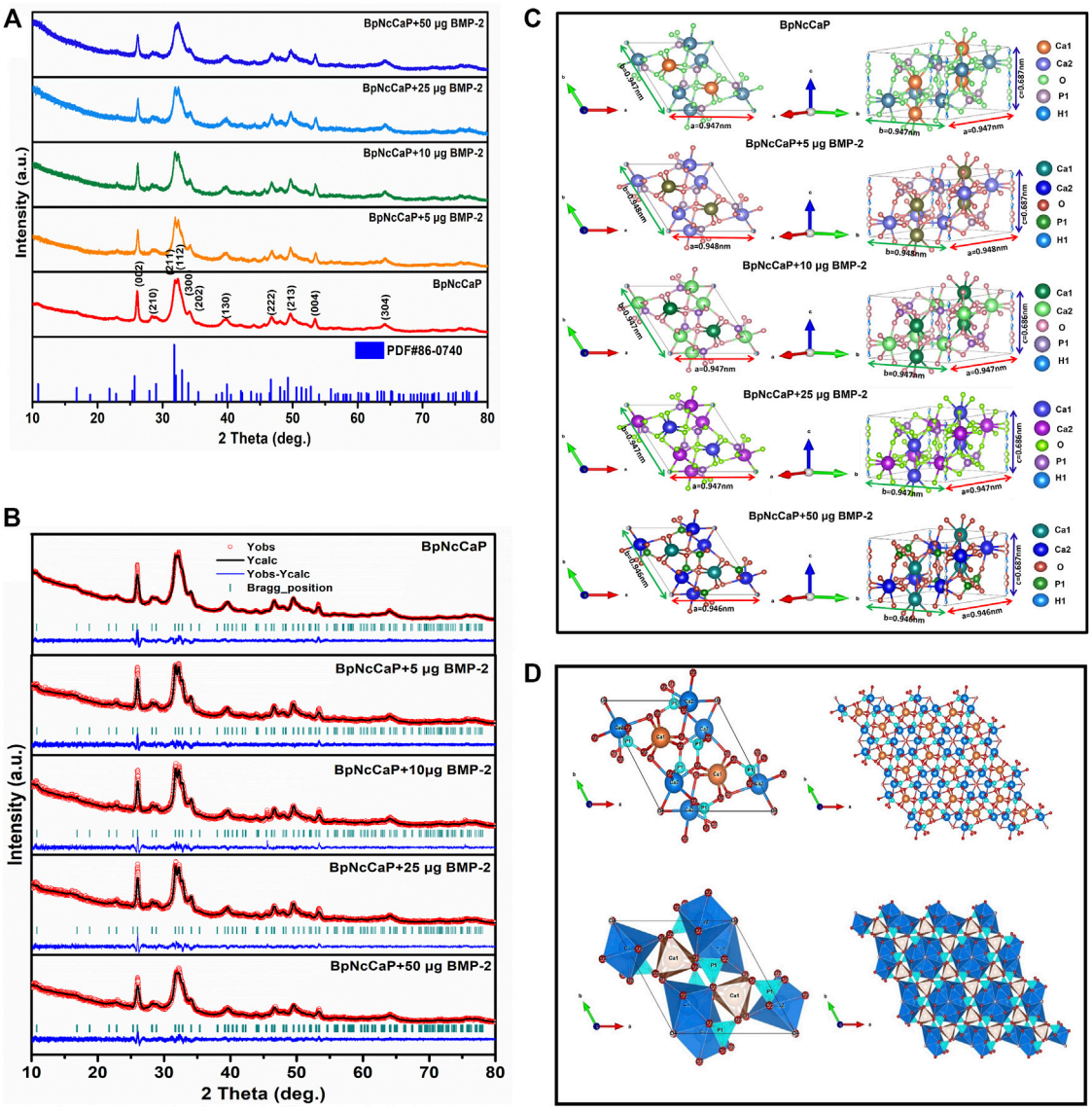

FIGURE 3 | (A) XRD patterns of BpNcCaPs without or with 5/10/25/50 μg BMP-2 as well as the standard ICSD no. 86-0740. **(B)** Rietveld refinement of XRD patterns for BpNcCaP without or with different amounts (5/10/25/50 μg) of BMP-2. Black lines: XRD patterns; Red circles: Rietveld refined results; Blue curves: The differences between the XRD patterns and Rietveld refinement results; Green bars: The calculated Bragg peak positions. **(C)** Representation of the unit cells of BpNcCaPs without or with different amounts (5/10/25/50 μg) of BMP-2. **(D)** Visualization of structures of ball-and-stick and polyhedral models along with the c-axis for BpNcCaP.

2.7 Statistical Analysis

All data are presented as mean ± standard deviation (SD). Data were compared using one-way analysis of variance (ANOVA), and Bonferroni's correction was used for post-hoc comparison. The significance level was set at $p < 0.05$.

3 RESULTS

3.1 Characterizations of BpNcCaPs

3.1.1 Surface Morphology of BpNcCaPs

Low-magnification SEM images showed that BpNcCaP bore a slightly rough and uneven morphology (**Figure 2**). This morphology was not changed by the presence of various amounts of BMP-2. High-magnification SEM images showed that BpNcCaP (**Figure 2A1**) and BpNcCaP+50 μg BMP-2 (**Figure 2E1**) were mainly comprised of needle-like crystals. The grain length distribution was shown in **Figure 2F**. The grain lengths of the crystals for BpNcCaP and BpNcCaP+50 μg BMP-2 were about 85.14 ± 24.48 nm and 84.13 ± 28.46 nm, respectively. The incorporation of 50 μg BMP-2 did not significantly change the morphology and the grain size.

3.1.2 Crystallinity and Phase Composition of BpNcCaPs

We performed XRD analysis to identify the phases and crystallinities of the BpNcCaP without or with various

TABLE 2 | Unit cell parameters, crystallite sizes and crystallinities of BpNcCaPs without or with different amounts (5/10/25/50 μg) of BMP-2.

Groups	Unit Cell Parameters				Crystallite Size	Crystallinity
	a(Å)	b(Å)	c(Å)	V(Å^3)	Å	(%)
BpNcCaP	9.4643(4)	9.4643(4)	6.8666(3)	532.66(4)	246	92.27
BpNcCaP+5 μg BMP-2	9.4753(4)	9.4753(4)	6.8653(3)	533.79(4)	206	92.05
BpNcCaP+10 μg BMP-2	9.4683(5)	9.4683(5)	6.8609(4)	532.67(5)	251	94.07
BpNcCaP+25 μg BMP-2	9.4711(4)	9.4711(4)	6.8640(3)	533.22(4)	199	91.12
BpNcCaP+50 μg BMP-2	9.4590(6)	9.4590(6)	6.8655(4)	531.98(5)	197	92.12

amounts of incorporated BMP-2. The peaks were observed at around 2θ = 25.87°, 29.15°, 31.97°, 32.27°, 33.16°, 34.17°, 40.11°, 46.95°, 49.62° and 53.19°(**Figure 3A**), which, according to the ICSD-PDF card 86-0740, were the typical reflections of the respective crystalline planes (002), (210), (211), (112), (300), (202), (130), (222), 213) and (004) of hexagonal hydroxyapatite (HA). These characteristic peaks were not significantly influenced by the incorporation of BMP-2. The crystallite sizes were calculated as 24.6, 20.6, 25.1, 19.9, and 19.7 nm for BpNcCaP, BpNcCaP+5 μg BMP-2, BpNcCaP+10 μg BMP-2, BpNcCaP+25 μg BMP-2 and BpNcCaP+50 μg BMP-2, respectively (**Table 2**).

Thereafter, we adopted the Rietveld refinement to analyze the approximation of the XDR patterns of BpNcCaPs to the structural model of the Crystallographic Information File (CIF) available in crystallographic databases for HA. Furthermore, we also used this analysis to investigate the crystalline phase fractions of BpNcCaP without or with BMP-2 incorporation. The calculated patterns (red line in **Figure 3B**) were adjusted to the observed experimental pattern (black line in **Figure 3B**). The observed and calculated XRD profiles of BpNcCaP without or with incorporated BMP-2 as well as the difference between both profiles (YObs-YCal) were shown in **Figure 3B**. All the diffraction peaks were perfectly indexed to the ICSD card 86-0740 (hexagonal lattice system and space group P63/m). The refined lattice parameters of BpNcCaP unit cell were a = b = 0.946 nm and c = 0.687 nm. Regardless of the incorporation amount, the presence of BMP-2 did not significantly change the lattice parameters (**Table 2**). With the network parameters (a, b, c, α, β, and γ) and atomic positions (x, y and z) obtained after Rietveld refinement, we further adopted the VESTA (Visualization for Electronic and Structural Analysis) program (Momma and Izumi, 2011) to simulate the unit cell structure of BpNcCaPs (**Figures 3C,D**). All these data indicated that BpNcCaP bore a hexagonal-type HA structure.

3.1.3 Surface Spectra of BpNcCaPs

The FTIR spectra of BpNcCaP without or with the incorporation of BMP-2 were presented in **Figure 4**. The most prominent peak for BpNcCaP was the ν3 asymmetric stretching mode of the PO_4^{3-} group with maxima at 1,029 cm^{-1}. This peak shifted gradually to 1,031 cm^{-1} with the increase of BMP-2 amount. Another characteristic peak was the ν4 bending mode of PO_4^{3-} with doublets at 564–566 cm^{-1} and 604–605 cm^{-1} for all BpNcCaP with different amounts of BMP-2. The full widths at half-maxima (FWHM) of the major ν3 band gradually decreased from 222.5 cm^{-1} in BpNcCaP to 192.3 cm^{-1} in BpNcCaP+5 μg BMP-2, 193.5 cm^{-1} in BpNcCaP+10 μg BMP-2, 177.2 cm^{-1} in BpNcCaP+25 μg BMP-2 (**Figure 4B**). In contrast, in BpNcCaP+50 μg BMP-2, the FWHM increased to 248.7 cm^{-1}. A similar pattern was also found for the ν4 bending mode of PO_4^{3-} (**Figure 4C**).

The weak bands of BpNcCaPs at 1,415–1,419 cm^{-1} and 866–872 cm^{-1} might be assigned to carbonate. Carbonates are constituents of bone structures, whose presence may improve the bioactivity of HA (Vallet-Regi and González-Calbet, 2004; Hoang et al., 2020). According to the literature (Fahami et al., 2012; Ignjatović et al., 2019; Edén, 2021), the functional groups generally observed in the FTIR spectra of CaP-based materials are PO_4^{3-}, OH^- and CO_3^{2-} groups in the range 4000–300 cm^{-1}. The phosphate group (PO_4^{3-}) appeared at around 1,100–1,019 cm^{-1} for the ν3 mode, 958 cm^{-1} for the ν1 mode, 605–530 cm^{-1} for the ν4 mode, and 500–400 cm^{-1} for the ν2 mode. Furthermore, three modes of OH^- ions, i.e., stretching, vibrational, and translational modes were at 3700-2500, 630, and 390 cm^{-1}, respectively (Markovic et al., 2004; Alqap and Sopyan, 2009). The FTIR spectra of PO_4^{3-}, OH^- and CO_3^{2-} groups of BpNcCaPs were identical to those of HA (Rodríguez-Lugo et al., 2018; Senthilkumar et al., 2021).

3.1.4 Surface Composition of BpNcCaPs

Figure 5A showed the XPS survey spectra of BpNcCaP without and with BMP-2 incorporation, consisting of the photoelectron peaks corresponding to oxygen (O), calcium (Ca) and phosphorus (P). These peaks corresponded to the HA (Rojas-Mayorga et al., 2016; Gomes et al., 2017). A detailed analysis of these XPS results was performed. The Ca 2p peak for BpNcCaP had been deconvoluted into two peaks: Ca 2p3/2 peak at 347.04 eV and Ca 2p1/2 peak at 350.57 eV (**Figure 5B**). These signals indicated the interaction Ca-POx. The P 2p spectrum had been deconvoluted into two peaks P 2p3/2 at 132.86 eV and P 2p1/2 at 133.73 eV (**Figure 5C**). These energies could be associated with P-O bonds from the phosphate group. The oxygen spectra (O 1 s) for BpNcCaP showed two peaks at 530.86 and 532.61 eV (**Figure 5D**). The O 1 s signal at 530.86 eV corresponded to O-C or P-O bonds, while the peak at 532.61 eV could be attributed to C-O groups. These findings were consistent with XPS results reported for Ca 2p, P 2p, and O 1 s in HA (Rojas-Mayorga et al., 2016; Gomes et al., 2017).

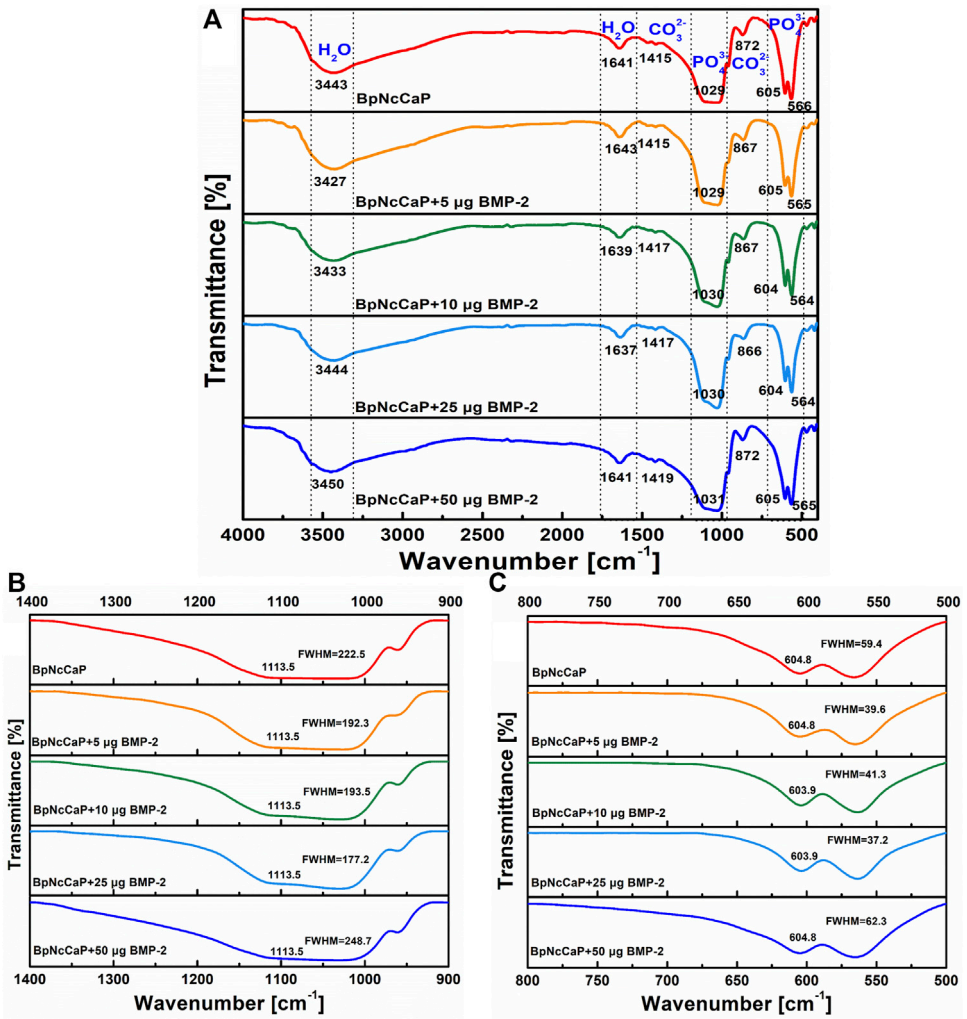

FIGURE 4 | Total FTIR spectra **(A)**, FTIR spectra focusing on ν3 phosphate stretch in the 900–1,400 cm^{-1} wavenumber range **(B)**, and FTIR spectra focusing on ν4 bend in the 500–800 cm^{-1} wavenumber range **(C)** for BpNcCaPs without or with different amounts (5/10/25/50 μg) of BMP-2.

After BMP-2 incorporation, Ca 2p peaks at 347.30–347.97 eV, P 2p peaks at 133.37–133.97 eV, O 1s peaks at 531.33–531.88 eV for BpNcCaP + BMP-2 groups. The Ca 2p, P 2p, O 1s energy levels of BpNcCaP at 347.95, 133.96 and 531.88 eV shifted to lower energy values of 347.30, 133.37 and 531.33 eV of BpNcCaP+50 μg BMP-2, respectively (**Figure 5A**). And other binding energy changes in XPS spectra of BpNcCaPs were identified in the region of Ca 2p, P 2p, and O 1 s (**Figures 5B–D**), which suggested an interaction between BMP-2 with BpNcCaP. Regardless of the incorporation amount, the presence of BMP-2 did not significantly change the composition of BpNcCaP.

3.1.5 Hardness of BpNcCaP

We adopted Vickers hardness test method to detect the hardness of BpNcCaP granules and added the data in **Supplementary Figure S1**. The vickers hardness of BpNcCaP was 32.50 ± 3.58 HV 0.025.

3.2 Cytotoxicity and Cytocompatibility of BpNcCaP

PrestoBlue assay was adopted to assess the cytotoxicity of BpNcCaP. As shown in **Figure 6A**, the metabolic viability (fluorescence units) of the MC3T3-E1 cells of three groups (5, 10, 15 mg/ml of BpNcCaP extracts) increased gradually with the culture time. The cell viability was also the highest in the group of 10 mg/ml of BpNcCaP extracts, while although no significant difference was found among all the groups at each culture time point. This result indicated that the BpNcCaP has no obvious cytotoxicity. We further adopted Rhodamine-Phalloidin and DAPI to stain the actin and nuclei of attached cells as an indicator for the cytocompatibility of BpNcCaP. As shown in **Figure 6B**, after 3 days post-seeding, MC3T3-E1 pre-osteoblasts spread on the BpNcCaP discs with a high density. This result indicated that the BpNcCaP was favorable for the adhesion, spreading and proliferation of osteogenic cells.

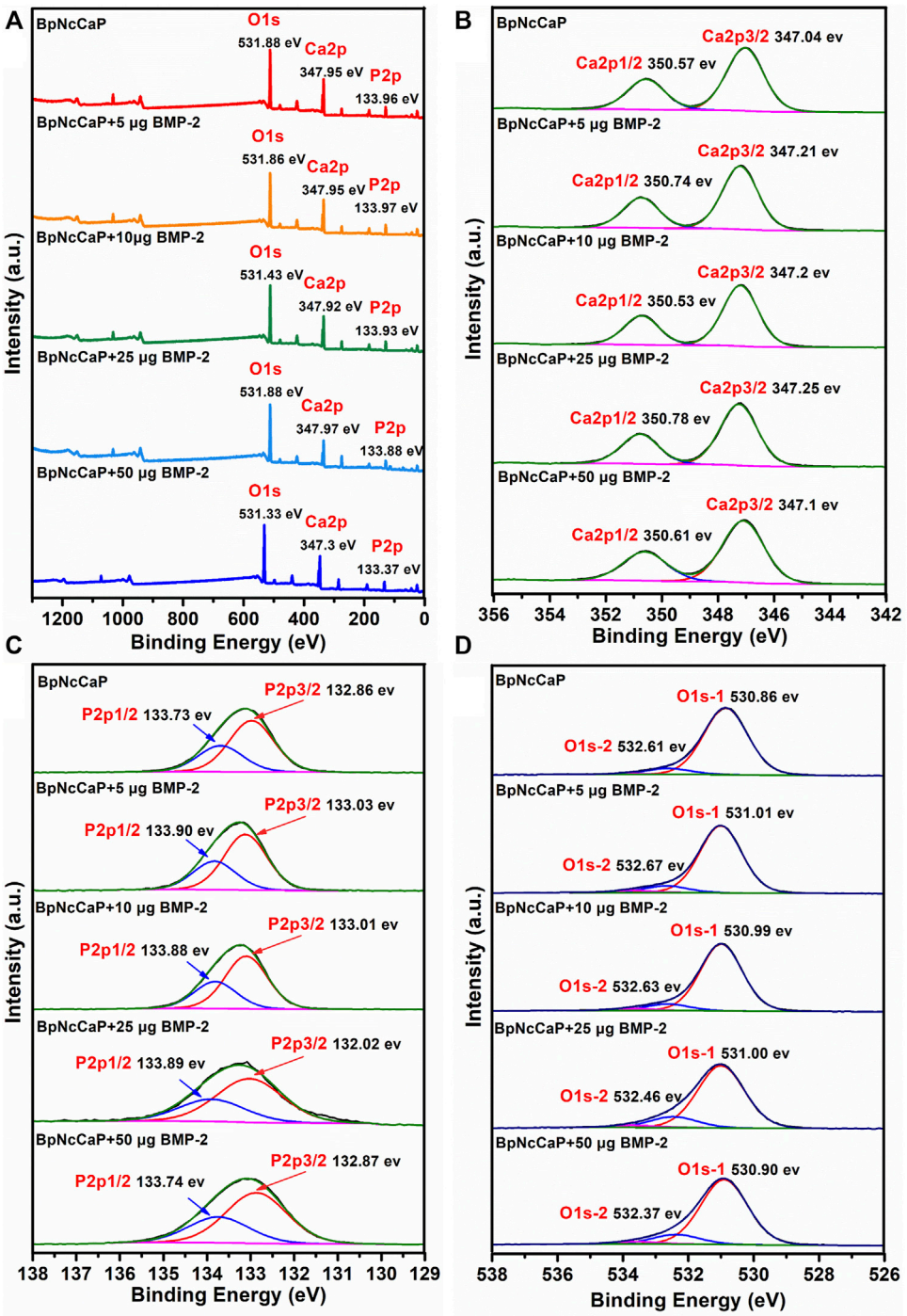

FIGURE 5 | Total XPS survey spectra **(A)**, XPS spectra of Ca 2p **(B)**, XPS spectra of P 2p **(C)** and XPS spectra of O 1s **(D)** for BpNcCaPs without or with different amounts (5/10/25/50 μg) of BMP-2.

3.3 BMP-2 Dosage in BpNcCaP

Using the ELISA kit, the internally-incorporated BMP-2 dosage in BpNcCaP was determined and shown in **Table 1**. The amounts of BMP-2 in the groups of BpNcCaP+5 μg BMP-2, BpNcCaP+10 μg BMP-2, BpNcCaP+25 μg BMP-2 and BpNcCaP+50 μg BMP-2 were 4.31 ± 0.17 μg, 9.39 ± 0.14 μg, 23.06 ± 2.19 μg and 52.03 ± 4.81 μg, respectively. The corresponding loading efficiencies were 43.08 ± 1.67%, 46.97 ± 0.68%, 57.65 ± 5.47% and 65.04 ± 6.01%, respectively.

3.4 Micro-CT Analysis

We adopted micro-CT analysis to qualitatively and quantitively evaluate the new bone formation surrounding BpNcCaP without

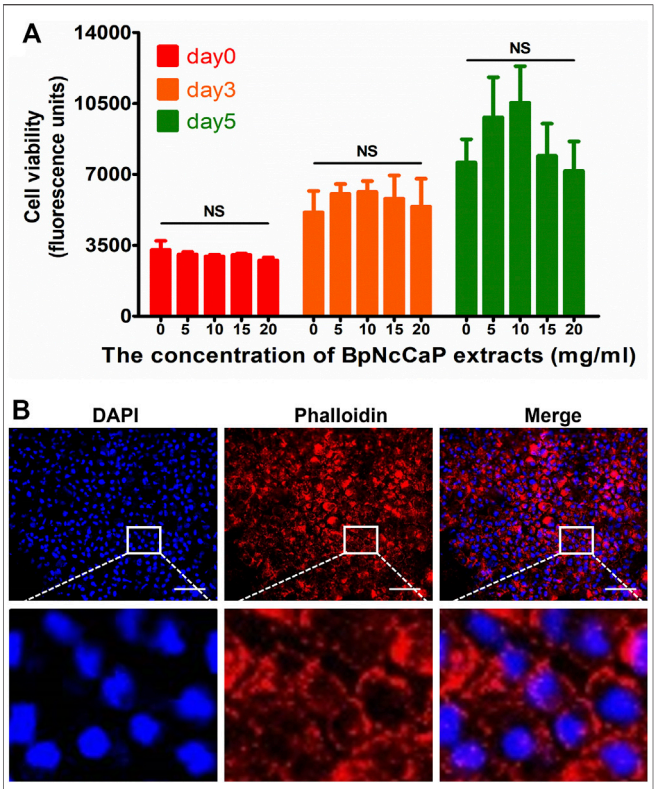

FIGURE 6 | Graph depicting the metabolic activity of MC3T3-E1 exposed to the different concentrations of BpNcCaP extracts using a PrestoBlue assay **(A)**. Fluorescent micrographs showing the nuclei (blue) and actin filaments (red) of MC3T3-E1 pre-osteoblasts cultured on BpNcCaP discs **(B)**. The cells were cultured for 3 days and then fixed and stained with rhodamine-phalloidin and DAPI. Bar = 100 μm.

and with BMP-2 incorporation (**Figure 7**). Micro-CT images (**Figure 7A**) showed that newly formed bone (red arrows) occurred on BpNcCaP granules or in the intra-granular space. More newly formed bone was detected with the increase of BMP-2 incorporation amount. No new bone was found in the group of BpNcCaP without BMP-2. The total bone volume (BV) (**Figure 7B1**) in the group of BpNcCaP+50 μg BMP-2 was significantly higher than those of the other BMP-2 containing groups. The same pattern was also found for BS (**Figure 7B2**). The SMI (**Figure 7B4**) in the group of BpNcCaP+50 μg BMP-2 was significantly lower than those of the other BMP-2-containing groups. No significant difference was found in BMD (**Figure 7B3**) among the BMP-2-containing groups.

3.5 Histological and Histomorphometric Analysis

Five weeks after the subcutaneous implantation, no new bone formation was detected in the group of BpNcCaP without BMP-2 incorporation (**Figures 8A1**, **9A**). Instead, a large amount of foreign body giant cells (FBGCs) (**Figure 9A**) were found along the surfaces of BpNcCaP. In the group of BpNcCaP+5 μg BMP-2 (**Figure 8A2**), only very little bone occurred and distributed sporadically in the intra-granular space. In the group of BpNcCaP+10 μg BMP-2 (**Figure 8A3**), many bone tissues aligned along the surfaces of BpNcCaP granules and extended to the adjacent BpNcCaP granules, which formed an integrated network. In the groups of BpNcCaP+25 μg BMP-2 (**Figures 8A4**, 50 μg BMP-2 (**Figures 8**, **9B–D**), many bone marrow-like tissues (BMLT) occurred in the intra-granular space with newly formed bone tissue as borders. Newly formed osteoid tissues with purple color were more frequently found aligned on mineralized bone tissue. On the osteoid tissue, there was a layer of uniformly aligned osteoblasts with cuboid or cube-like morphology. Less FBGCs were detected with the increase of BMP-2 incorporation amount. Quantitative analysis (**Figure 8B**) showed an increasing trend of volume density of newly formed bone (**Figure 8B1**) with the increase of incorporated BMP-2 amount. The volume density of newly formed bone in the group of BpNcCaP+50 μg BMP-2 was significantly higher than those in the groups of BpNcCaP+5 μg BMP-2 and BpNcCaP+10 μg BMP-2. The volume density of blood vessels (**Figure 8B2**) was also the highest in the group of BpNcCaP+50 μg BMP-2 although no significant difference was found among all the groups. In comparison with BpNcCaP without BMP-2, the volume densities of BpNcCaP material (**Figure 8B3**) in the groups of BpNcCaP+25 μg BMP-2 and BpNcCaP+50 μg BMP-2 were significantly decreased. The volume density of FGBCs (**Figure 8B4**) showed a decreasing trend with the increase of BMP-2 incorporation amount with the lowest value detected in the group of BpNcCaP+50 μg BMP-2.

4 DISCUSSION

Most of the clinically available bone-defect-filling materials lack proper degradability and efficient osteoinductivity (Bhat et al., 2021). In this study, through greatly improving our previous biomimetic precipitation protocol, we synthesized novel BpNcCaP granules with internally incorporated BMP-2. *In-vitro* characterization data showed that the BpNcCaP + BMP-2 granules were comprised of hexagonal HA with an average crystallite size ranging from 19.7 to 25.1 nm, a crystallinity ranging from 91.12 to 94.07% and a grain size at 84.13 ± 28.46 nm. The vickers hardness of BpNcCaP was 32.50 ± 3.58 HV 0.025. BMP-2 incorporation rate could even reach 65.04 ± 6.01%. BpNcCaP showed no obvious cytotoxicity and was favorable for the adhesion of pre-osteoblasts. *In-vivo* histomorphometric analysis showed that the total volume of new bone induced by BpNcCaP exhibited a BMP-2 amount-dependent increasing manner. The BpNcCaP+50 μg BMP-2 exhibited significant degradation and less FBGCs reaction in comparison with BpNcCaP. These data suggested a promising application potential of BpNcCaP + BMP-2 in repairing LVBDs.

In the family of CaP, one of the most relevant materials for bone regeneration is HA due to its bone-like composition and thus excellent biocompatibility and osteoconductivity (Bhat et al., 2021). One method to produce HA-based bone-defect-filling materials for clinical application is to harvest natural HA from

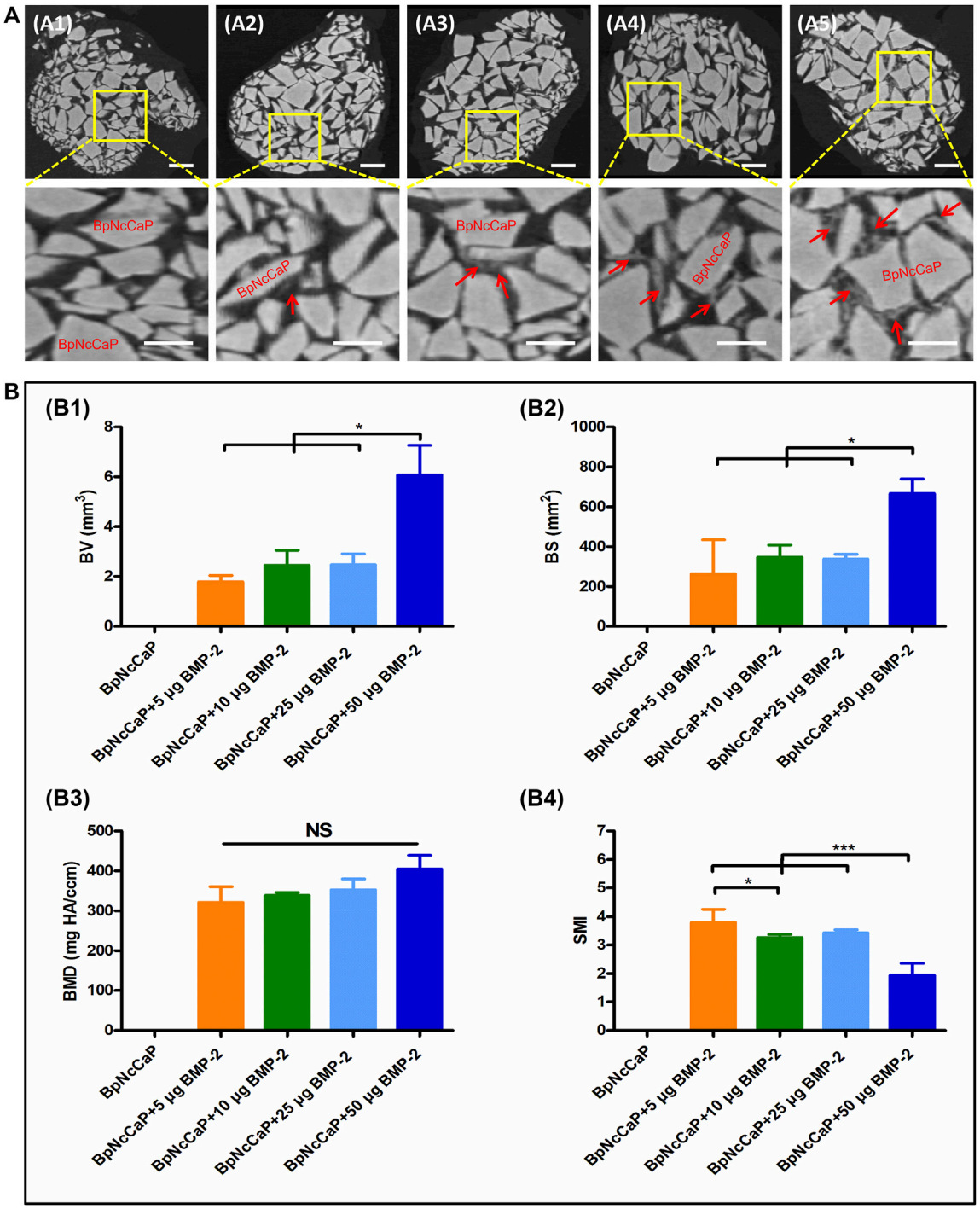

FIGURE 7 | Micro-CT images **(A)** showed newly formed bone and grafted biomaterials of BpNcCaP without **(A1)** or with different amount (5/10/25/50 μg) of BMP-2 **(A2–A5)** 5 weeks post implantation. White granules: BpNcCaP; Red arrow: new bone tissue. Bar = 1 mm. Micro-CT analysis **(B)** of the new bone volume **(B1)**, bone surface area **(B2)**, bone mineral density **(B3)**, structure mode index **(B4)** for BpNcCaPs without or with different amounts (5/10/25/50 μg) of BMP-2. Data were presented as mean ± SD. Significant effect of the treatment, $^{*}p < 0.05$; $^{**}p < 0.01$; $^{***}p < 0.001$.

allogenic bone tissues (Ramesh et al., 2018), which involves various decellularization processes, such as washing using enzyme, acetone or supercritical CO_2 (Crapo et al., 2011; Ha et al., 2013; Chalard, 2021; Jiang et al., 2021). Since the organic compositions are not completely removed, their usage is associated with a potential risk of severe immune reaction and rejection (Li et al., 2014). Xenogeneic grafts, such as Bio-Oss® or Cerabone® are conventionally further processed by sintering at

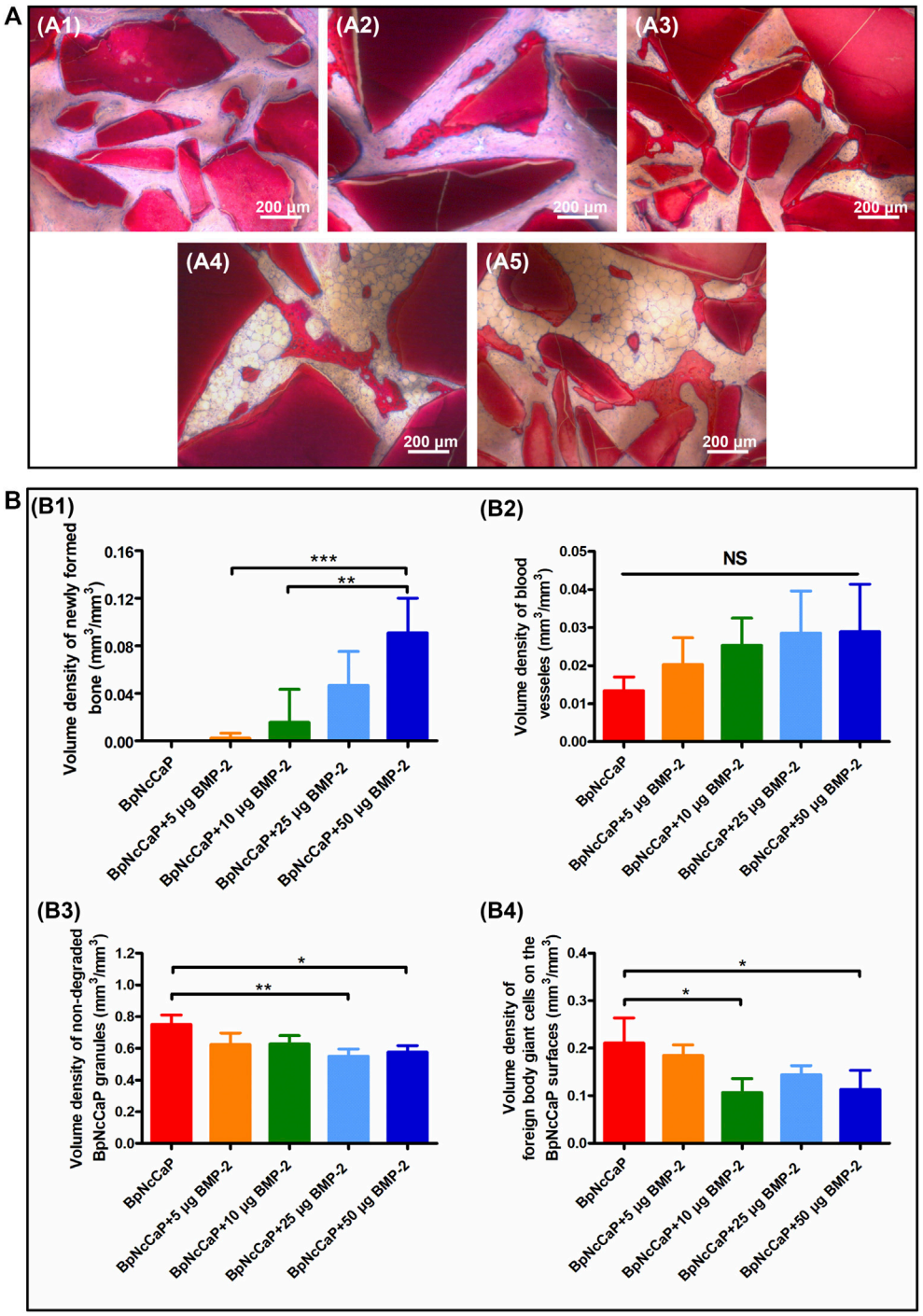

FIGURE 8 | Light micrographs **(A)** of newly formed bone and remaining BpNcCaP without **(A1)** or with different amount (5/10/25/50 μg) of BMP-2 **(A2-A5)** 5 weeks after implantation. Graphs **(B)** depicting the volume densities of newly formed bone **(B1)**, blood vessels **(B2)**, undegraded particles **(B3)** and foreign body giant cells **(B4)** on the surfaces of BpNcCaP and 5/10/25/50 μg BMP-2 incorporated BpNcCaP granules. The sections were surface-stained with McNeal's Tetrachrome, basic Fuchsine and Toluidine Blue O. Mean values ($n = 6$) were represented together with the standard deviation, significant effect of the treatment: $^{*}p < 0.05$; $^{**}p < 0.01$; $^{***}p < 0.001$.

300 or even 1,250°C for at least several hours to remove all organic compositions, which confers them excellent biocompatibility (Barbeck et al., 2017). However, such a sintering causes a significant increase in crystallinity of HA and thus a dramatic decrease of degradation, hindering natural bone replacement. Many *in-vivo* studies have proved that even after 9 months of

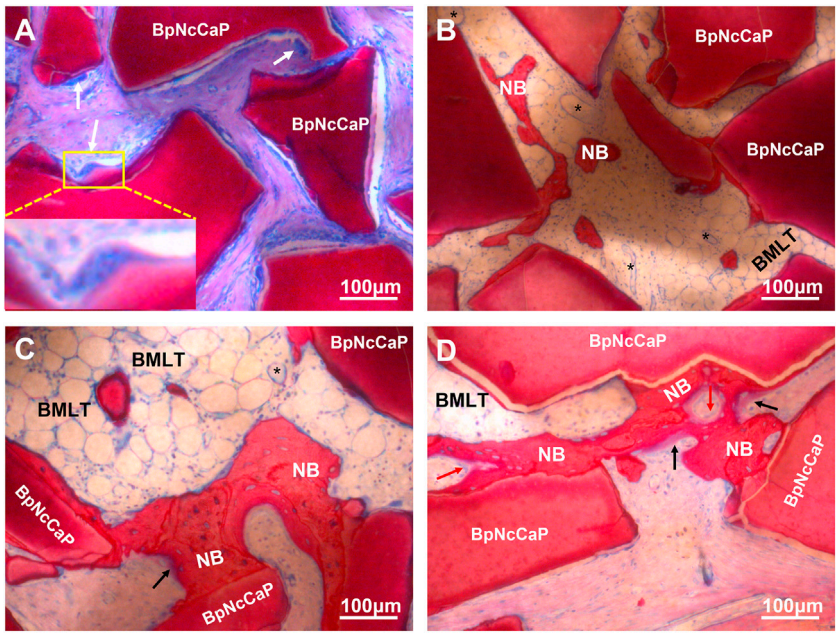

FIGURE 9 | Light micrographs in high magnification of BpNcCaP **(A)** and BpNcCaP+50 μg BMP-2 **(B–D)** 5 weeks after subcutaneous implantation in rats. NB: New bone; Black asterisk: Blood vessels; Black arrow: Unmineralized bone areas; White arrow: Foreign body giant cells (FBGCs); Red arrow: Osteoblasts; BMLT: Bone marrow-like tissues.

implantation sintered HA remained at the implantation sites with hardly any sign of resorption (Klein et al., 1983; Okuda et al., 2008; Diez-Escudero et al., 2017). Synthetic HA for fabricating bone-defect-filling materials is usually achieved via wet chemical precipitation, where calcium and phosphate precursors are mixed with ammonium hydroxide (NH_4OH) as a precipitation agent (Massit et al., 2018; López-Ortiz et al., 2020; Nimishakavi et al., 2021). The thereby-achieved HA is in fine powder and still needs to be sintered at 600–1,300°C for 1–48 h, where the grain size is significantly increased to facilitate the formation of granules with sufficient stiffness (Champion, 2013; Rodríguez-Lugo et al., 2018). Therefore, the disadvantages of sintered HA, such as low degradability and high hardness pursues (Zhou et al., 2018; Sikder et al., 2020). Furthermore, bioactive agents, such as proteinous growth factors (e.g., BMP-2) can only be adsorbed on to these materials, which exhibits too burst a release to continuously sustain bone regeneration (Agrawal and Sinha, 2017). Such a problem is hardly solved by simply adding polymeric materials since regulatory difficulties will be greatly increased. Consequently, it is in a great need to develop a novel fabrication method to produce HA-based bone-defect-filling materials with slow delivery, proper degradability, and stiffness. To provide a viable option, following a biomimetic principle, we have already developed a new type of CaP granules with a slow delivery property and cancellous bone-like stiffness (Zheng et al., 2014; Liu et al., 2017; Wang et al., 2017). However, the thereby-produced CaP granules are still suboptimal due to the simultaneous incorporation of chemicals, such as Tris base and sodium chloride, which may compromise the biocompatibility of the granules and the osteoinductive efficacy of BMP-2 (Konar and Sahoo, 2019). Furthermore, the incorporation rate of BMP-2 is also low (about 20–30%) (Wu et al., 2011; Wang et al., 2017), which greatly increases the cost of the products. In this study, we improved the fabrication method to synthesize novel biomimetic CaP granules with minimized presence of the unintended chemicals and maximal incorporation rate of BMP-2.

One critical step in this novel fabrication method was to substitute BMP-2 co-precipitation with washing the precipitates using PBS before the addition of BMP-2, which was highly important to remove the unintended chemicals. We adopted EDS to evaluate the efficiency of washing with PBS in eliminating residual chemicals using Na element as an indicator. We found that wt% of Na element was as high as 33.86%, which indicated the abundant presence of NaCl in the granules before washing (**Supplementary Figure S2**). After washing for 5 times, wt% of Na element dramatically decreased to 1.34%, which suggested that most of the unintended chemicals were removed. In SEM, we found that BpNcCaP granules bore a rough and slightly uneven morphology. High-magnification SEM images showed that BpNcCaP was mainly comprised of needle/rod-like crystals with the grain length at 85.14 ± 24.48 nm. FTIR analyses showed that BpNcCaP contained the chemical groups of PO_4^{3-}, CO_3^{2-}, OH^-. The XPS survey spectra showed that BpNcCaP granules that contained the photoelectron peaks belonging to calcium (Ca), phosphorus (P) and oxygen (O) were consistent with XPS results reported for Ca 2p, P 2p, and O 1s in HA (Rojas-Mayorga et al., 2016; Gomes et al., 2017; Rodríguez-Lugo et al., 2018; Senthilkumar et al., 2021). In addition, the presence of CO_3^{2-} suggested that our BpNcCaP was at least partially carbonated, which may increase its bioactivity (Zapanta-Legeros,

1965; Barralet et al., 2002; Diez-Escudero et al., 2017). XRD analysis showed that the main chemical composition of BpNcCaP was hexagonal HA according to the ICSD-PDF card 86-0740. The unit cell parameters (a = b = 0.946 nm and c = 0.687 nm) of BpNcCaP resembled the characteristic parameters of HA (Vargas-Becerril et al., 2020). In conventional methods to fabricate granular bone-defect-filling materials, sintering is always adopted to increase the grain size, during which the crystallite size of HA also dramatically increases to 45–55 nm (Rodríguez-Lugo et al., 2018). A study by Liu et al. found high degrees crystallinity of sintered HA was 95–99% at heating temperatures between 600 and 1,000°C (Liu et al., 2015). Furthermore, the crystallinity of sintered HA was increased by high temperature, which resulted in significantly decreased degradability (Diez-Escudero et al., 2017; Safarzadeh et al., 2020). In our granules, the average crystallite size of BpNcCaP was kept as small as 24.6 nm since no sintering was adopted in our biomimetic production process. Albeit so, the grain size of the BpNcCaP was also increased to 85.14 ± 24.48 nm, which ensured the formation of granular form. Furthermore, the crystallinity was also kept as low as 92%, which contributed to a proper degradation. To our best knowledge, this was the first report to reveal the physicochemical properties of biomimetically produced CaP granules. Furthermore, these physicochemical properties were not significantly changed by the presence of BMP-2 irrespective of its amount, which was also reasonable since BMP-2 was not co-precipitated but added after precipitation, washing and condensation.

Another advantage of this novel method was the significantly enhanced incorporation rate of BMP-2. BMP-2 is an expensive bioactive agent with about several thousand euros per 12 mg. Therefore, enhancing the incorporation rate is highly important to reduce the cost of BpNcCaP + BMP-2, which is beneficial for its wide-spreading in clinic. Our previous study shows that, using our biomimetic coating procedure to functionalize a xenogenic deproteinized bovine bone, the incorporation rate of BMP-2 is about 20.0 ± 0.7% (Wu et al., 2011). When using our previous biomimetic precipitate with the co-precipitation of BMP-2, the incorporation rate of BMP-2 is about 30.1 ± 5.7% (Liu et al., 2017; Wang et al., 2017). For both methods, BMP-2 is added into a large volume of the biomimetic solution to facilitate the co-precipitation with CaP, during which a large portion of BMP-2 maintains in the solutions, thereby resulting in a low incorporation rate. In comparison, in this novel method, we added BMP-2 into a much smaller volume of the collected, washed and centrifuged precipitates, which significantly reduced the waste of BMP-2 during removing the much smaller volume of solution. We showed that the incorporation rate of BMP-2 of BpNcCaP was 43.08 ± 1.67 when 4.31 ± 0.17 μg/sample BMP-2 was incorporated and could be enhanced to as high as 65.04 ± 6.01% when 52.03 ± 4.81 μg BMP-2 per gram BpNcCaP was incorporated. These incorporation rates were already 1.4 to 2.2 times of that for the granules produced using our previous methods, which was highly meaningful to enhance its clinical applicability.

Thereafter, we adopted the subcutaneous bone induction model (Liu et al., 2005; Wu et al., 2011) to assess the osteoinductive efficacy of the BpNcCaP granules with different amounts of incorporated BMP-2. We first adopted micro-CT to quantitatively and qualitatively evaluate the new bone formation 5 weeks post-implantation, the BpNcCaP without BMP-2 did not induce any new bone formation. New bone formation occurred in the group of BpNcCaP+5 μg BMP-2 and the BVs were similar in the groups of BpNcCaP+10 μg BMP-2 and BpNcCaP+25 μg BMP-2. In comparison, BV in the group of BpNcCaP+50 μg BMP-2 was significantly higher than those in the other three BMP-2-containing groups. The same pattern was also found in BS. These data indicated the bone-inducing capacity of BpNcCaP+50 μg BMP-2 was much stronger than the other granules. SMI is the quantification of the balance between rod-like and plate-like trabecular structures. The SMI value is 0 for an ideal plate structure, and 3 for a perfect rod structure or an infinite circular cylinder; round spheres have an SMI of 4 (Jiang et al., 2005). The SMI in the group of BpNcCaP+50 μg BMP-2 was significantly lower than that in other groups, which suggested that the trabecular structure of BpNcCaP+50 μg BMP-2 became thicker and denser after bone remodeling. While no significant difference was found in BMD, which suggested that the quality of new bone induced by BpNcCaPs with different amounts of BMP-2 was similar to each other. These data indicated that BpNcCaP+50 μg BMP-2 bore a significantly higher osteoinductive capacity, resulting in not only significantly enhanced bone quantity but also optimized bone microstructures.

We adopted the non-demineralized (hard) tissue sectioning technique to analyze the tissue reactions surrounding BpNcCaP without or with different mounts (5, 10, 25, 50 μg) of internally incorporated BMP-2 as we previously reported (Hägi et al., 2010; Wu et al., 2011). The advantages of this technique over a demineralized tissue sectioning are the maximal preservation of mineralized phases, including bone tissues and CaP-based bone grafts, thus their interfaces (Erben, 1997). With the aid of this staining, we can histomorphometrically analyze and stereologically quantify volume densities of bone, blood vessels and FBGCs (Wu et al., 2010b; Wu et al., 2011; Liu et al., 2017). Histological staining showed that the volume density of newly formed bone in the group of BpNcCaP+50 μg BMP-2 was significantly higher than those in the groups of BpNcCaP+5 μg BMP-2 and BpNcCaP+10 μg BMP-2. This phenomenon indicated that BpNcCaP+50 μg BMP-2 bore the most osteogenic capacity. Another important parameter for bone regeneration is the formation of blood vessels. Blood vessel is important for providing nutrients to osseous tissue. Moreover, blood vessels also release paracrine signals to modulate the growth, differentiation and regeneration of bone cells (Diomede et al., 2020). Our data showed that the volume density of blood vessels exhibited an increasing trend with the increasing loading of BMP-2. The average volume density of blood vessels was about 2.2 times that in BpNcCaP, suggesting that BMP-2 also promoted the formation of blood vessels accompanying its-induced osteogenesis although no significant difference was found among all the groups. In previous studies, co-administration of angiogenic bioactive agents, such as hyaluronic acid and human salivary histatin-1 with BMP-2 on absorbable collagen sponge lead to significantly enhanced angiogenesis and osteogenesis (Huang et al., 2017; Sun et al., 2020). Consequently, we may further improve the angiogenic and osteogenic efficacy of BpNcCaP + BMP-2 by simultaneously internally incorporating these materials. The volume density of FBGCs showed a

decreasing trend with the increase of BMP-2 incorporation amount with the lowest value detected in the group of BpNcCaP+50 μg BMP-2. The foreign body reaction is mediated by monocytes, macrophages and FBGCs (Sheikh et al., 2015; Martin and García, 2021). When monocytes/macrophages can hardly resorb large foreign body objectives, they can fuse into multinucleated FBGCs to enhance their resorbing efficacy. Therefore, FBGCs are regarded as a marker of chronic inflammation and foreign-body reaction (Wu et al., 2011; Liu et al., 2013; Liu et al., 2017). Therefore, the lowest volume density of FBGCs in the group of BpNcCaP+50 μg BMP-2 suggested a higher biocompatibility and less risk of immune rejection than BpNcCaP.

In our previous study, we find that biomimetically precipitated CaP coating is resorbed much faster when extensive bone formation was induced by its incorporated BMP-2 than that when no new bone formation occurs due to the absence of BMP-2 (Wu et al., 2010b). Thereafter, we further show a similar phenomenon for our biomimetically layer-by-layer (alternate amorphous CaP and crystalline CaP) assembled CaP granules (Zheng et al., 2014). It seems that the degradation of biomimetic CaP coating-based material shows a bone formation-responsive property, e.g., the more new bone formation and the more degradation of biomimetic CaP coating-based materials. This property may be largely attributed to the absence of sintering during its production process. In this study, our BpNcCaP also inherited such a bone formation-responsive property, which was evidenced by the decreasing trend of remaining BpNcCaP with the increase of new bone at 5 weeks post-implantation. Such a property of BpNcCaP granules holds a dramatic contrast to sintered HA that barely degrades even after an implantation for several months (Okuda et al., 2008; Diez-Escudero et al., 2017). This property of BpNcCaP is highly beneficial for both space preservation before bone ingrowth and the subsequent substitution of these bone-defect-filling materials with host bone tissue. In addition, the more bone formation was also associated with the less volume density of FBGCs. This was consistent with our previous finding that volume density of new bone is negatively correlated with the volume density of FBGCs. This might be largely due to the reduced direct exposure of BpNcCaP to connective tissues and thus immune system when more new bone formed on the surface of BpNcCaP, thereby causing less foreign-body reaction.

One limitation in this study was that we adopted an ectopic bone induction model to evaluate the osteogenic efficacy of BpNcCaP + BMP-2. Further studies can be performed to evaluate its performance in orthopedic bone defects. Furthermore, large animal studies should also be performed before extrapolating the present data to clinical application.

5 CONCLUSION

In this study, we synthesized novel BpNcCaP granules with internally incorporated BMP-2 with an aim to develop properly degradable and highly osteoinductive granules to repair LVBDs. *In-vitro* characterization data showed that the BpNcCaP + BMP-2 granules were comprised of hexagonal HA with an average crystallite size ranging from 19.7 to 25.1 nm and a grain size at 84.13 ± 28.46 nm. The vickers hardness of BpNcCaP was 32.50 ± 3.58 HV 0.025. BpNcCaP showed no obvious cytotoxicity and was favorable for the adhesion of pre-osteoblasts. BMP-2 incorporation rate could even reach 65.04 ± 6.01%. *In-vivo* histomorphometric analysis showed that total volume of new bone induced by BpNcCaP exhibited a BMP-2 amount-dependent increasing manner. The BpNcCaP+50 μg BMP-2 exhibited significant degradation and less FBGCs reaction in comparison with BpNcCaP. These data suggested a promising application potential of BpNcCaP + BMP-2 in repairing LVBDs.

DATA AVAILABILITY STATEMENT

The original contributions presented in the study are included in the article/**Supplementary Material**, further inquiries can be directed to the corresponding authors.

ETHICS STATEMENT

The animal study was reviewed and approved by The animal experiment was approved by the Ethical Committee of Zhejiang Chinese Medical University (No. IACUC-20210104-02).

AUTHOR CONTRIBUTIONS

GX, GW, NA, CS, HL, TF, BW, and NA: study concept and design. GX, CS, ZJ, TW, BW, and MA: data acquisition and analysis. GX, CS, ZJ, TW, MA, HL, NA, BW, and GC: performed experiments. CS, HL, TW, ZJ, BW, and GC: animal experiments. GX, CS, MA, and GC: manuscript preparation. HL, TF, NA, and GW: manuscript review. GX: preparation of BpNcCaP granules. All authors: read and approved the submitted version.

FUNDING

This study was supported by Deanship of Scientific Research at Princess Nourah Bint Abdulrahman University (Grant No. 265S39), Key Research and Development Plan of Zhejiang Province (Grant No. 2021C04013), High-End Foreign Expert Recruitment Plan of China (Grant No. G20200216024), Zhejiang Medical and Health Science and Technology Project (Grant No. 2021446434), China Scholarship Council (Grant No. 201808330467).

SUPPLEMENTARY MATERIAL

The Supplementary Material for this article can be found online at: https://www.frontiersin.org/articles/10.3389/fbioe.2022.920696/full#supplementary-material

REFERENCES

Agrawal, V., and Sinha, M. (2017). A Review on Carrier Systems for Bone Morphogenetic Protein-2. *J. Biomed. Mat. Res.* 105 (4), 904–925. doi:10.1002/jbm.b.33599

Alqap, A. S. F., and Sopyan, I. (2009). *Low Temperature Hydrothermal Synthesis of Calcium Phosphate Ceramics: Effect of Excess Ca Precursor on Phase Behaviour*. New Delhi: CSIR.

Baldwin, P., Li, D. J., Auston, D. A., Mir, H. S., Yoon, R. S., and Koval, K. J. (2019). Autograft, Allograft, and Bone Graft Substitutes: Clinical Evidence and Indications for Use in the Setting of Orthopaedic Trauma Surgery. *J. Orthop. Trauma* 33 (4), 203–213. doi:10.1097/bot.0000000000001420

Barbeck, M., Unger, R., Witte, F., Wenisch, S., and Schnettler, R. (2017). Xenogeneic Bone Grafting Materials. *Int. Mag. Oral Implant* 3, 34–36.

Barralet, J., Knowles, J. C., Best, S., and Bonfield, W. (2002). Thermal Decomposition of Synthesised Carbonate Hydroxyapatite. *J. Mater. Sci. Mater. Med.* 13 (6), 529–533. doi:10.1023/a:1015175108668

Bhat, S., Uthappa, U., Altalhi, T., Jung, H.-Y., and Kurkuri, M. D. (2021). Functionalized Porous Hydroxyapatite Scaffolds for Tissue Engineering Applications: A Focused Review. *ACS Biomater. Sci. Eng.* 2021. doi:10.1021/acsbiomaterials.1c00438

Chalard, J.-J. (2021). Supercritical CO 2 Viral-Inactivated Allogenic Bone Graft in Maxillary Sinus Augmentation Procedures: 10-Year Retrospective Clinical and Radiographic Results. *Int. J. Periodontics Restor. Dent.* 41 (3), 433. doi:10.11607/prd.4877

Champion, E. (2013). Sintering of Calcium Phosphate Bioceramics. *Acta biomater.* 9 (4), 5855–5875. doi:10.1016/j.actbio.2012.11.029

Crapo, P. M., Gilbert, T. W., and Badylak, S. F. (2011). An Overview of Tissue and Whole Organ Decellularization Processes. *Biomaterials* 32 (12), 3233–3243. doi:10.1016/j.biomaterials.2011.01.057

de Groot, K. (1984). Bioceramics of Calcium Phosphate. *J. Clin. Eng.* 9 (1), 52. doi:10.1097/00004669-198401000-00010

de Melo Pereira, D., and Habibovic, P. (2018). Biomineralization-Inspired Material Design for Bone Regeneration. *Adv. Healthc. Mat.* 7 (22), 1800700. doi:10.1002/adhm.201800700

Diez-Escudero, A., Espanol, M., Beats, S., and Ginebra, M.-P. (2017). *In Vitro* degradation of Calcium Phosphates: Effect of Multiscale Porosity, Textural Properties and Composition. *Acta biomater.* 60, 81–92. doi:10.1016/j.actbio.2017.07.033

Diez-Escudero, A., Espanol, M., and Ginebra, M.-P. (2020). "Synthetic Bone Graft Substitutes: Calcium-Based Biomaterials," in *Dental Implants and Bone Grafts* (Amsterdam, Netherlands: Elsevier), 125–157. doi:10.1016/b978-0-08-102478-2.00006-4

Diomede, F., Marconi, G. D., Fonticoli, L., Pizzicanella, J., Merciaro, I., Bramanti, P., et al. (2020). Functional Relationship between Osteogenesis and Angiogenesis in Tissue Regeneration. *Ijms* 21 (9), 3242. doi:10.3390/ijms21093242

Edén, M. J. M. (2021). Structure and Formation of Amorphous Calcium Phosphate and its Role as Surface Layer of Nanocrystalline Apatite: Implications for Bone Mineralization. *Materialia* 17, 101107. doi:10.1016/j.mtla.2021.101107

Erben, R. G. (1997). Embedding of Bone Samples in Methylmethacrylate: an Improved Method Suitable for Bone Histomorphometry, Histochemistry, and Immunohistochemistry. *J. Histochem Cytochem.* 45 (2), 307–313. doi:10.1177/002215549704500215

Fahami, A., Nasiri-Tabrizi, B., and Ebrahimi-Kahrizsangi, R. (2012). Synthesis of Calcium Phosphate-Based Composite Nanopowders by Mechanochemical Process and Subsequent Thermal Treatment. *Ceram. Int.* 38 (8), 6729–6738. doi:10.1016/j.ceramint.2012.05.064

Gomes, G. C., Borghi, F. F., Ospina, R. O., López, E. O., Borges, F. O., Mello, A., et al. (2017). Nd:YAG (532 Nm) Pulsed Laser Deposition Produces Crystalline Hydroxyapatite Thin Coatings at Room Temperature. *Surf. Coatings Technol.* 329, 174–183. doi:10.1016/j.surfcoat.2017.09.008

Ha, T. L. B., Quan, T. M., and Vu, D. N. (2013). "Naturally Derived Biomaterials: Preparation and Application," in *Regenerative Medicine and Tissue Engineering* IntechOpen. doi:10.5772/55668

Hägi, T. T., Wu, G., Liu, Y., and Hunziker, E. B. (2010). Cell-mediated BMP-2 Liberation Promotes Bone Formation in a Mechanically Unstable Implant Environment. *Bone* 46 (5), 1322–1327. doi:10.1016/j.bone.2010.02.010

Hoang, V. H., Troubitsin, M. A., Furda, L. V., and Nguyen, T. T. H. (2020). Synthesis of Silicon-And Carbonate-Doped Biomimetic Hydroxyapatite in the Presence of Citrate Ions and its Physicochemical, Bioactivity Properties. *J. Biomimetics, Biomaterials Biomed. Eng.* 47, 1–12. doi:10.4028/www.scientific.net/JBBBE.47.1

Huang, H., Feng, J., Wismeijer, D., Wu, G., and Hunziker, E. B. (2017). Hyaluronic Acid Promotes the Osteogenesis of BMP-2 in an Absorbable Collagen Sponge. *Polym. (Basel)* 9 (8), 339. doi:10.3390/polym9080339

Hunziker, E., Jovanovic, J., Jovanovic, J., Horner, A., Keel, M., Lippuner, K., et al. (2016). Optimisation of BMP-2 Dosage for the Osseointegration of Porous Titanium Implants in an Ovine Model. *eCM* 32, 241–256. doi:10.22203/ecm.v032a16

Ignjatović, N. L., Mančić, L., Vuković, M., Stojanović, Z., Nikolić, M. G., Škapin, S., et al. (2019). Rare-earth (Gd 3+, Yb 3+/Tm 3+, Eu 3+) Co-doped Hydroxyapatite as Magnetic, Up-Conversion and Down-Conversion Materials for Multimodal Imaging. *Sci. Rep.* 9 (1), 1–15. doi:10.1038/s41598-019-52885-0

James, A. W., LaChaud, G., Shen, J., Asatrian, G., Nguyen, V., Zhang, X., et al. (2016). A Review of the Clinical Side Effects of Bone Morphogenetic Protein-2. *Tissue Eng. Part B Rev.* 22 (4), 284–297. doi:10.1089/ten.teb.2015.0357

Jiang, S., Wang, M., and He, J. (2021). A Review of Biomimetic Scaffolds for Bone Regeneration: Toward a Cell-free Strategy. *Bioeng. Transl. Med.* 6 (2), e10206. doi:10.1002/btm2.10206

Jiang, Y., Zhao, J., Liao, E. Y., Dai, R. C., Wu, X. P., and Genant, H. K. (2005). Application of Micro-CT Assessment of 3-D Bone Microstructure in Preclinical and Clinical Studies. *J. Bone Min. Metab.* 23 (1), 122–131. doi:10.1007/BF03026336

Klein, C. P. A. T., Driessen, A. A., De Groot, K., and Van Den Hooff, A. (1983). Biodegradation Behavior of Various Calcium Phosphate Materials in Bone Tissue. *J. Biomed. Mat. Res.* 17 (5), 769–784. doi:10.1002/jbm.820170505

Konar, M., and Sahoo, H. (2019). Phosphate and Sulphate-Mediated Structure and Stability of Bone Morphogenetic Protein - 2 (BMP - 2): A Spectroscopy Enabled Investigation. *Int. J. Biol. Macromol.* 135, 1123–1133. doi:10.1016/j.ijbiomac.2019.06.015

Kowalczewski, C. J., and Saul, J. M. (2018). Biomaterials for the Delivery of Growth Factors and Other Therapeutic Agents in Tissue Engineering Approaches to Bone Regeneration. *Front. Pharmacol.* 9, 513. doi:10.3389/fphar.2018.00513

Layrolle, P., and Daculsi, G. (2009). "Physicochemistry of Apatite and its Related Calcium Phosphates," in *Thin Calcium Phosphate Coatings for Medical Implants* (New York: Springer), 19–21. doi:10.1007/978-0-387-77718-4_2

Li, J., Baker, B. A., Mou, X., Ren, N., Qiu, J., Boughton, R. I., et al. (2014). Biopolymer/calcium Phosphate Scaffolds for Bone Tissue Engineering. *Adv. Healthc. Mat.* 3 (4), 469–484. doi:10.1002/adhm.201300562

Liu, Q., Matinlinna, J. P., Chen, Z., Ning, C., Ni, G., Pan, H., et al. (2015). Effect of Thermal Treatment on Carbonated Hydroxyapatite: Morphology, Composition, Crystal Characteristics and Solubility. *Ceram. Int.* 41 (5), 6149–6157. doi:10.1016/j.ceramint.2014.11.062

Liu, T., Zheng, Y., Wu, G., Wismeijer, D., Pathak, J. L., and Liu, Y. (2017). BMP2-coprecipitated Calcium Phosphate Granules Enhance Osteoinductivity of Deproteinized Bovine Bone, and Bone Formation during Critical-Sized Bone Defect Healing. *Sci. Rep.* 7 (1), 41800–41812. doi:10.1038/srep41800

Liu, T., Wu, G., Wismeijer, D., Gu, Z., and Liu, Y. (2013). Deproteinized Bovine Bone Functionalized with the Slow Delivery of BMP-2 for the Repair of Critical-Sized Bone Defects in Sheep. *Bone* 56 (1), 110–118. doi:10.1016/j.bone.2013.05.017

Liu, T., Wu, G., Zheng, Y., Wismeijer, D., Everts, V., and Liu, Y. (2014). Cell-mediated BMP-2 Release from a Novel Dual-Drug Delivery System Promotes Bone Formation. *Clin. Oral Impl. Res.* 25 (12), 1412–1421. doi:10.1111/clr.12283

Liu, Y., Hunziker, E. B., Layrolle, P., De Bruijn, J. D., and De Groot, K. (2004). Bone Morphogenetic Protein 2 Incorporated into Biomimetic Coatings Retains its Biological Activity. *Tissue Eng.* 10 (1-2), 101–108. doi:10.1089/107632704322791745

Liu, Y., Wu, G., and de Groot, K. (2010). Biomimetic Coatings for Bone Tissue Engineering of Critical-Sized Defects. *J. R. Soc. Interface* 7 (Suppl. l_5), S631–S647. doi:10.1098/rsif.2010.0115.focus

Liu, Y., Degroot, K., and Hunziker, E. (2005). BMP-2 Liberated from Biomimetic Implant Coatings Induces and Sustains Direct Ossification in an Ectopic Rat Model. *Bone* 36 (5), 745–757. doi:10.1016/j.bone.2005.02.005

Liu, Y., and Hunziker, E. B. (2009). "Biomimetic Coatings and Their Biological Functionalization," in *Thin Calcium Phosphate Coatings for Medical Implants* (New York, NY: Springer), 301–314. doi:10.1007/978-0-387-77718-4_11

Liu, Y., Hunziker, E. B., Randall, N. X., De Groot, K., and Layrolle, P. (2003). Proteins Incorporated into Biomimetically Prepared Calcium Phosphate Coatings Modulate Their Mechanical Strength and Dissolution Rate. *Biomaterials* 24 (1), 65–70. doi:10.1016/s0142-9612(02)00252-1

Liu, Y., Huse, R. O., de Groot, K., Buser, D., and Hunziker, E. B. (2007). Delivery Mode and Efficacy of BMP-2 in Association with Implants. *J. Dent. Res.* 86 (1), 84–89. doi:10.1177/154405910708600114

Liu, Y., Li, J. P., Hunziker, E. B., and De Groot, K. (2006). Incorporation of Growth Factors into Medical Devices via Biomimetic Coatings. *Phil. Trans. R. Soc. A* 364 (1838), 233–248. doi:10.1098/rsta.2005.1685

Liu, Y., Schouten, C., Boerman, O., Wu, G., Jansen, J. A., and Hunziker, E. B. (2018). The Kinetics and Mechanism of Bone Morphogenetic Protein 2 Release from Calcium Phosphate-Based Implant-Coatings. *J. Biomed. Mat. Res.* 106 (9), 2363–2371. doi:10.1002/jbm.a.36398

Lo, K. W.-H., Ulery, B. D., Ashe, K. M., and Laurencin, C. T. (2012). Studies of Bone Morphogenetic Protein-Based Surgical Repair. *Adv. Drug Deliv. Rev.* 64 (12), 1277–1291. doi:10.1016/j.addr.2012.03.014

López-Ortiz, S., Mendoza-Anaya, D., Sánchez-Campos, D., Fernandez-García, M., Salinas-Rodríguez, E., Reyes-Valderrama, M., et al. (2020). The pH Effect on the Growth of Hexagonal and Monoclinic Hydroxyapatite Synthesized by the Hydrothermal Method. *J. Nanomater.* 2020, 1–10. doi:10.1155/2020/5912592

Ma, L., Yu, Y., Liu, H., Sun, W., Lin, Z., Liu, C., et al. (2021). Berberine-releasing Electrospun Scaffold Induces Osteogenic Differentiation of DPSCs and Accelerates Bone Repair. *Sci. Rep.* 11 (1), 1–12. doi:10.1038/s41598-020-79734-9

Mansour, A., Al-Hamed, F. S., Torres, J., and Marino, F. T. (2020). "Alveolar Bone Grafting: Rationale and Clinical Applications," in *Dental Implants and Bone Grafts* (Amsterdam, Netherlands: Elsevier), 43–87. doi:10.1016/b978-0-08-102478-2.00003-9

Markovic, M., Fowler, B. O., and Tung, M. S. (2004). Preparation and Comprehensive Characterization of a Calcium Hydroxyapatite Reference Material. *J. Res. Natl. Inst. Stand. Technol.* 109 (6), 553. doi:10.6028/jres.109.042

Martin, K. E., and García, A. J. (2021). Macrophage Phenotypes in Tissue Repair and the Foreign Body Response: Implications for Biomaterial-Based Regenerative Medicine Strategies. *Acta biomater.* 133, 4–16. doi:10.1016/j.actbio.2021.03.038

Massit, A., Fathi, M., El Yacoubi, A., Kholtei, A., and Chafik El Idrissi, B. (2018). Effect of Physical and Chemical Parameters on the β-Tricalcium Phosphate Synthesized by the Wet Chemical Method. *Mediterr. J. Chem.*, 7 (3), 234–242. doi:10.13171/mjc7310268-elidrissi

Migliorini, F., La Padula, G., Torsiello, E., Spiezia, F., Oliva, F., and Maffulli, N. J. E. J. o. M. R. (2021). Strategies for Large Bone Defect Reconstruction after Trauma, Infections or Tumour Excision: a Comprehensive Review of the Literature. *Eur. J. Med.* 26 (1), 1–10. doi:10.1186/s40001-021-00593-9

Momma, K., and Izumi, F. (2011). VESTA 3for Three-Dimensional Visualization of Crystal, Volumetric and Morphology Data. *J. Appl. Cryst.* 44 (6), 1272–1276. doi:10.1107/s0021889811038970

Nimishakavi, S., Rao, V. M., Aishwarya, T., and Singh, A. (2021). Green Chemistry Synthesis of Nano-Hydroxyapatite: Effect of Natural Stabilisers on Ca/P, doi:10.32628/IJSRSET218459

Okuda, T., Ioku, K., Yonezawa, I., Minagi, H., Gonda, Y., Kawachi, G., et al. (2008). The Slow Resorption with Replacement by Bone of a Hydrothermally Synthesized Pure Calcium-Deficient Hydroxyapatite. *Biomaterials* 29 (18), 2719–2728. doi:10.1016/j.biomaterials.2008.03.028

Piccinini, M., Rebaudi, A., Sglavo, V. M., Bucciotti, F., and Pierfrancesco, R. (2013). A New HA/TTCP Material for Bone Augmentation. 22(1), 83–90.doi:10.1097/id.0b013e31827afc19

Ramesh, N., Moratti, S. C., and Dias, G. J. (2018). Hydroxyapatite-polymer Biocomposites for Bone Regeneration: A Review of Current Trends. *J. Biomed. Mat. Res.* 106 (5), 2046–2057. doi:10.1002/jbm.b.33950

Rodríguez-Lugo, V., Karthik, T. V. K., Mendoza-Anaya, D., Rubio-Rosas, E., Villaseñor Cerón, L. S., Reyes-Valderrama, M. I., et al. (2018). Wet Chemical Synthesis of Nanocrystalline Hydroxyapatite Flakes: Effect of pH and Sintering Temperature on Structural and Morphological Properties. *R. Soc. open Sci.* 5 (8), 180962. doi:10.1098/rsos.180962

Rojas-Mayorga, C., Mendoza-Castillo, D., Bonilla-Petriciolet, A., Silvestre-Albero, J., and Technology (2016). Tailoring the Adsorption Behavior of Bone Char for Heavy Metal Removal from Aqueous Solution. *Adsorpt. Sci. Technol.* 34 (6), 368–387. doi:10.1177/0263617416658891

Safarzadeh, M., Chee, C. F., Ramesh, S., and Fauzi, M. N. A. (2020). Effect of Sintering Temperature on the Morphology, Crystallinity and Mechanical Properties of Carbonated Hydroxyapatite (CHA). *Ceram. Int.* 46 (17), 26784–26789. doi:10.1016/j.ceramint.2020.07.153

Senthilkumar, S., Dhivya, V., Sathya, M., and Rajendran, A. (2021). RETRACTED ARTICLE: Synthesis and Characterization of Magnetite/hydroxyapatite Nanoparticles for Biomedical Applications. *J. Exp. Nanosci.* 16 (1), 159–179. doi:10.1080/17458080.2021.1931685

Sheikh, Z., Brooks, P., Barzilay, O., Fine, N., and Glogauer, M. (2015). Macrophages, Foreign Body Giant Cells and Their Response to Implantable Biomaterials. *Materials* 8 (9), 5671–5701. doi:10.3390/ma8095269

Sikder, P., Ren, Y., and Bhaduri, S. B. (2020). Microwave Processing of Calcium Phosphate and Magnesium Phosphate Based Orthopedic Bioceramics: A State-Of-The-Art Review. *Acta Biomater.* 111, 29–53. doi:10.1016/j.actbio.2020.05.018

Sohn, H. S., and Oh, J. K. (2019). Review of Bone Graft and Bone Substitutes with an Emphasis on Fracture Surgeries. *Biomater. Res.* 23 (1), 9–7. doi:10.1186/s40824-019-0157-y

Sun, P., Shi, A., Shen, C., Liu, Y., Wu, G., and Feng, J. (2020). Human Salivary Histatin-1 (Hst1) Promotes Bone Morphogenetic Protein 2 (BMP2)-induced Osteogenesis and Angiogenesis. *FEBS Open bio* 10 (8), 1503–1515. doi:10.1002/2211-5463.12906

Teng, F., Wei, L., Yu, D., Deng, L., Zheng, Y., Lin, H., et al. (2020). Vertical Bone Augmentation with Simultaneous Implantation Using Deproteinized Bovine Bone Block Functionalized with a Slow Delivery of BMP-2. *Clin. Oral Impl Res.* 31 (3), 215–228. doi:10.1111/clr.13558

Vallet-Regi, M., and González-Calbet, J. M. (2004). Calcium Phosphates as Substitution of Bone Tissues. *Prog. solid state Chem.* 32 (1-2), 1–31. doi:10.1016/j.progsolidstchem.2004.07.001

Vargas-Becerril, N., Sánchez-Téllez, D. A., Zarazúa-Villalobos, L., González-García, D. M., Álvarez-Pérez, M. A., de León-Escobedo, C., et al. (2020). Structure of Biomimetic Apatite Grown on Hydroxyapatite (HA). *Ceram. Int.* 46 (18), 28806–28813. doi:10.1016/j.ceramint.2020.08.044

Vidal, L., Kampleitner, C., Brennan, M. Á., Hoornaert, A., Layrolle, P., and Biotechnology (2020). Reconstruction of Large Skeletal Defects: Current Clinical Therapeutic Strategies and Future Directions Using 3D Printing. *Front. Bioeng. Biotechnol.* 8, 61. doi:10.3389/fbioe.2020.00061

Wang, D., Tabassum, A., Wu, G., Deng, L., Wismeijer, D., and Liu, Y. (2017). Bone Regeneration in Critical-Sized Bone Defect Enhanced by Introducing Osteoinductivity to Biphasic Calcium Phosphate Granules. *Clin. Oral Impl. Res.* 28 (3), 251–260. doi:10.1111/clr.12791

Wang, J., Guo, J., Liu, J., Wei, L., and Wu, G. (2014). BMP-functionalised Coatings to Promote Osteogenesis for Orthopaedic Implants. *Ijms* 15 (6), 10150–10168. doi:10.3390/ijms150610150

Wei, L., Yu, D., Wang, M., Deng, L., Wu, G., and Liu, Y. (2020). Dose Effects of Slow-Released Bone Morphogenetic Protein-2 Functionalized β-Tricalcium Phosphate in Repairing Critical-Sized Bone Defects. *Tissue Eng. Part A* 26 (3-4), 120–129. doi:10.1089/ten.TEA.2019.0161

Wei, L., Teng, F., Deng, L., Liu, G., Luan, M., Jiang, J., et al. (2019). Periodontal Regeneration Using Bone Morphogenetic Protein 2 Incorporated Biomimetic Calcium Phosphate in Conjunction with Barrier Membrane: A Pre-clinical Study in Dogs. *J. Clin. Periodontol.* 46 (12), 1254–1263. doi:10.1111/jcpe.13195

Wu, G., Hunziker, E. B., Zheng, Y., Wismeijer, D., and Liu, Y. (2011). Functionalization of Deproteinized Bovine Bone with a Coating-Incorporated Depot of BMP-2 Renders the Material Efficiently

Osteoinductive and Suppresses Foreign-Body Reactivity. *Bone* 49 (6), 1323–1330. doi:10.1016/j.bone.2011.09.046

Wu, G., Liu, Y., Iizuka, T., and Hunziker, E. B. (2010a). Biomimetic Coating of Organic Polymers with a Protein-Functionalized Layer of Calcium Phosphate: the Surface Properties of the Carrier Influence Neither the Coating Characteristics Nor the Incorporation Mechanism or Release Kinetics of the Protein. *Tissue Eng. Part C. Methods* 16 (6), 1255–1265. doi:10.1089/ten.tec.2009.0588

Wu, G., Liu, Y., Iizuka, T., and Hunziker, E. B. (2010b). The Effect of a Slow Mode of BMP-2 Delivery on the Inflammatory Response Provoked by Bone-Defect-Filling Polymeric Scaffolds. *Biomaterials* 31 (29), 7485–7493. doi:10.1016/j.biomaterials.2010.06.037

Zapanta-Legeros, R. (1965). Effect of Carbonate on the Lattice Parameters of Apatite. *Nature* 206 (4982), 403–404. doi:10.1038/206403a0

Zheng, Y., Wu, G., Liu, T., Liu, Y., Wismeijer, D., Liu, Y., et al. (2014). A Novel BMP2-Coprecipitated, Layer-By-Layer Assembled Biomimetic Calcium Phosphate Particle: A Biodegradable and Highly Efficient Osteoinducer. *Clin. Implant Dent. Relat. Res.* 16 (5), 643–654. doi:10.1111/cid.12050

Zhou, C., Li, X., Cheng, J., Fan, H., and Zhang, X. (2018). "Bioactive Ceramics and Metals for Regenerative Engineering," in *Regenerative Engineering: Advanced Materials Science Principles* (Florida, US: CRC Press), 31–43. doi:10.1201/9781315121079-3

Conflict of Interest: CS and BW were employed by Hangzhou Huibo Science and Technology Co. Ltd.

The remaining authors declare that the research was conducted in the absence of any commercial or financial relationships that could be construed as a potential conflict of interest.

frontiers | Frontiers in Materials

TYPE Original Research
PUBLISHED 10 August 2022
DOI 10.3389/fmats.2022.941311

OPEN ACCESS

EDITED BY
Hasan Uludag,
University of Alberta,

REVIEWED BY
Ying Zhao,
Shenzhen Institutes of Advanced Technology, (CAS),
Fatemeh Kabirian,
Faculty of Medicine, KU Leuven,

*CORRESPONDENCE
Hai Kuang,
kuanghai@hotmail.com
Bo Li,
bli24@cmu.edu.cn

SPECIALTY SECTION
This article was submitted to Biomaterials, a section of the journal Frontiers in Materials

RECEIVED 11 May 2022
ACCEPTED 27 June 2022
PUBLISHED 10 August 2022

CITATION
Yan J, Huang W, Kuang H, Wang Q and Li B (2022), The effect of etched 3D printed Cu-bearing titanium alloy on the polarization of macrophage. *Front. Mater.* 9:941311. doi: 10.3389/fmats.2022.941311

The effect of etched 3D printed Cu-bearing titanium alloy on the polarization of macrophage

Jinge Yan[1], Wanyi Huang[1], Hai Kuang[2]*, Qiang Wang[1] and Bo Li[1]*

[1]School and Hospital of Stomatology, China Medical University, Liaoning Provincial Key Laboratory of Oral Disease, Shenyang, China, [2]Department of Oral and Maxillofacial Surgery, College of Stomatology, Guangxi Medical University, Nanning, China

3D printed titanium alloys have been widely used as implants in orthopedic surgery and dentistry. In recent years, Cu-bearing titanium alloys have shown great advantages in tissue engineering due to their excellent antibacterial activity and biological effect. In the current study, three alloys, namely, TC4 alloy, TC4-5Cu alloy, and TC4-6Cu alloy were fabricated by the use of selective laser melting (SLM) technology. Acid etching treatment was used to remove the metal powders on the samples and modify the surface of the manufactured alloys. The effect of different etched alloys on the biological behavior of macrophages (RAW 264.7) was studied comprehensively. Results showed that acid etching had no effect on the hydrophilicity, while contributing to the adhesion and polarization of macrophages with a lower ROS level. Moreover, Cu-bearing titanium exhibited better cell adhesion, macrophage polarization potential, and a lower ROS level. In summary, acid etching treatment provided a promising strategy to improve the biological properties of the Cu-bearing titanium alloys by SLM.

KEYWORDS

3D printing, copper, Ti6Al4V, acid etching, macrophage, ROS, oxidative stress

1 Introduction

As a common disease of oral surgery, maxillofacial bone defect caused by tumors, trauma, and other reasons affects the patients' appearance and directly harms the swallowing, chewing, and conversing functions of patients. In recent years, there have been two main approaches to repairing maxillofacial bone defects: surgical reconstruction and bone tissue engineering. However, surgical reconstruction has relative limitations in clinical application. Hence, bone tissue engineering plays an important role in maxillofacial bone repair. As one of the general bone tissue engineering technologies, 3D printing technology has been widely used in clinical practice in recent years due to its excellent characteristics, such as the ability to achieve personalized precise designs, be produced quickly and efficiently, and reduce the time and risk of surgical exposure (Dawood et al., 2015).

3D printing, also called additive manufacturing (AM), is a quick advanced technology that creates solid models by adding powder layer by layer. This technology has already been used for maxillofacial bone defects, dental defects, and dentition defects (Javaid and Haleem, 2019). The commonly used biomaterials are metals, alloys, ceramics, and polymers. These materials are used in different medical disciplines according to the requirements of specific applications. Previous research illustrated that metal materials were the most commonly used materials in dentistry due to their excellent mechanical properties (strength, hardness, wear resistance, durability, toughness, etc.) compared with ceramic materials and resin materials (Palaskar et al., 2010). Clinicians in the field of dentistry and orthopedic surgery demand materials with good mechanical properties, corrosion resistance, and biocompatibility, and titanium alloys largely meet these requirements.

In recent years, different metal elements are added to titanium alloys to improve the properties of the alloys. As one of the necessary micro-elements for the body, copper is a cofactor of various enzymes involved in the life activities of the body. In addition, copper is also widely used in various biomaterial research studies due to its excellent antimicrobial activity and biological activity (Zhang et al., 2016). Carter et al. (Carter et al., 2017) have verified that copper-bearing implants can inhibit the activity of both Gram-positive and Gram-negative bacteria. Huang et al. (Huang et al., 2019) demonstrated that copper-containing titanium alloy has good biocompatibility, and copper ions released from its surfaces could act as an inflammatory regulator to promote osteogenesis and sterilization.

A retrospective study on failed dental implants by Sun et al. (Sun et al., 2017) showed that 47% of early implant failures were caused by inflammation. Peri-implant diseases and infections have become the focus of oral implantology prevention and treatment (Spriano et al., 2018). Research studies have proven that compared with stainless steel materials (Chen et al., 2015) and poly-ether-ether-ketone (PEEK) (Olivares-Navarrete et al., 2015), titanium and titanium alloys have a lower level of inflammation and less abundance of macrophages on the surfaces. The implant-related inflammatory response can be summarized in the following eight steps: exudation, protein surface adsorption, growth of a temporary provisional matrix based on blood, the capacity of cells of the innate immune system to proliferate (white blood cells, platelets, complement, and blood coagulation system), neutrophil migration, by replacing the differentiation of the mononuclear cell into macrophages, foreign body reaction, generation of reactive oxygen species, and monocyte/macrophage fusion to form foreign body giant cells or apoptosis. Among them, reactive oxygen species production is an important step in the process of inflammatory response.

Reactive oxygen species (ROS) are cooperative or independent regulators of cellular signaling in response to different environmental stimuli and are mainly derived from superoxide anions (O_2^-), hydrogen peroxide (H_2O_2), and hydroxyl radicals (OH^-) (Mittal et al., 2014). It has been reported that ROS are involved in DNA repair, cell cycling, cell differentiation, chromatin remodeling, self-renewal, and other cell processes by Rendra et al. (Rendra et al., 2019). Furthermore, ROS plays an essential role in the regulation of macrophage polarization. A reduced ROS level suppresses the M1 phenotype and promotes macrophage polarization into the M2 phenotype (Zhou et al., 2018). However, the link between ROS and alloy-induced macrophage polarization has not been well-clarified.

Macrophages play a crucial role in the process of inflammation. Macrophages are able to secrete cytokines, chemokines, and growth factors to attract fibroblasts to produce extracellular matrix (ECM) and collagen. In addition, macrophages express different functional procedures by polarization according to different micro-environmental signals (McWhorter et al., 2015). Macrophages have two specific phenotypes, either M1-type macrophages (typically pro-inflammatory macrophages activated in response to Th1 cell–derived cytokines) or M2-type macrophages (anti-inflammatory macrophages activated in response to Th2 cell-derived cytokines) (Zhang et al., 2018).

In the process of 3D medical printing of titanium alloy, there may be partially melted or un-melted powder left on the surface of the material, which may lead to residual particle pollution in the later stage. Yi et al. (Yi et al., 2022) showed that acid etching treatment of porous Ti alloy scaffolds could remove residual powder on the surface of scaffolds and significantly improve the osteogenesis properties.

This study combines etched and unetched 3D printed Cu-bearing titanium with RAW 264.7 cells to explore the effect of macrophage biological behaviors, including the occurrence of an alloy being in direct contact with cells and alloy extracting culture macrophages. It could provide the experimental basis for animal and clinical use of this surface treatment technology.

2 Materials and methods

2.1 Material preparation

Plate samples with a size of 10 × 10 × 2 mm were fabricated by 3D printing technology. Selective laser melting (SLM) is one of the rapidly developed additive manufacturing techniques that creates solid models by adding powder layer by layer. The fabrication detail can be found in the previous studies (Zong et al., 2020); (Liu et al., 2021). According to a previous study, a Class 1 laser system equipped with a ProX DMP 200 fiber laser (a wavelength of 1070 nm and maximum output power of 300 W) was used to prepare Ti6Al4V-5Cu and Ti6Al4V-6Cu alloys (Zong et al., 2020). Laser power, scanning speed, scanning spacing, and single layer thickness are the major parameters

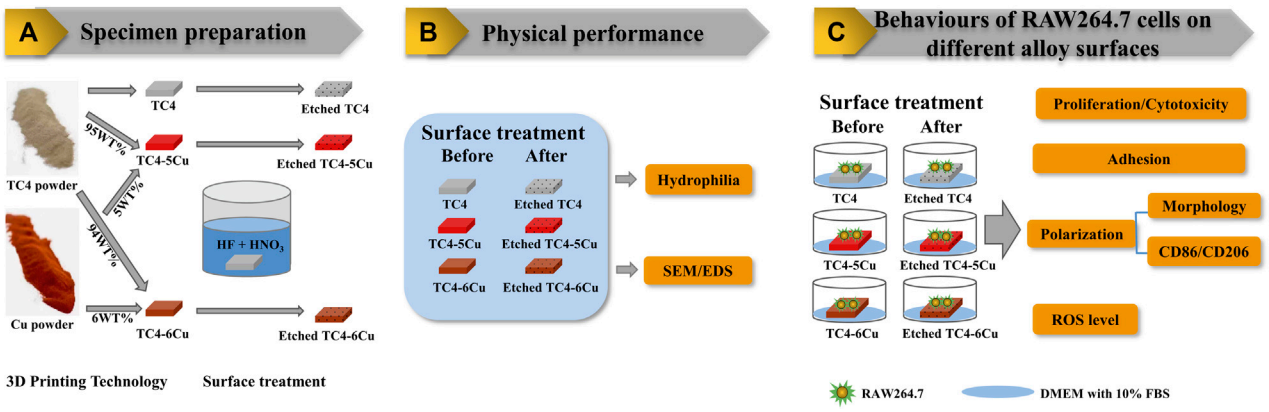

FIGURE 1
Flow diagram of the study: **(A)** Specimen preparation; **(B)** Physical performance; **(C)** Behaviours of RAW264.7 cells on different alloy surfaces.

in the process of selective laser melting. Different laser processing parameters were compared, and the optimal parameters were selected in this study: laser power of 260 W, scanning distance of 45 μm, and laser spot diameter of 70 μm. Then, all the samples were ground with waterproof SiC paper from 800 to 2000 grits. The specimens were subsequently immersed in nitric acid–hydrogen fluoride acid solution and finally washed with deionized water, acetone, and anhydrous ethanol for 10 min and dried by cold air. The ratio between nitric acid, fluoride acid, and distilled water is 1:4:5, and the etching duration is 30 s. The experimental samples were divided into six groups: unetched TC4 (TC4), unetched TC4-5Cu (TC4-5Cu), unetched TC4-6Cu (TC4-6Cu), etched TC4 (ETC4), etched TC4-5Cu (ETC4-5Cu), and etched TC4-6Cu (ETC4-6Cu). The preparation of the extract is according to ISO 10993–12 standards. Figure 1 illustrates the flow diagram of the study.

2.2 Surface characterization

2.2.1 Morphology

The structural morphology of the experimental samples was tested by using a scanning electron microscope (SEM, Zeiss Merlin Compact, Germany) equipped with energy-dispersive spectroscopy (EDS).

2.2.2 Hydrophilicity measurement

The surface wettability of the alloys was detected by the wettability measuring instrument (DataPhysics Instruments Gmbh, Germany) with the droplet method. The initial volume of the droplet is about 2 μl. SCA20 software was used to calculate the contact angles on the left and right sides of the samples. Three different areas were measured on each sample surface, and the process was repeated once.

2.3 Behaviors of RAW 264.7 cells on different material surfaces

2.3.1 Cell culture

Murine macrophage RAW 264.7 cells were used in this study. The cells were cultured in Dulbecco's modified Eagle's medium (DMEM, Hyclone, United States) supplemented with 10% FBS (Gibco) in an atmosphere of 5% CO_2 at 37°C. The cells were passaged at approximately 80% confluence and used at early passages (P5). The preparation of extracts included immersing the plate samples of etched and unetched titanium alloys in a cell culture medium for 72 h at a ratio of 0.2 g/ml according to ISO 10993–12 standard. After that, the extracts were collected, filtered by a 0.2-μm filter, and stored at 4°C.

2.3.2 Cell proliferation and cytotoxicity assay

RAW 264.7 cell proliferation was analyzed by the Cell Counting Kit-8 (CCK-8) for 12 and 24 h. RAW 264.7 cells were cultured at a concentration of 2×10^4 cells/ml and then seeded on all samples in a 96-well culture plate (500 μl/well, 37°C, 5% CO_2). The extract was changed the next day. After incubation for 12 and 24 h, respectively, the culture media was removed and 100 μl of DMEM medium with 10% CCK-8 (Beyotime, China) was added. Then, the samples were incubated in a dark incubator for 2 h at 37°C. Afterward, the 450 nm optical density (OD) was obtained with an Enzyme standard instrument (Multiskan GO, Thermo Scientific, United States). The cell relative growth rate (RGR) was calculated according to the following formula:

$$RGR = OD_{experimental\ group} / OD_{control\ group} \times 100\%.$$

2.3.3 Cell adhesion

RAW264.7 cells were seeded on different material surfaces at a concentration of 2×10^4 cell/ml for 24 h. After incubation, the medium was removed and the cells on alloys were washed three

times with phosphate-buffered saline (PBS) and fixed with 4% (w/v) paraformaldehyde for 10 min. And then, they were rinsed twice by PBS again and permeabilized with 0.2% (v/v) Triton X-100 (Beyotime, China) for 6 min. After that, 50 μL of rhodamine-phalloidin (Molecular, Probes Thermo Fisher Scientific, China) was added to stain cells in darkness. Finally, 5 mg/ml 40.6-diamidino-2-phenylindole (DAPI) solution was added to stain cells in darkness. The photographed stain images were observed by an optical microscope.

2.3.4 Cell morphology

RAW 264.7 cells were seeded in confocal dishes at a concentration of 2×10^4 cells/ml and cultured in different kinds of material extracts for 24 h. After incubation, the medium was removed and the cells were washed three times with phosphate-buffered saline (PBS) and fixed with 4% (w/v) paraformaldehyde for 10 min. Then, they were rinsed twice by PBS again and permeabilized with 0.2% (v/v) Triton X-100 (Beyotime, China) for 6 min. After that, 50 μl rhodamine–phalloidin (Molecular, Probes Thermo Fisher Scientific, China) was added to stain cells in darkness. Finally, 5 mg/ml Hoechst 33,342 (Boster, China) solution was added to stain cells in darkness. The photographed stain images were observed by a laser scanning confocal microscope.

2.3.5 Flow cytometry test

A total of 1×10^6 RAW 264.7 cells were collected and washed with PBS three times after being cultured in different material extracts for 12 and 24 h. APC-conjugated CD86 antibody (0.312 μg/test, Thermo Fisher Scientific) and PE-conjugated CD206 antibody (0.625 μg/test, Thermo Fisher Scientific) were incubated with the macrophages for 30 min on ice. Finally, PBS was added to the tubes to keep the final volume at 200–300 μL for flow cytometry (BD Pharmingen, San Diego, CA).

2.3.6 Measurement of intracellular reactive oxygen species

The intracellular ROS production was determined by a reactive oxygen species assay kit (Beyotime Biotechnology Ltd., Shanghai, China) for 12 and 24 h. RAW 264.7 cells were collected and incubated with DCFH-DA (1:1,000) for 30 min. The cells were washed twice with PBS, and fluorescence intensity was monitored by a flow cytometer (Becton Dickinson, America).

2.3.7 Statistical analysis

All experiments were analyzed with SPSS 23.0 software. The results are presented as mean ± standard deviation. Differences between groups were analyzed using one-way analysis of variance (ANOVA) followed by Tukey's test. p values less than 0.05 were considered statistically significant.

3 Result

3.1 Material preparation

A class 1 laser system equipped with a ProX DMP 200 fiber laser (a wavelength of 1070 nm and maximum output power of 300 W) was used to prepare Ti6Al4V-5Cu and Ti6Al4V-6Cu alloys, and the optimal parameters were selected in this study: laser power of 260W, scanning distance of 45 μm, and laser spot diameter of 70 μm (Zong et al., 2020).

According to ISO 10993–12 guidelines, the preparation of extracts included immersing the plate samples of etched and unetched titanium alloys in a cell culture medium for 72 h at a ratio of 0.2 g/ml. An analytical balance is used to measure the weight of each sample (Table 1). The average weight of the TC4 alloy, TC4-5Cu alloy, and TC4-6Cu alloy before etching and after etching are 0.0200g, 0.0236 g, and 0.0281 g, respectively, and there is no statistical difference ($p > 0.05$).

3.2 Characterizations of alloy

3.2.1 Surface morphology

Figure 2 shows the microstructures of the TC4 alloy surface, TC4-5Cu alloy surface, and TC4-6Cu alloy surface before and after acid etching technology. From the macro-graph of material samples (Figure 2A), the surface of each alloy sample after grinding and polishing is relatively smooth. SEM analysis reveals that the surface of TC4 alloy (Figures 2A,B), TC4-5Cu alloy (Figure 2B), and TC4-6Cu alloy (Figures 2B,C) is flat and smooth, while the surface of ETC4 alloy (Figure 2B–A'), ETC4-5Cu alloy (Figure 2B–B'), and ETC4-6Cu alloy (Figure 2B–C') was characterized by micro-porous structures. Most of the visible elements in the present alloys are titanium (Ti) and a small amount of aluminum (AI) and vanadium (V). Meanwhile, copper (Cu) can be detected in TC4-5Cu alloy (as shown in Figures 2B,C) and TC4-6Cu alloy (as shown in Figure 2C).

3.2.2 Hydrophilicity

As shown in Figure 3, the contact angle of TC4, TC4-5Cu, and TC4-6Cu groups and ETC4, ETC4-5Cu, and ETC4-6Cu groups are 72.14 ± 4.081, 63.23 ± 8.321, and 67.81 ± 3.763 and 68.95 ± 8.536, 64.3 ± 3.972, and 71.07 ± 3.854, respectively. The contact angle of TC4-5Cu and ETC4-5Cu groups is smaller than that of the others, but had no statistical significance ($p > 0.05$).

3.3 Behaviors of RAW 264.7 cells on different material surfaces

3.3.1 Cell proliferation and cytotoxicity

Figure 4A shows the optical densities of RAW 264.7 cells in different alloy extracts. With the increase in incubation time, there is a significant increase in OD values in each group, indicating the number of RAW 264.7 cells in each alloy

TABLE 1 Weight of the samples.

Sample	Before etching (g)	After etching (g)	Weight loss (g)	Average weight loss (g)
TC4	0.8347	0.8152	0.0195	0.0200
	0.8343	0.8103	0.0240	
	0.8354	0.8116	0.0238	
	0.8351	0.8213	0.0138	
TC4-5Cu	0.6280	0.6156	0.0124	0.0236
	0.6258	0.6155	0.0103	
	0.6248	0.5942	0.0306	
	0.6153	0.5743	0.041	
TC4-6Cu	0.8908	0.8797	0.0111	0.0281
	0.8874	0.8574	0.0300	
	0.8861	0.8546	0.0315	
	0.8847	0.8449	0.0398	

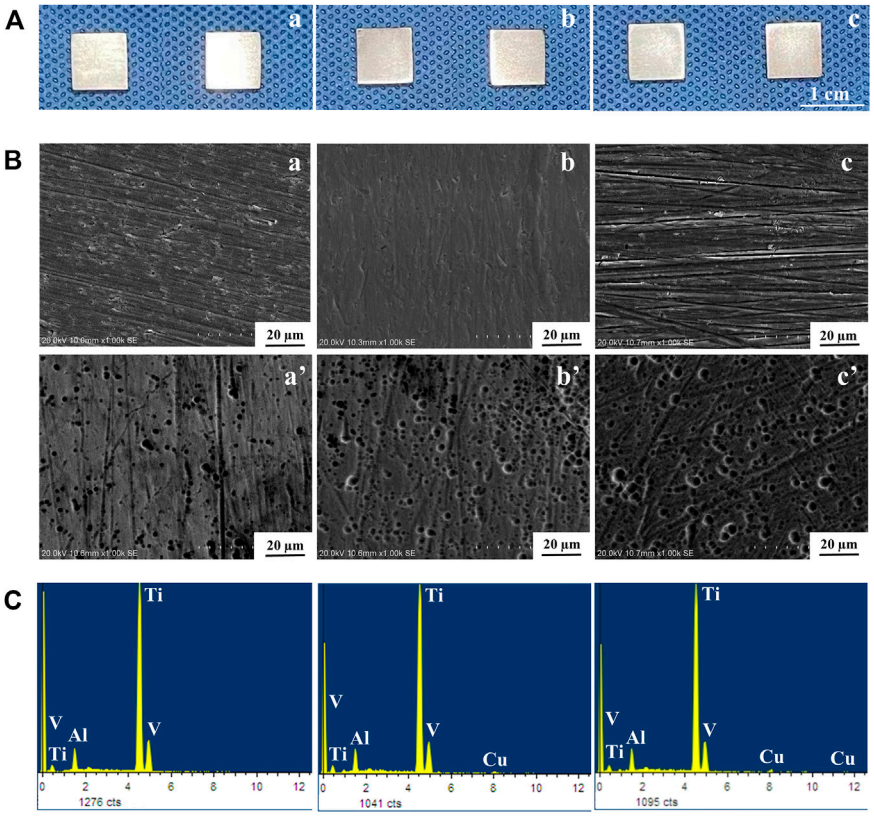

FIGURE 2
Surface morphology of alloys: **(A)** macro images of alloys; **(B)** SEM images of alloys; **(C)** EDS analyses of alloys: **(A)** TC4 alloy and **(a')** ETC4 alloy; **(B)** TC4-5Cu alloy and **(b')** ETC4-5Cu alloy; **(C)** TC4-6Cu alloy and **(c')** ETC4-6Cu alloy.

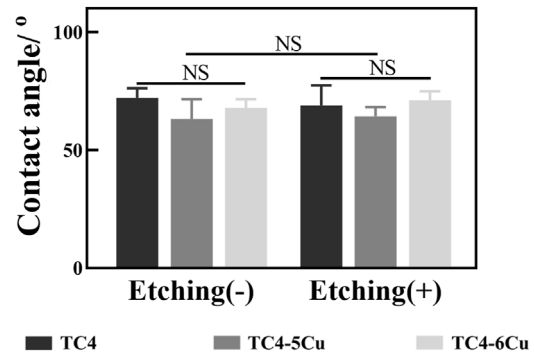

FIGURE 3
Contact angle of samples (n = 10, NS: No significant difference).

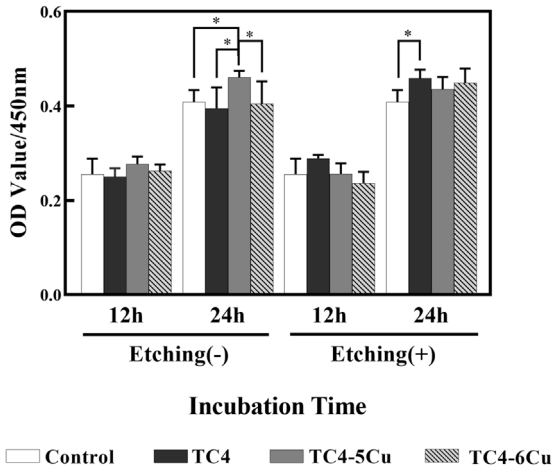

FIGURE 4
Cell proliferation of RAW 264.7 cells cultured in different alloy extracts for 12 and 24 h (n = 5, *p < 0.05)

extract increased. At the time of 12h, there is no difference between groups among unetched alloy groups. At the time of 24 h, the absorbance of the TC4-5Cu group is significantly higher than that of other groups ($p < 0.05$) among unetched groups; the absorbance of the ETC4 group is higher than that of the control group ($p < 0.05$). The relative growth rates (RGR) of RAW 264.7 cells in different alloy extracts are shown in Table 2. The cell toxicity grade (CTG) is obtained according to the standard United States Pharmacopeia. From 12 to 24 h of incubation, all the experimental groups show grades 0 to 1 (no toxicity).

3.3.2 Cell adhesion

Figure 5A shows the adhesion of RAW 264.7 macrophages cultured on different alloy samples for 24 h. Red fluorescence represents F-actin, and blue fluorescence represents the nucleus. Compared with the TC4-5Cu group, the numbers of RAW 264.7 cells in TC4-6Cu are higher. It could be seen that compared with all unetched groups and the ETC4 group, the numbers of RAW 264.7 cells in ETC4-5Cu and ETC4-6Cu groups are higher, and the areas of the red stained cytoskeleton of RAW 264.7 cells are also larger, that indicated that the morphology of RAW 264.7 cells is also more extended (Figure 5A).

TABLE 2 Relative growth rate (RGR) and cytotoxicity level at different detection periods.

		12 h		24 h	
		RGR	grade	RGR	grade
Before etching	TC4	97.96 ± 7.17	1	96.66 ± 10.90	1
	TC4-5Cu	108.70 ± 6.04	0	112.69 ± 3.36	0
	TC4-6Cu	102.77 ± 5.40	0	98.99 ± 11.65	0
After etching	TC4	113.13 ± 3.11	0	112.26 ± 4.41	1
	TC4-5Cu	100.40 ± 8.66	0	106.55 ± 6.32	1
	TC4-6Cu	92.72 ± 9.32	1	109.89 ± 7.47	1

3.3.3 Cell morphology

The morphology of RAW 264.7 cells cultured in all alloy extracts for 24 h is shown in Figure 6A. Red fluorescence stands for F-actin, and blue fluorescence represents the nucleus. The unactivated M0 phenotype macrophages are spherical-like. M1 phenotype macrophages are characterized by rounded-like shapes with extended spread area, while macrophages with M2 phenotype are usually elongated. After 24 h of inoculation, RAW 264.7 cells in extracts of all alloy samples expand pseudopodia and connect, while the cells incubated in different exact alloy samples show different morphology. Most RAW 264.7 cells are activated in etched groups, showing M1 or M2 phenotype, and generally showing elongated spindle shape with an obvious extension of filamentous pseudopodia. However, in unetched groups, RAW 264.7 macrophages show round structure in almost all alloy extracts except TC4-6Cu alloy. The extension of RAW 264.7 cells is more obvious in the ETC4-5Cu and ETC4-6Cu groups than in the ETC4 group (Figure 6A).

3.3.4 M1/M2 phenotype of macrophages

Figure 7A,B shows the expression of M1-type marker CD86 and M2-type marker CD206 in RAW 264.7 cells cultured on the surface of different alloy samples for 12 and 24 h. After 12 h culture (Figure 7A), the expression of CD86 in TC4 alloy, TC4-5Cu alloy, and TC4-6Cu alloy increased by 2.26%, 2.54%, and 4.73%, respectively, and the expression of

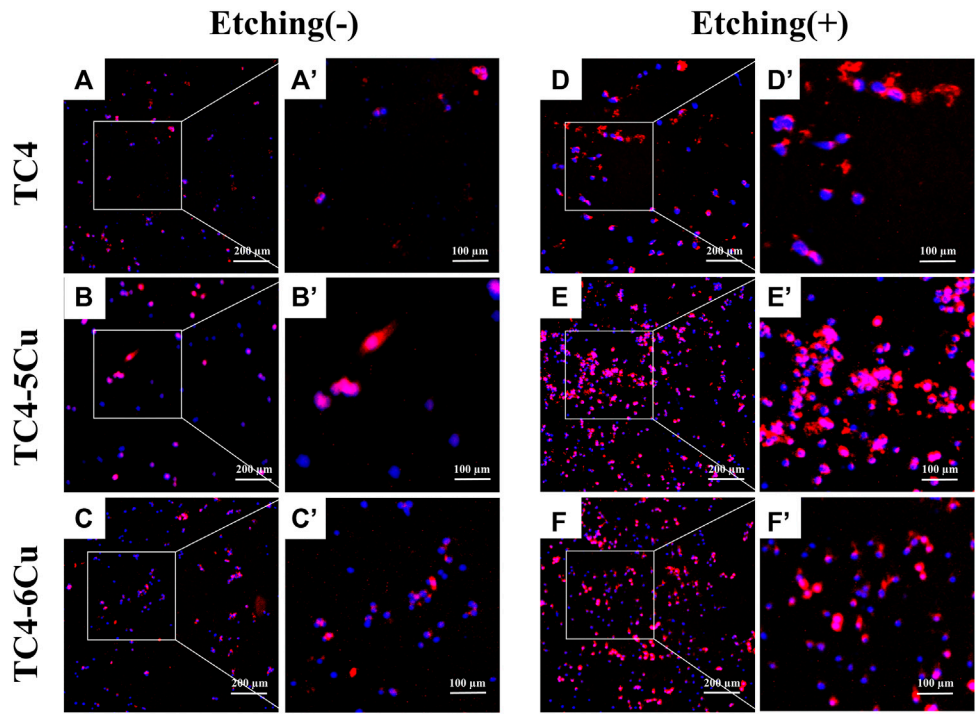

FIGURE 5
Cell adhesion of RAW 264.7 cells cultured on the surface of different alloys for 24 h. **(a′–f′)** is a partial enlargement of the selected area of **(A–F)**.

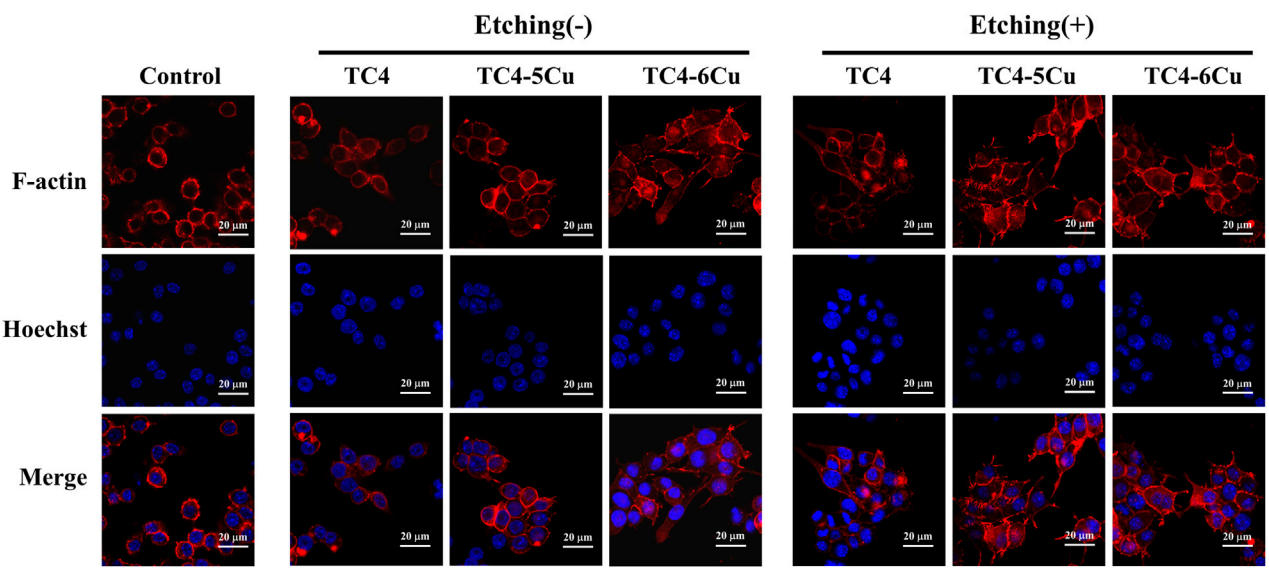

FIGURE 6
Morphology of RAW 264.7 cells cultured in different alloy extracts for 24 h.

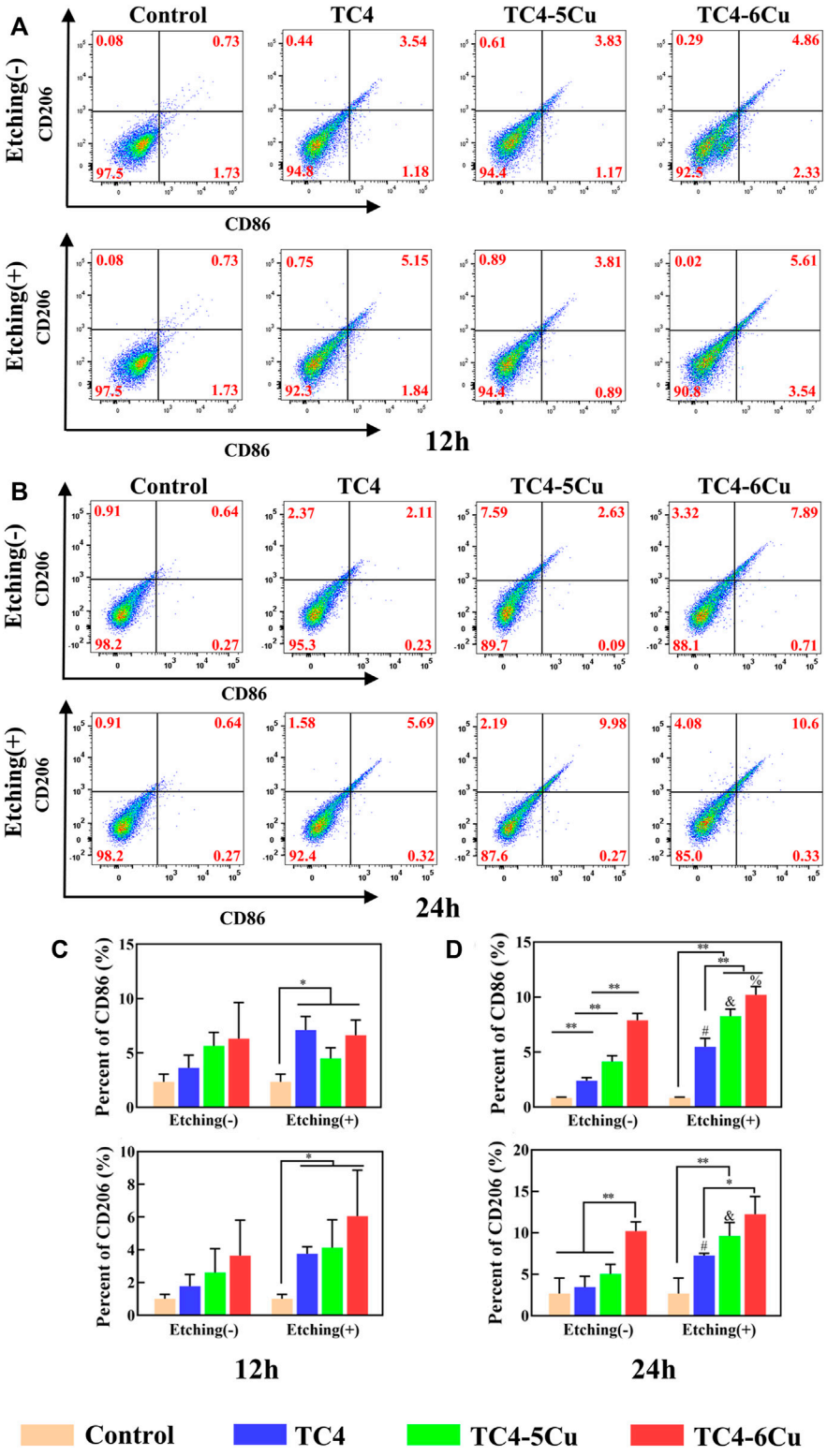

FIGURE 7
Flow cytometry analysis of RAW 264.7 cell surface markers cultured in different alloy extracts for 12 and 24 h **(A,C)** Expression of CD86 and CD206 in different alloy extracts for 12 h; **(B,D)** expression of CD86 and CD206 in different alloy extracts for 24 h (NS: No significant difference; *$p < 0.05$; **$p < 0.01$; #, compared with TC4 alloy, $p < 0.05$; and, compared with TC4-5Cu alloy, $p < 0.05$; %, compared with TC4-6Cu alloy, $p < 0.05$)

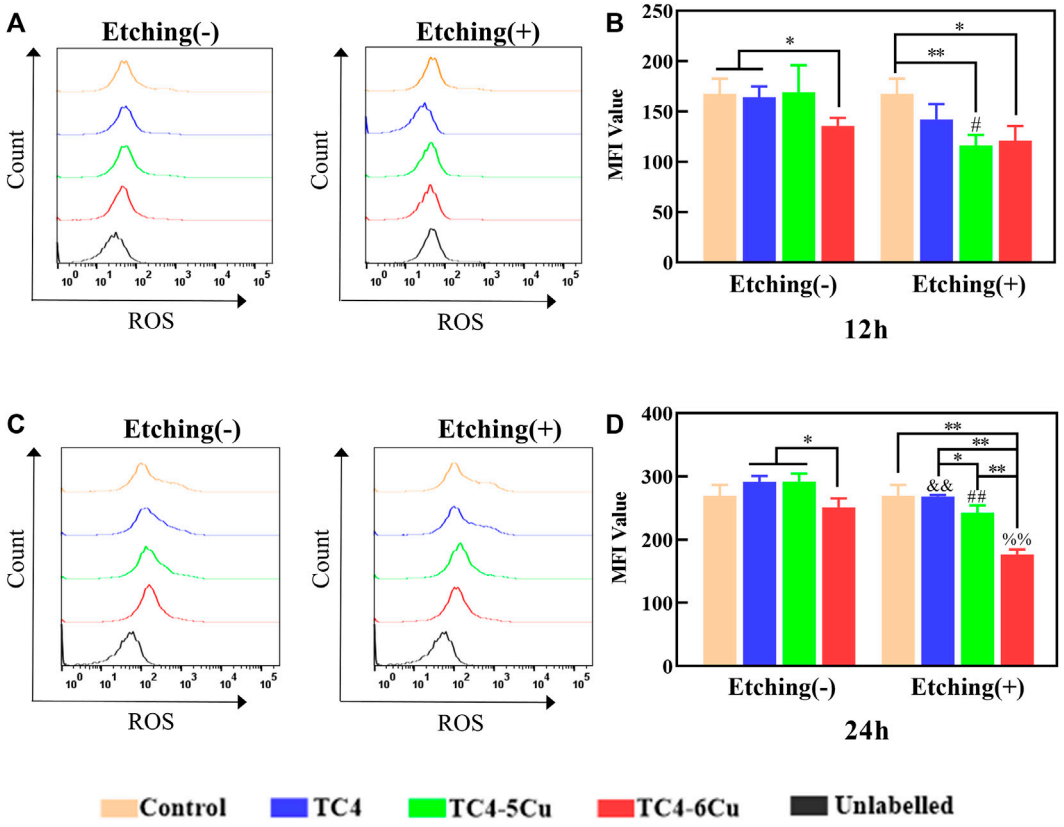

FIGURE 8
Flow cytometry analysis of intracellular ROS levels on RAW 264.7 cells in different material extracts for 12 and 24 h. **(A,C)** Expression of ROS in different alloy groups for 12 and 24 h; **(B,D)** quantification of mean fluorescence intensity (MFI) of intracellular ROS level in different alloy groups for 12 and 24 h (n = 3, NS: No significant difference; *$p < 0.05$; **$p < 0.01$; and, compared with TC4 alloy, $p < 0.01$; ##, compared with TC4-5Cu alloy, $p < 0.01$; %%, compared with TC4-6Cu alloys, $p < 0.01$)

CD206 increased by 3.17%, 3.63%, and 4.34% compared with the control group, respectively. The CD86 marker of ETC4 alloy, ETC4-5Cu alloy, and ETC4-6Cu alloy increased by 4.53%, 2.24%, and 6.69%, respectively, and the CD206 marker of ETC4 alloy, ETC4-5Cu alloy, and ETC4-6Cu alloy increased by 5.09%, 3.89%, and 4.82% compared with the control group, respectively. After 24 h of culture (Figure 7B), the expression of CD86 in TC4 alloy, TC4-5Cu alloy, and TC4-6Cu alloy increased by 1.43%, 1.81%, and 7.69%, and the expression of CD206 increased by 2.93%, 8.67%, and 9.66% compared with the control group, respectively. The expression of CD86 of ETC4 alloy, ETC4-5Cu alloy, and ETC4-6Cu alloy increased by 5.1%, 9.34%, and 10.02%, and the expression of CD206 of ETC4 alloy, ETC4-5Cu alloy, and ETC4-6Cu alloy increased by 5.72%, 10.62%, and 13.13% compared with the control group, respectively.

Statistical analysis results display that after 12 h of culture (Figure 7C), there is no significant difference in CD86 and CD206 expression between unetched alloy groups and the control group, but the expression levels of CD86 and CD206 of etched alloy groups are significantly higher than those of the control group ($p < 0.05$). After 24 h (Figure 7D), the expression levels of CD86 and CD206 in the ETC4, ETC4-5Cu, and ETC4-6Cu groups increase compare to the TC4, TC4-5Cu and TC4-6Cu groups ($p < 0.05$), indicating that acid etching could increase the expression of CD86 and CD206. The expression of CD86 in the TC4-6Cu, TC4-5Cu, and TC4 group decreases gradually ($p < 0.05$), and the expression of CD206 in the TC4-6Cu group is significantly higher than that of the TC4 group ($p < 0.05$), indicating that Cu-bearing titanium alloy could increase the expression of CD86 and CD206. The expression of CD86 of ETC4-5Cu and ETC4-6Cu groups is significantly higher than that of the ETC4 group ($p < 0.01$), and the expression of CD206 of ETC4-6Cu alloy is significantly higher than that of ETC4 alloy ($p < 0.05$).

3.3.5 Intracellular reactive oxygen species level

Flow cytometry is used to detect the ROS expression of RAW 264.7 cells cultured in different alloy sample extracts for 12 and 24 h (Figure 8). After 12 h, the ROS level in ETC4-5Cu is significantly lower than that of the TC4-5Cu group ($p < 0.05$).

The ROS level of TC4-6Cu alloy is significantly lower than that of the control group and TC4 group ($p < 0.01$); the ROS levels of ETC4-5Cu alloy ($p < 0.01$) and ETC4-6Cu alloy ($p < 0.05$) are significantly lower than those of the control group. After 24 h, the ROS level in etched groups is significantly lower than that of unetched groups ($p < 0.01$). The ROS level of TC4-6Cu alloy is significantly lower than that of TC4 alloy and TC4-5Cu alloy ($p < 0.05$); the ROS level of the ETC4-6Cu group is significantly lower than that of other etched groups ($p < 0.01$), and the ROS level of ETC4-5Cu alloy is significantly lower than that of ETC4 alloy ($p < 0.05$).

4 Discussion

The 3D printing technology used in this study is selective laser melting (SLM), which creates solid models by adding powder layer by layer. Laser power, scanning speed, scanning spacing, and single layer thickness are the major parameters in the process of selective laser melting. Different laser processing parameters were compared, and the optimal parameters were selected in this study: laser power of 260 W, scanning distance of 45 μm, and laser spot diameter of 70 μm. Physical and chemical characteristics of implant material surfaces, such as surface morphology and hydrophilicity, can play a crucial role in the process of bone integration (Smeets et al., 2016). Copper, as an essential trace mineral for human beings, has been proven to have excellent antibacterial properties and has been widely used in titanium alloy–related studies (Fan et al., 2022). In this study, TC4-5Cu alloy and TC4-6Cu alloy were made by adding different content of copper into TC4 alloy using 3D printing technology, and the printed alloys were treated by a traditional acid etching technique.

The ratio of HF, HNO_3, and H_2O used in acid etching treatment and the acid etching duration all affect the surface morphology of TC4 alloy, and the etching duration is particularly important. It is reported that hydrophilic surfaces with lower contact angles are more conducive to cell attachment and proliferation (Rupp et al., 2017). It was found that the hydrophilicity was not significantly affected by acid etching (Figure 3). Therefore, the differences in cell growth and attachment between groups were not related to their hydrophilicity. In addition to hydrophilicity, the release of metal ions may also affect cell proliferation and adhesion (Lai et al., 2020). Acid etching may generate increased immersion of copper ions that could affect cell proliferation and adhesion. In a previous study, it was shown that etched TC4 alloy surface in HF-HNO3 solution may lead to selective dissolution of α-phase and selective enrichment of β-phase on the alloy surface (Sittig et al., 1999). In addition, acid etching treatment could also clean pollution particles on the surface of TC4 alloy (Yi et al., 2022).

This study prepared alloy extracts from TC4, TC4-5Cu, and TC4-6Cu alloys ETC4, ETC4-5Cu, and ETC4-6Cu alloys according to ISO10993-12. The copper element in the alloy was gradually dissolved and released into the medium, thus affecting the biological behavior of macrophages in the material alloy extracts. However, high doses of copper can lead to formation of free radicals and induce cytotoxicity by causing chromosome and DNA damage (Sharma et al., 2021). In this study, the CCK-8 test showed that Cu-bearing titanium alloys (TC4-5Cu alloy and TC4-6Cu alloy) had no effect on the viability of RAW 264.7 cells compared with the TC4 alloy, and all Cu-bearing TC4 alloy samples had no cytotoxicity (Figure 4). Therefore, Cu-bearing titanium alloys could be used as long-term implantation materials. In addition, acid etching treatment did not affect the cell viability of various alloys and proven to have no cytotoxicity.

In this study, the adhesion of RAW 264.7 cells on the surface of alloy materials was observed by staining. The results showed that RAW 264.7 cells could attach and extend well on the surface of all alloy samples after 24 h incubation (Figure 5). Meanwhile, compared with the surface of the TC4 alloy, the surface of Cu-bearing titanium alloys (TC4-5Cu alloy and TC4-6Cu alloy) is beneficial for the adhesion of RAW 264.7 macrophages (Figure 5). The surface of TC4-6Cu alloy shows better cell adhesion ability than that of TC4-5Cu alloy. The possible reasons are as follows: 1) with the increase of copper content, the porosity of TC4 alloy also increases, and the surface area of Cu-bearing titanium alloy and cells also increases correspondingly, which improves the ability of cell adhesion; 2) Protein adsorption is the prerequisite for cell adhesion to biomaterials (Yang et al., 2021), and the hydrophilic surface of Cu-bearing titanium alloy may promote protein adsorption. The possible reasons are as follows: 1) with the increase of copper content, the porosity of TC4 alloy also increases, and the surface area of Cu-bearing titanium alloy and cells also increases correspondingly, which improves the ability of cell adhesion; 2) protein adsorption is the prerequisite for cell adhesion to biomaterials (Yang et al., 2021), and the hydrophilic surface of Cu-bearing titanium alloy may promote protein adsorption. The etched alloy samples showed stronger cell adhesion to RAW 264.7 cells than that of unetched alloy samples (Figure 5). The reasons may be as follows: 1) acid etching treatment improves the surface morphology of the alloy, and micro-porous structures, which were observed by SEM (Figure 2B), could increase the surface area of material alloys and immerse more copper ions to promote cell adhesion; 2) acid etching treatment can clean the pollution particles on the surface of TC4 alloy, which is more conducive to the growth of cells.

Confocal microscopy was used to observe the cell morphology of RAW 264.7 cells in different alloy extracts. Macrophages can polarize into different phenotypes to perform different functions. The shapes of polarized macrophages are different. M1-type macrophages are generally “fried egg-shaped” and M2-type macrophages were mostly long spindle-shaped (McWhorter et al., 2013). In this study, the RAW

264.7 cells cultured in etched sample extracts for 24 h are activated and show the structural features of the M2 phenotype, including elongated spindle shape and filamentous pseudopodia; while the cell structures of unetched groups are mostly round. (Figure 6). In addition, RAW 264.7 cells in etched Cu-bearing titanium alloy groups (ETC4-5Cu alloy and ETC4-6Cu alloy) have more obvious filamentous pseudopod extension and interconnection. (Figure 6).

The observed macrophage surface marker proteins were detected by flow cytometry in different groups. The results showed that the expression of M1-type surface marker CD86 and M2-type surface marker CD206 was increased in Cu-bearing titanium alloy groups, indicating that copper in Cu-containing titanium alloys could promote the polarization of macrophages. Compared with the same alloy before and after acid etching, CD86 and CD206 in etched groups were significantly higher than those in unetched groups, indicating that etching treatment could promote the polarization of macrophages (Figure 7).

The production of reactive oxygen species (ROS) is the core of inflammatory response in the early implantation stage. Oxidative stress occurs when ROS levels exceed the antioxidant defenses in cells, leading to irreversible intracellular damage (Schieber and Chandel, 2014). In the production process of 3D printed medical titanium alloy, partially melted or un-melted powder may remain on the surface of the materials and may lead to residual particle pollution and ROS generation in the adhesion cells. In this study, RAW 264.7 cells were cultured in the alloy sample extracts to detect the ROS production level. The results showed that at the time of 24 h, ROS levels in all etched alloy groups were significantly reduced compared with those in unetched alloy groups (Figure 8). The possible reason is that the acid etching treatment cleans the residual particles on the surface of the alloy. The ROS level in ETC4-5Cu and ETC4-6Cu alloy groups is obviously lower than that of other groups. The ROS level in the TC4-6Cu alloy group is lower than that of TC4-5Cu, and the ROS level in the ETC4-6Cu alloy group is lower than that of the ETC4-5Cu alloy group. With the increase in copper content, the ROS levels decreased. These results suggest that ROS production may be closely related to phenotype switching of macrophages, and ROS production may promote the M1-type macrophage polarization.

Macrophages are considered to be one of the earliest cells reaching the surface of the implant. The appropriate inflammatory reaction between the macrophage and implant is beneficial for the success of implantation (Franz et al., 2011). Macrophages polarize into M1 type (classical activation type) or M2 type (alternative activation type), expressing different functional programs according to different micro-environmental signals (Linares et al., 2016). M1 macrophages mainly exist in the early stage of inflammation and act as pro-inflammatory cells to spread the inflammatory response to downstream immune cells. M2 macrophages mainly contribute to stopping inflammation and promoting tissue repair and wound healing. It was reported that M1-type macrophages are dominant in the failed tissues surrounding implants, while M2-type macrophages are dominant in the normal tissues surrounding implants by Tazzyman et al. (Tazzyman et al., 2013). In this study, the etched alloy surfaces with lower ROS levels could promote macrophages to polarize to the M2-type phenotype, thus contributing to the increase in the success rate of implant implantation. This may be caused by acid etching treatment which makes the surface of the material form a microporous structure and more copper-element can be precipitated from the copper-bearing titanium alloy. The copper element can activate macrophages and tends to polarize macrophages to M2-phenotype.

However, the polarization of macrophages on different Cu-bearing alloy surfaces is not only closely related to ROS levels but also affected by the levels of many inflammatory factors. Therefore, the relevant inflammatory factors on RNA and protein levels need further exploration in the following experiments.

5 Conclusion

All samples had no toxicity to RAW 264.7 cells. With the increase of copper content, the adhesion ability of cells on the surface of the material was enhanced. Adding copper to TC4 alloys could activate the polarization of macrophages on the surface of TC4 alloy and reduce the ROS level. Surface treatment by acid etching had no effect on the hydrophilicity of the alloy surface. Acid etching treatment also could enhance cell adhesion, activate macrophage polarization, and reduce ROS levels. The *in vitro* experiments of this study indicated that acid-etched 3D printed copper-bearing titanium alloy could promote the adhesion and polarization of macrophages and provide a promising implant material for the treatment of peri-implant inflammation.

Data availability statement

The original contributions presented in the study are included in the article/Supplementary Material; further inquiries can be directed to the corresponding authors.

Author contributions

BL and HK contributed to the conception and design of the study. QW designed and prepared the materials. JY performed

the experiments and wrote the manuscript. HK helped perform the analysis with constructive discussion. WH polished the language of the article. All authors have read and approved the final version of the manuscript.

Funding

This study was financially supported by the Natural Science Foundation Project of Liaoning Province (Nos. 2020-MS-150 and 2018225059) and Guangxi Key Laboratory of the Rehabilitation and Reconstruction for Oral and Maxillofacial Research Funded Project (No. GXKLRROM2107).

Conflict of interest

The authors declare that the research was conducted in the absence of any commercial or financial relationships that could be construed as a potential conflict of interest.

Publisher's note

References

Carter, S.-S. D., Costa, P. F., Vaquette, C., Ivanovski, S., Hutmacher, D. W., Malda, J., et al. (2017). Additive biomanufacturing: an advanced approach for periodontal tissue regeneration. *Ann. Biomed. Eng.* 45 (1), 12–22. doi:10.1007/s10439-016-1687-2

Chen, X., Li, H. S., Yin, Y., Feng, Y., and Tan, X. W. (2015). Macrophage proinflammatory response to the titanium alloy equipment in dental implantation. *Genet. Mol. Res.* 14 (3), 9155–9162. doi:10.4238/2015.August.7.25

Dawood, A., Marti, B. M., Sauret-Jackson, V., and Darwood, A. (2015). 3D printing in dentistry. *Br. Dent. J.* 219 (11), 521–529. doi:10.1038/sj.bdj.2015.914

Fan, D.-Y., Yi, Z., Feng, X., Tian, W.-Z., Xu, D.-K., Cristino Valentino, A. M., et al. (2022). Antibacterial property of a gradient Cu-bearing titanium alloy by laser additive manufacturing. *Rare Met.* 41 (2), 580–593. doi:10.1007/s12598-021-01826-w

Franz, S., Rammelt, S., Scharnweber, D., and Simon, J. C. (2011). Immune responses to implants - a review of the implications for the design of immunomodulatory biomaterials. *Biomaterials* 32 (28), 6692–6709. doi:10.1016/j.biomaterials.2011.05.078

Huang, Q., Ouyang, Z., Tan, Y., Wu, H., and Liu, Y. (2019). Activating macrophages for enhanced osteogenic and bactericidal performance by Cu ion release from micro/nano-topographical coating on a titanium substrate. *Acta Biomater.* 100, 415–426. doi:10.1016/j.actbio.2019.09.030

Javaid, M., and Haleem, A. (2019). Current status and applications of additive manufacturing in dentistry: a literature-based review. *J. oral Biol. craniofacial Res.* 9 (3), 179–185. doi:10.1016/j.jobcr.2019.04.004

Lai, Y., Xu, Z., Chen, J., Zhou, R., and Cai, Y. (2020). Biofunctionalization of microgroove surfaces with antibacterial nanocoatings. *BioMed Res. Int.* 2020, 1–13. doi:10.1155/2020/8387574

Linares, J., Fernandez, A. B., Feito, M. J., Matesanz, M. C., Sanchez-Salcedo, S., Arcos, D., et al. (2016). Effects of nanocrystalline hydroxyapatites on macrophage polarization. *J. Mat. Chem. B* 4 (11), 1951–1959. doi:10.1039/c6tb00014b

Liu, Z., Liu, Y., Liu, S., Wang, D., Yi, Z., Sun, L., et al. (2021). The effects of TiO_2 nanotubes on the biocompatibility of 3D printed Cu-bearing TC4 alloy. *Mater. Des.* 207 (20), 109831. doi:10.1016/j.matdes.2021.109831

McWhorter, F. Y., Davis, C. T., and Liu, W. F. (2015). Physical and mechanical regulation of macrophage phenotype and function. *Cell. Mol. Life Sci.* 72 (7), 1303–1316. doi:10.1007/s00018-014-1796-8

McWhorter, F. Y., Wang, T., Phoebe, N., Thanh, C., and Liu, W. F. (2013). Modulation of macrophage phenotype by cell shape. *Proc. Natl. Acad. Sci. U. S. A.* 110 (43), 17253–17258. doi:10.1073/pnas.1308887110

Mittal, M., Siddiqui, M. R., Tran, K., Reddy, S. P., and Malik, A. B. (2014). Reactive oxygen species in inflammation and tissue injury. *Antioxidants Redox Signal.* 20 (7), 1126–1167. doi:10.1089/ars.2012.5149

Olivares-Navarrete, R., Hyzy, S. L., Slosar, P. J., Schneider, J. M., Schwartz, Z., Boyan, B. D., et al. (2015). Implant materials generate different peri-implant inflammatory factors. *Spine* 40 (6), 399–404. doi:10.1097/brs.0000000000000778

Palaskar, J., Nadgir, D. V., and Shah, I. (2010). Effect of recasting of nickel: chromium alloy on its castability. *J. Indian Prosthodont. Soc.* 10 (3), 160–164. doi:10.1007/s13191-010-0033-x

Rendra, E., Riabov, V., Mossel, D. M., Sevastyanova, T., Harmsen, M. C., Kzhyshkowska, J., et al. (2019). Reactive oxygen species (ROS) in macrophage activation and function in diabetes. *Immunobiology* 224 (2), 242–253. doi:10.1016/j.imbio.2018.11.010

Rupp, F., Liang, L., Geis-Gerstorfer, J., Scheideler, L., and Hüttig, F. (2017). Surface characteristics of dental implants: a review. *Dent. Mater. official Publ. Acad. Dent. Mater.* 34. doi:10.1016/j.dental.2017.09.007

Schieber, M., and Chandel, N. S. (2014). ROS function in redox signaling and oxidative stress. *Curr. Biol.* 24 (10), R453–R462. doi:10.1016/j.cub.2014.03.034

Sharma, P., Goyal, D., Baranwal, M., and Chudasama, B. (2021). Oxidative stress induced cytotoxicity of colloidal copper nanoparticles on RAW 264.7 macrophage cell line. *J. Nanosci. Nanotechnol.* 21 (10), 5066–5074. doi:10.1166/jnn.2021.19365

Sittig, C., Textor, M., Spencer, N. D., Wieland, M., and Vallotton, P. H. (1999). Surface characterization of implant materials c.p. Ti, Ti-6Al-7Nb and Ti-6Al-4V with different pretreatments. *J. Mat. Sci. Mat. Med.* 10 (1), 35–46. doi:10.1023/a:1008840026907

Smeets, R., Stadlinger, B., Schwarz, F., Beck-Broichsitter, B., Jung, O., Precht, C., et al. (2016). Impact of dental implant surface modifications on osseointegration. *Biomed Res. Int.* 2016, 6285620. doi:10.1155/2016/6285620

Spriano, S., Yamaguchi, S., Baino, F., and Ferraris, S. (2018). A critical review of multifunctional titanium surfaces: new frontiers for improving osseointegration and host response, avoiding bacteria contamination. *Acta Biomater.* 79, 1–22. doi:10.1016/j.actbio.2018.08.013

Sun, Y., Li, Y., Wu, B., Wang, J., Lu, X., Qu, S., et al. (2017). Biological responses to M13 bacteriophage modified titanium surfaces *in vitro*. *Acta Biomater.* 58, 527–538. doi:10.1016/j.actbio.2017.06.019

Tazzyman, S., Niaz, H., and Murdoch, C. (2013). Neutrophil-mediated tumour angiogenesis: subversion of immune responses to promote tumour growth. *Seminars Cancer Biol.* 23 (3), 149–158. doi:10.1016/j.semcancer.2013.02.003

Yang, J., Qin, H., Chai, Y., Zhang, P., Chen, Y., Yang, K., et al. (2021). Molecular mechanisms of osteogenesis and antibacterial activity of Cu-bearing Ti alloy in a bone defect model with infection *in vivo*. *J. Orthop. Transl.* 27, 77–89. doi:10.1016/j.jot.2020.10.004

Yi, Z., Liu, Y., Ma, Y., Liu, Z., Sun, H., Zhou, X., et al. (2022). Surface treatment of 3D printed Cu-bearing Ti alloy scaffolds for application in tissue engineering. *Mater. Des.* 213, 110350. doi:10.1016/j.matdes.2021.110350

Zhang, B., Liu, Y., Lan, X., Xu, X., Zhang, X., Li, X., et al. (2018). Oral *Escherichia coli* expressing IL-35 meliorates experimental colitis in mice. *J. Transl. Med.* 16, 71. doi:10.1186/s12967-018-1441-7

Zhang, E., Ren, J., Li, S., Yang, L., and Qin, G. (2016). Optimization of mechanical properties, biocorrosion properties and antibacterial properties of as-cast Ti-Cu alloys. *Biomed. Mat.* 11 (6), 065001. doi:10.1088/1748-6041/11/6/065001

Zhou, Y., Que, K. T., Zhang, Z., Yi, Z. J., Zhao, P. X., You, Y., et al. (2018). Iron overloaded polarizes macrophage to proinflammation phenotype through ROS/acetyl-p53 pathway. *Cancer Med.* 7 (8), 4012–4022. doi:10.1002/cam4.1670

Zong, W., Zhang, S., Zhang, C., Ren, L., and Wang, Q. (2020). Design and characterization of selective laser-melted Ti6Al4V–5Cu alloy for dental implants. *Mater. Corros.* 71, 1697. doi:10.1002/maco.202011650

frontiers | Frontiers in Materials

TYPE Original Research
PUBLISHED 07 September 2022
DOI 10.3389/fmats.2022.992351

OPEN ACCESS

EDITED BY
Monireh Kouhi,
Isfahan University of Medical Sciences, Iran

REVIEWED BY
Liping Tong,
Shenzhen Institutes of Advanced Technology (CAS), China
Mosab Kaseem,
Sejong University, South Korea

*CORRESPONDENCE
Jiang Chen,
jiangchen@fjmu.edu.cn

†These authors have contributed equally to this work

SPECIALTY SECTION
This article was submitted to Biomaterials, a section of the journal Frontiers in Materials

RECEIVED 12 July 2022
ACCEPTED 05 August 2022
PUBLISHED 07 September 2022

CITATION
Su J, Xing X, Lin Y, Gao Y, Xing Y, Xu Z and Chen J (2022), In vitro physicochemical and biological properties of titanium alloy, zirconia, polyetheretherketone, and carbon fiber-reinforced polyetheretherketone. *Front. Mater.* 9:992351. doi: 10.3389/fmats.2022.992351

In vitro physicochemical and biological properties of titanium alloy, zirconia, polyetheretherketone, and carbon fiber-reinforced polyetheretherketone

Jingjing Su[1,2,3†], Xiaojie Xing[1,2,3†], Yanjun Lin[3†], Yuerong Gao[2], Yifeng Xing[3], Zhiqiang Xu[4] and Jiang Chen[5*]

[1]Fujian Key Laboratory of Oral Diseases, School and Hospital of Stomatology, Fujian Medical University, Fuzhou, China, [2]Fujian Provincial Engineering Research Center of Oral Biomaterial, School and Hospital of Stomatology, Fujian Medical University, Fuzhou, China, [3]Stomatological Key Lab of Fujian College and University, School and Hospital of Stomatology, Fujian Medical University, Fuzhou, China, [4]Department of Stomatology, Affiliated Hospital of Putian University, Putian, China, [5]School and Hospital of Stomatology, Fujian Medical University, Fuzhou, China

Implant repair is a common means to restore the normal function of the hard tissues (bone or teeth). At present, the commonly and potentially used implant materials include titanium alloy (Ti), zirconia (Zr), polyetheretherketone (PEEK), and 30% carbon fiber reinforced PEEK (CFR-PEEK). This study compares their physicochemical and biological properties, including surface morphology, contact angle, nano hardness, elastic modulus, and the impact on the proliferation and osteogenic differentiation of bone marrow mesenchyml stem cell. Additionally, the differences in bacteria adhesion rates among materials were compared. CFR-PEEK had the highest contact angle, followed by PEEK, Zr, and Ti. Zr had the highest nano hardness and modulus of elasticity, followed by Ti, CRF-PEEK, and PEEK. There was no statistically significant difference in cytotoxicity among materials based on the liquid extract test. However, the relative cell proliferation rate on the surface of CFR-PEEK was slightly lower than that of Ti and Zr. Moreover, alkaline phosphatase activity, extracellular matrix mineralization, and osteogenic gene expression with the Ti and Zr materials were higher than with the PEEK and CFR-PEEK materials at Day 7, and Zr showed the highest osteogenic gene expression level among materials at Day 14. Ti had the greatest number of bacterial colonies that adhered to it, followed by Zr, CFR-PEEK, and PEEK. While the mechanical properties of PEEK and CFR-PEEK were closer to bone tissue and their anti-adhesion effect against bacteria was better than those of Ti and Zr, modification methods are needed to improve the osteogenic properties of these biopolymers.

KEYWORDS

implant materials, physicochemical properties, osteogenic differentiation, bacterial adhesion, cytotoxicity

1 Introduction

Orthopedic and dental implant restoration is a common technique for patients with bone loss caused by trauma, cancer, inflammation, and congenital abnormalities (Qin et al., 2019). While metals and ceramics are often used in this field, their application has limitations. Specifically, in terms of mechanical properties, the "stress shielding" effect is caused by the significant difference in elastic modulus between titanium (Ti, 110 GPa), zirconia (Zr, 210 GPa), and bone tissue (13–18 GPa), leading to peri-implant bone resorption and even implant loss (Mishra and Chowdhary, 2019; Knaus et al., 2020). In terms of biological properties, tiny metal particles can be released from the implant's surface, causing aseptic inflammatory reactions (Sadowsky, 2020). Although Ti is an inert metal, sensitization and corrosion reactions still exist, and metal artifact reduction also influences the presence of peri-implant tissue (Sivaraman et al., 2018). Moreover, the silver-grey metal abutment impacts the visual aesthetics of implant restoration in patients with a thin-scalloped gingival biotype (Bathala et al., 2019). While ceramic material has biocompatibility and aesthetic advantages, its application remains restricted by its low fracture toughness and high brittleness (Yan et al., 2018).

Recently, biopolymers have attracted significant attention due to their unique physicochemical and biological properties. Polyetheretherketone (PEEK) is a polymer with one ketone and two ether bonds in its main chain structure, approved by the US Food and Drug Administration (FDA) as an implant material in orthopedics, cardiac and maxillofacial surgery, and cranioplasty (Zhang et al., 2019). In dentistry, PEEK is broadly used in prosthetics, implants, and orthodontics due to its good biocompatibility and high stability (Ma and Tang, 2014; Knaus et al., 2020). In addition, PEEK has an elastic modulus comparable to natural bone, effectively avoiding "stress shielding." Moreover, PEEK's color palette can match those of the teeth, and it is easy to process due to its good ductility (Khurshid et al., 2020; da Cruz et al., 2021).

While the mechanical properties of PEEK cannot meet the mechanical demands of dental implants, its mechanical strength can be improved by adding carbon fiber (Yu et al., 2020). Studies have shown that 30% carbon fiber-reinforced PEEK (CFR-PEEK) has improved elastic modulus and tensile strength compared with PEEK, with values closer to bone tissue or dentin (Fabris et al., 2022). Indeed, when CFR-PEEK and Ti were assessed using the finite element method (FEM) after compressive loading tests, the compressive strength of CFR-PEEK (450 N) completely met masticatory function requirements, with a maximal occlusal force of 140–170 N for anterior teeth and 250–400 N for posterior teeth (Lee et al., 2012). The biocompatible CFRPEEK combines the advantages of PEEK and carbon fiber, making it a promising new implant material (Hahnel et al., 2015; Li et al., 2015).

The mechanical properties and osseointegration of implants are the critical factors for the long-term stability of implant restorations (Cheng et al., 2018; Wang et al., 2021). Implant failure is often associated with bacterial adhesion to the implant's surface and subsequent biofilm formation (Blanco et al., 2021). While the performance of these implant materials has been studied previously, the biological responses of cells and bacteria to these biomaterials remain unclear (Hahnel et al., 2015; Peng et al., 2021; Rozeik et al., 2022). Therefore, this is the first study to evaluate and compare the physicochemical and biological properties of four implant materials: Ti, Zr, PEEK, and CFR-PEEK. In addition, it examines their surface properties and mechanical strength, their effects on viability and osteogenic differentiation of bone marrow mesenchymal stem cells (BMSCs), and their anti-adhesive properties against *Staphylococcus aureus (S. aureus)* and *Porphyromonas gingivalis (P. gingivalis)*.

2 Materials and methods

2.1 Sample preparation

Four implant materials: Ti (Ti6Al4V; Falcontech; Wuxi City, China), Zr (Wieland; Ulm, Germany), PEEK (Gehr; Mannheim, Germany), and 30% CFR-PEEK (Roeching; Mannheim, Germany) were cut into disc specimens with a diameter of 10 ± 0.1 mm and thickness of 2 ± 0.1 mm, then highly polished with silicon carbide abrasive paper (240-600-800 grit), ultrasonically cleaned with acetone, ethanol, deionized water, and sterilized at 121°C for 30 min.

2.2 Surface characterization

2.2.1 Morphology and roughness

Thermal-field emission scanning electron microscope (FE-SEM; Magellan 400; Phoenix, AZ, United States) was used to observe material morphology. The materials were sprayed with gold under a vacuum for 60 s before observation. The arithmetic means deviation of the surface (Ra) was obtained with a probe contact profiler (SEF 680; Kosaka Laboratory Ltd; Tokyo, Japan) over a measuring length of 4.0 mm by sampling a length of 0.8 mm at a scanning speed of 1.0 mm/s.

2.2.2 Contact angle

Hydrophilicity was evaluated at room temperature (RT) using a contact angle analyzer (OCA20; Dataphysics; Filderstadt, Germany). The initial orientation of the deionized water droplet was perpendicular to the sample, and the contact angle of 3 μL deionized water on the sample surface was measured for 10 s.

2.2.3 Nano hardness and elastic modulus

We used an experimental nanoindentation NHT2 instrument (Anton Paar; Buchs, Switzerland) with a Berkovich-type indenter, a load resolution of 50 nN, and a displacement resolution of 0.01 nm. The experimental loading process was performed as follows: the load control mode was used, and a constant loading rate of 30 mN/min was applied throughout the loading process until the load reached a maximum of 15 mN. The maximal load was held for 10 s to avoid the creep effect, then unloaded at the same rate until the indenter was entirely disengaged, and five points were measured.

2.3 In vitro biological performance

2.3.1 Cell culture

BMSCs were isolated from the bone marrow of 4-week-old male Sprague-Dawley rats (SPF class; Shanghai Laboratory Animal Center [SLAC]; Shanghai, China). This project was reviewed and approved by the ethics committee of Fujian Medical University (FJMU-2021073; Fuzhou, China). BMSCs were cultured in a low sugar Dulbecco's modified Eagle's medium (DMEM; Hyclone; Logan, UT, United States) with 10% fetal bovine serum (FBS; Hyclone), and 1% penicillin and streptomycin antimycotic (Hyclone) in a constant temperature incubator (37°C, 5% CO_2). The culture medium was renewed every 3 days, and cells of the third to fifth generation were used in all experiments.

2.3.2 Cell morphology

BMSCs were inoculated onto material samples in 24-well plates at a density of 5×10^4/well. After incubation for 24 h, samples were transferred to a new 24-well plate, rinsed twice with phosphate-buffered saline (PBS), and cells were fixed with 2.5% glutaraldehyde overnight at 4°C. Then, the samples were dehydrated in a graded ethanol series (30, 50, 70, 80, 90, 100%) for 10 min, dried in a critical point dryer, sputter-coated with gold, and observed with SEM (SUPRA 55; Zeiss; Oberkochen, Germany).

2.3.3 Cytotoxicity evaluation with extract and direct contact test

The extracted liquid of the material samples was obtained according to ISO 10993-12: 2021 with the medium surface area/volume of 3 cm^2/ml and incubated at 37 °C for 24 h. The BMSCs were seeded into 96-well plates and onto the samples at a density of 4×10^3/well and 2×10^4/well, respectively. After culturing for 24 h, the culture medium was replaced with liquid extracts in the experimental group and a fresh culture medium in the control group. DMEM containing 10% cell counting kit (CCK)-8 solution (Dojindo; Kumamoto, Japan) was added to each well on days 1, 3, and 5, and the optical density (OD) at 450 nm was obtained using a spectrophotometer (SpectraMax iD3; Molecular Devices; San Jose, CA, United States). The equation used to calculate the relative growth rate (RGR) was: RGR = OD of experimental group/OD of negative control group × 100%. Cytotoxicity was evaluated according to the toxicity grading method of US Pharmacopoeia (USP XXII, NF XVII, 1990).

2.3.4 Alkaline phosphatase activity

The BMSCs were seeded onto samples in 24-well plates at a density of 5×10^4/well. After culturing for 24 h, the medium was removed and replaced with an osteogenic medium (DMEM with 10% FBS, 1% β-glycerophosphate, 1% vitamin C, and 0.01% dexamethasone), and culturing continued for an additional 7 days. Then, cells were stained for ALP with the 5-bromo-4-chloro-3-indolyl-phosphate (BCIP)/nitro blue tetrazolium (NBT) color development kit (Beyotime; Haimen, China), and the samples were observed under a stereomicroscope (Stemi 508; Zeiss). Quantitative determination was performed using an ALP assay kit (Beyotime), and the OD of each culture was measured at 520 nm. Total protein content was determined using a bicinchoninic acid (BCA) assay kit (Beyotime). ALP activity is presented as King unit/g total protein.

2.3.5 Extracellular matrix mineralization

Fourteen days after BMSC osteogenic induction, the samples were washed with PBS and fixed with 4% paraformaldehyde (PFA) for 15 min. Samples were stained with Alizarin Red dye (ARS; pH = 6.6; Solarbio; Beijing, China) for 10 min at RT and observed under a stereomicroscope. Then, the adsorbed alizarin red dyes were dissolved in 10 mm sodium phosphate (pH 7.0) with 10% cetylpyridinium chloride (Boc Sciences; Shirley, NY, United States), and their absorbance was measured at 562 nm.

2.3.6 Real-time quantitative reverse transcription PCR analysis

Osteogenic-related gene expression was quantified using RT-qPCR. BMSCs were seeded onto material samples at 5×10^4/well and cultured in the osteogenic medium for 7 days. Total RNA was extracted with the TRIZOL reagent (Takara; Kusatsu, Japan) and reversely transcribed into complementary DNA (cDNA) according to the manufacturer's protocols. The cDNA was used as a PCR template to quantify the expression of biomineralization associated alkaline phosphatase (*Alpl*), type 1 collagen (*Col1a1*), runt-related transcription factor 2 (*Runx2*), osteocalcin (*Bglap*), osteopontin (*Spp1*), bone sialoprotein (*Ibsp*), and glyceraldehyde 3-phosphate dehydrogenase (*Gapdh*). The primers used are listed in Table 1.

TABLE 1 Primer sequences used for RT-qPCR.

Gene	Forward primer sequence (5′-3′)	Reverse primer sequence (5′-3′)
Gapdh	ACGGCAAGTTCAACGGCACAG	GAAGACGCCAGTAGACTCCACGAC
Alpl	CGTTTTCACGTTTGGTGGCT	ACCGTCCACCACCTTGTAAC
Col1a1	CGAGTATGGAAGCGAAGGTT	CTTGAGGTTGCCAGTCTGTT
Runx2	CAGATTACAGATCCCAGGCAGAC	AGGTGGCAGTGTCATCATCTGAA
Bglap	AATAGACTCCGGCGCTACCT	ATAGATGCGCTTGTAGGCGT
Spp1	GAGCAGTCCAAGGAGTATAAGC	AACTCGTGGCTCTGATGTTC
Ibsp	ACAACACTGCGTATGAAACCTATGAC	AGTAATAATCCTGACCCTCGTAGCC

2.4 Antibacterial activity

2.4.1 Bacteria culture

A frozen strain of *S. aureus* (ATCC25923; American Type Culture Collection [ATCC]; Manassas, VA, United States) was revived by aerobic culturing in Luria-Bertani (LB) medium (Hopebio; Qingdao, China) for 24 h, and a frozen strain of *P. gingivalis* (ATCC33277; ATCC) was revived by anaerobic culturing in the brain-heart infusion broth medium (BHI; Oxoid; Basingstoke, UK) containing 5 mg/L of hemins, 1 mg/L of vitamin K3, and 5% yeast extract for 48 h. The concentration of bacterial liquid was adjusted to 1×10^8 colony forming units (CFU)/mL based on absorbance at 600 nm.

2.4.2 Bacteria morphology

The samples were co-incubated with 1 ml of bacterial suspension at 37°C for 24 h. After removing the liquid medium, samples were rinsed with PBS and fixed with 2.5% glutaraldehyde at 4°C overnight. Then, samples were dehydrated and dried for 10 min with 30, 50, 70, 80, 90, 95, and 100% ethanol. The morphology and numbers of bacteria on the surface of the samples were observed by scanning electron microscopy (QUANTA 450; Field Electron and Ion Company [FEI]; Hillsboro, OR, United States).

2.4.3 CFU counting

100 μL of *S. aureus and P. gingivalis* suspension with a concentration of 1×10^8 CFU/ml were dripped onto material samples, and 1 ml of medium was added to the wells. After culturing for 24 h, the medium was discarded, and samples were washed twice with PBS to remove non-adhered bacteria. Then, adhered bacteria were collected using a vortex mixer. Aliquots of the bacterial suspension were diluted with PBS to ratios of 1:10, 1:100, 1:1,000, and 1:10,000. Each dilution was evenly coated onto an agar plate. *S. aureus and P. gingivalis* colonies were counted according to *ISO 7218:2007* after culturing for 24 and 48 h, respectively.

2.5 Statistical analysis

All the data are presented as mean ± standard deviations. Data were tested for normality (Shapiro-Wilk normality test) and variance homogeneity (Brown-Forsythe test) and analyzed with one-way analysis of variance (ANOVA) using the GraphPad Prism 9.0 software (GraphPad Software Inc.; San Diego, CA, United States). The following symbols are used to denote statistical significance in the graphs: *, $p < 0.05$; **, $p < 0.01$; ***, $p < 0.005$.

3 Results

3.1 Surface characterization

The disc-shaped samples of the four different implant materials are shown in Figure 1A. Representative FE-SEM images show that Ti and Zr had fewer scratches than PEEK and CFR-PEEK (Figure 1B). All tested samples had a similar surface roughness with a Ra of ~1.0 μM (Table 2), with no significant differences among groups ($p > 0.05$). Zr showed the highest nanohardness and elastic modulus value, followed by Ti, CFR-PEEK, and PEEK. PEEK had a significantly larger contact angle than the Ti and Zr groups, and its nanohardness and elastic modulus improved significantly with the addition of carbon fibers (Figure 1C; Table 2). However, the inhomogeneous distribution of carbon fibers caused fluctuations in nanohardness (Figure 1D).

3.2 Cell morphology

The morphology of BMSCs adhered to the Ti, Zr, PEEK, and CFR-PEEK samples are shown in Figure 2A. The cell distribution on each material was relatively uniform. While cells on the Ti, Zr, and PEEK showed expanded shapes with obvious pseudopodia, those on CFR-PEEK were smaller, spindle-shaped, or triangular, with relatively few pseudopods.

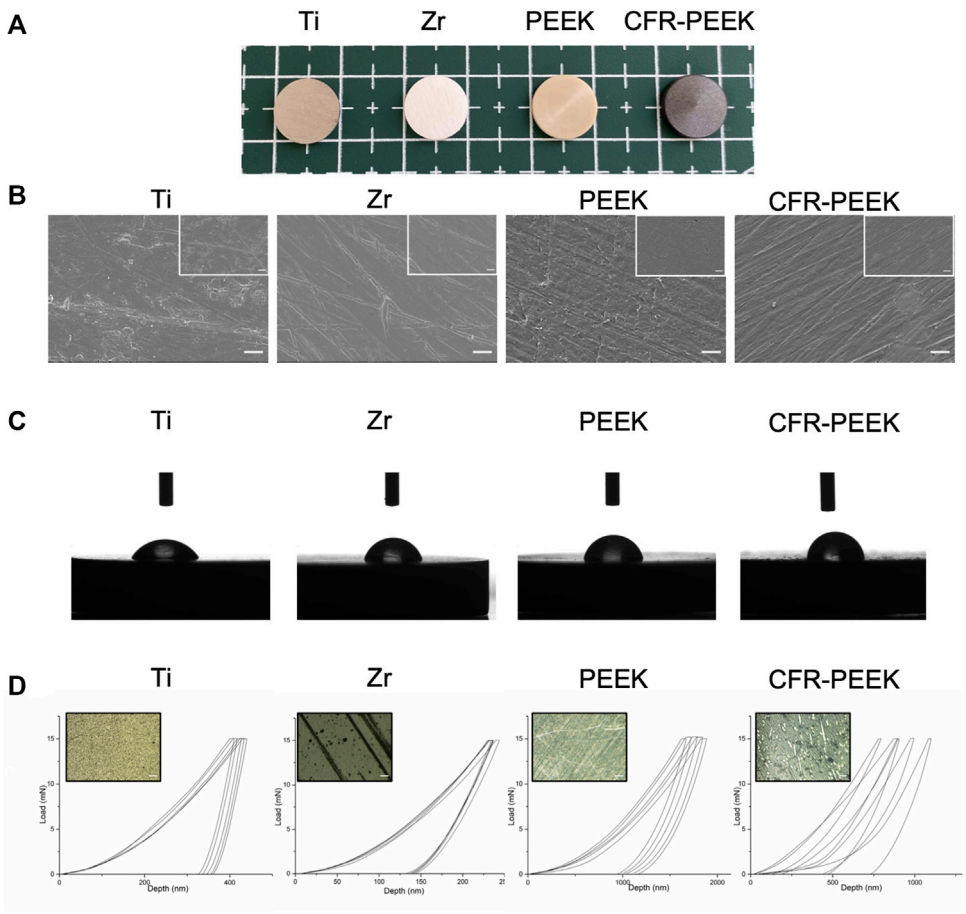

FIGURE 1
Surface characterization of four different implant materials. **(A)** Photographs of four different implant samples: Ti, Zr, PEEK, and CFR-PEEK. **(B)** FE-SEM images of Ti, Zr, PEEK, and CFR-PEEK samples under low and high magnifications (2000×, bar = 5 μM; 5,000×, bar = 2 μM). **(C)** The contact angle of different samples. **(D)** The load-displacement curves for different samples, where the upper-left image shows an optical microscope image (1,000×, bar = 10 μM) of the punctured area.

TABLE 2 Comparison of different materials (mean ± SD).

Group	Roughness (μm)	Contact angle (°)	Nano hardness (GPa)	Elastic modulus (GPa)
Ti	1.05 ± 0.07	65.68 ± 2.75	4.71 ± 0.27	133.17 ± 7.01
Zr	0.99 ± 0.04	77.36 ± 2.65	18.54 ± 0.19	250.50 ± 12.35
PEEK	1.04 ± 0.06	87.80 ± 4.70	0.29 ± 0.04	4.49 ± 0.25
CFR-PEEK	1.01 ± 0.06	97.75 ± 4.92	1.46 ± 0.70	13.20 ± 1.48

3.3 Cytotoxicity

Cytotoxicity did not differ significantly among groups at any time point ($p > 0.05$). The relative proliferation rates were all >95% in the liquid extract test (Figure 2B). In addition, there was no noticeable difference in BMSC proliferation rates on the Ti, Zr, and PEEK surfaces ($p > 0.05$; Figure 2C), while the rate on the CFR-PEEK surface was slightly lower than those of the Ti and Zr surfaces ($p < 0.05$) in the direct contact test.

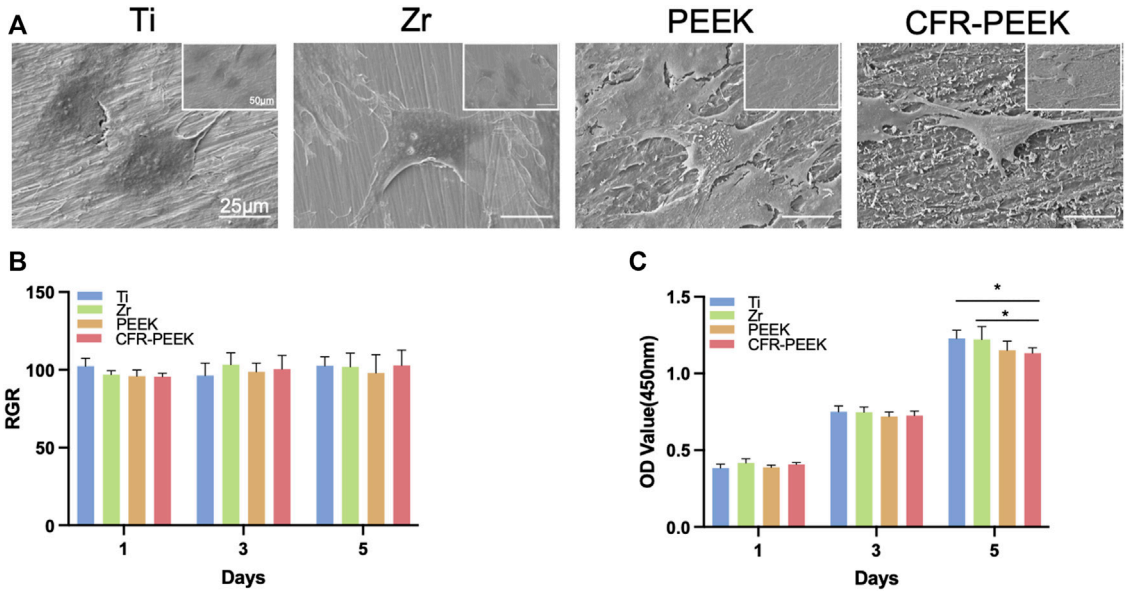

FIGURE 2
The morphology of BMSCs and cytotoxicity of four different implant materials. **(A)** SEM images of BMSCs adhered on Ti, Zr, PEEK, and CFR-PEEK materials at low and high magnifications (1,000×, bar = 25 μM; 500×, bar = 50 μM). **(B)** Cytotoxicity evaluation of the Ti, Zr, PEEK, and CFR-PEEK materials on days 1, 3, and 5 with the liquid extract test. **(C)** Cytotoxicity evaluation of the Ti, Zr, PEEK, and CFR-PEEK materials on days 1, 3, and 5 with the direct contact test. *$p < 0.05$.

3.4 ALP assay

The ALP staining images of BMSCs cultured on the different materials for 7 days are shown in Figure 3A. ALP activity was similar on Ti and Zr ($p > 0.05$), which were significantly higher than PEEK and CFR-PEEK ($p < 0.05$; Figure 3B).

3.5 ECM mineralization

The results of the ARS staining of BMSCs cultured on the different materials for 14 days are shown in Figure 3C. Zr had the greatest number of mineralization nodules, followed by Ti, PEEK, and CFR-PEEK, consistent with the quantitative analysis results (Figure 3D).

3.6 RT-qPCR

Relative gene expression levels in BMSCs cultured on the different materials for 7 and 14 days were shown in Figure 4. In the early stages of osteogenic differentiation, *Alpl* expression was consistent with the ALP activity assay. *Col1a1*, *Runx2*, and *Bglap* expression with Ti and Zr were significantly higher than with PEEK and CFR-PEEK (Figure 4A). Gene expression differences became more apparent among groups on day 14 (Figure 4B) and were highest with Zr.

3.7 Bacterial morphology and number

The morphology and the number of colonies of *S. aureus* and *P. gingivalis* adhered to Ti, Zr, PEEK, and CFR-PEEK are shown in Figure 5A. The morphology of *S. aureus* and *P. gingivalis* was typical of coccus and bacillus, respectively. The number of adhered bacteria was greatest with Ti, followed by Zr and CFR-PEEK, where bacteria were found in groups. A small number of bacteria was observed on PEEK, scattered across its surface.

3.8 CFU

The number of adhered *S. aureus* and *P. gingivalis* colonies was greatest on Ti, followed by Zr, CFR-PEEK, and PEEK ($p < 0.005$; Figures 5B–D).

4 Discussion

The surface and mechanical properties, biocompatibility, osteogenic ability, and antibacterial effect of four implant materials (Ti, Zr, PEEK, CFR-PEEK) were studied. The morphology, roughness, and wettability of biomaterials play essential roles in cell attachment and viability (Mehl et al., 2016). While PEEK and CFR-PEEK showed more textures

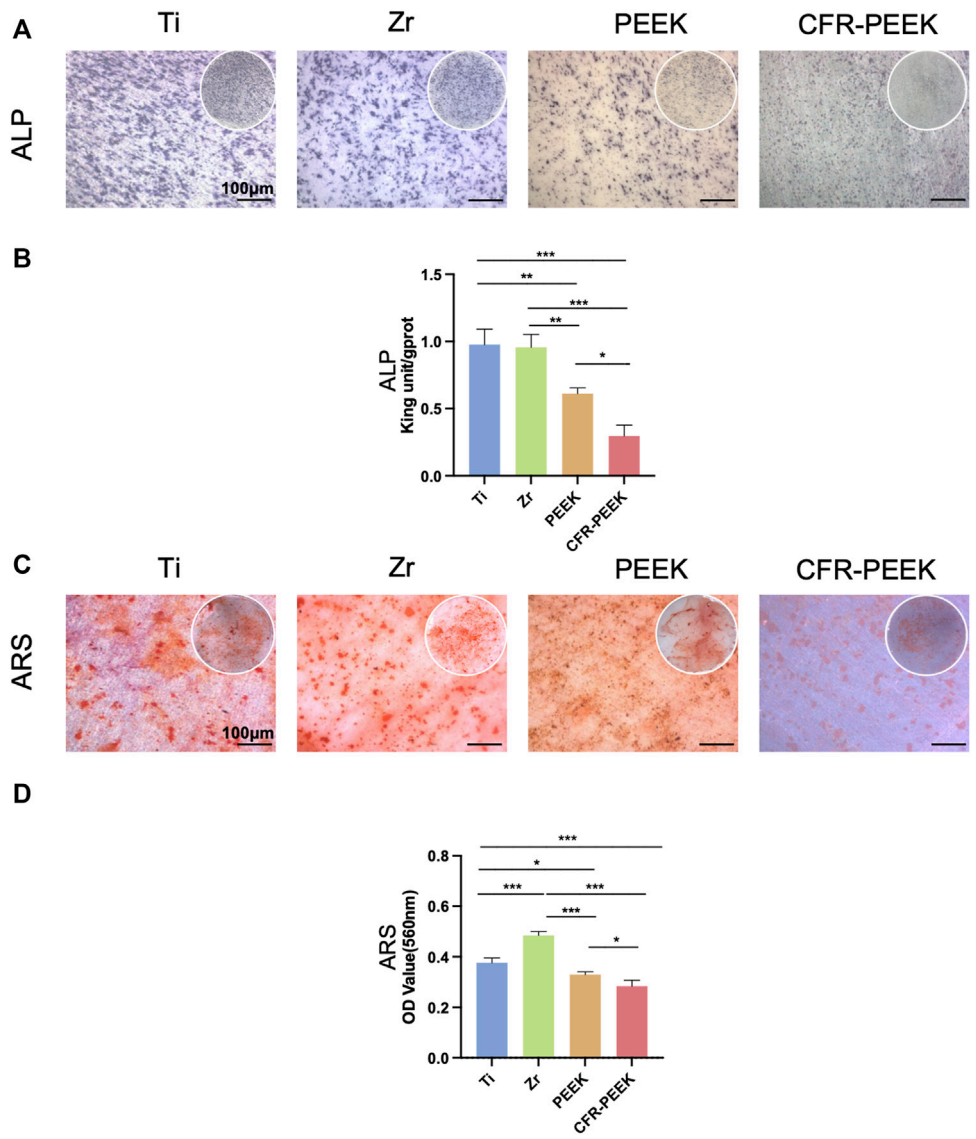

FIGURE 3
The ALP and ARS staining and quantification of four different implant materials. **(A)** ×25 magnification (bar = 100 μM) images of ALP staining of BMSCs cultured on Ti, Zr, PEEK, and CFR-PEEK for 7 days. **(B)** The quantitative ALP activity results of BMSCs on day 7. **(C)** Images of ARS staining of BMSCs cultured on the different materials for 14 days (25×, bar = 100 μM). **(D)** The quantitative ARS results for BMSCs on day 14. *$p < 0.05$; **$p < 0.01$; ***$p < 0.005$.

under SEM, there was no significant difference in the roughness among groups after polishing. The lower the water contact angle, the higher the material's hydrophilic properties (Lu et al., 2017). Ti showed the best wettability, followed by Zr, PEEK, and CFR-PEEK. This result may be due to the absence of polar functional groups on the surface of polymers (Peng et al., 2021). Moreover, the ideal mechanical property should benefit force distribution at the implant-bone interface (Ding et al., 2021), a suitable elastic modulus may promote the formation of new bone around the implant (Brizuela et al., 2019). Table 2 shows that the elastic modulus of PEEK (4.49 ± 0.25 GPa) and CFR-PEEK (13.20 ± 1.48 GPa) is closer to that of native bone tissue, which may avoid the stress shielding effect and enhance osseointegration (Fabris et al., 2022). Moreover, surface hardness is associated with resistance to force (Zhang et al., 2017). The hardness of trabecular and cortical bone lamellae in the human femur is between 0.234 and 0.760 GPa, which is close to that of alveolar bone (Zysset et al., 1999), and for native dentin is about 0.72 ± 0.10 GPa (Han et al., 2017). While the hardness of PEEK was significantly lower than Ti and Zr, it could be improved by the

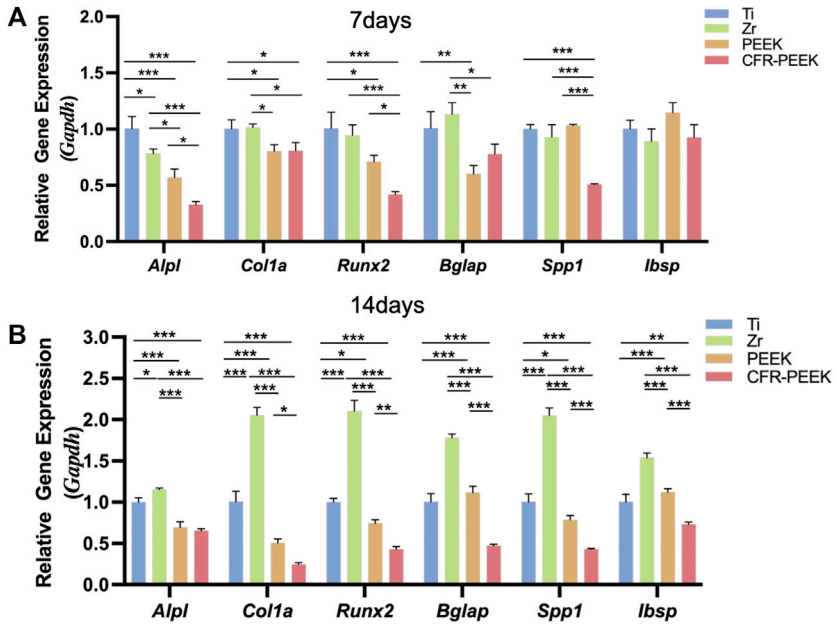

FIGURE 4
The osteogenic gene expression of four different implant materials. **(A)** The relative gene expression level of BMSCs cultured on Ti, Zr, PEEK, and CFR-PEEK for 7 days. **(B)** The relative gene expression level of BMSCs cultured on the different materials for 14 days. *$p < 0.05$; **$p < 0.01$; ***$p < 0.005$.

addition of carbon fiber, increasing to 1.46 ± 0.70 GPa for CFR-PEEK. Fabris et al. (2022) compared the tensile strength of PEEK and 30% CFR-PEEK, finding that the tensile strength of CFR-PEEK (217 MPa) was significantly higher than that of PEEK (115 MPa).

The morphology of BMSCs adhered to the surface of different materials was observed by SEM. The cells were evenly distributed and showed numerous filopodia with Ti, Zr, and PEEK, while CFR-PEEK showed weaker cell affinity, potentially related to its hydrophobicity (Jiao et al., 2021). Importantly, there were no significant differences in cytotoxicity among materials in the liquid extract test ($p > 0.05$), indicating good biocompatibility. However, the relative BMSC proliferation rate with CFR-PEEK first increased and then slightly decreased after 5 days in the direct contact test, but this reduction was not significant. There may be residues of nano-sized fiber debris resulting from the preparation of the carbon fibers, which adversely affects cell growth (Li et al., 2019). Qin et al. (2019) found a positive relationship between carbon fiber content and cytotoxicity. However, their long-term effects could be ignored.

This study evaluated the osteogenic differentiation of BMSCs cultured on the materials based on ALP activity, ARS staining, and qRT-PCR analysis. *Alpl*, *Col1a1*, and *Runx2* are primarily expressed in the early stages of osteoblasts differentiation, while mineralized nodules form, and *Bglap*, *Spp1*, and *Ibsp* are mainly expressed in the middle and late stages (Deng et al., 2015; Shalumon et al., 2018). The staining and RT-qPCR results showed that the osteogenic differentiation level with Ti and Zr was higher than with PEEK and CFR-PEEK on days 7 and 14.

Various surface properties, including morphology, hydrophilicity, and functional groups, influence the biological performance of biomaterials (Santoro et al., 2017). In previous studies, amorphous and smooth surfaces were more suitable for attachment and provided faster proliferation of osteoblast-like cells than highly crystalline surfaces (Sultana et al., 2017). PEEK and CFR-PEEK are semi-crystalline polymers containing both amorphous and crystalline phases owing to thermal processing, which may affect osteoblasts (Sagomonyants et al., 2008). Their hydrophilic surfaces also facilitate early blood contact, protein absorption, cell attachment, proliferation, differentiation, and bone regeneration (Hotchkiss et al., 2016). In this study, the CFR-PEEK was the most hydrophobic; water molecules could not form hydrogen bonds with the material's surface in the early stage, which is not conducive to protein adhesion in the later stage, leading to weak biological activity (Dubiel et al., 2011). High osteogenic gene expression with Zr on day 14 suggests that Zr could provide favorable conditions for cell mineralization (Lee et al., 2021). Based on the hydration and hydroxylation of surface oxide ions of Zr, abundant hydroxyl groups are believed to form on the surface, improving its wettability, facilitating cell adhesion, and enhancing bioactivity (Tamura et al., 2001; Zhao et al., 2014; Li et al., 2016).

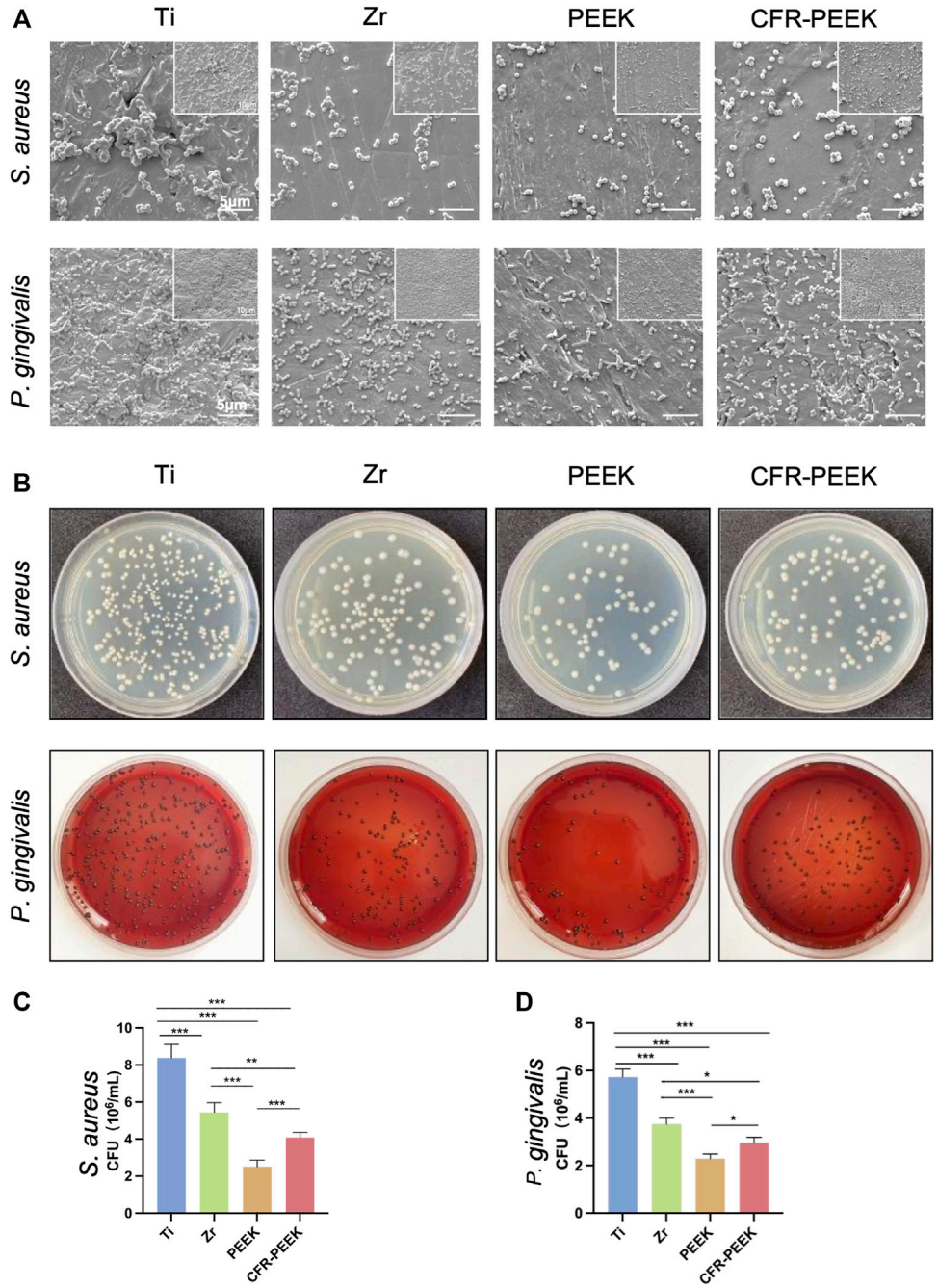

FIGURE 5
The anti-adhesion effect against bacteria of four different implant materials. **(A)** SEM images of bacterial morphology and the numbers of the colonies of *S. aureus* and *P. gingivalis* on Ti, Zr, PEEK, and CFR-PEEK samples under low and high magnifications (×10000, bar = 5 μM and 5,000×, bar = 10 μM). **(B)** The number of the colonies of *S. aureus and the P. gingivalis* cultured on agar. **(C)** The quantitative results of *S. aureus* colony counting. **(D)** The quantitative results of *P. gingivalis* colony counting. *$p < 0.05$, **$p < 0.01$, and ***$p < 0.005$.

While the osteogenic ability of PEEK and CFR-PEEK was significantly lower than that of Ti and Zr, many effective modifications were introduced to resolve this issue. For example, Zhang et al. (2022) developed a rough PEEK surface with a 200 nm patterned nanorod using a thermoforming technique, finding that this modification enhanced ALP activity and osteogenic gene expression in adipose stem cells and promoted the degree of peri-implant

neovascularization and osseointegration in rat femoral defect model. In addition, Guo et al. (2022) used the arc ion plating technique to apply a TiCu/TiCuN coating to CFR-PEEK, which showed excellent osteogenic activity *in vitro* and *in vivo*, as copper (Cu) could promote bone regeneration and antibacterial activity.

Gram-positive *S. aureus* and Gram-negative *P. gingivalis* have been associated with peri-implantitis (Persson and Renvert, 2014). The number of bacterial colonies on PEEK and CFR-PEEK was significantly lower than on Ti and Zr, consistent with Hahnel's findings (Hahnel et al., 2015). Biofilm formation on PEEK's surface was lower than on Ti and Zr, which may reflect differences in composition and morphology among materials (Qin et al., 2021). In addition, bacteria are more likely to adhere to the hydrophilic surface of Ti and Zr than PEEK (Malaikozhundan et al., 2016). Moreover, adding carbon fibers inhibited bacteria, possibly due to nanoscale carbon fragments and the "nano-blade" effect (Mei et al., 2020). The sharp edges of the nano-scaled sheets may destroy the integrity of bacterial membranes in physical contact (Malaikozhundan et al., 2016).

5 Conclusion

The new implant biocompatible materials PEEK and CFR-PEEK have comparable elastic modulus to native bone tissue and better bacterial anti-adhesion effects than Ti and Zr. However, the osteogenic ability of PEEK and CFR-PEEK still require improvement, and further studies are required to evaluate the effectiveness of different modification methods.

Data availability statement

The original contributions presented in the study are included in the article/supplementary material, further inquiries can be directed to the corresponding author.

Ethics statement

The animal study was reviewed and approved by the Affiliated Hospital of Fujian Medical University.

Author contributions

JS, XX, and YL contributed equally to this article. JS and XX: writing—original draft and editing. YL:writing—original draft, and formal analysis. YG: methodology, resources. YX: methodology, formal analysis. ZX: conceptualization. JC: conceptualization, supervision, project administration, funding acquisition.

Funding

This work was supported by the Joint Funds for the innovation of science and Technology of Fujian province (2019Y9031) and Startup Fund for scientific research, Fujian Medical University (2021QH2046).

Conflict of interest

The authors declare that the research was conducted in the absence of any commercial or financial relationships that could be construed as a potential conflict of interest.

Publisher's note

All claims expressed in this article are solely those of the authors and do not necessarily represent those of their affiliated organizations, or those of the publisher, the editors and the reviewers. Any product that may be evaluated in this article, or claim that may be made by its manufacturer, is not guaranteed or endorsed by the publisher.

References

Bathala, L., Majeti, V., Rachuri, N., Singh, N., and Gedela, S. (2019). The role of polyether ether ketone (peek) in dentistry - a review. *JMedLife.* 12 (1), 5–9. doi:10.25122/jml-2019-0003

Blanco, F. G., Hernández, N., Rivero-Buceta, V., Maestro, B., Sanz, J. M., Mato, A., et al. (2021). From residues to added-value bacterial biopolymers as nanomaterials for biomedical applications. *Nanomater. (Basel)* 11 (6), 1492. doi:10.3390/nano11061492

Brizuela, A., Herrero-Climent, M., Rios-Carrasco, E., Rios-Santos, J. V., Pérez, R. A., Manero, J. M., et al. (2019). Influence of the elastic modulus on the osseointegration of dental implants. *Mater. (Basel)* 12 (6), 980. doi:10.3390/ma12060980

Cheng, B. C., Koduri, S., Wing, C. A., Woolery, N., Cook, D. J., and Spiro, R. C. (2018). Porous titanium-coated polyetheretherketone implants exhibit an improved bone-implant interface: An *in vitro* and *in vivo* biochemical, biomechanical, and histological study. *Med. devices Auckl. N.Z).* 11, 391–402. doi:10.2147/mder.s180482

da Cruz, M. B., Marques, J. F., Peñarrieta-Juanito, G. M., Costa, M., Souza, J., Magini, R. S., et al. (2021). Bioactive-enhanced polyetheretherketone dental implant materials: Mechanical characterization and cellular responses. *J. Oral Implantol.* 47 (1), 9–17. doi:10.1563/aaid-joi-D-19-00172

Deng, Y., Zhou, P., Liu, X., Wang, L., Xiong, X., Tang, Z., et al. (2015). Preparation, characterization, cellular response and *in vivo* osseointegration of polyetheretherketone/nano-hydroxyapatite/carbon fiber ternary biocomposite. *Colloids Surfaces B Biointerfaces* 136, 64–73. doi:10.1016/j.colsurfb.2015.09.001

Ding, S. J., Chu, Y. H., and Chen, P. T. (2021). Mechanical biocompatibility, osteogenic activity, and antibacterial efficacy of calcium silicate-zirconia biocomposites. *ACS omega* 6 (10), 7106–7118. doi:10.1021/acsomega.1c00097

Dubiel, E. A., Martin, Y., and Vermette, P. (2011). Bridging the gap between physicochemistry and interpretation prevalent in cell-surface interactions. *Chem. Rev.* 111 (4), 2900–2936. doi:10.1021/cr9002598

Fabris, D., Moura, J., Fredel, M. C., Souza, J., Silva, F. S., and Henriques, B. (2022). Biomechanical analyses of one-piece dental implants composed of titanium, zirconia, PEEK, CFR-PEEK, or GFR-PEEK: Stresses, strains, and bone remodeling prediction by the finite element method. *J. Biomed. Mat. Res.* 110 (1), 79–88. doi:10.1002/jbm.b.34890

Guo, Y., Chen, C., Zhang, S., Ren, L., Zhao, Y., and Guo, W. (2022). Mediation of mechanically adapted TiCu/TiCuN/CFR-PEEK implants in vascular regeneration to promote bone repair *in vitro* and *in vivo*. *J. Orthop. Transl.* 33, 107–119. doi:10.1016/j.jot.2022.02.008

Hahnel, S., Wieser, A., Lang, R., and Rosentritt, M. (2015). Biofilm formation on the surface of modern implant abutment materials. *Clin. Oral Impl. Res.* 26 (11), 1297–1301. doi:10.1111/clr.12454

Han, M., Li, Q. L., Cao, Y., Fang, H., Xia, R., and Zhang, Z. H. (2017). *In vivo* remineralization of dentin using an agarose hydrogel biomimetic mineralization system. *Sci. Rep.* 7, 41955. doi:10.1038/srep41955

Hotchkiss, K. M., Reddy, G. B., Hyzy, S. L., Schwartz, Z., Boyan, B. D., and Olivares-Navarrete, R. (2016). Titanium surface characteristics, including topography and wettability, alter macrophage activation. *Acta Biomater.* 31, 425–434. doi:10.1016/j.actbio.2015.12.003

Jiao, J., Peng, C., Li, C., Qi, Z., Zhan, J., and Pan, S. (2021). Dual bio-active factors with adhesion function modified electrospun fibrous scaffold for skin wound and infections therapeutics. *Sci. Rep.* 11 (1), 457. doi:10.1038/s41598-020-80269-2

Khurshid, Z., Hafeji, S., Tekin, S., Habib, S. R., Ullah, R., Sefat, F., et al. (2020). "Titanium, zirconia, and polyetheretherketone (PEEK) as a dental implant material," in *Dental implants*. (Woodhead Publishing, Series), 5–35. doi:10.1016/B978-0-12-819586-4.00002-0

Knaus, J., Schaffarczyk, D., and Cölfen, H. (2020). On the future design of bio-inspired polyetheretherketone dental implants. *Macromol. Biosci.* 20 (1), e1900239. doi:10.1002/mabi.201900239

Lee, S. S., Huber, S., and Ferguson, S. J. (2021). Comprehensive *in vitro* comparison of cellular and osteogenic response to alternative biomaterials for spinal implants. *Mater. Sci. Eng. C* 127, 112251. doi:10.1016/j.msec.2021.112251

Lee, W. T., Koak, J. Y., Lim, Y. J., Kim, S. K., Kwon, H. B., and Kim, M. J. (2012). Stress shielding and fatigue limits of poly-ether-ether-ketone dental implants. *J. Biomed. Mat. Res.* 100 (4), 1044–1052. doi:10.1002/jbm.b.32669

Li, C. S., Vannabouathong, C., Sprague, S., and Bhandari, M. (2015). The use of carbon-fiber-reinforced (CFR) PEEK material in orthopedic implants: A systematic review. *Clin. Med. Insights Arthritis Musculoskelet. Disord.* 8, 33–45. doi:10.4137/CMAMD.S20354

Li, J., Qian, S., Ning, C., and Liu, X. (2016). rBMSC and bacterial responses to isoelastic carbon fiber-reinforced poly(ether-ether-ketone) modified by zirconium implantation. *J. Mat. Chem. B* 4 (1), 96–104. doi:10.1039/c5tb01784j

Li, Y., Wang, D., Qin, W., Jia, H., Wu, Y., Ma, J., et al. (2019). Mechanical properties, hemocompatibility, cytotoxicity and systemic toxicity of carbon fibers/poly(ether-ether-ketone) composites with different fiber lengths as orthopedic implants. *J. Biomaterials Sci. Polym. Ed.* 30 (18), 1709–1724. doi:10.1080/09205063.2019.1659711

Lu, H., Wang, J., Hao, H., and Wang, T. (2017). Magnetically separable MoS2/Fe3O4/nZVI nanocomposites for the treatment of wastewater containing Cr(VI) and 4-chlorophenol. *Nanomater. (Basel)* 7 (10), 303. doi:10.3390/nano7100303

Ma, R., and Tang, T. (2014). Current strategies to improve the bioactivity of PEEK. *Int. J. Mol. Sci.* 15 (4), 5426–5445. doi:10.3390/ijms15045426

Malaikozhundan, B., Vaseeharan, B., Vijayakumar, S., Sudhakaran, R., Gobi, N., and Shanthini, G. (2016). Antibacterial and antibiofilm assessment of Momordica charantia fruit extract coated silver nanoparticle. *Biocatal. Agric. Biotechnol.* 8, 189–196. doi:10.1016/j.bcab.2016.09.007

Mehl, C., Kern, M., Schütte, A. M., Kadem, L. F., and Selhuber-Unkel, C. (2016). Adhesion of living cells to abutment materials, dentin, and adhesive luting cement with different surface qualities. *Dent. Mat.* 32 (12), 1524–1535. doi:10.1016/j.dental.2016.09.006

Mei, L., Zhu, S., Yin, W., Chen, C., Nie, G., Gu, Z., et al. (2020). Two-dimensional nanomaterials beyond graphene for antibacterial applications: Current progress and future perspectives. *Theranostics* 10 (2), 757–781. doi:10.7150/thno.39701

Mishra, S., and Chowdhary, R. (2019). PEEK materials as an alternative to titanium in dental implants: A systematic review. *Clin. Implant Dent. Relat. Res.* 21 (1), 208–222. doi:10.1111/cid.12706

Peng, T. Y., Shih, Y. H., Hsia, S. M., Wang, T. H., Li, P. J., Lin, D. J., et al. (2021). *In vitro* assessment of the cell metabolic activity, cytotoxicity, cell attachment, and inflammatory reaction of human oral fibroblasts on polyetheretherketone (PEEK) implant-abutment. *Polym. (Basel)* 13 (17), 2995. doi:10.3390/polym13172995

Persson, G. R., and Renvert, S. (2014). Cluster of bacteria associated with peri-implantitis. *Clin. Implant Dent. Relat. Res.* 16 (6), 783–793. doi:10.1111/cid.12052

Qin, W., Li, Y., Ma, J., Liang, Q., and Tang, B. (2019). Mechanical properties and cytotoxicity of hierarchical carbon fiber-reinforced poly (ether-ether-ketone) composites used as implant materials. *J. Mech. Behav. Biomed. Mat.* 89, 227–233. doi:10.1016/j.jmbbm.2018.09.040

Qin, W., Ma, J., Liang, Q., Li, J., and Tang, B. (2021). Tribological, cytotoxicity and antibacterial properties of graphene oxide/carbon fibers/polyetheretherketone composite coatings on Ti-6Al-4V alloy as orthopedic/dental implants. *J. Mech. Behav. Biomed. Mat.* 122, 104659. doi:10.1016/j.jmbbm.2021.104659

Rozeik, A. S., Chaar, M. S., Sindt, S., Wille, S., Selhuber-Unkel, C., Kern, M., et al. (2022). Cellular properties of human gingival fibroblasts on novel and conventional implant-abutment materials. *Dent. Mat.* 38 (3), 540–548. doi:10.1016/j.dental.2021.12.139

Sadowsky, S. J. (2020). Has zirconia made a material difference in implant prosthodontics? A review. *Dent. Mat.* 36 (1), 1–8. doi:10.1016/j.dental.2019.08.100

Sagomonyants, K. B., Jarman-Smith, M. L., Devine, J. N., Aronow, M. S., and Gronowicz, G. A. (2008). The *in vitro* response of human osteoblasts to polyetheretherketone (PEEK) substrates compared to commercially pure titanium. *Biomaterials* 29 (11), 1563–1572. doi:10.1016/j.biomaterials.2007.12.001

Santoro, F., Zhao, W., Joubert, L. M., Duan, L., Schnitker, J., van de Burgt, Y., et al. (2017). Revealing the cell-material interface with nanometer resolution by focused ion beam/scanning electron microscopy. *ACS Nano* 11 (8), 8320–8328. doi:10.1021/acsnano.7b03494

Shalumon, K. T., Kuo, C. Y., Wong, C. B., Chien, Y. M., Chen, H. A., and Chen, J. P. (2018). Gelatin/nanohyroxyapatite cryogel embedded poly(lactic-co-glycolic acid)/nanohydroxyapatite microsphere hybrid scaffolds for simultaneous bone regeneration and load-bearing. *Polym. (Basel)* 10 (6), 620. doi:10.3390/polym10060620

Sivaraman, K., Chopra, A., Narayan, A. I., and Balakrishnan, D. (2018). Is zirconia a viable alternative to titanium for oral implant? A critical review. *J. Prosthodont. Res.* 62 (2), 121–133. doi:10.1016/j.jpor.2017.07.003

Sultana, T., Amirian, J., Park, C., Lee, S. J., and Lee, B. T. (2017). Preparation and characterization of polycaprolactone-polyethylene glycol methyl ether and polycaprolactone-chitosan electrospun mats potential for vascular tissue engineering. *J. Biomater. Appl.* 32 (5), 648–662. doi:10.1177/0885328217733849

Tamura, H., Mita, K., Tanaka, A., and Ito, M. (2001). Mechanism of hydroxylation of metal oxide surfaces. *J. Colloid Interface Sci.* 243 (1), 202–207. doi:10.1006/jcis.2001.7864

Wang, W., Qiao, S. C., Wu, X. B., Sun, B., Yang, J. G., Li, X., et al. (2021). Circ_0008542 in osteoblast exosomes promotes osteoclast-induced bone resorption through m6A methylation. *Cell Death Dis.* 12 (7), 628. doi:10.1038/s41419-021-03915-1

Yan, J. H., Wang, C. H., Li, K. W., Zhang, Q., Yang, M., Di-Wu, W. L., et al. (2018). Enhancement of surface bioactivity on carbon fiber-reinforced polyether ether ketone via graphene modification. *Int. J. Nanomedicine* 13, 3425–3440. doi:10.2147/IJN.S160030

Yu, W., Zhang, H., Yang, S., Zhang, J., Wang, H., Zhou, Z., et al. (2020). Enhanced bioactivity and osteogenic property of carbon fiber reinforced polyetheretherketone composites modified with amino groups. *Colloids Surf. B Biointerfaces* 193, 111098. doi:10.1016/j.colsurfb.2020.111098

Zhang, J., Tian, W., Chen, J., Yu, J., Zhang, J., and Chen, J. (2019). The application of polyetheretherketone (PEEK) implants in cranioplasty. *Brain Res. Bull.* 153, 143–149. doi:10.1016/j.brainresbull.2019.08.010

Zhang, S., Feng, Z., Hu, Y., Zhao, D., Guo, X., Du, F., et al. (2022). Endowing polyetheretherketone implants with osseointegration properties: *In situ* construction of patterned nanorod arrays. *Small* 18 (5), e2105589. doi:10.1002/smll.202105589

Zhang, Y., Chen, Y. Y., Huang, L., Chai, Z. G., Shen, L. J., and Xiao, Y. H. (2017). The antifungal effects and mechanical properties of silver bromide/cationic polymer nano-composite-modified Poly-methyl methacrylate-based dental resin. *Sci. Rep.* 7 (1), 1547. doi:10.1038/s41598-017-01686-4

Zhao, Y., Jamesh, M. I., Li, W. K., Wu, G., Wang, C., Zheng, Y., et al. (2014). Enhanced antimicrobial properties, cytocompatibility, and corrosion resistance of plasma-modified biodegradable magnesium alloys. *Acta Biomater.* 10 (1), 544–556. doi:10.1016/j.actbio.2013.10.012

Zysset, P. K., Guo, X. E., Hoffler, C. E., Moore, K. E., and Goldstein, S. A. (1999). Elastic modulus and hardness of cortical and trabecular bone lamellae measured by nanoindentation in the human femur. *J. Biomech.* 32 (10), 1005–1012. doi:10.1016/s0021-9290(99)00111-6

frontiers | Frontiers in Bioengineering and Biotechnology

TYPE Original Research
PUBLISHED 14 September 2022
DOI 10.3389/fbioe.2022.990249

OPEN ACCESS

EDITED BY
Monireh Kouhi,
Isfahan University of Medical Sciences, Iran

REVIEWED BY
Md. Shaifur Rahman,
Institute of Tissue Banking and Biomaterial Research, Bangladesh;
Center for Craniofacial Molecular Biology, United States
Hui Cen,
Xuchang University, China

*CORRESPONDENCE
Ruifang An,
anruifang@163.com

SPECIALTY SECTION
This article was submitted to Biomaterials, a section of the journal Frontiers in Bioengineering and Biotechnology

RECEIVED 09 July 2022
ACCEPTED 29 August 2022
PUBLISHED 14 September 2022

CITATION
Gao L, He X, Zhang T, Li P and An R (2022), Preparation and characterization of polyethylene glycol/chitosan composite water-based wound healing lubricant.
Front. Bioeng. Biotechnol. 10:990249.
doi: 10.3389/fbioe.2022.990249

Preparation and characterization of polyethylene glycol/chitosan composite water-based wound healing lubricant

Li Gao, Xinyi He, Taohong Zhang, Peipei Li and Ruifang An*

Department of Obstetrics and Gynecology, The First Affiliated Hospital of Xi'an Jiaotong University, Xi'an Jiaotong University, Xi'an, Shaanxi, China

The proportion of pregnant women giving birth through cesarean section is increasing annually worldwide. However, post-cesarean section scar diverticulum is a common condition that occurs and requires better surgical strategies than the methods currently used. We hypothesized that using biological lubricant topically on the incision area during C-section could be an option to minimize the scar. This water-based polyethylene glycol (PEG)/chitosan (CS) composite lubricant was prepared via ultrasonic blending. The product was characterized using scanning electron microscopy, X-ray photoelectron spectroscopy, X-ray diffraction, Fourier-transform infrared spectroscopy, and Raman spectroscopy. The thermal stability of the materials and their heat absorption and release during heating were analyzed using thermogravimetric analysis and differential scanning calorimetry. Tribological tests proved that the PEG/CS composite had a better lubrication effect than either the PEG or CS lubricant alone, and the cell viability experiments verified that it had good biocompatibility. Finally, application of the composite lubricant onto the backs of mice modeling full-thickness skin incisions further confirmed that the product improved both the re-epithelialization and the collagen levels of the wounded skin. In conclusion, we expect our newly formulated PEG/CS composite lubricant to be useful not only for managing post-cesarean section scar diverticulum but also for healing skin wounds in general.

KEYWORDS

water-based lubricant, wound healing, polyethylene glycol (PEG), chitosan (CS), biocompatibility

1 Introduction

In the future, the world is expected to face a severe problem of "population aging," caused mainly by the increase in average life expectancy due to improvements in medical treatments and the decrease in fertility rates stemming from the ever-increasing cost of living that renders child rearing financially prohibitive (Luo et al., 2021). Additionally, the expansion of the aging population could lead to labor shortages (Phiromswad et al., 2022), more environmental pollution (Zha et al., 2022), and an increased burden on medical care

sector and old-age benefit dividends (Kollerup et al., 2022). At present, China is encountering a severe problem of population aging. To effectively solve this problem, the government has issued various policies to encourage childbirth, such as a three-child policy, extended maternity leave, and birth subsidies. Then, the development of obstetrics and gynecology services accelerated with the policy of encouraging childbirth. Although natural birth is still the most common form of delivery, increasingly more pregnant women are choosing painless birthing options, such as water delivery and cesarean section (Fobelets et al., 2019), especially those with a narrow pelvis, abnormal placenta, abnormal birth canal, premature water rupture, and abnormal fetus. However, post-cesarean section scar diverticulum (PCSD), which generally refers to lacunae formed as a result of poor healing of the uterine incision after the cesarean procedure (Zheng et al., 2020; Huang et al., 2022), is a common condition that can cause many problems in the new mother, such as chronic inflammation (Negro et al., 2017; Bi et al., 2021). Therefore, new medical strategies are required to effectively reduce the occurrence of PCSD.

At present, surgery is the main treatment option for this condition. (Zhou et al., 2018) found through clinical observations that vaginal repair surgery could restore the anatomical structure of patients with PCSD, allowing the women to obtain satisfactory obstetric results. Using the hysteroscopic electrocauterization method, (Dai et al., 2022) cauterized part of the endometrium to treat PCSD and found obvious repair effects, with the technique completely removing the scar from the previous cesarean section and the surrounding ectopic endometrium, thereby reducing the recurrence rate of the condition. However, although surgical treatment of PCSD is effective, it can also cause harm to the mother. Before cesarean section, a large amount of normal saline is usually applied to the wound site (the part cut with the scalpel). However, normal saline disinfects only the epidermis. Therefore, a useful strategy would be to replace normal saline with a liquid that can assist with wound repair and promote muscle growth. Water-based lubricants exhibiting good biocompatibility with the human body and a high lubrication effect have already been developed by some researchers (Qin et al., 2018; Lu et al., 2021). These are composed mainly of deionized water and lubricant additives, such as nanoparticles (Chen et al., 2021; Perumalsamy et al., 2021; Rahman et al., 2021; Sun et al., 2021; Tang et al., 2022), polymers (Liu et al., 2021; Perumalsamy et al., 2021; Wang et al., 2021; Zheng et al., 2021), and ionic liquids (Tang et al., 2018; Wang et al., 2018; Tang et al., 2019; Amann et al., 2020; Dong et al., 2020). Various types of additives are used for slightly different purposes. For example, nanoparticles and ionic liquids are commonly used in the mechanical field, whereas polymers are applied in the biomedical field owing to their good biocompatibility and antibacterial effects. Polyethylene glycol (PEG), a high-molecular-weight polymer that dissolves easily in water, exhibits good compatibility with many organic components as well as excellent lubricity, moisture retention capability, dispersibility, and adhesivity (Hu et al., 2021). Another polymer, soluble chitosan (CS), also displays excellent dispersibility in water, lubrication and antibacterial effects, and biocompatibility; therefore, it is also widely used in the biomedical field. For example, (Lu et al., 2017) prepared a sol using CS and PEG, which have good biocompatibility and applied it to the human body, revealing that it has an excellent lubrication effect under a high load.

In this study, we prepared a new type of composite lubricant by combining PEG and CS under ultrasonic conditions. The surface micromorphology of the composite lubricant was examined using scanning electron microscopy (SEM), and the materials were also characterized using X-ray photoelectron spectroscopy (XPS), X-ray diffraction (XRD), Fourier-transform infrared (FT-IR) spectroscopy, and Raman spectroscopy. The thermal stability of the materials and their heat absorption and release during heating were analyzed using thermogravimetric analysis (TGA) and differential scanning calorimetry (DSC). Tribological tests confirmed that the lubricant had a good lubrication effect and made cutting with the scalpel easier. Moreover, cell viability tests confirmed that the lubricant did not inhibit cell growth and demonstrated good biocompatibility, indicating that it could be applied to the human body. Additionally, a mouse model of a full-thickness skin incision created on the back of the animals was used to prove that the lubricant could accelerate wound healing. Our novel lubricant is expected to be widely used in future cesarean sections.

2 Materials and methods

2.1 Materials

PEG (average molecular weight: 3,500–4,500 Da; melting point: 54–58°C; pH: 4–7; chemical formula: $HO(CH_2CH_2O)_nH$; elements: C, H, O) was purchased from Tianjin Damao Chemical Reagent Factory (Tianjin, China). CS (carboxymethyl carboxylation degree ≥80%; chemical formula: $C_{20}H_{37}N_3O_{14}$; elements: C, H, N, O) was purchased from Shanghai Lanji Biology (Shanghai, China). The reagents and chemicals used in this study were of analytical grade.

2.2 Sample preparation

PEG (3 g), CS (0.15 g), and deionized water (6.85 g) were weighed separately using an electronic balance and then mixed in a beaker. The mixture-containing beaker was then sealed with

cling film and placed in an ultrasonic cleaner for 30 min of sonication, which finally yielded the water-based PEG/CS (30 wt %/1.5 wt%) composite lubricant (the PEG/CS lubricant).

2.3 Biocompatibility test

L929 cells at the logarithmic stage of growth were trypsinized, counted, and inoculated into a 96-well plate at a density of 1×10^4 cells/well. Six wells were allocated for each of the following four groups: control, PEG, CS, and PEG/CS. The cells were cultured at 37°C under 5% CO_2 and 95% humidity for 12 h, by which time they had adhered stably to the plate walls. The following treatments were then carried out: For the PEG/CS group, 10 μL of the fabricated PEG/CS lubricant was added; for the PEG group, 10 μL of 30 wt% PEG was added; for the CS group, 10 μL of 1.5 wt% CS was added; and for the control group, 10 μL of phosphate-buffered saline (PBS) was added. The 96-well plate was maintained under the same culture conditions as before. After 24 h, the plate was placed on an ultra-clean table and 10 μL of Cell Counting Kit-8 reagent was added to each well. Then, after incubation at 37°C for 1 h, the absorbance of the cells in each well was measured at 450 nm with a microplate reader (Bio-Rad, Hercules, CA, United States) and the number of viable cells was counted. The test was repeated three times for each group to ensure the accuracy of the experiment.

2.4 Wound-healing effect test

All animal experiments were approved by the Animal Care and Experiment Committee of the Medical College of Xi'an Jiaotong University. Eight-week-old male Balb/c mice (purchased from the Medical Experimental Animal Center of Xi'an Jiaotong University) weighing 20 ± 0.4 g each were randomly divided into a control group and a PEG/CS group (3 mice in each group). All mice were raised under specific pathogen-free conditions before and after the operation. The animals were first anesthetized with isoflurane. Then, under a sterile environment, an equal volume of the PEG/CS lubricant or PBS was applied to the intended incision site of the skin on the backs of the mice in the respective groups. Subsequently, a 10-mm-long full-thickness skin incision was created with a scalpel. The wound was rinsed with sterile saline and covered with a skin patch (3M Health Care). On the 14th day, the mice were euthanized by cervical dislocation under anesthesia, and a 1 cm^2 patch of skin was excised using sterile instruments. The skin sample was fixed with paraformaldehyde for 24 h and then embedded in paraffin blocks for the generation of paraffin tissue sections for hematoxylin and eosin (H&E), Masson and CD31 immunofluorescence staining. The test was repeated three times for each group to ensure the accuracy of the experiment.

2.5 Tribological test

The lubricity of the fabricated product was tested using a reciprocating friction tester (GSR-2; Shenzhen, China). Ultra-high-molecular-weight polyethylene (UHMWPE) balls and 304 stainless steel disks were used as the friction-making materials, the relevant parameters of which are shown in Table 1. The balls and disks were wiped with acetone before use. The experiment was carried out at an ambient temperature, with a load of 10 N, a speed of 2 cm/s, and an experimental time of 30 min. The results for each group are an average of three replicate tests.

2.6 Characterization of the lubricants

The surface micromorphology of the PEG/CS lubricant was observed using SEM (OXFORD Instruments, Oxfordshire, United Kingdom). XRD analysis (D8 Advance Diffractometer; Bruker, Rheinstetten, Germany) was carried out using Cu-Kα radiation (λ = 0.15406 nm), with the system run at 40 kV and 40 mA, and the crystal phase structure of the prepared samples was 5–50°. The chemical composition of the prepared samples was analyzed using XPS (Escalab 250Xi; Thermo Fisher Scientific, Waltham, MA, United States) at 0–1,300 eV, and the multi-peak fitting of the C and O elements was carried out using XPSpeak41 software. The corresponding functional groups were determined by comparing the binding energies of C and O. The chemical functional groups of the prepared samples were analyzed using FT-IR spectroscopy (Nicolet iS50 spectrometer, spectral resolution of 4 cm^{-1}; Thermo Fisher Scientific) in the range of 500–4,000 cm^{-1}. The interaction between materials was analyzed in the range of 100–3,500 cm^{-1} using Raman spectroscopy (Hr800; Horiba Jobin Yvon, Edison, NJ, United States) at an excitation wavelength of 532 nm. The thermal stability of the prepared samples was analyzed from ambient temperature to 1,000°C using TGA (NETZSCH Group, Selb, Germany). DSC was used to analyze heat absorption and release by the prepared samples during heating from ambient temperature to 1,000°C.

3 Results and discussion

3.1 SEM analysis

Figure 1 presents the SEM images of the PEG/CS lubricant at different scales. As seen in Figure 1A, the dried PEG/CS composite particles are lumpy in structure. Further enlargement of the image (Figure 1B) revealed that the massive particles were formed by the stacking of a large number of sheets. The edge of the flake is very obvious in the further enlarged images (Figures 1C,D). Thus, the dried PEG/CS

TABLE 1 Properties of the tribological test materials.

Material	Diameter (mm)	Density (g × cm−3)	Hardness (HV)	Tensile strength (MPa)
304 stainless steel disk	Φ30	7.93	≤210	520
UHMWPE ball	Φ9.525	0.93	35	40

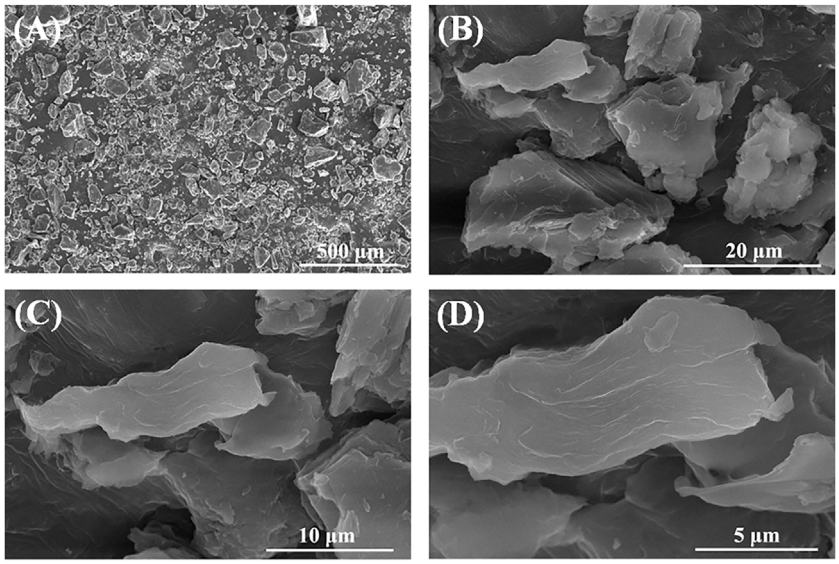

FIGURE 1
SEM images of PEG/CS composite lubricant at different scales: **(A)** 500 μm, **(B)** 20 μm, **(C)** 10 μm, and **(D)** 5 μm.

lubricant was confirmed to be mainly flaky in structure, with the flakes appearing wrinkled. The spherical shape of CS could not be seen in the SEM images, likely because of its low content in the PEG/CS lubricant (Melo et al., 2020).

3.2 XPS and XRD analyses

The XPS spectrum of the PEG/CS lubricant and the fitted graphs corresponding to C 1s and O 1s are shown in Figures 2A,C. There were two high-intensity peaks in the spectrum for the PEG/CS lubricant; C 1s at 285.09 eV and O 1s at 531.7 eV. This proved that the PEG/CS lubricant was composed mainly of C and O elements. Further analysis of the two peaks using XPSpeak41 software revealed that the element C was mainly present in the form of C-C, C-O, C-H, and C-N (Figure 2B). C-C, C-O, and C-H were present in large quantities in both the PEG and CS monomers, whereas C-N was mainly present in CS. The element O was mainly present in the form of C-OH (Figure 2C) (Xu et al., 2016; Ren et al., 2019; Zhang et al., 2021). Thus, these results confirmed the presence of both PEG and CS in the fabricated lubricant.

Figure 2D shows the XRD signals of CS, PEG, and the PEG/CS composite. CS had a low and wide diffraction peak at 23.5°, indicating the low crystallinity of the sample. By contrast, PEG showed two relatively high and narrow diffraction peaks of higher intensity at 23.3° and 26.1° (Ren et al., 2019), indicating its higher crystallinity relative to that of CS. The composite sample also showed two relatively high and narrow diffraction peaks at 23.3° and 26.3°, and it can be seen that the intensity of the peak at 23.3° was enhanced, which may be related to the addition of CS. The PEG/CS composite mainly showed the diffraction peaks of the PEG sample, which may be related to the high content of this polymer. Moreover, the addition of a small amount of CS did not cause a great impact on the crystallinity of PEG.

3.3 Raman spectroscopy, FT-IR spectroscopy, TGA, and DSC analyses

A Raman spectrum usually indicates the interactions between the materials of a substance. Figure 3A shows the Raman spectrum of the PEG/CS lubricant. According to a

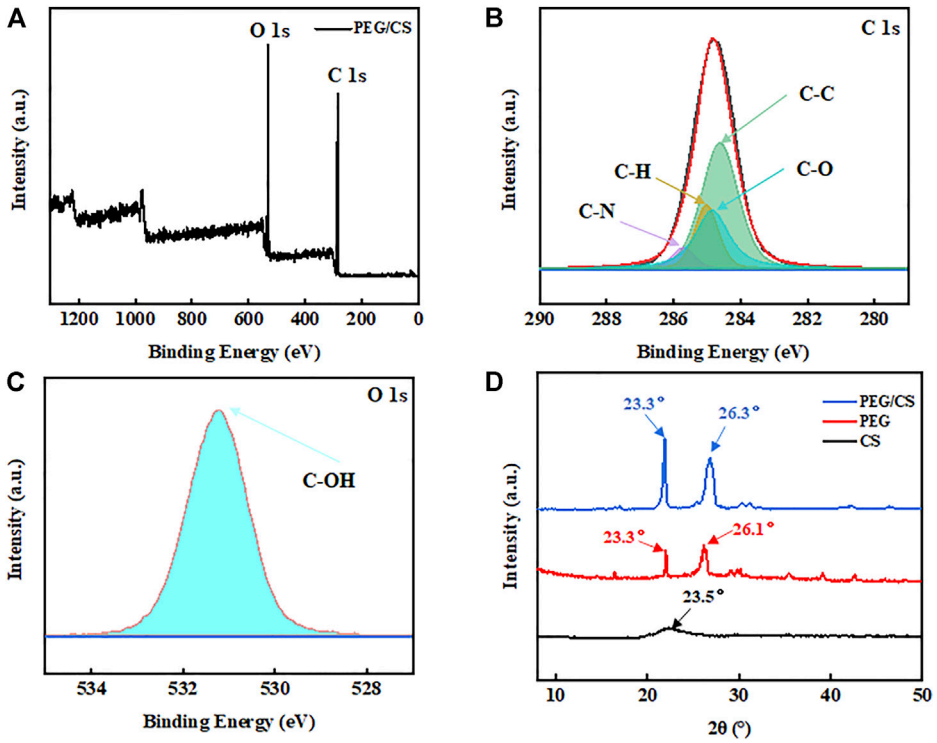

FIGURE 2
X-ray photoelectron spectroscopy (XPS) spectra of the PEG/CS composite lubricant: **(A)** Survey, **(B)** C 1s, **(C)** O 1s. **(D)** X-ray diffraction patterns of PEG, CS, and the PEG/CS composite.

previous study, it can be inferred that the characteristic Raman bands at 843, 1,127, 1,142, 1,282, 1,481, and 2,886 cm^{-1} are mainly those of PEG (Lu et al., 2017), and the characteristic Raman bands at the other positions are similar to those of CS, proving that the PEG and CS molecules were well cross-linked by hydrogen bonds.

FT-IR imaging is an important method for detecting chemical functional groups. Figure 3B shows the FT-IR spectrum of the PEG/CS lubricant. The absorption bands at 3,443, 2,889, and 1,111 cm^{-1} correspond to the terminal hydroxyl group, the extension of the C-H bond in CH_2, and the C-O-C functional group, respectively (Lu et al., 2017; Ren et al., 2019). These three characteristic absorption bands and monomers can be inferred from previous studies. The characteristic absorption bands at 962 and 842 cm^{-1} indicate the existence of C-C-O bonds, which are mainly due to PEG in the complex. It can be inferred from the above results that the chemical functional groups of PEG and CS did not change after ultrasonic mixing and that both polymers may be connected by hydrogen bonding, which is consistent with the results shown in Figure 3A.

TGA is usually applied to confirm the thermal stability of a sample. Figure 3C shows the TGA curves of PEG, CS, and the PEG/CS composite. The PEG sample showed a small mass loss at 80–150°C, which was mainly due to the small amount of water in the air and a large number of oxygen-containing functional groups in the molecule. By contrast, the sample showed a large mass loss at 250–550°C, which was due to degradation of the PEG backbone (Chen et al., 2021). The CS sample showed a small mass loss at 50–300°C, the reasons for which are similar to those for the PEG sample. It was apparent that CS had a higher mass than PEG from 300°C onward, which may indicate that CS has a better ability to bind water in the air, and residues still existed after heating to 950°C. The TGA curve of the PEG/CS sample was similar to that of PEG, which may be due to the high content of this polymer in the composite. Similar to the CS sample, there were still trace residues of the PEG/CS composite at 950°C (Gupta et al., 2009).

DSC typically indicates the amount of heat absorbed and released by a sample during heating. Figure 3D shows DSC traces for PEG, CS, and the PEG/CS composite. The PEG sample was endothermic at 75°C but showed an upward-trending peak at 450–600°C, indicating that it was exothermic. By contrast, the composite sample exhibited an exothermic reaction at 75°C. Comparison of the curves reveals that the peak position moved forward after the addition of CS, and the other positions also changed to different degrees. This may be due to the formation of a large number of hydrogen bonds between CS and PEG, which reduced the fluidity of the composite (Zhang et al., 2021).

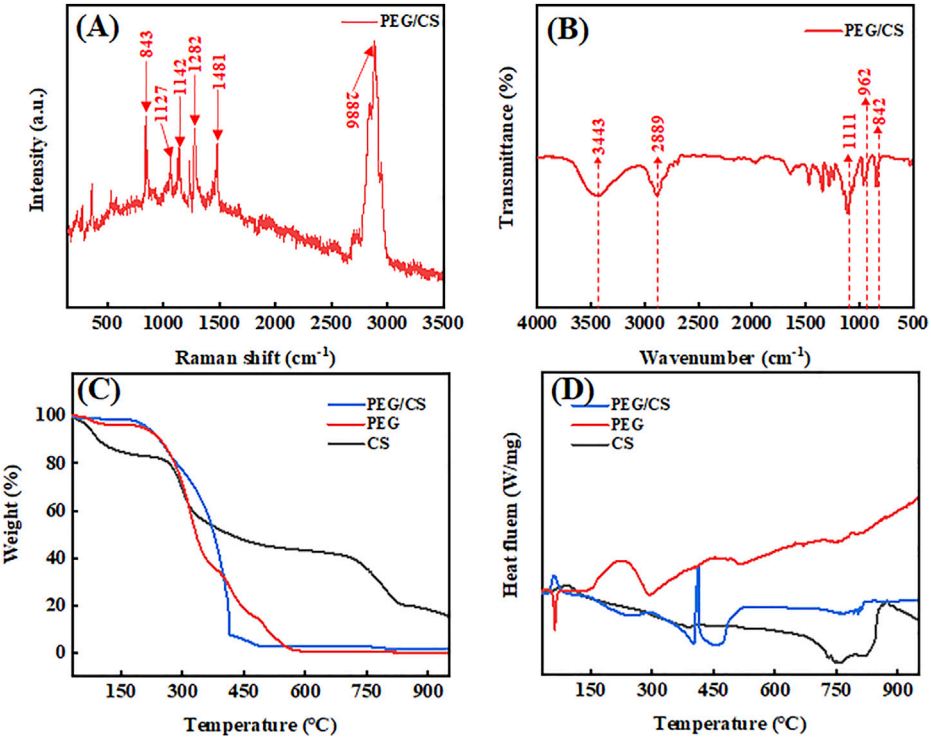

FIGURE 3
Results of the **(A)** Raman spectroscopy, **(B)** Fourier-transform infrared spectroscopy, **(C)** thermogravimetric analysis, and **(D)** differential scanning calorimetry analysis of the PEG/CS composite lubricant.

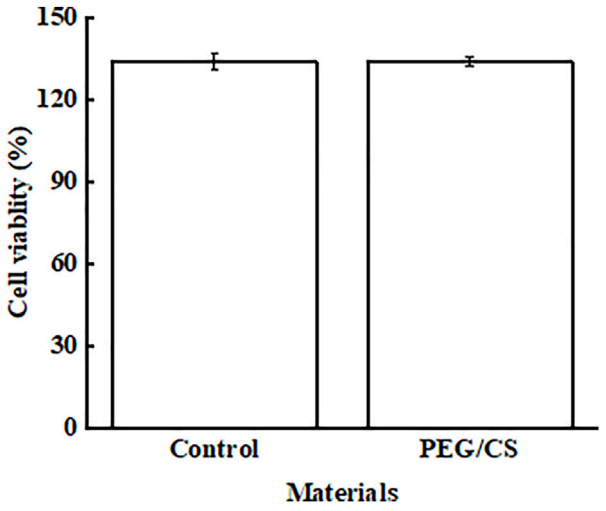

FIGURE 4
Viability of L929 cells treated with PBS (control) and PEG/CS, as determined with the Cell Counting Kit-8 assay.

3.4 Biocompatibility of the PEG/CS lubricant

Figure 4 shows the biocompatibility test results of the blank control group and PEG/CS lubricant. The survival rate of control L929 cells was 133.89%, which indicated that the cells proliferated in PBS buffer. Compared with the blank control L929 cells, the viability of cells treated with PEG/CS decreased slightly, and the cell survival rate was about 133.82%. However, the survival rate of the opposite cells decreased in value, but it also indicated that L929 cells proliferated in the presence of PEG/CS, which also proved that the polymer had good biocompatibility. (Lu et al., 2017; Hu et al., 2021).

3.5 Lubrication effects of the various polymers

3.5.1 Lubrication affects PEG and CS alone

In this experiment, the lubrication effects of PEG and CS individually, measured as the average coefficient of friction

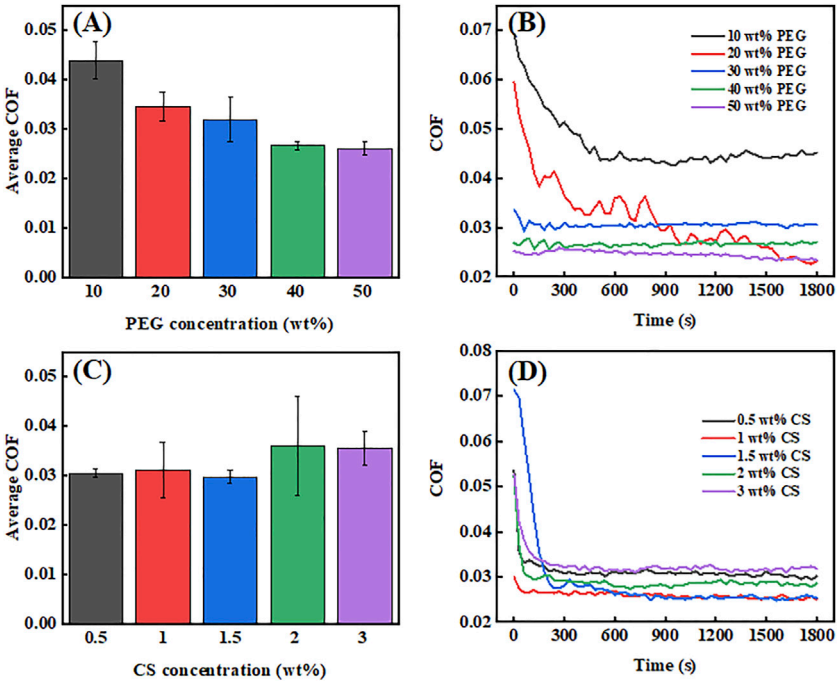

FIGURE 5
Average coefficient of friction (COF) values **(A)** and COF curves **(B)** of PEG at different concentrations. Average COF values **(C)** and COF curves **(D)** of CS at different concentrations.

(COF), were investigated for different concentrations of each polymer. As evident in Figures 5A, 10 wt% PEG had an excellent lubrication effect, exhibiting a very low average COF of approximately 0.045. When the concentration of PEG was increased from 10% to 20 wt%, the average COF showed a faster reduction trend (Figure 5B). This was probably due to the increased concentration of the polymer and the greater contact area between its molecules and the friction contact area, resulting in more adequate lubrication. From the curves in Figure 5B, it can be seen that the COF values for the 10 wt% and 20 wt% PEG concentrations are high at the initial stage and then drop sharply within 10 min. This is because the film-forming characteristics of low-concentration PEG are poor, resulting in the peak COF values at the initial stage. With the increase in time, the UHMWPE balls start to wear out, resulting in wear debris that fills the uneven stainless steel disk and makes the contact surface smoother. With a further increase of the lubricant additive concentration to 50 wt %, the average COF showed a slow decline and dropped to a minimum of approximately 0.026, which is probably close to the optimum value for PEG lubrication. We speculate that with higher concentrations of PEG, the effect of the lubricant may barely change, and the average COF value may even increase. The reason for this is that the surface of PEG molecules contains a large number of oxygen-containing groups (e.g., -OH, -COOH, etc.), the high energies of which make them attract one another to form hydrogen bonds, resulting in the formation of large PEG agglomerates. It is difficult for such large agglomerated PEG molecules to enter the friction contact area, resulting in poor lubrication and serious wear on the contact surfaces of the friction-making pairs. Moreover, when the concentration of PEG is increased, the overall viscosity of the lubricant increases, resulting in a large viscous force in the friction contact area, which will have a significant impact on the situation where the average COF value is small; however, in this case, the contact surfaces of the friction-making pair will not be worn. As evident in Figure 5B, the higher the PEG concentration is, the lower the COF curves are over time, and the friction force is smaller. Moreover, the trends of four of the COF curves were relatively stable throughout the reciprocating process. Only the 20 wt% concentration showed slight changes in the average COF pattern over time, which may have been caused by other factors in the experimental process, but this had little influence on the average value of the overall curve.

Figure 5C shows the average COF values of CS at different concentrations. At the CS concentration of 0.5 wt%, the average COF value was already very low (~0.03). It was also found that the average COF value changed only slightly between the CF concentrations of

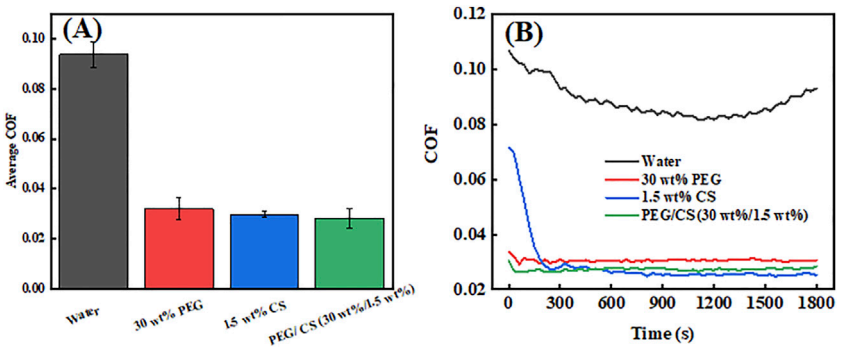

FIGURE 6
Average coefficient of friction (COF) values **(A)** and COF curves **(B)** of different lubricants.

0.5–1.5 wt%, dropping to a minimum of ~0.028 at 15 wt% and then increasing at the concentrations of 2 and 3 wt%. However, the overall trend in average COF values was an increase rather than a decrease. The reasons for this phenomenon may be similar to those for PEG, in that the average COF value increases with the increase in lubrication additive concentration. First, agglomeration may occur, which prevents the lubrication additive from entering the friction contact area, resulting in an increase in the average COF value. Second, the increase in the concentration of the lubrication additive leads to increases in the viscosity of the lubricant, the viscosity of the contact surface, and thereby the average COF value. The COF curves in Figure 5D show the same trends as those in Figure 5C; that is, decreasing and then increasing with increasing CS concentration. All five friction curves showed a rapid decrease in the COF value during 300 s of reciprocating motion, followed by the maintenance of a relatively stable trend thereafter. This may be due to the initial stage of friction in the boundary lubrication. During the contact between the convex body and the small friction contact area, the friction caused by the reciprocating motion creates serious plastic deformation, which produces a large amount of friction debris that eventually fills the surface of the friction contact area. Therefore, after 300 s, the friction contact surface became smooth and flat because of the large amount of friction debris filling the substrate surface, which stabilized the COF curve.

3.5.2 Lubrication effect of the PEG/CS lubricant

The newly formulated PEG/CS lubricant was also subjected to tribological testing, and the results were compared with those of the single PEG and CS lubricants and water lubrication. Figure 6A shows the average COF images of four lubricants. The maximum average COF value with the water lubrication was approximately 0.09. By contrast, the single PEG and CS lubricants had much lower average COF values of approximately 0.032 and 0.028, respectively, which are approximately one-third that of the water lubrication result, indicating the excellent lubrication effect of the two single lubricants. However, the lubrication effect of the composite lubricant was the best, with an average COF value of approximately 0.027. This may be due to the synergistic lubrication effects of PEG and CS caused by the hydrogen bonds connecting them in the composite (which was confirmed by the Raman and FT-IR spectroscopy results). Figure 6B shows the changes in the COF curves of the different lubricants over time. For the water lubrication test, it can be seen that the curve is very high in the graph and the COF values are very large. With the increase in time, the COF values decreased gradually to the 1,200 s time point and then increased gradually again from 1,200 to 1,800 s, proving that the long-term lubrication effect of water cannot be maintained. However, for the other three lubricants, the COF values initially decreased and then tended to stabilize throughout the friction process. There were no significant abrupt changes in the curves during the 280–1,800 s period of the friction process, which proved that the three lubricants could maintain a good lubrication effect for a long time.

Figure 7 shows the surface morphologies of the UHMWPE balls and the stainless steel disk wear in the tests using 30 wt% PEG (Figures 7A,D), 1.5 wt% CS (Figures 7B,E), and PEG/CS (30 wt%/1.5 wt%) lubricants (Figures 7C,F). Slight scratches were evident on the disk surface in the single PEG and CS lubrication tests, but almost no scratches appeared on the disk surface under PEG/CS lubrication, and the same situation occurred on the corresponding ball surface. It was confirmed that the composite lubricant was better than the single lubricants at protecting surfaces from frictional wear.

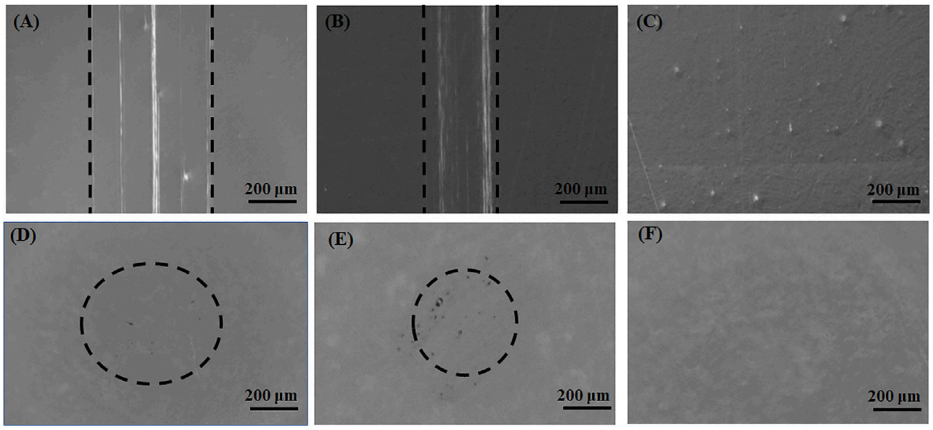

FIGURE 7
Optical microscopy images of the surfaces of stainless steel disks after tribological testing: **(A)** 30 wt% PEG, **(B)** 1.5 wt% CS, **(C)** PEG/CS (30 wt %/1.5 wt%). Optical microscopy images of the surfaces of ultra-high-molecular-weight polyethylene balls after tribological testing: **(D)** 30 wt% PEG, **(E)** 1.5 wt% CS, **(F)** PEG/CS (30 wt%/1.5 wt%).

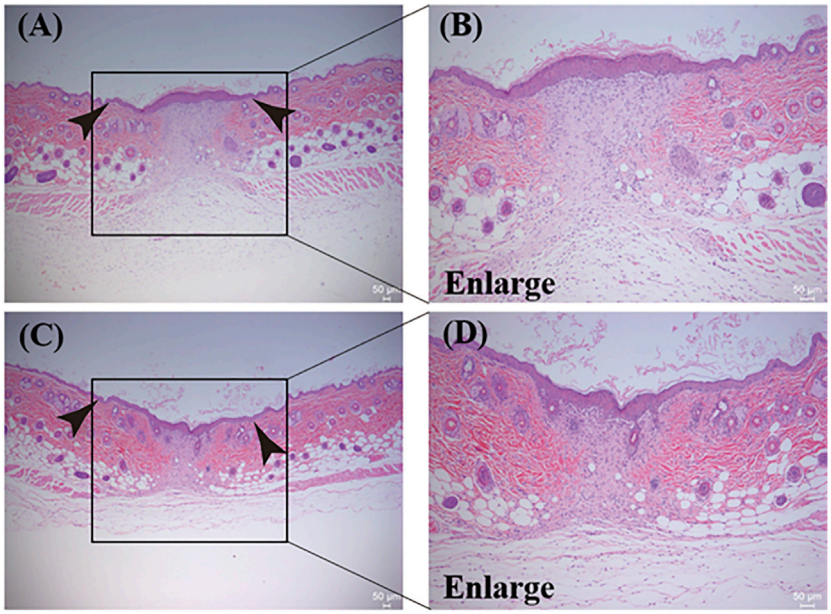

FIGURE 8
H&E staining results of mouse dorsal skin tissue protected by **(A)** PBS and **(C)** the water-based PEG/CS composite lubricant. **(B)** and **(D)** are magnified images of the corresponding boxed areas.

In summary, the PEG/CS lubricant maintained excellent lubrication for a long period of time during the tribological test, effectively reducing the shear force between the scalpel and skin during scalpel cutting, resulting in minimal damage at the skin incision, as confirmed by the later experiments on skin incision wound healing in a mouse model.

3.6 Wound-healing effect of the PEG/CS lubricant

3.6.1 H&E

A very important process in skin wound healing is skin re-epithelialization, the level of which directly affects the wound-

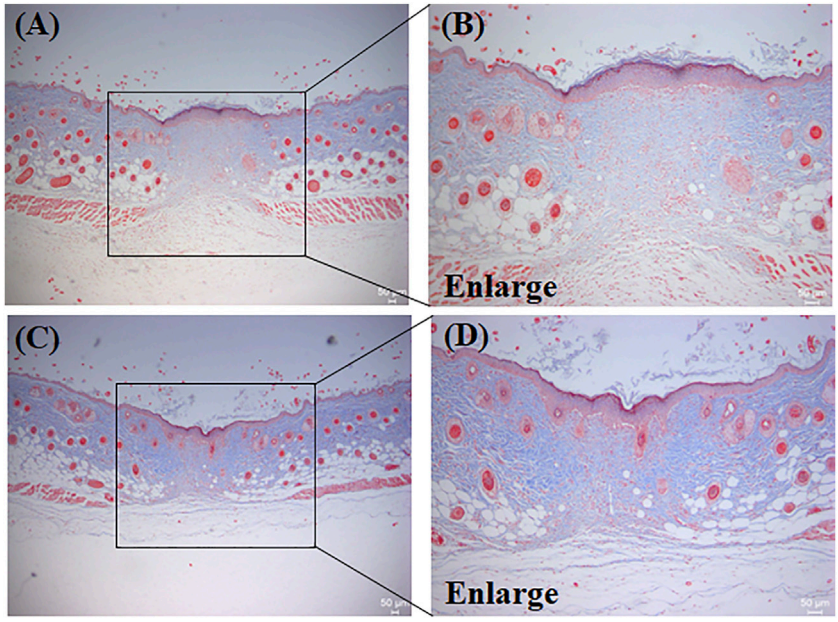

FIGURE 9
Masson staining results of mouse dorsal skin tissue protected by **(A)** PBS and **(C)** the water-based PEG/CS composite lubricant. **(B)** and **(D)** are magnified images of the corresponding boxed areas.

healing rate (Chen et al., 2018; Leng et al., 2020). In this experiment, the level of skin wound re-epithelialization was investigated using H&E staining of mouse tissue. Figures 8A,C show the H&E staining results for the PBS group and the PEG/CS lubricant group, respectively, whereas Figures 8B,D show magnified images of the boxed areas. A large number of inflammatory cells were evident in the PBS group, whereas there were significantly fewer inflammatory cells in the PEG/CS lubricant group. This may be due to the significant anti-inflammatory effect of CS in the PEG/CS composite (Chen et al., 2018). However, the arrangement of fibroblasts in both groups was regular, and there was a clear boundary between the dermis and epidermis and a clear cuticle on the edge of the epidermis. In summary, the wound tissue of the PEG/CS lubricant group showed better re-epithelialization and less scar formation, results that were supported by the quantitative analysis of the scar width (described below).

3.6.2 Masson

Collagen synthesis and collagen level are important factors in the healing of skin wounds (Chen et al., 2018; Leng et al., 2020). Masson staining was used to evaluate the collagen levels in the skin wounds of the PBS (Figures 9A,B) and PEG/CS lubricant groups (Figures 9C,D). The PEG/CS lubricant group had significantly more new collagen fibers in the skin wound than the PBS group. This may be because the PEG/CS lubricant promotes the growth of collagen fibrils. In summary, the tissue wound in the PEG/CS lubricant group exhibited a higher level of extracellular matrix deposition than that in the PBS group, and a large number of thick and tightly arranged collagen fibrils were observed.

3.6.3 Summary of wound healing effect

Figure 10A shows the results of the quantitative analyses of the H&E-stained scar width and Masson staining for the collagen volume fraction. The PBS group had a scar width of 640 μm and a collagen volume fraction of 43.8%, whereas the PEG/CS lubricant group had a scar width of 501 μm and a collagen volume fraction of 59.3%. The PEG/CS group had a 139 μm reduction in the scar width and a 15.5% increase in the collagen volume fraction compared with the PBS group, confirming that it can accelerate the healing of skin wounds. Figure 10B shows the statistical image of CD31 positive staining area. It can be clearly seen from the image that the area of staining area in PEG/CS group is larger, about 2.5 times that of PBS group, which fully proves that the healing level of PEG/CS group is better.

3.7 Analysis of the wound-healing mechanism

Figure 11 shows the wound-healing mechanism of the PEG/CS lubricant. First, the lubricant forms a dense protective film on the skin surface. Thus, the shear force between the scalpel and the skin is decreased, which can effectively reduce skin damage during the cutting process. Additionally, the PEG and CS molecules in the composite

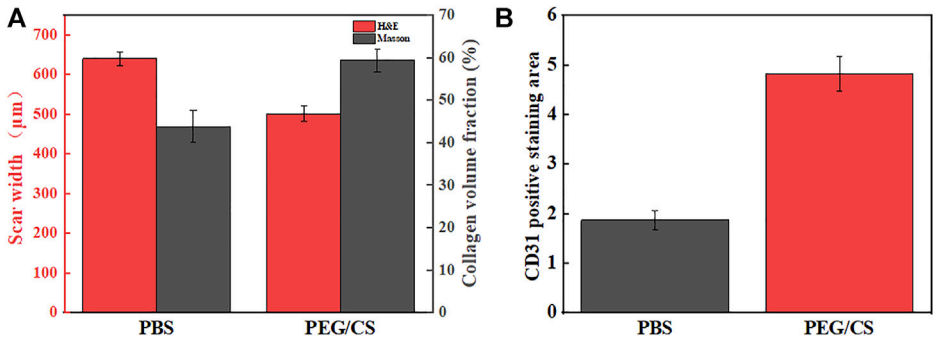

FIGURE 10
(A) Quantitative results of the H&E-stained scar width and Masson staining for collagen volume fraction, **(B)** statistical image of CD31 positive staining area.

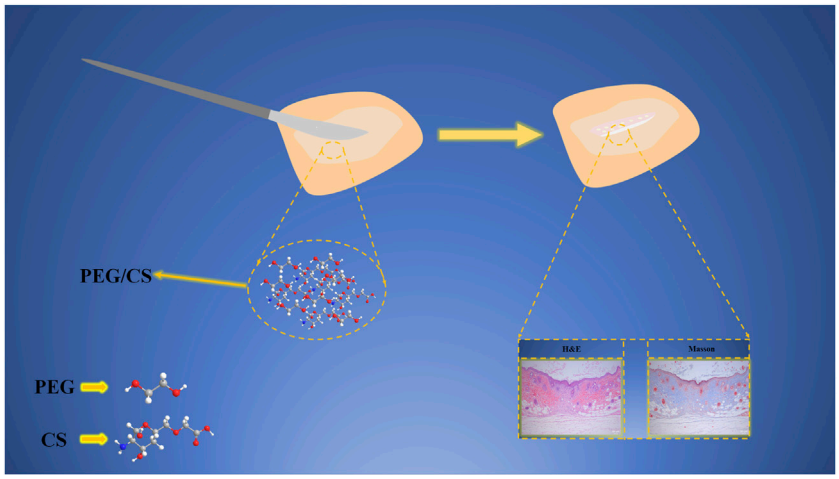

FIGURE 11
Wound-healing mechanism of the water-based PEG/CS composite lubricant.

lubricant are connected by hydrogen bonds, forming a dense network structure on the skin incision surface, which effectively isolates external pollutants. At this time, the lubricant compound quickly enters the wound, where the CS component accelerates wound healing mainly by promoting fibroblast proliferation and improving macrophage phagocytosis (Zhang et al., 2016; Yuan et al., 2018) while the PEG component promotes granulation tissue growth (Goh et al., 2016). Therefore, the PEG and CS molecules connected by hydrogen bonds in the composite can act synergistically to accelerate wound healing. Histological analyses by H&E and Masson staining verified that the application of the composite lubricant on the skin incision significantly reduced the inflammatory cell numbers and the scar size and significantly improved the re-epithelialization and collagen levels of the skin cells, confirming that the PEG/CS lubricant can effectively accelerate wound healing.

4 Conclusion

In this study, a water-based PEG/CS composite lubricant was successfully applied for wound healing. First, the PEG/CS lubricant was prepared via ultrasonic dispersion. Second, the samples were characterized by SEM, XRD, XPS, Raman spectroscopy, and FT-IR spectroscopy. The thermal stability of the sample was analyzed by TGA and its heat absorption and release were analyzed by DSC. The cell viability test verified that the PEG/CS lubricant had good biocompatibility, and the tribological test showed that it had a good lubrication effect. Finally, by establishing a full-thickness skin incision model on the backs of mice, and through H&E, Masson and CD31 immunofluorescence staining of the resultant skin tissue, we proved that the PEG/CS lubricant has a good

wound-healing effect. We expect the PEG/CS lubricant to be applicable clinically.

Data availability statement

The raw data supporting the conclusion of this article will be made available by the authors, without undue reservation.

Ethics statement

Ethical review and approval was not required for the animal study because this paper contains only simple cell experiments and a full-layer skin incision model of the mouse dorsal body without ethical implications.

Author contributions

LG and XH conceived the study and were in charge of overall direction and planning. XH, TZ, and PL performed the measurements; RA were involved in planning and supervising the work; and XH and LG processed the experimental data and performed the analysis. All authors discussed the results and commented on the manuscript.

Funding

This work was supported by the Natural Science Basic Research Program of Shaanxi (Program No.2020JQ-524).

Conflict of interest

The authors declare that the research was conducted in the absence of any commercial or financial relationships that could be construed as a potential conflict of interest.

Publisher's note

All claims expressed in this article are solely those of the authors and do not necessarily represent those of their affiliated organizations, or those of the publisher, the editors and the reviewers. Any product that may be evaluated in this article, or claim that may be made by its manufacturer, is not guaranteed or endorsed by the publisher.

References

Amann, T., Chen, W., Baur, M., Kailer, A., and Ruehe, J. (2020). Development of galvanically coupled plain bearings to reduce friction and wear. *Forsch. Ingenieurwes.* 84, 315–322. doi:10.1007/s10010-020-00416-z

Bi, B., Gao, S., Ruan, F., Shi, Y., Jiang, Y., Liu, S., et al. (2021). Analysis on clinical association of uterine scar diverticulum with subsequent infertility in patients underwent cesarean section. *Med. Baltim.* 100, e27531. doi:10.1097/MD.0000000000027531

Chen, L., Tu, N., Wei, Q., Liu, T., Li, C., Wang, W., et al. (2021). Inhibition of cold-welding and adhesive wear occurring on surface of the 6061 aluminum alloy by graphene oxide/polyethylene glycol composite water-based lubricant. *Surf. Interface Anal.* 54, 218–230. doi:10.1002/sia.7044

Chen, X., Cao, X., Jiang, H., Che, X., Xu, X., Ma, B., et al. (2018). SIKVAV-modified chitosan hydrogel as a skin substitutes for wound closure in mice. *Molecules* 23, 2611. doi:10.3390/molecules23102611

Dai, L., Wang, H., Xing, X., Peng, Y., Wang, Q., Li, Q., et al. (2022). An analysis of curative effect of combined transvaginal and hysteroscopic electrocauterization of partial endometrium to treat previous cesarean scar diverticulum. *Minerva Surg.* 77, 139–146. doi:10.23736/s2724-5691.21.08999-1

Dong, R., Yu, Q., Bai, Y., Wu, Y., Ma, Z., Zhang, J., et al. (2020). Towards superior lubricity and anticorrosion performances of proton-type ionic liquids additives for water-based lubricating fluids. *Chem. Eng. J.* 383, 123201. doi:10.1016/j.cej.2019.123201

Fobelets, M., Beeckman, K., Buyl, R., Healy, P., Grylka-Baeschlin, S., Nicoletti, J., et al. (2019). Preference of birth mode and postnatal health related quality of life after one previous caesarean section in three European countries. *Midwifery* 79, 102536. doi:10.1016/j.midw.2019.102536

Goh, M., Hwang, Y., and Tae, G. (2016). Epidermal growth factor loaded heparin-based hydrogel sheet for skin wound healing. *Carbohydr. Polym.* 147, 251–260. doi:10.1016/j.carbpol.2016.03.072

Gupta, B., Arora, A., Saxena, S., and Alam, M. S. (2009). Preparation of chitosan–polyethylene glycol coated cotton membranes for wound dressings: Preparation and characterization. *Polym. Adv. Technol.* 20, 58–65. doi:10.1002/pat.1280

Hu, F., Lu, H., Ye, Z., Zhang, S., Wang, W., and Gao, L. (2021). Slow-release lubrication of artificial joints using self-healing polyvinyl alcohol/polyethylene glycol/graphene oxide hydrogel. *J. Mech. Behav. Biomed. Mat.* 124, 104807. doi:10.1016/j.jmbbm.2021.104807

Huang, L., Huang, S., Yuan, Y., Li, Y., Chen, M., and Zhou, C. (2022). Reduced pregnancy and live birth rates after *in vitro* fertilization in women with cesarean section scar diverticulum: A retrospective cohort study. *J. Obstet. Gynaecol. Res.* 48, 146–154. doi:10.1111/jog.15061

Kollerup, A., Kjellberg, J., and Ibsen, R. (2022). Ageing and health care expenditures: The importance of age per se, steepening of the individual-level expenditure curve, and the role of morbidity. *Eur. J. Health Econ.* 23, 1121–1149. doi:10.1007/s10198-021-01413-x

Leng, Q., Li, Y., Pang, X., Wang, B., Wu, Z., Lu, Y., et al. (2020). Curcumin nanoparticles incorporated in PVA/collagen composite films promote wound healing. *Drug Deliv. (Lond).* 27, 1676–1685. doi:10.1080/10717544.2020.1853280

Liu, C., Yin, Q., Li, X., Hao, L., Zhang, W., Bao, Y., et al. (2021). A waterborne polyurethane-based leather finishing agent with excellent room temperature self-healing properties and wear-resistance. *Adv. Compos. Hybrid. Mat.* 4, 138–149. doi:10.1007/s42114-021-00206-3

Lu, H., Chen, L., Liu, Q., Li, Y., and Gao, L. (2021). Tribological properties of biocompatible molybdenum selenide nanoparticles as water lubrication additives for ultra-high molecular weight polyethylene/304 stainless steel contact. *Mat. Chem. Phys.* 272, 125053. doi:10.1016/j.matchemphys.2021.125053

Lu, H., Ren, S., Guo, J., Li, Y., Li, J., and Dong, G. (2017). Laser textured Co-Cr-Mo alloy stored chitosan/poly(ethylene glycol) composite applied on artificial joints lubrication. *Mater. Sci. Eng. C* 78, 239–245. doi:10.1016/j.msec.2017.03.195

Luo, Y., Su, B., and Zheng, X. (2021). Trends and challenges for population and health during population aging — China, 2015–2050. *China CDC Wkly.* 3, 593–598. doi:10.46234/ccdcw2021.158

Melo, M. N., Pereira, F. M., Rocha, M. A., Ribeiro, J. G., Diz, F. M., Monteiro, W. F., et al. (2020). Immobilization and characterization of horseradish peroxidase into chitosan and chitosan/PEG nanoparticles: A comparative study. *Process Biochem.* 98, 160–171. doi:10.1016/j.procbio.2020.08.007

Negro, S., Boutsikou, T., Briana, D. D., Tataranno, M. L., Longini, M., Proietti, F., et al. (2017). Maternal obesity and perinatal oxidative stress: The strength of the association. *J. Biol. Regul. Homeost. Agents* 31, 221–227.

Perumalsamy, J., Gupta, P., and Sangwai, J. S. (2021). Performance evaluation of esters and graphene nanoparticles as an additives on the rheological and lubrication properties of water-based drilling mud. *J. Pet. Sci. Eng.* 204, 108680. doi:10.1016/j.petrol.2021.108680

Phiromswad, P., Srivannaboon, S., and Sarajoti, P. (2022). The interaction effects of automation and population aging on labor market. *PLoS One* 17, e0263704. doi:10.1371/journal.pone.0263704

Qin, L., Feng, X., Hafezi, M., Zhang, Y., Guo, J., Dong, G., et al. (2018). Investigating the tribological and biological performance of covalently grafted chitosan coatings on Co-Cr-Mo alloy. *Tribol. Int.* 127, 302–312. doi:10.1016/j.triboint.2018.06.018

Rahman, M. H., Warneke, H., Webbert, H., Rodriguez, J., Austin, E., Tokunaga, K., et al. (2021). Water-based lubricants: Development, properties, and performances. *Lubricants* 9, 73. doi:10.3390/lubricants9080073

Ren, S., Lv, L., Ma, J., Lu, H., Guo, J., Li, X., et al. (2019). Slow-release lubrication effect of graphene oxide/poly(ethylene glycol) wrapped in chitosan/sodium glycerophosphate hydrogel applied on artificial joints. *Mater. Sci. Eng. C* 98, 452–460. doi:10.1016/j.msec.2018.12.109

Sun, J., Meng, Y., and Zhang, B. (2021). Tribological behaviors and lubrication mechanism of water-based MoO_3 nanofluid during cold rolling process. *J. Manuf. Process.* 61, 518–526. doi:10.1016/j.jmapro.2020.11.044

Tang, L., Zhang, Y., Li, C., Zhou, Z., Nie, X., Chen, Y., et al. (2022). Biological stability of water-based cutting fluids: Progress and application. *Chin. J. Mech. Eng.* 35, 3. doi:10.1186/s10033-021-00667-z

Tang, W., Huang, Z., and Wang, B. (2018). Synthesis of ionic liquid functionalized graphene oxides and their tribological property under water lubrication. *Fullerenes Nanotub. Carbon Nanostructures* 26, 175–183. doi:10.1080/1536383X.2017.1422246

Tang, W., Wang, B., Li, J., Li, Y., Zhang, Y., Quan, H., et al. (2019). Facile pyrolysis synthesis of ionic liquid capped carbon dots and subsequent application as the water-based lubricant additives. *J. Mat. Sci.* 54, 1171–1183. doi:10.1007/s10853-018-2877-0

Wang, L., Tieu, A. K., Zhu, H., Deng, G., Cui, S., and Zhu, Q. (2021). A study of water-based lubricant with a mixture of polyphosphate and nano-TiO_2 as additives for hot rolling process. *Wear* 477, 203895. doi:10.1016/j.wear.2021.203895

Wang, Y., Yu, Q., Cai, M., Zhou, F., and Liu, W. (2018). Halide-free PN ionic liquids surfactants as additives for enhancing tribological performance of water-based liquid. *Tribol. Int.* 128, 190–196. doi:10.1016/j.triboint.2018.07.018

Xu, X.-L., Zhou, G.-Q., Li, X.-J., Zhuang, X.-P., Wang, W., Cai, Z.-J., et al. (2016). Solution blowing of chitosan/PLA/PEG hydrogel nanofibers for wound dressing. *Fibers Polym.* 17, 205–211. doi:10.1007/s12221-016-5800-9

Yuan, T. T., Foushee, A. M. D., Johnson, M. C., Jockheck-Clark, A. R., and Stahl, J. M. (2018). Development of electrospun chitosan-polyethylene oxide/fibrinogen biocomposite for potential wound healing applications. *Nanoscale Res. Lett.* 13, 88. doi:10.1186/s11671-018-2491-8

Zha, D., Liu, P., and Shi, H. (2022). Does population aging aggravate air pollution in China? *Mitig. Adapt. Strateg. Glob. Chang.* 27, 15. doi:10.1007/s11027-021-09993-y

Zhang, W., Wang, Y., Sui, X., Sun, Y., and Chen, D. (2016). Effects of chitin and sepia ink hybrid sponge on the healing of burning wound rats and its impact on macrophages *in vitro*. *Acta Cir. Bras.* 31, 119–125. doi:10.1590/S0102-865020160020000006

Zhang, Z., Ye, Z., Hu, F., Wang, W., Zhang, S., Gao, L., et al. (2021). Double-network polyvinyl alcohol composite hydrogel with self-healing and low friction. *J. Appl. Polym. Sci.* 139, 51563. doi:10.1002/app.51563

Zheng, F., Kong, L., Wang, H., Fan, H., Gong, H., Zhang, K., et al. (2020). Transvaginal three-dimensional ultrasound combined with HD flow model for uterus scar diverticulum. *J. Infect. Public Health* 13, 2014–2019. doi:10.1016/j.jiph.2019.06.030

Zheng, Y., Asif, A., Amiri, A., and Polycarpou, A. A. (2021). Graphene-based aqueous drilling muds as efficient, durable, and environmentally friendly alternatives for oil-based muds. *ACS Appl. Nano Mat.* 4, 1243–1251. doi:10.1021/acsanm.0c02852

Zhou, X., Yang, X., Chen, H., Fang, X., and Wang, X. (2018). Obstetrical outcomes after vaginal repair of caesarean scar diverticula in reproductive-aged women. *BMC Pregnancy Childbirth* 18, 407. doi:10.1186/s12884-018-2015-7

frontiers | Frontiers in Bioengineering and Biotechnology

TYPE Original Research
PUBLISHED 28 September 2022
DOI 10.3389/fbioe.2022.921336

OPEN ACCESS

EDITED BY
Monireh Kouhi,
Isfahan University of Medical Sciences, Iran

REVIEWED BY
Masayuki Otsuki,
Tokyo Medical and Dental University, Japan
Loulwa Al-Saud,
King Saud University, Saudi Arabia

*CORRESPONDENCE
Beizhan Jiang,
jiangbeizhan@tongji.edu.cn

†These authors have contributed equally to this work

SPECIALTY SECTION
This article was submitted to Biomaterials, a section of the journal Frontiers in Bioengineering and Biotechnology

RECEIVED 15 April 2022
ACCEPTED 06 September 2022
PUBLISHED 28 September 2022

CITATION
Yan Y, Guan Y, Luo L, Lu B, Chen F and Jiang B (2022), Effects of immunoglobulin Y-loaded amorphous calcium phosphate on dentinal tubules occlusion and antibacterial activity. *Front. Bioeng. Biotechnol.* 10:921336. doi: 10.3389/fbioe.2022.921336

Effects of immunoglobulin Y-loaded amorphous calcium phosphate on dentinal tubules occlusion and antibacterial activity

Yanhong Yan[1†], Yun Guan[1†], Linjuan Luo[1], Bingqiang Lu[2], Feng Chen[2] and Beizhan Jiang[1*]

[1]Department of Pediatric Dentistry, Stomatological Hospital and Dental School of Tongji University, Shanghai Engineering Research Center of Tooth Restoration and Regeneration, Shanghai, China, [2]Department of Orthopedic, Spinal Pain Research Institute, Shanghai Tenth People's Hospital, School of Medicine, Tongji University, Shanghai, China

Aim: This study aimed to evaluate the effects of immunoglobulin Y (IgY)-loaded amorphous calcium phosphate (ACP) (IgY@ACP) on dentinal tubule occlusion and antibacterial activity.

Methodology: IgY@ACP was synthesized based on a biomimetic mineralization strategy. The structure was examined by transmission electron microscopy and Fourier transform infrared spectroscopy. The IgY release property was assessed *in vitro*. The cell biocompatibility of IgY@ACP was evaluated by CCK-8. The dentin disks were prepared using healthy human molars, and their dentinal tubules were exposed to EDTA. Subsequently, they were randomly selected and treated with or without IgY@ACP for 7 days. The tubule occlusion morphologies and newly formed layers were observed by scanning electron microscopy (SEM) and x-ray diffraction, respectively. To evaluate the acid resistance and abrasion resistance of IgY@ACP, dentin disks that were treated for 1 day were immersed in acid solution or subjected to a toothbrush. The antibacterial effects against *Streptococcus mutans* (*S. mutans*) were evaluated by colony-forming unit (CFU) counting, adhesion property assessment, and crystal violet and live/dead bacterial staining. Finally, the occlusion effect was evaluated in rat incisors *in vivo*. One-way analysis of variance (ANOVA) was performed for statistical analysis. The level of significance was set at 0.05.

Results: IgY@ACP presented an amorphous phase with a nanosize (60–80 nm) and sustained release of protein within 48 h. The CCK-8 results showed that IgY@ACP had good biocompatibility. After treatment with IgY@ACP for 1 day, the majority of dentinal tubules were occluded by a 0.3-μm-thick mineralized layer. Seven days later, all dentinal tubules were occluded by mineralization with a thickness of 1.4 μm and a depth of 16 μm. The newly mineralized layer showed hydroxyapatite-like diffraction peaks. In addition, IgY@ACP had good acid and abrasion resistance. After treatment with IgY@ACP, the CFU counting and adhesion rate of *S. mutans* were

significantly reduced, the crystal violet staining was lighter, and the *S. mutans* staining revealed more dead cells. Most importantly, IgY@ACP had a certain occluding property in rat incisors *in vivo*.

Conclusion: IgY@ACP can effectively occlude dentinal tubules with acid-resistant stability and has prominent anti-*S. mutans* effects, rendering it a potentially suitable desensitization material in the clinic.

KEYWORDS

dentin hypersensitivity, amorphous calcium phosphate, mineralization, antibacterial activity, IgY

1 Introduction

Dentin hypersensitivity (DH) is a common dental symptom that originally results from exposure of dentinal tubules in response to various stimuli such as physical, chemical, mechanical, and other physiological stimuli (Liu et al., 2020). DH often results in severe pain, with a high incidence rate ranging from 4 to 74% (Anthoney et al., 2020). The accepted "hydrodynamic theory" states that external stimuli could cause abnormal movement of fluid within dentinal tubules, stimulating the terminals of pulpal nerve fibers and then causing transient acute pain (Brännström and Aström, 1972). Based on the theory, there are several approaches to DH treatment: 1) the application of desensitizing agents to reduce intra-dental nerve excitability, such as potassium nitrate or potassium chloride (Liu and Hu, 2012). 2) Dental lasers aim to reduce dentin hypersensitivity by coagulating proteins in dentinal tubules, while lasers might destroy the dentin (Ozlem et al., 2018). 3) Physical occlusion of the exposed dentinal tubules, such as glutaraldehyde, oxalate fluoride, calcium sodium phosphosilicate (CSPS; NovaMin, Weybridge, United Kingdom), and casein phosphopeptide-amorphous calcium phosphate-containing crème (CPP-ACP). NovaMin is a bioactive glass material that will release calcium and phosphate ions to form hydroxycarbonate apatite on the dentin surface. Clinical studies showed that toothpastes containing NovaMin are efficacious for DH relief (Hall et al., 2017). CPP-ACP is commonly used for remineralization actin in dentin and enamel, which will lead to the occlusion of the dentinal tubules (Guanipa Ortiz et al., 2019). In addition, due to the defects of enamel and dentin in DH, the exposed dentin is susceptible to dental caries caused by *Streptococcus mutans* (*S. mutans*) (Takahashi and Nyvad, 2016). Therefore, it is highly desirable to develop a biomaterial that can not only effectively alleviate DH by occluding exposed dentinal tubules, but also can simultaneously inhibit *S. mutans* to prevent caries (Kawasaki et al., 2001).

In various desensitization materials based on occluding dentinal tubules, calcium phosphate which has excellent biocompatibility and bioactivity occupies an important position due to chemical properties similar to the inorganic component of human teeth (Prati and Gandolfi, 2015; Berg et al., 2020). The diameter of dentinal tubules is about 4–8 μm, and the pressure of dentinal tubules is outward. The calcium phosphate nanoparticles have facilitation to flow into the dentinal tubules. Then, these nanoparticles can further induce the formation of insoluble mineral deposits on the wall of deep dentinal tubules in the oral environment, to achieve the desired occluding effect on dentinal tubules. There are many strategies to prepare calcium phosphate-based materials. For example, co-precipitation is one of the simple methods to prepare calcium phosphate by using calcium and phosphate salts, which can control the crystal structure to obtain amorphous calcium phosphate (ACP), hydroxyapatite (HA), and other chemical phases (Wang et al., 2017). In these different calcium phosphate materials, ACP, which is usually a precursor of HA, was widely used as a nanocarrier to load and deliver biological macromolecules, such as proteins, peptides, and enzymes (Chen et al., 2011; Qi et al., 2014). It has been reported that ACP was successfully synthesized in simulated body fluid solution (Tas, 2000). As a conventional cell culture medium, Dulbecco's modified Eagle's medium (DMEM) has abounded ions of calcium and phosphate, and organic molecules of amino acids, which can simulate the microenvironment of natural biological cells and has indicated a potential for preparing ACP and its complex. Zhou et al. have recently reported a biomimetic mineralization strategy to prepare mineralized ALP nanoparticles (ALP-contained ACP), by using the inter-reaction between ALP and calcium ions from DMEM (Zhou et al., 2022). This biomimetic mineralization strategy has high universality in constructing different protein–ACP complex materials.

Immunoglobulin Y (IgY), the antibody derived from the eggs of hens immunized against anti-*S. mutans*, is normally used for caries treatment (Pereira et al., 2019). As a product of biological immune antibody technology, IgY has the advantages of better biocompatibility and high specificity to cariogenic bacteria. Studies have demonstrated that it is a specific inhibitor against *S. mutans* that prevents it from adhering to the tooth surface by blocking adhesion receptors involved in colonization

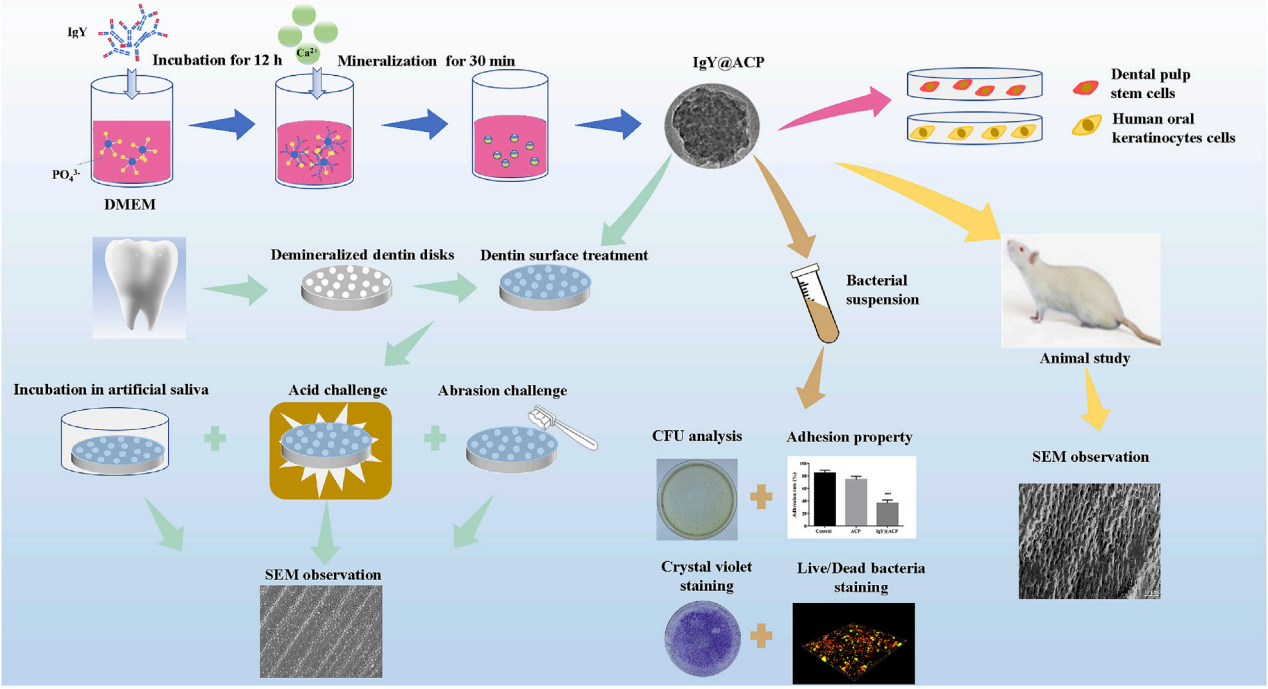

FIGURE 1
Schematic diagram of the IgY@ACP samples prepared based on the DMEM biomimetic mineralization strategy.

or aggregation (glucan-binding site) or blocking the activation of glucosyltransferase (GTF) (Krüger et al., 2004; Bachtiar et al., 2016b). In our previous study (Ma et al., 2017), IgY loaded on porous calcium carbonate microspheres was applied to treat DH. But the complex synthesis process and the cytotoxicity of the porous calcium carbonate microspheres limited its clinical conversion, due to its different chemical compositions with the teeth.

In this study, a strategy for the preparation of IgY-loaded ACP (IgY@ACP) has been developed, which combines and maximizes the advantages of IgY and ACP in enabling the dentin surface to combat dentin hypersensitivity and caries. The characterization, biocompatibility, and *in vitro* and *in vivo* effects on dentinal tubule occlusion and antibacterial activity against *S. mutans* of IgY@ACP have been well studied. The results from these experiments have indicated a significant potential of IgY@ACP as a multifunctional material in effectively occlude dentinal tubules and anti-*S. mutans*.

2 Materials and methods

All experiments were approved and performed according to the principles recommended for experimentation with humans and animals established by the Ethics Committee of the Affiliated Stomatology Hospital of Tongji University ([2019]-DW-059). The complete schematic diagram of the IgY@ACP study is shown in Figure 1.

2.1 Preparation of IgY@ACP

IgY@ACP was prepared by biomimetic mineralization in Dulbecco's modified Eagle's medium (DMEM; HyClone, USA) following a previous study with some modifications (Chen et al., 2017). Briefly, 100 mg of IgY powder (Yasheng Biological Technology, Hangzhou, China) was added to 50 ml of fresh DMEM medium and then incubated in a constant-temperature oscillator (Zhichu, Shanghai, China) for 12 h (37°C, 180 rpm) to reach equilibrium. Afterward, 1 ml of prepared $CaCl_2$ (1 mol/L) (Aladdin, Shanghai, China) was added to the previously mentioned solution to induce mineralization of IgY, which was subsequently maintained at 37°C and 5% CO_2. After incubation for 30 min, the resulting mixture was transferred into centrifugal tubes and centrifuged at a speed of 9,000 rpm/min for 5 min to obtain the precipitates, and the precipitates were thoroughly triple-washed with deionized water to obtain IgY@ACP samples. Based on the preparation procedure mentioned earlier, the corresponding IgY-free calcium phosphate (named ACP) was prepared without the addition of IgY. After centrifugation, some samples were dispersed and kept in absolute ethanol for material characterization and protein determination *in vitro*, and the others were freeze-dried for subsequent studies.

2.2 Characterizations of IgY@ACP

The microstructures of ACP and IgY@ACP samples were observed by transmission electron microscopy (TEM, Tecnai G2 F20 S-TWIN, FEI, CA, USA). Briefly, the samples were suspended in ethanol and fully treated in an ultrasonic processor to form dispersions. A drop (50 uL) of dispersion was placed on a copper wire for TEM observation, and selected electron diffraction (SAED) and elemental mapping analysis were performed simultaneously. The size distributions of the samples were obtained by measuring the size of the particles in the TEM micrographs at the same magnification using ImageJ software (National Institutes of Health, Bethesda, MD, USA). Fourier transform infrared (FTIR) was used to analyze the elements in the samples. For this experiment, the KBr pellet technique was used by mixing 1 mg of the powdered sample with 100 mg of spectroscopic-grade KBr in an agate mortar and pressing it into round flakes. The prepared samples were detected using an FTIR spectrometer (FTIR-IS50, Thermo Fisher, Waltham, MA, United States) in the 4,000–400 cm^{-1} wavelength range.

2.3 Analysis of IgY release *in vitro*

For assessment of the IgY protein release property *in vitro*, 10 mg of freeze-dried IgY@ACP powder was dissolved in 10 ml of phosphate-buffered saline (PBS; Keygen Biotech, Nanjing, China) (pH = 7.4) and placed in a temperature oscillator with constant shaking (37°C, 180 rpm). At the given time points (5, 10, 20, and 40 min; 1, 2, 3, 6, 12, 18, 24, 30, 42, and 48 h), a certain volume of solution was extracted and centrifuged to collect the supernatant, which was then replaced with an equal volume of fresh PBS solution. The previously mentioned supernatant was incubated with a BCA protein assay kit (Beyotime, Shanghai, China) in a 96-well plate (Corning, USA) for 2 h in the dark to detect protein concentrations at corresponding time points. The OD value of each well at a wavelength of 562 nm was observed with a microplate reader (Biotek, Winooski, Vermont, USA). The protein concentrations of the samples at corresponding time points were calculated according to the standard protein curve equation and the sample volume used, and finally, the cumulative protein release rate curve was generated.

2.4 Biocompatibility study

Human oral keratinocytes (HOK) were kindly provided by Professor He Yuan from Tongji University. Human dental pulp stem cells (hDPSCs) were isolated and characterized by flow cytometry as described in our previous study (Xu et al., 2019). HOK and hDPSCs were chosen for cell biocompatibility evaluation using Cell Counting Kit-8 (CCK-8; Beyotime, Shanghai, China). Cells (5×10^3 cells/well) were seeded in 96-well plates and incubated at 37°C until 80–85% confluence was achieved. Then, DMEM containing 10% fetal bovine serum (FBS; Gibco, CA, USA) with different concentrations (25, 50, 100, and 200 μg/ml) of IgY@ACP and ACP were added into 96-well plates at a volume of 200 μL/well. After incubation for 24 h, all media were removed and washed with PBS twice. Then, 100 μL of DMEM with 10 μL of CCK-8 solution was added to each well (n = 6, each group). The medium without samples served as the control, and the wells without cells were set as the blank control. After 2 h, the absorbance of the supernatant at 450 nm was examined using a microplate reader.

2.5 Evaluation of tubule occlusion

The artificial saliva used in our study was prepared following a previous study (Zhang et al., 2018). Then, 0.07 g $CaCl_2$, 0.04 g $MgCl_2$, 2.23 g KCl, 0.54 g KH_2PO_4, and 4.76 g hydroxyethyl piperazine ethanesulfonic acid were dissolved in 80 ml of deionized water, and 0.1 mol/L sodium hydroxide was added to adjust the pH to 7.0. The solution was then transferred to a volumetric flask, and deionized water was added until the solution volume reached 1.00 L. A small amount of thymol was added to prevent fungal growth. The prepared artificial saliva was stored at room temperature for the study. All the aforementioned chemical reagents were purchased from Shanghai Aladdin Biochemical Technology Co., Ltd.

Healthy human molars were collected after informed consent was obtained from the donors and cleaned by ultrasound. Using a slow cutting machine under water cooling, 1 ± 0.1-mm dentin disks were prepared by cutting teeth perpendicular to dentinal tubules, removing the crown enamel, and exposing the middle dentin. The obtained dentin disks were polished with different meshes of silicon carbide (SiC; Goral, USA) sandpaper to make the surface smooth. Then, dentin disks were cleaned with deionized water for 1 min and stored in a 0.1% thymol solution.

2.5.1 The dentinal tubule occlusion of IgY@ACP

Demineralized dentin disks were obtained by immersion in 17% ethylene diamine tetraacetic acid (EDTA; Sigma–Aldrich, MO, USA) for 5 min (João-Souza et al., 2019) to expose the dentinal tubules and were randomly treated with ACP, IgY@ACP, or NovaMin (Sensodyne Repair and Protect, GSK, Canada) (n = 12, each group). In the ACP and IgY@ACP groups, the freeze-dried sample powder and deionized water were fully mixed to make a slurry of samples with a powder/liquid ratio of 10 mg/200 μL. The disposable micro applicator (TPC Advanced Technology, CA, USA) was dipped into the slurry, and the surface of the dentin disks was evenly smeared with the attached samples for 2 min. Then, the treated dentin disks were cleaned with deionized water to remove residual samples, immersed in the prepared artificial saliva, and incubated at

37 °C. Demineralized dentin disks without material treatment immersed in artificial saliva were used as the control group. The artificial saliva was replaced with fresh solution every day. Then, dentin disks that were treated for 1 and 7 days were randomly selected (n = 6, each group), rinsed several times with deionized water, and air-dried at room temperature before examination. The surface and cross-section of all dentin disks were observed using scanning electron microscopy (SEM, S4800, Hitachi, Japan) at 5 kV. Micrographs at magnifications of 1,000× and 5,000× were captured. Subsequently, the crystal orientation and mineral phase of the newly formed layer of dentin disks were analyzed by x-ray diffraction (XRD; Rigaku D/max2500, Japan) and compared with normal and demineralized dentin disks.

2.5.2 Acid resistance and abrasion resistance of IgY@ACP

To test the acid and abrasion resistance of IgY@ACP, dentin disks (n = 6, each group) treated with ACP, IgY@ACP, or NovaMin for 1 day were randomly divided into two subgroups. One subgroup was immersed in a 6% (W/V) citric acid solution (pH = 1.5) for 2 min to test the resistance to strong acid erosion, and the other subgroup was mechanically brushed with a soft-bristled toothbrush (Colgate, NY, USA) at an inclination of approximately 90° with a constant loading for 2 min to test the resistance to daily abrasion. All dentin disks were rinsed several times with deionized water. Then, the surface morphology of the treated dentin disks was observed by SEM at 5 kV.

2.6 Antibacterial effects of IgY@ACP

S. mutans (ATCC25175) was obtained from the American Type Culture Collection (Manassas, VA, USA). *S. mutans* preserved in cryoprotectant was resuscitated on brain heart infusion (BHI; Haibo, Qingdao, China) agar plates and cultured in a 37 °C anaerobic environment (80% N_2, 10% CO_2, and 10% H_2) for 48 h. A single colony was selected and incubated in a fresh BHI liquid medium for 2–3 generations until the logarithmic growth stage. Then, the bacterial suspension was adjusted to a concentration of approximately 10^5 colony-forming units (CFUs)/mL prior to use.

2.6.1 CFU analysis

The ACP and IgY@ACP samples were dispersed and diluted to a 10 mg/ml sample suspension in a BHI medium. The bacterial suspension (100 μL) and sample suspension (100 μL) were thoroughly mixed, which obtained a final concentration of 5 mg/ml, and then 200 μL mixture were added to each well of a 96-well plate and incubated in an anaerobic environment at 37°C for 24 h (n = 6, each group). Then, after fully mixing the suspension, 5 μL of each mixture was extracted and diluted ten-fold serially, then 50 μL mixture was added onto BHI agar plates, and the plates were anaerobically cultivated for 48 h. Bacterial suspension and an equivalent volume of BHI medium (without samples) were added to each well as a control group. Then, the CFUs of each plate were photographed by a camera (Canon, Japan) and manually calculated.

2.6.2 Bacterial adhesive study

The adhesion property of *S. mutans* was further investigated. Some original tubes were obtained and divided into the following three groups (n = 6, each group). Group 1: 4.5 ml of ACP (10 mg/ml) suspension with 500 μL of bacterial suspension; Group 2: 4.5 ml of IgY@ACP (10 mg/ml) suspension with 500 μL of bacterial suspension; and Group 3: 4.5 ml of BHI medium with 500 μL of the bacterial suspension. All tubes were placed at a 30° inclination and incubated anaerobically. Take Group 1 as an example. After 24 h of anaerobic culture, the supernatant liquid in the original tube was gently poured into the first new tube, which included nonadhesive bacteria and was named A-1. Subsequently, 5 ml of fresh PBS was added to the original tube, gently washed, shaken, and poured into the second new tube, which included nontightly adhered bacteria and was named B-1. Finally, 5 ml of fresh PBS was added to the original tube, and all the bacteria was scraped off the wall and poured into the third new tube, which included tightly adhered bacteria and was named C-1. Three new tubes were centrifuged, and the supernatants were discarded. Then, after 5 ml of fresh PBS was added and fully mixed, the absorbance of bacteria in the three new tubes was determined at 600 nm by a microplate reader. The adhesion rate of tightly adhered bacteria in Group 1 was obtained by the following calculation: adhesion rate (%) = C-1/(A-1+B-1+C-1) ×100%, where A-1, B-1, and C-1 corresponded to OD 600 values in the three new tubes. Group 2 and Group 3 underwent the same procedure.

2.6.3 Crystal violet staining

The biofilm formation of *S. mutans* was investigated by crystal violet staining. Similarly, the bacterial suspension (500 μL) and sample suspension (500 μL) were thoroughly mixed, and then 1 ml mixture was added to each well of a 24-well plate (Corning, USA) and incubated in an anaerobic environment (n = 6, each group). Bacterial suspension and an equivalent volume of BHI medium (without samples) were added to each well as a control group. After culturing for 24 h, the medium was aspirated, and the remaining bacteria were gently washed with PBS three times. Then, the plate was fixed with 4% (W/V) paraformaldehyde (Sinopharm Chemical, Shanghai, China) for 20 min and washed with PBS three times. At room temperature, 0.1% crystal violet staining solution (Sangon Biotech, Shanghai, China) was added to each well. The staining was applied for 20 min, and the samples were then washed with PBS and photographed by a camera. For quantitative analysis, 400 μL of 95% ethanol (Sinopharm Chemical, Shanghai, China) was added to each well after air

drying and shaking for 15 min to dissolve the crystal violet staining solution. The absorbance was measured at 600 nm with a microplate reader. The lighter the dye color was, the less the biofilm that had formed.

2.6.4 Live/dead bacterial staining

To further assess the live and dead status of *S. mutans* in the formed biofilm, live/dead bacterial staining was performed. Similarly, 1 ml of the earlier mentioned mixture was added to the confocal microscopy dishes (Corning, USA) at 37 °C for 24 h in an anaerobic environment (n = 6, each group). Bacterial suspension and an equivalent volume of BHI medium (without samples) were added to each well as a control group. After incubation, the samples were gently rinsed with PBS three times to remove nonadherent bacteria. Subsequently, the *S. mutans* biofilms grown on the dishes were stained using a Live/Dead BacLight Bacterial Viability Kit (40274ES60, Yeasen, Shanghai, China) according to the manufacturer's instructions. Live bacterial cells were stained with DMAO and, thus, emitted green fluorescence, whereas dead cells were stained with EthD-III and, therefore, emitted red fluorescence. Then, for each dish, a 20-μm-thick 3D image was captured using confocal laser scanning microscopy (CLSM; Carl Zeiss, Oberkochen, Germany) at excitation wavelengths of 530 nm (DMAO) and 620 nm (EthD-III). Images were obtained with a ×40 objective, and at least three images were randomly collected from each dish.

2.7 Animal study

Six SD rats (6–8 weeks old), weighing 200–250 g, provided 24 teeth (upper and lower incisors) for this study and were randomly divided into the control group and IgY@ACP group. After anesthetization with 2% pentobarbital (Sinopharm Chemical, Shanghai, China) intraperitoneal injection, cavities of 0.3 mm depth were prepared in the buccal and cervical regions of rat incisors using a standard bur (Komet, Germany) on a high-speed handpiece with water cooling. Prior to the treatments, all the cavities were treated with 17% EDTA on small cotton pellets, which were changed every 30 s for 15 min, to remove the smear layer. Each tooth was repeated to smear the IgY@ACP slurry daily for 2 min and then rinsed with PBS. The teeth were treated without IgY@ACP as a control group. After daily treatment for four consecutive days, the animals were anesthetized, and the teeth were carefully extracted to avoid damage to their surface. The tooth surface morphology of the rats was also observed by SEM at 5 kV.

2.8 Statistical analysis

All studies were repeated at least three times, and mean values were calculated and expressed with an error bar representing ±SD. SPSS (SPSS 16.0, IBM Corporation, Armonk, NY, USA) was applied for statistical analysis with a one-way analysis of variance (ANOVA). Significant differences were assessed at $p < 0.05$.

3 Results

3.1 Characterization of IgY@ACP

The morphology and particle size of the IgY@ACP composite prepared by the DMEM biomimetic mineralization strategy were observed by TEM. As shown in Figure 2, ACP exhibited the morphology of nanospheres with sizes of approximately 120–160 nm (Figures 2A,G), while IgY@ACP had a similar shape but a much smaller size, 60–80 nm (Figures 2B,H). SAED results indicated that neither sample showed distinct reflections, revealing their amorphous phases. Element mapping analysis revealed that IgY@ACP contained Ca, P, C, and N (Figures 2C–F). In the FTIR spectra of IgY@ACP, the bands at 2,998, 2,965, and 1,556 cm^{-1} could be assigned to IgY molecules, and those at 567, 870, and 1,061 cm^{-1} corresponded to calcium phosphate (Figure 2I).

3.2 IgY release *in vitro*

The IgY protein release profiles of IgY@ACP in PBS are shown in Figure 2J. Within the first 2 h, approximately 19.3% of the loaded protein was released into the PBS medium. Then, the IgY protein continued to be released at a gradually slower rate, and the cumulative release rate reached 29.0% at 24 h and 32.3% at 48 h.

3.3 Biocompatibility study

The biocompatibility of IgY@ACP and ACP samples was investigated by coculture with HOK cells and hDPSCs and is shown in Figure 3. For HOK cells, the cell viability increased with increasing sample concentration (Figure 3A). Interestingly, the cell viability of HOK cells was much higher in the IgY@ACP group, ranging from 100 to 200 μg/ml ($p < 0.05$). For hDPSCs, the cell viability was above 90% at all concentrations in both samples, with no significant difference ($p > 0.05$) (Figure 3B).

3.4 Evaluation of tubule occlusion

The surface and cross-sectional images of dentin disks in all groups are shown in Figure 4. As in the DH mimic model, the dentinal tubules in the control group were completely exposed, and the inner space was vacant due to EDTA demineralization

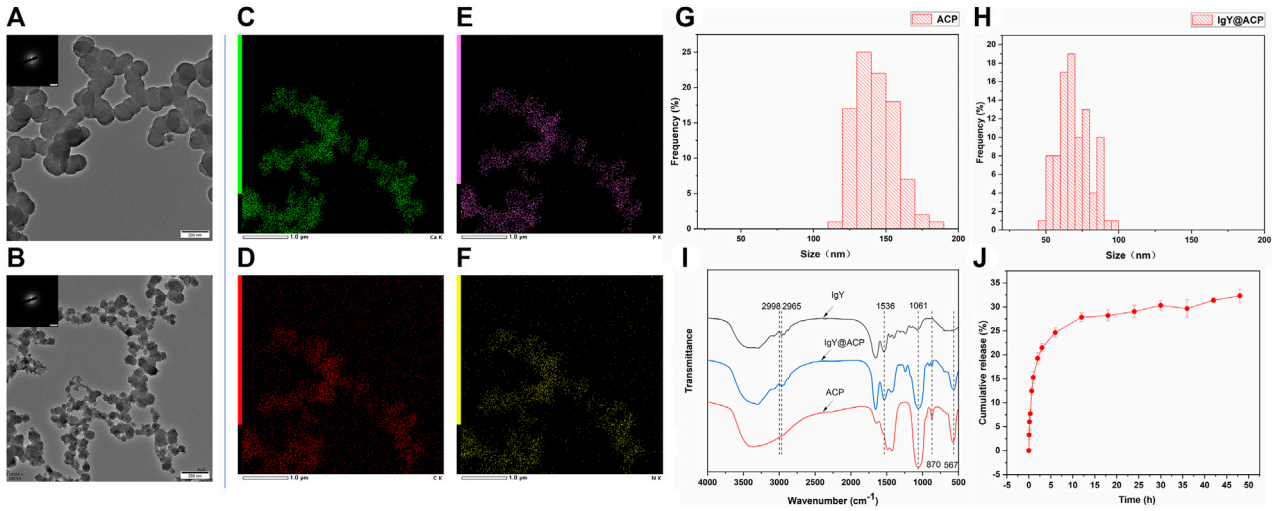

FIGURE 2
Characterization of ACP and IgY@ACP. TEM images of ACP **(A)** and IgY@ACP **(B)**. Element surface scanning of IgY@ACP **(C–F)**. Size distribution analysis of ACP **(G)** and IgY@ACP **(H)**. FTIR spectra of ACP, IgY, and IgY@ACP **(I)**. The release IgY protein curve of IgY@ACP in PBS **(J)**.

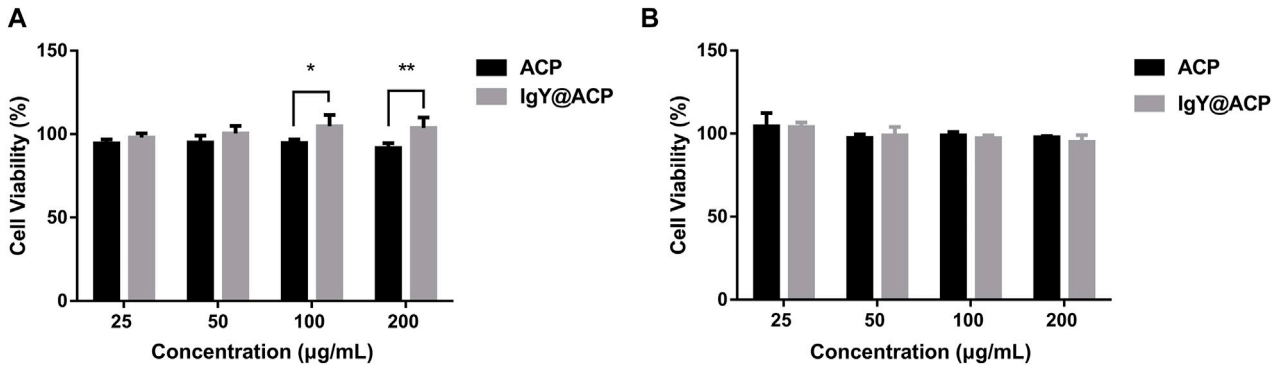

FIGURE 3
The cell viability of HOK **(A)** and hDPSCs **(B)** cocultured with ACP and IgY@ACP at different concentrations (25, 50, 100, and 200 μg/ml) for 24 h, indicating that the samples had better biocompatibility. Statistical significance was set at $*p < 0.05$, $**p < 0.01$, and $***p < 0.001$.

(Figures 4A,E,I and M). To treat DH, ACP, IgY@ACP, or NovaMin were evenly applied to the surface of dentin disks, followed by incubation in artificial saliva. After treatment with the NovaMin for 1 day, only a few dentinal tubules were occluded, and the inner space was still vacant (Figures 4B,F). Also, similar results were found in the ACP group (Figures 4C,G). After treatment with IgY@ACP for 1 day, most of the dentinal tubules were occluded by a layer of materials with an average thickness of 0.3 μm, and the remaining opening of nonfully covered tubules was significantly narrowed due to the partially occluding effect of the materials (Figures 4D,H), which was better than that of NovaMin and ACP group. Seven days later, all dentinal tubules were occluded, and sparse lamellar material existed in the inner space in the ACP group (Figures 4K,O). Similarly, all dentinal tubules were occluded, with their surface presenting a thicker (1.4 μm) dense mineralized granular layer in the IgY@ACP group. The cross-sectional images show that the IgY@ACP precipitates intratubularly with a penetration depth of approximately 16 μm and was closely adhered to the wall (Figures 4L,P). However, some tubules were still open in the NovaMin group, with a few particles inside the tubules (Figures 4J,N).

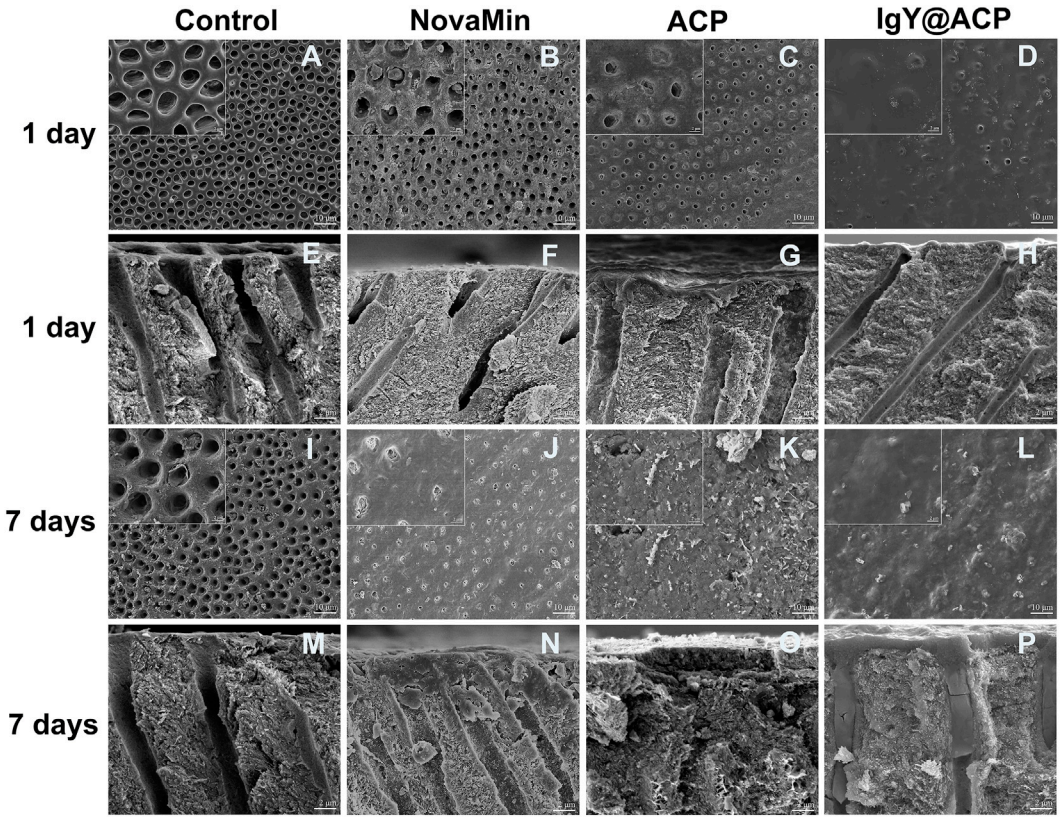

FIGURE 4
SEM micrographs of the surface and cross-section of dentin disks after treatment with NovaMin **(B,F)**, ACP **(C,G)**, and IgY@ACP **(D,H)** for 1 day and treatment with NovaMin **(J,N)**, ACP **(K,O)**, and IgY@ACP **(L,P)** for 7 days. Dentin disks without treatment for 1 day **(A,E)** and 7 days **(I,M)** were used as the control group.

The types of newly formed crystals on the dentin disks were investigated by XRD. As shown in Figure 5, the diffraction peaks of (002), (210), (211), (112), (213), and (004) at 2θ = 25.9°, 28.9°, 31.7°, 32.8°, 49.5°, and 53.2°, respectively, are characteristic of HAp and appear on the normal dentin disks. In the XRD pattern of demineralized dentin disks, some characteristic peaks, such as those reflected by (210) and (112), were obviously weakened or disappeared. After treatment with ACP or IgY@ACP for 1 day or 7 days, the characteristic diffraction peaks were clearly recovered or even enhanced, which was similar to that of NovaMin.

The acid- and abrasion-resistances of dentin disks treated with IgY@ACP for 1 day are shown in Figure 6. Compared with the control group, the majority of dentinal tubules remained occluded in the IgY@ACP group after acid treatment, even though a few occluded tubules were damaged and washout traits could be seen on the dentin surface. However, most of the dentinal tubules were exposed in the NovaMin and ACP groups (Figures 6A–D). After the abrasion treatment, compared with the control group, there were still some occluded tubules in the NovaMin and ACP group, and occluding materials still existed in the deep part of the tubules in the IgY@ACP group, although the occluding materials on the dentin surface fell off (Figures 6E–H). In the animal model, the surface images of rat dentin were observed using SEM, as shown in Figure 7. In the control group, most of the dentinal tubules of the rats were exposed to different sizes due to EDTA demineralization (Figures 7A,C). After treatment with IgY@ACP, the dentin surface was covered with mineralized particles, and a few exposed dentin tubules remained (Figures 7B,D).

3.5 In *vitro* antibacterial effects

The antibacterial effects of IgY@ACP against planktonic *S. mutans in vitro* were evaluated by CFU counting and assessing the adhesion rate. As shown in Figures 8A,B, the CFU counting showed that the total number of viable bacterial colonies in the IgY@ACP group decreased significantly compared with that in the ACP and control groups (without any materials) ($p < 0.001$). The adhesion property of *S. mutans* was also evaluated after IgY@ACP treatment. The adhesion rate in the IgY@ACP group

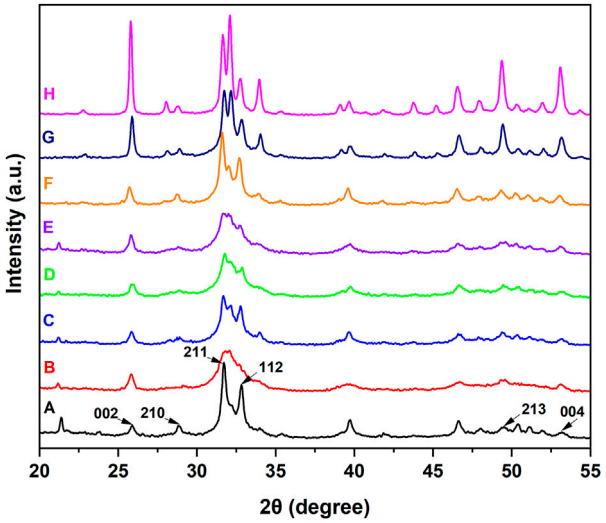

FIGURE 5
XRD patterns of dentin disks after treatment with NovaMin **(C)**, ACP **(D)**, or IgY@ACP **(E)** for 1 day and treatment with NovaMin **(F)**, ACP **(G)**, or IgY@ACP **(H)** for 7 days. Normal **(A)** and demineralized dentin disks **(B)** were used as the control group.

decreased significantly after incubation for 24 h, as shown in Figure 8C ($p < 0.001$).

The biofilm formation of *S. mutans* after treatment with IgY@ACP was evaluated, as shown in Figure 9. In Figure 9A, a dense biofilm structure can be observed with strong staining in the ACP and control groups. The IgY@ACP group presented a thin and loose structure with an obviously lighter staining color. The quantitative analysis showed that the OD value of the IgY@ACP group decreased significantly compared with that of the ACP and control groups ($p < 0.001$). Similar results were also found by CLSM after live/dead bacterial staining; green and red fluorescence imaging showed the live (green) and dead (red) bacterial distribution within the biofilms, respectively. As shown in Figure 9B, after treatment for 24 h, the biofilm structure of *S. mutans* in the IgY@ACP group displayed mostly red fluorescence, while that of *S. mutans* in the ACP and control groups displayed mostly green fluorescence.

4 Discussion

To treat DH by both occluding exposed dentinal tubules and inhibiting the main oral bacteria, a new desensitization material, IgY@ACP, was synthesized via biomimetic mineralization. Unlike the conventional strategy in which protein is simply adsorbed on prepared calcium phosphate, we loaded IgY in ACP using a biomimetic mineralization strategy. Briefly, IgY was mineralized with ACP in DMEM to form calcium phosphate products. Similar to simulated body fluid (SBF), DMEM has supersaturated Ca^{2+} and PO_4^{3-} ions stabilized mainly by extra organic components, for example, amino acids and glucose (Tas, 2013; Tas, 2014; Fu et al., 2019). Upon further addition of Ca^{2+} ions, the stability is disturbed, and ACP forms with adsorbed IgY. TEM and SAED results showed that the products were amorphous as well as that the metastable feature favored the release of Ca^{2+} and PO_4^{3-} ions and further promoted mineralization of dentin. The IgY@ACP particle size was approximately 60–80 nm, much smaller than the diameter of the dentinal tubule (4–8 μm), enabling it to enter the inner dentinal tubule to achieve deep occlusion. The FTIR results showed that the spectrum of IgY@ACP had a specific IgY

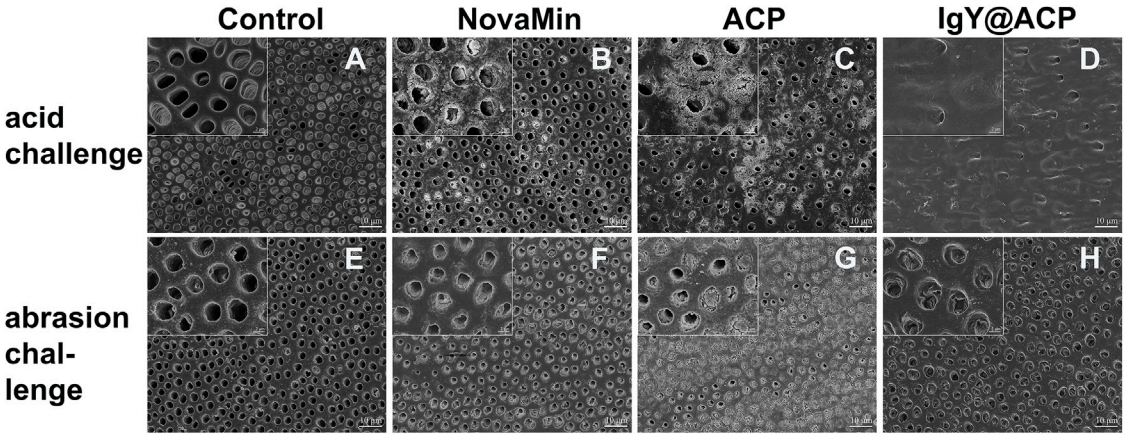

FIGURE 6
SEM micrographs of dentin disks treated with NovaMin, ACP, or IgY@ACP after 6% critic acid **(B–D)** and abrasion **(F–H)** challenges. Dentin disks without treatment **(A,E)** were used as the control group.

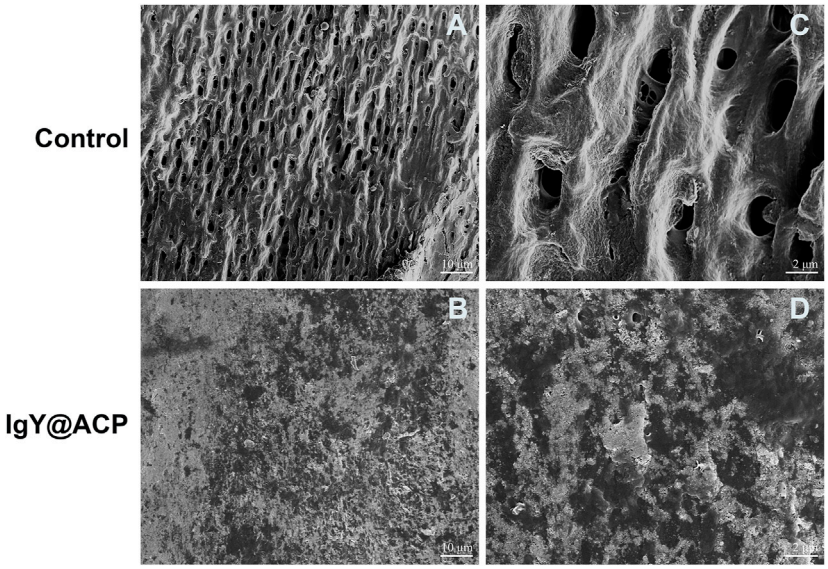

FIGURE 7
SEM micrographs of the rat dentin surface after treatment with the control **(A)** and IgY@ACP **(B)** for 4 days. **(C)** and **(D)** correspond to the enlarged images of **(A)** and **(B)**, respectively.

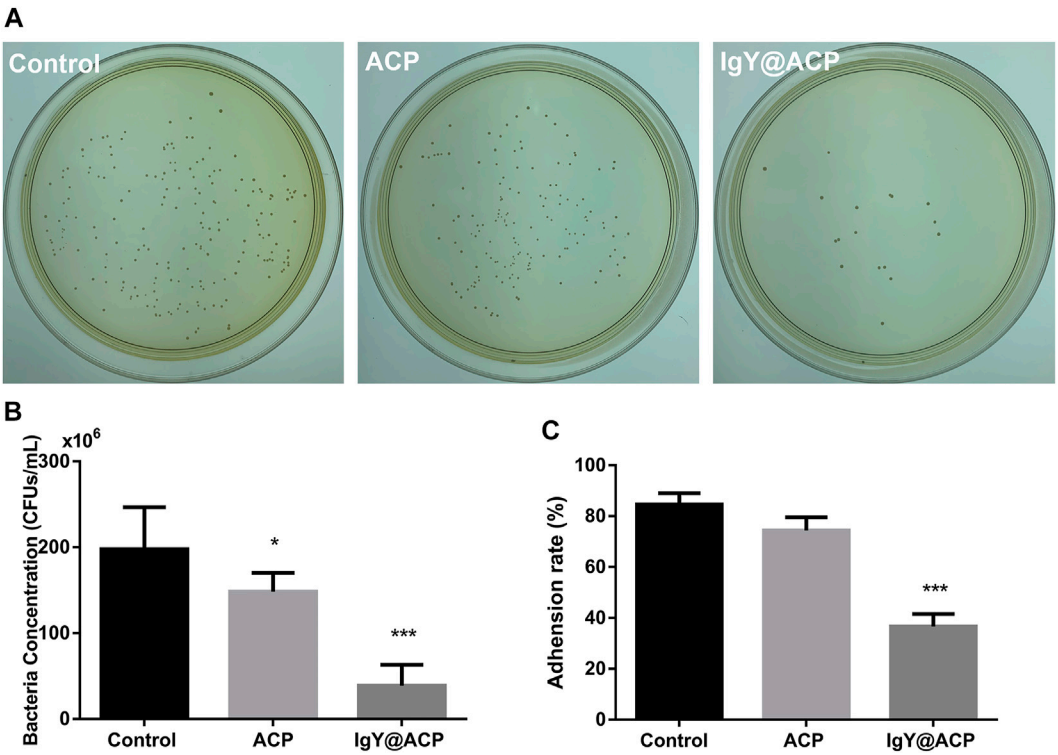

FIGURE 8
The antibacterial effects of IgY@ACP against planktonic *S. mutans* on CFU counting **(A,B)** and adhesion rate **(C)**. The significance level was set at $*p < 0.05$, $**p < 0.01$, and $***p < 0.001$.

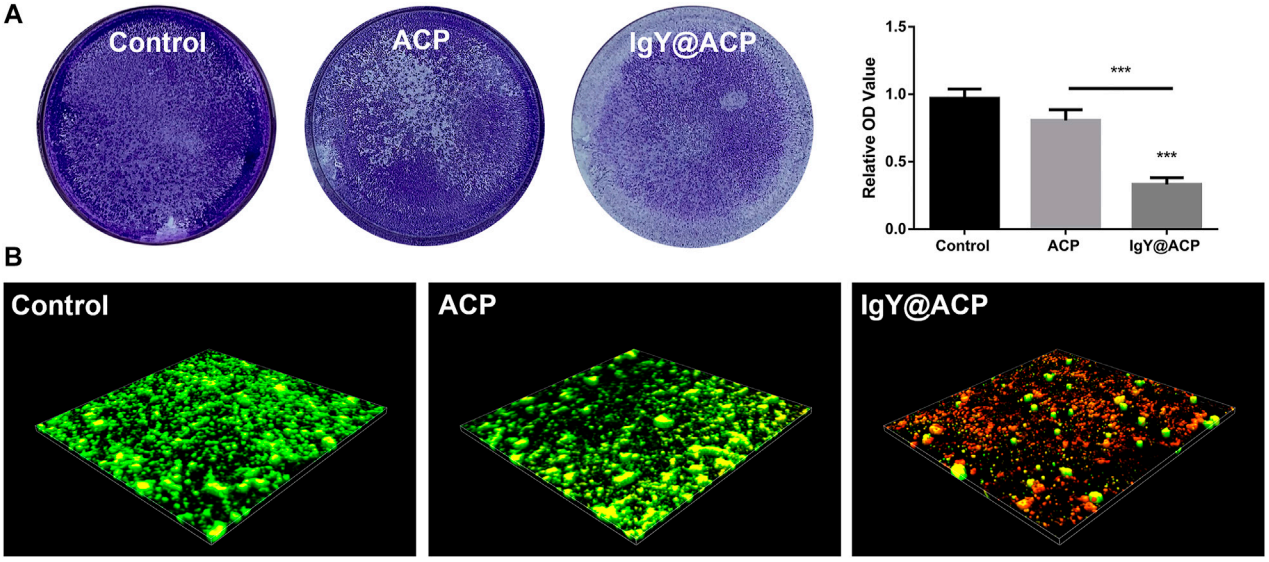

FIGURE 9
The biofilm formation of *S. mutans* after treatment with control, ACP, and IgY@ACP. Crystal violet staining with quantitative analysis **(A)** and live-/dead-stained 3D images **(B)**. Statistical significance was set at $*p < 0.05$, $**p < 0.01$, and $***p < 0.001$.

peak (Chen et al., 2016), indicating that IgY molecules were successfully loaded into this calcium phosphate. Meanwhile, IgY@ACP exhibited a sustained release of protein for 48 h. At the early stage, the loaded IgY showed a relatively rapid release, which can be explained by the release of weakly adsorbed IgY molecules on the surface of the ACP nanostructure. Subsequently, IgY exerted a further continuous release, which played a key role in inhibiting *S. mutans* biofilm formation.

Biocompatibility is an essential consideration for materials used in biomedicine. In particular, the applied material for DH inevitably contacts mucosal tissue, as the defect related to DH is usually located at the cervical margin of the tooth (West et al., 2013). Therefore, HOK, a common cell in mucosal tissue, was selected to evaluate the cell biocompatibility of the prepared materials *in vitro*. In addition, considering that nanosized materials may influence healthy pulp tissue through dentinal tubules (Chiang et al., 2014), hDPSC viability was also investigated. The CCK-8 results showed that IgY@ACP had relative cell viability above 90% on HOK cells and hDPSCs. Specifically, amino acids and other organic components adsorbed on IgY@ACP from DMEM may improve the biocompatibility of calcium phosphate products (Schultheiss et al., 2013). In addition, IgY is an immune antibody produced by immunized hens and is commonly used in the form of mouthwash or toothpaste in the oral environment (Nguyen et al., 2011; Rahman et al., 2013). Therefore, the prepared IgY@ACP has reliable biosafety and application potential for DH treatment.

To evaluate the occluding performance of IgY@ACP in DH treatment, the NovaMin, which is used in clinics and toothpastes was chosen as the positive control. In our study, after treatment with IgY@ACP for 1 day, most of the exposed dentinal tubules were occluded, which was similar to that found in Iafisco M's study, resulting from the consistent ion release (Iafisco et al., 2018). After treatment with IgY@ACP for 7 days, all dentinal tubules were completely occluded by a thicker material layer, more importantly, which extended into the tubules and the mineralized slices were interestingly found in the deep tubules up to a 16-μm depth. In addition, according to the XRD results, these dense minerals are similar to hydroxyapatite crystals, which are close to the natural dentin structure. The ACP phase could be separated and transformed into mature crystals to form bionic minerals in various solutions. Song J attempted to synthesize a nanogel containing ACP and then form crystals similar to dentin, thus achieving a surface-occluding thickness of 1–2 μm with a depth of 4–8 μm (Song et al., 2018). In addition, Berg Unosson synthesized ACP–magnesium particles and formed mineralized material in Tris-HCl buffer or saliva, which could even penetrate the tubules from the dentin surface up to 100 μm (Berg et al., 2020). We infer that a portion of IgY@ACP nanospheres penetrates into the dentinal tubules and then reacts with saliva, and Ca^{2+} and PO_4^{3-} ions are repeatedly released and reprecipitated to form dense minerals on both the top surface and inner tubules, thereby occluding the dentinal tubules.

The oral acidic environment and acidophilic diet often impair the durable efficacy of desensitization treatment. Another challenge to the efficacy of desensitization treatment

is daily abrasion. The acid resistance and abrasion resistance of the desensitization materials from IgY@ACP were evaluated. In our study, we used 6% (w/v) citric acid solution at pH = 1.5 to simulate the acidic conditions in the oral cavity, which is the main acidic component of fruit juices and beverages (Thanatvarakorn et al., 2013; Wang et al., 2015; Bastos-Bitencourt et al., 2021). The occluding materials on the dentin surface treated with IgY@ACP still existed, with little peeling and erosion traces after acid etching. Although acidic solutions may etch calcium phosphate components of the occluding materials on the dentin surface, the minerals in the dentinal tubules could continue to protect the tubules by further releasing Ca^{2+} and PO_4^{3-} ions to promote remineralization (Huang et al., 2011). The mineralization of IgY@ACP shows a similar trend for the remineralization mechanism with acid resistance. Meanwhile, a soft-bristled toothbrush was used to imitate our daily abrasion. In the IgY@ACP group, the occluding materials on the dentin surface were worn away, but those in tubules remained due to their deep occlusion. Machado AC et al. evaluated the dentin permeability and tubule occlusion effects of several in-office desensitizing treatments containing calcium and phosphate and found that none of the products were able to resist acid and abrasive challenges (Machado et al., 2019). Researchers have been looking for improvements in the durable properties of desensitization materials. Our results indicated that loading IgY into ACP could improve the durability of calcium phosphate products.

Some researchers have attempted to load antibacterial materials, including antibiotics, metal ions, and other substances, into desensitization materials to improve their capacity to inhibit cariogenic bacteria (Fan et al., 2016; Huang et al., 2019; Jung et al., 2019; Wu et al., 2020). However, these improvements are limited to drug-resistant strains due to cytotoxicity, tooth discoloration, and other side effects. Antibacterial effects should be fully considered because caries often results in the worsening of DH teeth due to cariogenic bacteria. *S. mutans* is the main cariogenic bacterium in the early stages of caries. It forms biofilms that adhere to the tooth surface and cause tooth demineralization in the presence of fermentable carbohydrates (Chen et al., 2020). It is necessary to inhibit the growth of *S. mutans* while occluding the dentinal tubules. Our results showed that *S. mutans* was significantly decreased after treatment with IgY@ACP according to CFU counting changes, suggesting that IgY@ACP could effectively inhibit the growth of *S. mutans*. Furthermore, the number of tightly adhering bacteria decreased significantly in our study. It is believed that the biofilms formed by the bacteria adhering to each other on the tooth surface have stronger resistance to antibacterial drugs and play a vital role in protecting bacteria (Zhang et al., 2020). Biofilm formation following treatment with IgY@ACP was evaluated by crystal violet staining and CLSM, which showed a trend similar to IgY@ACP on *S. mutans*. Compared with the ACP and control groups, the IgY@ACP group showed lighter crystal violet staining and more dead bacterial cells. Therefore, IgY@ACP showed valuable antibacterial effects for IgY released from IgY@ACP. IgY could inhibit the glucosyltransferase (gtfs) activity of *S. mutans* and then inhibit their adhesion and aggregation (Bachtiar et al., 2016a; Wang et al., 2020). In addition, the continuous release of phosphate ions through calcium phosphate product degradation may play a non-negligible role, as these ions could relieve the effects of bacteria on teeth by neutralizing the oral acidic environment.

Until now, there have been few studies on DH *in vivo*, and there is no standard modeling metric. In our study, an animal model of DH was established *in vivo*. Pinto found that the depth between the pulp and enamel of mature rat incisors is approximately 1 mm (Pinto et al., 2009). The cavity preparation with a depth of 0.3 mm, which is equivalent to 1/3 of the above normal depth, will not damage the pulp tissue. In the control group, most of the dentinal tubules were exposed, indicating that the 0.3-mm depth could ensure the successful establishment of animal models simulating DH. In the IgY@ACP group, mineralized particles such as calcium phosphate were deposited on the dentin surface, which showed the occluding performance, while the antibacterial effect *in vivo* needed further experiments.

5 Conclusion

IgY@ACP could stably occlude dentinal tubules with acid challenge and effectively inhibit the growth and biofilm formation of *S. mutans*. These results suggest that IgY@ACP could be a promising desensitization material for DH therapy in the future. However, the limitation of IgY@ACP in achieving antibacterial and anti-caries effects should be evaluated over a long time *in vivo*. Meanwhile, there are different types of oral pathogenic bacteria in dental caries, and the improvement of biomaterials used for the inhibition of different caries-related pathologies will be further researched.

Data availability statement

The original contributions presented in the study are included in the article/Supplementary Material; further inquiries can be directed to the corresponding author.

Ethics statement

The studies involving human participants were reviewed and approved by the Ethics Committee of the Affiliated Stomatology Hospital of Tongji University ((2019)-DW-059). Written informed consent to participate in this study was provided by the participants' legal guardian/next of kin.

The animal study was reviewed and approved by the Ethics Committee of the Affiliated Stomatology Hospital of Tongji University ((2020)-DW-27.

Author contributions

YY and YG have contributed equally to this work. YY and FC developed the concept. YY and YG performed the experiment and wrote the manuscript. LL analyzed the data and made the figure. BL, FC and BJ organized the structure of the manuscript, revised the manuscript and approved the final version. All authors have read and agreed to the published version of the manuscript.

Funding

This study was supported by the grants from Shanghai Municipal Health Commission (202140357 and 202040095).

Acknowledgments

The authors would like to thank Shengcai Qi for their detailed guidance on the experimental design and results analysis.

Conflict of interest

The authors declare that the research was conducted in the absence of any commercial or financial relationships that could be construed as a potential conflict of interest.

Publisher's note

All claims expressed in this article are solely those of the authors and do not necessarily represent those of their affiliated organizations, or those of the publisher, the editors, and the reviewers. Any product that may be evaluated in this article, or claim that may be made by its manufacturer, is not guaranteed or endorsed by the publisher.

References

Anthoney, D., Zahid, S., Khalid, H., Khurshid, Z., Shah, A. T., Chaudhry, A. A., et al. (2020). Effectiveness of thymoquinone and fluoridated bioactive glass/nano-oxide contained dentifrices on abrasion and dentine tubules occlusion: An *ex vivo* study. *Eur. J. Dent.* 14, 045–054. doi:10.1055/s-0040-1703418

Bachtiar, E. W., Afdhal, A., Meidyawati, R., Soejoedono, R. D., and Poerwaningsih, E. (2016a). Effect of topical anti-Streptococcus mutans IgY gel on quantity of S. mutans on rats' tooth surface. *Acta Microbiol. Immunol. hung.* 63, 159–169. doi:10.1556/030.63.2016.2.2

Bachtiar, E. W., Bachtiar, B. M., Soejoedono, R. D., Wibawan, I. W., and Afdhal, A. (2016b). Biological and immunogenicity property of IgY anti S. Mutans ComD. *Open Dent. J.* 10, 308–314. doi:10.2174/1874210601610010308

Bastos-Bitencourt, N., Velo, M., Nascimento, T., Scotti, C., Da Fonseca, M. G., Goulart, L., et al. (2021). *In vitro* evaluation of desensitizing agents containing bioactive scaffolds of nanofibers on dentin remineralization. *Mater. (Basel)* 14, 1056. doi:10.3390/ma14051056

Berg, C., Unosson, E., Engqvist, H., and Xia, W. (2020). Amorphous calcium magnesium phosphate particles for treatment of dentin hypersensitivity: A mode of action study. *ACS Biomater. Sci. Eng.* 6, 3599–3607. doi:10.1021/acsbiomaterials.0c00262

Brännström, M., Aström, A., and Astrom, A. (1972). The hydrodynamics of the dentine; its possible relationship to dentinal pain. *Int. Dent. J.* 22, 219–227.

Chen, F., Zhu, Y. J., Zhang, K. H., Wu, J., Wang, K. W., Tang, Q. L., et al. (2011). Europium-doped amorphous calcium phosphate porous nanospheres: Preparation and application as luminescent drug carriers. *Nanoscale Res. Lett.* 6, 67. doi:10.1186/1556-276x-6-67

Chen, W., Wang, G., Yung, B. C., Liu, G., Qian, Z., and Chen, X. (2017). Long-acting release formulation of exendin-4 based on biomimetic mineralization for type 2 diabetes therapy. *ACS Nano* 11, 5062–5069. doi:10.1021/acsnano.7b01809

Chen, X., Daliri, E. B., Chelliah, R., and Oh, D. H. (2020). Isolation and identification of potentially pathogenic microorganisms associated with dental caries in human teeth biofilms. *Microorganisms* 8, 1596. doi:10.3390/microorganisms8101596

Chen, X., Yang, B., Qi, C., Sun, T. W., Chen, F., Wu, J., et al. (2016). DNA-templated microwave-hydrothermal synthesis of nanostructured hydroxyapatite for storing and sustained release of an antibacterial protein. *Dalton Trans.* 45, 1648–1656. doi:10.1039/c5dt03357h

Chiang, Y. C., Lin, H. P., Chang, H. H., Cheng, Y. W., Tang, H. Y., Yen, W. C., et al. (2014). A mesoporous silica biomaterial for dental biomimetic crystallization. *ACS Nano* 8, 12502–12513. doi:10.1021/nn5053487

Fan, W., Li, Y., Sun, Q., Ma, T., and Fan, B. (2016). Calcium-silicate mesoporous nanoparticles loaded with chlorhexidine for both anti- *Enterococcus faecalis* and mineralization properties. *J. Nanobiotechnology* 14, 72. doi:10.1186/s12951-016-0224-7

Fu, L. H., Hu, Y. R., Qi, C., He, T., Jiang, S., Jiang, C., et al. (2019). Biodegradable manganese-doped calcium phosphate nanotheranostics for traceable cascade reaction-enhanced anti-tumor therapy. *ACS Nano* 13, 13985–13994. doi:10.1021/acsnano.9b05836

Guanipa Ortiz, M. I., Alencar, C. M., Freitas De Paula, B. L., Alves, E. B., Nogueira Araújo, J. L., and Silva, C. M. (2019). Effect of the casein phosphopeptide-amorphous calcium phosphate fluoride (CPP-acpf) and photobiomodulation (pbm) on dental hypersensitivity: A randomized controlled clinical trial. *PLoS One* 14, e0225501. doi:10.1371/journal.pone.0225501

Hall, C., Mason, S., and Cooke, J. (2017). Exploratory randomised controlled clinical study to evaluate the comparative efficacy of two occluding toothpastes - a 5% calcium sodium phosphosilicate toothpaste and an 8% arginine/calcium carbonate toothpaste - for the longer-term relief of dentine hypersensitivity. *J. Dent.* 60, 36–43. doi:10.1016/j.jdent.2017.02.009

Huang, S., Gao, S., Cheng, L., and Yu, H. (2011). Remineralization potential of nano-hydroxyapatite on initial enamel lesions: An *in vitro* study. *Caries Res.* 45, 460–468. doi:10.1159/000331207

Huang, X., Haapasalo, M., Wang, Z., Hancock, R. E. W., Wei, X., and Shen, Y. (2019). Effect of long-term exposure to peptides on mono- and multispecies biofilms in dentinal tubules. *J. Endod.* 45, 1522–1528. doi:10.1016/j.joen.2019.09.003

Iafisco, M., Degli Esposti, L., Ramírez-Rodríguez, G. B., Carella, F., Gómez-Morales, J., Ionescu, A. C., et al. (2018). Fluoride-doped amorphous calcium phosphate nanoparticles as a promising biomimetic material for dental remineralization. *Sci. Rep.* 8, 17016–17019. doi:10.1038/s41598-018-35258-x

João-Souza, S. H., Scaramucci, T., Bühler Borges, A., Lussi, A., Saads Carvalho, T., and Corrêa Aranha, A. C. (2019). Influence of desensitizing and anti-erosive toothpastes on dentine permeability: An *in vitro* study. *J. Dent. (Shiraz).* 89, 103176. doi:10.1016/j.jdent.2019.07.014

Jung, J. H., Kim, D. H., Yoo, K. H., Yoon, S. Y., Kim, Y., Bae, M. K., et al. (2019). Dentin sealing and antibacterial effects of silver-doped bioactive glass/mesoporous silica nanocomposite: An *in vitro* study. *Clin. Oral Investig.* 23, 253–266. doi:10.1007/s00784-018-2432-z

Kawasaki, A., Ishikawa, K., Suge, T., Shimizu, H., Suzuki, K., Matsuo, T., et al. (2001). Effects of plaque control on the patency and occlusion of dentine tubules *in situ*. *J. Oral Rehabil.* 28, 439–449. doi:10.1046/j.1365-2842.2001.00682.x

Krüger, C., Pearson, S. K., Kodama, Y., Vacca Smith, A., Bowen, W. H., and Hammarström, L. (2004). The effects of egg-derived antibodies to glucosyltransferases on dental caries in rats. *Caries Res.* 38, 9–14. doi:10.1159/000073914

Liu, H., and Hu, D. (2012). Efficacy of a commercial dentifrice containing 2% strontium chloride and 5% potassium nitrate for dentin hypersensitivity: A 3-day clinical study in adults in China. *Clin. Ther.* 34, 614–622. doi:10.1016/j.clinthera.2012.01.027

Liu, X. X., Tenenbaum, H. C., Wilder, R. S., Quock, R., Hewlett, E. R., and Ren, Y. F. (2020). Pathogenesis, diagnosis and management of dentin hypersensitivity: An evidence-based overview for dental practitioners. *BMC Oral Health* 20, 220. doi:10.1186/s12903-020-01199-z

Ma, M., Yan, Y., Qi, C., Qi, S., Chern, S., Shang, G., et al. (2017). Symmetry-breaking assembled porous calcite microspheres and their multiple dental applications. *Sci. China Mat.* 60, 516–528. doi:10.1007/s40843-017-9038-5

Machado, A. C., Rabelo, F. E. M., Maximiano, V., Lopes, R. M., Aranha, A. C. C., and Scaramucci, T. (2019). Effect of in-office desensitizers containing calcium and phosphate on dentin permeability and tubule occlusion. *J. Dent. (Shiraz).* 86, 53–59. doi:10.1016/j.jdent.2019.05.025

Nguyen, S. V., Icatlo, F. C., Jr., Nakano, T., Isogai, E., Hirose, K., Mizugai, H., et al. (2011). Anti-cell-associated glucosyltransferase immunoglobulin Y suppression of salivary mutans streptococci in healthy young adults. *J. Am. Dent. Assoc.* 142, 943–949. doi:10.14219/jada.archive.2011.0301

Ozlem, K., Esad, G. M., Ayse, A., and Aslihan, U. (2018). Efficiency of lasers and a desensitizer agent on dentin hypersensitivity treatment: A clinical study. *Niger. J. Clin. Pract.* 21, 225–230. doi:10.4103/njcp.njcp_411_16

Pereira, E. P. V., Van Tilburg, M. F., Florean, E., and Guedes, M. I. F. (2019). Egg yolk antibodies (IgY) and their applications in human and veterinary health: A review. *Int. Immunopharmacol.* 73, 293–303. doi:10.1016/j.intimp.2019.05.015

Pinto, S. C. S., Pochapski, M. T., Wambier, D. S., Pilatti, G. L., and Santos, F. A. (2009). *In vitro* and *in vivo* analyses of the effects of desensitizing agents on dentin permeability and dentinal tubule occlusion. *J. Oral Sci.* 52, 23–32. doi:10.2334/josnusd.52.23

Prati, C., and Gandolfi, M. G. (2015). Calcium silicate bioactive cements: Biological perspectives and clinical applications. *Dent. Mat.* 31, 351–370. doi:10.1016/j.dental.2015.01.004

Qi, C., Zhu, Y. J., and Chen, F. (2014). Microwave hydrothermal transformation of amorphous calcium carbonate nanospheres and application in protein adsorption. *ACS Appl. Mat. Interfaces* 6, 4310–4320. doi:10.1021/am4060645

Rahman, S., Van Nguyen, S., Icatlo, F. C., Jr., Umeda, K., and Kodama, Y. (2013). Oral passive IgY-based immunotherapeutics: A novel solution for prevention and treatment of alimentary tract diseases. *Hum. Vaccin. Immunother.* 9, 1039–1048. doi:10.4161/hv.23383

Schultheiss, M., Januschowski, K., Ruschenburg, H., Schramm, C., Schnichels, S., Szurman, P., et al. (2013). Dulbecco's Modified Eagle Medium is neuroprotective when compared to standard vitrectomy irrigation solution. *Graefes Arch. Clin. Exp. Ophthalmol.* 251, 1613–1619. doi:10.1007/s00417-012-2255-6

Song, J., Wang, H., Yang, Y., Xiao, Z., Lin, H., Jin, L., et al. (2018). Nanogels of carboxymethyl chitosan and lysozyme encapsulated amorphous calcium phosphate to occlude dentinal tubules. *J. Mat. Sci. Mat. Med.* 29, 84–11. doi:10.1007/s10856-018-6094-9

Takahashi, N., and Nyvad, B. (2016). Ecological hypothesis of dentin and root caries. *Caries Res.* 50, 422–431. doi:10.1159/000447309

Tas, A. C. (2014). Grade-1 titanium soaked in a DMEM solution at 37°C. *Mater. Sci. Eng. C* 36, 84–94. doi:10.1016/j.msec.2013.11.045

Tas, A. C. (2000). Synthesis of biomimetic Ca-hydroxyapatite powders at 37°C in synthetic body fluids. *Biomaterials* 21, 1429–1438. doi:10.1016/s0142-9612(00)00019-3

Tas, A. C. (2013). X-ray-amorphous calcium phosphate (ACP) synthesis in a simple biomineralization medium. *J. Mat. Chem. B* 1, 4511–4520. doi:10.1039/c3tb20854k

Thanatvarakorn, O., Nakashima, S., Sadr, A., Prasansuttiporn, T., Ikeda, M., and Tagami, J. (2013). *In vitro* evaluation of dentinal hydraulic conductance and tubule sealing by a novel calcium-phosphate desensitizer. *J. Biomed. Mat. Res.* 101, 303–309. doi:10.1002/jbm.b.32840

Wang, R., Deng, L., Lei, Z., Wu, P., Wang, Y., Hao, L., et al. (2020). Nanoscale adhesion forces of glucosyltransferase B and C genes regulated Streptococcal mutans probed by AFM. *Mol. Oral Microbiol.* 35, 49–55. doi:10.1111/omi.12277

Wang, Y., Hao, H., and Zhang, S. (2017). Biomimetic coprecipitation of silk fibrin and calcium phosphate: Influence of selenite ions. *Biol. Trace Elem. Res.* 178, 338–347. doi:10.1007/s12011-017-0933-2

Wang, Z., Ma, X., Jiang, T., Wang, Y., Feng, Y., and Li, R. (2015). The dentin tubule occlusion effects of desensitizing agents and the stability against acids and brushing challenges. *Am. J. Dent.* 28, 128–132.

West, N. X., Lussi, A., Seong, J., and Hellwig, E. (2013). Dentin hypersensitivity: Pain mechanisms and aetiology of exposed cervical dentin. *Clin. Oral Investig.* 17 (1), S9–S19. doi:10.1007/s00784-012-0887-x

Wu, M., Xu, L., Cai, Z., Huang, S., Li, Y., Lei, L., et al. (2020). Disinfection of cariogenic pathogens in planktonic lifestyle, biofilm and carious dentine with antimicrobial photodynamic therapy. *Photochem. Photobiol.* 96, 170–177. doi:10.1111/php.13161

Xu, F., Qiao, L., Zhao, Y., Chen, W., Hong, S., Pan, J., et al. (2019). The potential application of concentrated growth factor in pulp regeneration: An *in vitro* and *in vivo* study. *Stem Cell Res. Ther.* 10, 134. doi:10.1186/s13287-019-1247-4

Zhang, Y. Y., Wong, H. M., Mcgrath, C. P. J., and Li, Q. L. (2018). *In vitro* and *in vivo* evaluation of electrophoresis-aided casein phosphopeptide-amorphous calcium phosphate remineralisation system on pH-cycling and acid-etching demineralised enamel. *Sci. Rep.* 8, 8904. doi:10.1038/s41598-018-27304-5

Zhang, Z., Lyu, X., Xu, Q., Li, C., Lu, M., Gong, T., et al. (2020). Utilization of the extract of Cedrus deodara (Roxb. ex D.Don) G. Don against the biofilm formation and the expression of virulence genes of cariogenic bacterium Streptococcus mutans. *J. Ethnopharmacol.* 257, 112856. doi:10.1016/j.jep.2020.112856

Zhou, Z., Fan, Y., Jiang, Y., Shi, S., Xue, C., Zhao, X., et al. (2022). Mineralized enzyme-based biomaterials with superior bioactivities for bone regeneration. *ACS Appl. Mat. Interfaces* 14, 36315–36330. doi:10.1021/acsami.2c05794

frontiers | Frontiers in Bioengineering and Biotechnology

TYPE Review
PUBLISHED 14 April 2023
DOI 10.3389/fbioe.2023.991821

OPEN ACCESS

EDITED BY
Monireh Kouhi,
Isfahan University of Medical Sciences, Iran

REVIEWED BY
Madhuri Dey,
Strand Therapeutics, Inc., United States
Anil Kumar PR,
Sree Chitra Tirunal Institute for Medical Sciences and Technology (SCTIMST), India

*CORRESPONDENCE
Hirokazu Kaji,
kaji.bmc@tmd.ac.jp

RECEIVED 12 July 2022
ACCEPTED 03 April 2023
PUBLISHED 14 April 2023

CITATION
Ostrovidov S, Ramalingam M, Bae H, Orive G, Fujie T, Shi X and Kaji H (2023), Bioprinting and biomaterials for dental alveolar tissue regeneration.
Front. Bioeng. Biotechnol. 11:991821.
doi: 10.3389/fbioe.2023.991821

Bioprinting and biomaterials for dental alveolar tissue regeneration

Serge Ostrovidov[1], Murugan Ramalingam[2,3,4,5,6,7], Hojae Bae[8], Gorka Orive[9,10,11], Toshinori Fujie[12,13], Xuetao Shi[14] and Hirokazu Kaji[1]*

[1]Department of Biomechanics, Institute of Biomaterials and Bioengineering (IBB), Tokyo Medical and Dental University (TMDU), Tokyo, Japan, [2]Institute of Tissue Regeneration Engineering, Dankook University, Cheonan, Republic of Korea, [3]Department of Nanobiomedical Science, BK21 PLUS NBM Global Research Center for Regenerative Medicine, Dankook University, Cheonan, Republic of Korea, [4]School of Basic Medical Science, Chengdu University, Chengdu, China, [5]Mechanobiology Dental Medicine Research Center, Dankook University, Cheonan, Republic of Korea, [6]UCL Eastman-Korea Dental Medicine Innovation Centre, Dankook University, Cheonan, Republic of Korea, [7]Department of Metallurgical and Materials Engineering, Faculty of Engineering, Atilim University, Ankara, Türkiye, [8]Department of Stem Cell and Regenerative Biotechnology, KU Convergence Science and Technology Institute, Konkuk University, Hwayang-dong, Seoul, Republic of Korea, [9]NanoBioCel Group, Laboratory of Pharmaceutics, School of Pharmacy, University of the Basque Country UPV/EHU, Vitoria-Gasteiz, Spain, [10]Bioaraba, NanoBioCel Research Group, Vitoria-Gasteiz, Spain, [11]Biomedical Research Networking Centre in Bioengineering, Biomaterials and Nanomedicine (CIBER-BBN), Vitoria-Gasteiz, Spain, [12]School of Life Science and Technology, Tokyo Institute of Technology, Yokohama, Japan, [13]Living System Materialogy (LiSM) Reseach Group, International Research Frontiers Initiative (IRFI), Tokyo Institute of Technology, Yokohama, Japan, [14]National Engineering Research Center for Tissue Restoration and Reconstruction, South China University of Technology, Guangzhou, Guangdong, China

Three dimensional (3D) bioprinting is a powerful tool, that was recently applied to tissue engineering. This technique allows the precise deposition of cells encapsulated in supportive bioinks to fabricate complex scaffolds, which are used to repair targeted tissues. Here, we review the recent developments in the application of 3D bioprinting to dental tissue engineering. These tissues, including teeth, periodontal ligament, alveolar bones, and dental pulp, present cell types and mechanical properties with great heterogeneity, which is challenging to reproduce *in vitro*. After highlighting the different bioprinting methods used in regenerative dentistry, we reviewed the great variety of bioink formulations and their effects on cells, which have been established to support the development of these tissues. We discussed the different advances achieved in the fabrication of each dental tissue to provide an overview of the current state of the methods. We conclude with the remaining challenges and future needs.

KEYWORDS

bioprinting, biomaterials, bioink, dental tissue engineering, dentistry

1 Introduction

Oral health is an important part of general health and is a daily consideration for most people. Dental alveolar tissues are various (e.g., alveolar bone, dental pulp, teeth, periodontal ligament, gums, blood vessels, and nerves) and work synergistically to ensure daily physiological mastication, and digestive function (Ma et al., 2019). The tissues are organized in an ordered and complex spatial structure (Figure 1), with the involvement of different cell types, and exhibit different mechanical properties; as a result, tissues range from soft to hard (Goudouri et al., 2017). They may be subjected to different damages, including cavities, tooth loss, periodontitis, gingivitis, and bone defects. Achieving full restoration of teeth is very challenging. However, several strategies have been established to restore these tissues. Thus, in the case of caries, the infected tissue is removed, and the space is cleaned and filled with

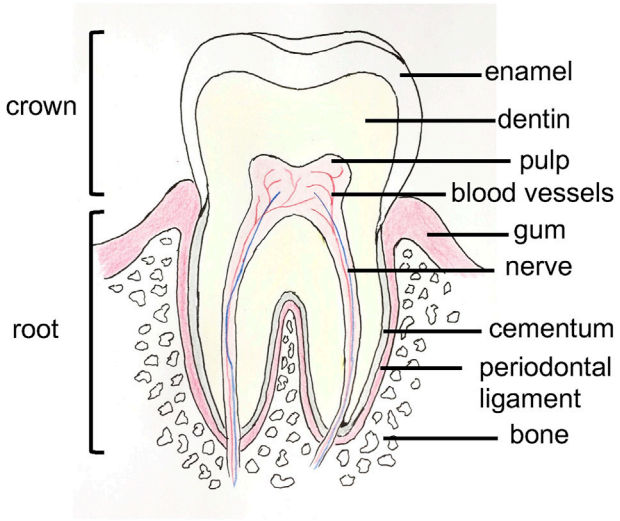

FIGURE 1
Anatomy of a tooth.

a synthetic inert material (Duarte Campos et al., 2020). However, if the caries is too significant, a root canal treatment will be performed, the dental pulp tissue will be sacrificed, and the tooth will lose important biological functions (e.g., sensory function, dentin production, immunology response) (Athirasala et al., 2017). Another well-known dental care is the use of dental implants to replace a lost tooth, and nearly 5 million dental implants are placed each year in the United States (Morrison and Tomlinson, 2021). In parallel with these current treatments, more regenerative strategies are being developed with the aim of restoring, maintaining, and replacing these dental alveolar tissues and functions. For example, advances have been made in bone tissue engineering and in dental pulp regeneration with the use of scaffolds and natural and synthetic hydrogels (Kim et al., 2009; Chen et al., 2010; Abbass et al., 2020). However, due to their variety, dental alveolar tissues create challenges for bioengineers, especially due to their strong interrelations; thus, these tissues should be considered more as one hybrid organ than separated tissues (Amoli et al., 2022). Furthermore, due to the variety of tissues, different biomaterials are needed with different mechanical properties to mimic the microenvironment of these tissues (Han et al., 2019). In recent years, 3D bioprinting has been considered a potential tissue engineering strategy to address this complexity. Indeed, 3D bioprinting allows the precise positioning of cells and matrix as the use of different cell types and materials in bioinks, and the speed of fabrication, resolution, and automation are advantageous (Vijayavenkataraman et al., 2018). In addition, 3D bioprinting has already been applied to the regeneration of many different tissues (Sun et al., 2020; Wang C.-Y.et al., 2021; Jain et al., 2022) such as skin (Weng et al., 2021), bones (Cheng et al., 2021), nerves (Cadena et al., 2021), heart (Wang Z. et al., 2021a), and skeletal muscle (Ostrovidov et al., 2019; Samandari et al., 2022). With images and data from computed tomography (CT) or magnetic resonance imaging (MRI), 3D bioprinting can produce patient personalized sophisticated constructs for the regeneration of dental alveolar tissue with complex architecture (Nesic et al., 2020a). Moreover, in combination with stem cell technology, which has provided an opportunity for the fabrication of human tissues, 3D bioprinting applied to dental and periodontal tissues is a very dynamic field of research (Mosaddad et al., 2022). Several advances have been achieved in 3D printed scaffolds, on which cells were seeded and in 3D bioprinted cell-encapsulated constructs for dentistry regeneration. Therefore, it is worth reviewing the latest advances in the field.

In this review, we begin by highlighting the different bioprinting techniques. Then, we review the different bioinks that have been fabricated and their use with different dental alveolar tissues (dental pulp, dentin, periodontal ligament, bone, gingiva, and whole tooth regeneration), providing an overview of the current state of the art. We then conclude by discussing the challenges and future developments of the field.

2 Bioprinting methods

In additive manufacturing or 3D printing, 3D structures are fabricated *via* a computer and a computer-aided design (CAD). When the materials printed contain cells, the method is called 3D bioprinting, and the usual techniques used are inkjet bioprinting, extrusion-based bioprinting, laser-assisted bioprinting, and stereolithography (Figure 2). Readers interested in bioprinting methods can reference previous reviews (Ashammakhi et al., 2018; Ostrovidov et al., 2019) and a briefly summary of the topic is provided in the following. In inkjet printing, the deposition of bioink is performed drop by drop (Ma et al., 2019). To generate these droplets of bioink, different systems are used, such as acoustic, piezoelectric, hydrodynamic, electrostatic, thermic process, and microvalves. The printer head is synchronized with a motorized stage, and the 3D structures are fabricated layer-by-layer by raster scanning. This technique usually requires low viscosity bioinks (3.5–12 mPa/s) and is fast, and the cell viability after printing is high (>85%) (Mandrycky et al., 2016; Amoli et al., 2022). In extrusion-based printing the bioink is compressed into a nozzle by mechanical or pneumatic force. Through this technique, bioinks can be used with a wide range of viscosities (30 mPa/s-60 × 10^7 mPa/s) (Mandrycky et al., 2016; Guzzi and Tibbitt, 2019). The 3D structures are fabricated by the deposition of lines or small beads of bioink and by raster scanning the printer head over the stage. The printer head then moves in the *Z* direction, allowing layer-by-layer fabrication. The technique is fast, and the cell viability after printing remains high (~80%). In laser-assisted printing, a bioink with a viscosity of 1–300 mPa/s is loaded on a ribbon coated by a thin metallic film (gold or titanium) (Zennifer et al., 2022). A laser pulse induces metal vaporization, which ejects a droplet of bioink toward the substrate. This is a fast printing technique with high precision deposition, and the cell viability after printing is high (>95%). In stereolithography, a photosensitive resin is cured point by point by a laser beam to fabricate a 3D structure. The technique is fast, and the cell viability after printing is high (>85%) (Grigoryan et al., 2021; Khorsandi et al., 2021).

3 Bioinks

The bioink encapsulates the cells and therefore must mimic the extracellular matrix (ECM) of the targeted tissue, supporting cell

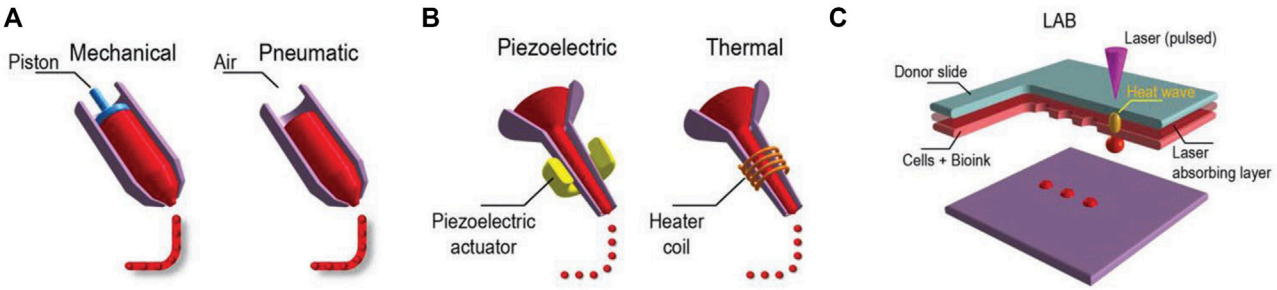

FIGURE 2
Three major bioprinting techniques **(A)** extrusion-based printers use mechanical or pneumatic dispensing systems to extrude the bioink, **(B)** to force bioink droplets out of the nozzle, inkjet printers use either a pulsed heater to heat the print head producing air bubbles or a piezoelectric actuator to generate localized pressure *via* ultrasonic waves, and **(C)** laser-assisted bioprinters (LABs) use a laser beam on an absorbing substrate to generate heat waves that dispense the bioink onto a substrate. Reprinted with permission from (Ostrovidov et al., 2019) © 2019 WILEY-VCH Verlag GmbH and Co. KGaA, Weinheim.

proliferation and differentiation (Ostrovidov et al., 2019). It must also be printable and maintain a given shape after printing; therefore, its rheological properties and gelling time are important (Chung et al., 2013). Furthermore, a homogeneous distribution of cells should occur within the bioink without cell sedimentation to allow long-term bioprinting (Ferris et al., 2013). In addition, the bioink should be biodegradable, ideally at a rate that fits the growth of the biological tissue, to be naturally replaced by the ECM components secreted by cells. Hydrogels are 3D polymeric networks with high water content that are stable in water due to the crosslinking of their polymeric chains and exhibit viscoelastic properties that mimic natural ECM (Peters et al., 2021). Due to these characteristics, hydrogels are optimal materials for tissue engineering applications, and for 3D bioprinting (Rana et al., 2014). Hydrogels can be classified as natural, synthetic, and composites. Natural hydrogels used for tooth regeneration include collagen, gelatin, fibrin, hyaluronic acid (HyA), alginate, agarose, and the important seminatural hydrogel gelatin methacryloyl (GelMA) (Fatimi et al., 2022). In this natural group, we can add natural decellularized matrices (dECM), which are very efficient in supporting cells and signaling to cells (Chae and Cho, 2022). Synthetic hydrogels include polycaprolactone (PCL), poly (ethylene glycol) (PEG), poly (ethylene glycol) dimethacrylate (PEGDA), poly (lactic acid) (PLA), and poly (lactide-co-glycolide) acid (PLGA) (Madduma-Bandarage and Madihally, 2021). In addition, different materials, such as ceramics, minerals (e.g., hydroxyapatite (HA), β-tricalcium phosphate (β-TCP), silicates), carbon nanotubes, and metals (e.g., titanium, magnesium alloys), have also been used in dental applications (Ma et al., 2019; Morrison and Tomlinson, 2021; Amoli et al., 2022). Natural hydrogels have arginine-glycine-aspartic acid (RGD) motifs that favor cell attachment and motifs for matrix metalloproteinase that favor polymer biodegradation (Xie et al., 2019). They usually exhibit cell supportive properties but show weak mechanical properties (Cui et al., 2017). In contrast, synthetic hydrogels lack RGD motifs, but their mechanical properties can be finely tuned (Cui et al., 2017). The formulation of a new bioink should balance cell supportive properties, printability, and mechanical properties that try to fit the microenvironment of the targeted tissue (Fatimi et al., 2022). To this end, different materials are often combined in composition and concentration, offering a large spectrum of possibilities.

To properly regenerate a dental tissue, a cell type should be chosen and used with the bioink. Different cell types have been used in dental alveolar tissue regeneration. Mesenchymal stem cells (MSCs), one of the stem cell used, can be obtained from adult tissues and have been isolated from various tissues and fluids (e.g., adipose tissue, placenta, bone marrow, amniotic fluid, umbilical cord, and urine) (Hass et al., 2011; Cai et al., 2013; Ostrovidov et al., 2015; Zhou et al., 2021). Interestingly, until now, eight dental-derived mesenchymal stem cells have been identified with dental pulp stem cells (DPSCs), stem cells from human exfoliated deciduous teeth (SHED), periodontal ligament stem cells (PDLSCs), dental follicle progenitor cells (DFPCs), alveolar bone marrow stromal cells (ABMSCs), stem cells from the apical papilla (SCAP), tooth germ progenitor cells (TGPCs), and gingival-derived mesenchymal stem cells (GMSCs) (Stefańska et al., 2020). Other stem cell sources for dental applications are adipose-derived stem cells (ASCs) and induced pluripotent stem cells (iPSCs) (Radwan et al., 2020). In the following section, we describe different bioinks that have been used with different dental alveolar tissues.

3.1 Bioinks for dental pulp regeneration

Dental pulp is the soft connective tissue inside the tooth that is composed of collagen fibers, proteoglycans, and cells (e.g., fibroblasts, hDSPCs, and immune cells). Dental pulp exhibits viscoelastic properties, and its Young's modulus is approximately 0.8 kPa. Odontoblasts, which are differentiated hDPSCs that produce dentin, are present at the interface with dentin. Dental pulp also contains a cell-free zone (zone de Weil) that houses a capillary network and nerves. This rich environment must be considered when designing a bioink for the regeneration of dental pulp to spatially control the localized differentiation of hDPSCs (Han et al., 2019).

Rosa et al. wrote a review on the different methods used to regenerate dental pulp (Rosa et al., 2022). Several studies have

compared bioprinted constructs with their equivalent hydrogels. Thus, Yu et al. compared alginate-GelMA hydrogel scaffolds and alginate-GelMA bioprinted constructs with a Bioplotter EnvisionTec (extrusion bioprinting) toward hDPSC proliferation and differentiation. The results showed higher cell adhesion and proliferation on bioprinted constructs than on hydrogel scaffolds. Furthermore, after 14 days in mineralization medium, alizarin red S and alkaline phosphatase (ALP) staining showed that more calcium nodules and bonelike nodules were present in the bioprinted constructs than in the hydrogel scaffolds (Yu et al., 2019). In another study, Choi et al. used the mineral trioxide aggregate (MTA) to fabricate a GelMA-MTA bioink. MTA is a calcium silicate (CS)-based cement that contains tricalcium silicate, tricalcium aluminate, tetracalcium aluminoferrite, gypsum, bismuth oxide, and other mineral oxides (Santos et al., 2021). The researchers printed 3D scaffolds of GelMA and GelMA-MTA with a ROKIT Healthcare INVIVO 3D bioprinter (extrusion bioprinting) and seeded primary hDPSCs on them to evaluate their proliferation and differentiation. After 7 days of culture in differentiation medium, they observed the promotion of odontogenic differentiation through ALP measurement and expression of the genes dentin sialophosphoprotein (DSPP) and dentin matrix acidic phosphoprotein 1 (DMP-1) on GelMA-MTA bioprinted constructs (Choi et al., 2022). In the dental pulp complex, hDPSCs are present in the center of the teeth, while dentin is in the outer region. Therefore, to examine the possibility of spatial regulation of hDPSC differentiation, Han et al. used fibrin-based bioinks (fibrinogen/gelatin/hyaluronic acid/glycerol) with different concentrations of fibrinogen (5, 10, 15, 20 mg/mL) to spatially control the stiffness; thus, hDPSCs were bioprinted with the ITOP system (custom bioprinter, extrusion bioprinting) following a dental shape recorded by computed tomography (CT). After 15 days of culture in differentiation medium, the results showed spatial odontogenic differentiation with the central pulp region remained undifferentiated, whereas there was localized deposition of dentin in the outer region (Han et al., 2019). Moreover, to regenerate dental pulp tissue, Duarte Campos et al. evaluated cocultures of hDPSCs and primary human umbilical vein endothelial cells (HUVECs) encapsulated in different bioinks (0.2% collagen type I-0.5% agarose, 0.5% fibrin, and 0.3% collagen type I) deposited into root canals of bovine teeth *via* a hand-held bioprinter (DropGun Black Drop Biodrucker GmbH, *in situ* inkjet bioprinting). After 14 days of culture, new capillary networks were observed in the all tested samples (Duarte Campos et al., 2020). Similarly, Khayat et al. encapsulated hDPSCs and HUVECs in GelMA hydrogel and filled it into root segments (H 6 mm × D 3 mm) closed on one side with white mineral trioxide aggregate (WTMA). After 13 days of culture *in vitro* in osteogenic medium, the researchers implanted them subcutaneously in nude rats for 4 and 8 weeks. The results showed cellularized pulp-like tissue at day 13 of culture, whereas neovascularization was observed at 4 and 8 weeks postsurgery. Furthermore, cellular extension into dentin tubules and formation of dentin matrix were promoted (Khayat et al., 2016). Moreover, Athirasala et al. encapsulated odontoblasts (OD21) into a GelMA 15% hydrogel with a central engineered channel obtained by the sacrificial template technique. Then, they filled the channel with endothelial colony forming cells (ECFCs) and placed the construct into human teeth roots (H 9 mm x D 1.5 mm). After 7 days of culture in DMEM-EGM-2MV (1:1) medium, ECFCs formed a monolayer, and angiogenic sprouting was observed through the whole GelMA hydrogel with pulp-like tissue (Athirasala et al., 2017).

3.2 Bioinks for dentin regeneration

Dentin is a mineralized tubular structure that surrounds the dental pulp and is composed of hydroxyapatite (HA) and an organic matrix (35% by weight) of collagenous and noncollagenous proteins (e.g., DSPP, DMP-1, osteopontin (OP), osteocalcin (OCN)) (Zhang et al., 2014). Dentin has a Young's modulus that ranges from 17–42 GPa following its mineral content. When designing a bioink for dentin regeneration the Young's modulus and a certain microporosity (~300 μm) are important parameters to consider.

Different bioinks have been fabricated for dentin regeneration. For example, Mousavi Nejad et al. fabricated two scaffolds, PCL/45S5 Bioglass (BG) composite and PCL/HyA, by 3D printing with a 3DPL Bioprinter N2 (extrusion bioprinting) and evaluated them with hDPSCs for dentin and dental pulp regeneration. Both scaffolds allowed cell adhesion, and after 21 days of culture in differentiation medium, significantly higher expression of DSPP, OCN and DMP-1 was observed in the PCL/BG group due to the presence of bioglass, as demonstrated by gene analysis. It was concluded that PCL/BG was a favorable scaffold for dentin regeneration, whereas PCL/HyA was a favorable scaffold for dental pulp regeneration (Mousavi Nejad et al., 2021). In another study, Wu et al. fabricated a bioink of PCL/MTA for the regeneration of dentin and used an E-jetting custom system to fabricate the scaffold. However, the construct did not mimic natural dentin in composition and structure (no collagen, pore size 200 μm which is 100 times larger than natural dentin pore size) (Wu et al., 2016). Naseri et al. used a CELLINK bioprinter Biox (extrusion bioprinting) at 10–12 mm/s and 40–50 kPa with a nozzle of 518 μm diameter to bioprint a scaffold of collagen type I-hydroxyapatite-alginate that exhibits homogeneous repartition of pores with 2–4 μm sizes after being freeze-dried; this scaffold compositionally and microstructurally mimics natural human dentin. An occlusion test was performed by using polystyrene microparticles (2–3 μm diameter), and hMSCs were seeded on the scaffold to show cytocompatibility (Naseri et al., 2021). Moreover, decellularized matrices are very efficient in tissue engineering due to the signaling proteins they contain. Demineralized dentin matrix (DDM) has similar components than dentin but in a different organic/inorganic ratio. Several growth factors, such as transforming growth factors β1 (TGF-β1), BMPs, vascular endothelial growth factor (VEGF), fibroblast growth factor-2 (FGF-2), platelet derived growth factor (PDGF), and IGF-1, are also present in DDM, which makes DDM a very interesting biomaterial for dentin regeneration (Gao et al., 2019). Thus, Han et al. fabricated a fibrinogen/gelatin/HyA/glycerol/DDM particle bioink and evaluated its printability and its activity on hDPSC differentiation (Figure 3). They observed that the viscosity of the bioink increases with the concentration of DDM particles (1, 3, 5, 10% w/v). They obtained a minimal printed line width of 363 μm with fibrinogen/gelatin/HyA/glycerol bioink (without DDM particles) used as a control and 252 μm with the fibrinogen/

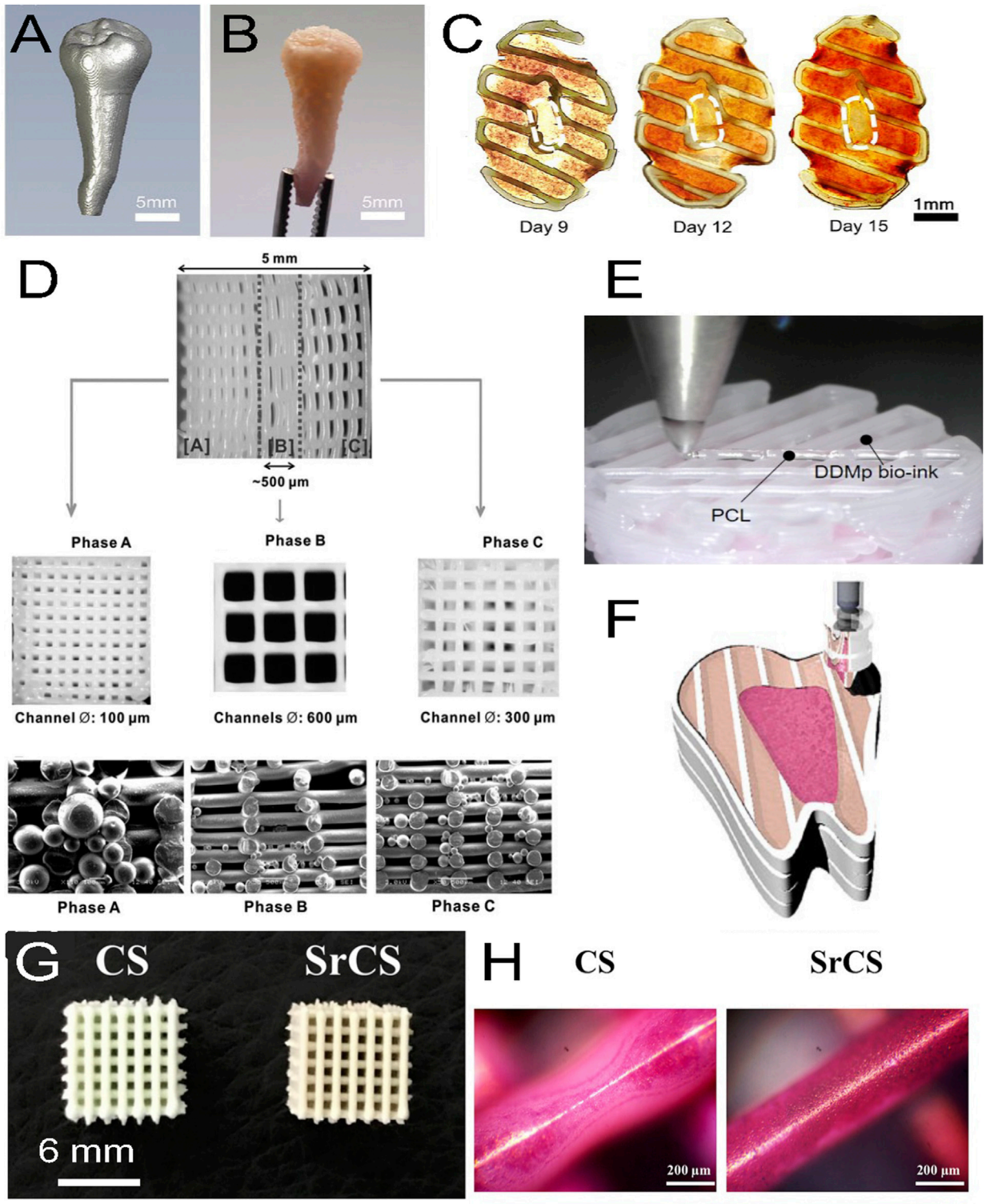

FIGURE 3
(A) Micro-CT image of a patient tooth, **(B)** with its 3D printed model with a fibrinogen-gelatin-hyaluronic acid-glycerol bioink loaded with hDPSCs. **(C)** Cross-sectional views of the construct stained with alizarin red S at different days of culture. The staining shows a spatial deposition of calcium, which corresponds to a spatial differentiation of hDPSCs that mimics the dental pulp complex, with an unmineralized central area (white dashed circles) similar to a pulp center and a mineralized outer area similar to a dentin region. **(D)** 3D printed triphasic scaffold of PCL-hydroxyapatite (HA) bioink used for PDL regeneration. Phase **(A)** A scaffold area with 100 µm microchannels and PLGA microspheres loaded with amelogenin was seeded with hDPSCs for dentin-cementum formation. Phase **(B)** A scaffold area with 600 µm microchannels and PLGA microspheres loaded with CTGF was seeded with hPDLSCs for periodontal ligament formation. Phase **(C)** A scaffold area with 300 µm microchannels and PLGA microspheres loaded with BMP-2 was seeded with hABSCs for alveolar bone formation. **(E)** Multimaterial bioprinting of a construct with a PCL bioink and a fibrinogen/gelatin/hyaluronic acid/glycerol/human demineralized dentin matrix (DDM 10%) bioink with hDPSCs for odontogenic differentiation. **(F)** Schematic showing the bioprinting
(*Continued*)

FIGURE 3 (Continued)
strategy for the generation of dental pulp (fuchsia pink area) and dentin (light pink area) complexes, which were generated by depositing two different bioinks with hDPSCs in a printed PCL frame (white area). The whole construct was obtained by a layer-by-layer process. **(G)** Top view of 3D printed calcium silicate (CS) and strontium calcium silicate (SrCS) scaffolds used for bone regeneration **(H)** with alizarin red S staining at day 7 of culture. Sr promotes MSC osteogenic differentiation with increased calcium deposition. **(A–F)** adapted with permission from (Han et al., 2019)©2019 The Authors (open access), **(D)** Reprinted with permission from (Lee et al., 2014)©Mary Ann Liebert, Inc, **(G, H)** adapted with permission from (Chiu et al., 2019) (open access).

gelatin/HyA-glycerol/DDM (10% w/v) bioink. Encapsulated hDPSCs (3×10^6 cells/mL) were bioprinted with the ITOP system (custom bioprinter, extrusion bioprinting), and the constructs were placed in odontogenic medium for 15 days. The results showed high cell viability (>95%) at day 7 of culture, and alizarin red S staining at day 15 of culture showed that mineralization increased with increasing DDM particle concentration. Furthermore, the expression levels of DSPP and DMP-1 were 22.86- and 59.76-fold higher than those in the control group, respectively (Han et al., 2021). Furthermore, dentin and dental pulp both protect and nourish the whole tooth and interact together. To prevent dental pulp exposure during cavity treatment, dental pulp capping materials, such as calcium hydroxide (CH), are used. However, CH involves some drawbacks such as inducing dental pulp inflammation; therefore, the search for new dental pulp capping materials is ongoing. Decellularized matrix-like treated dentin matrix (TDM) powder has been used as capping material and has been shown to stimulate stem cells in dental pulp to secrete dentin and correctly regenerate the dentin structure (Li et al., 2011; Zhang et al., 2011; Guo et al., 2012; Yang et al., 2012). Thus, Chen et al. fabricated a TDM paste (TDMP), which is easier to customize in dental pulp capping treatment due to its plasticity, and evaluated its effect on the differentiation of hDPSCs. At 6 and 10 weeks post capping in miniature swine, the results showed that the thickness of the regenerated dentin was 371.94 μm and 541.41 μm, respectively, in the TMDP group *versus* 285.15 μm and 324.48 μm, respectively, in the CH group (Chen et al., 2017). Furthermore, Athirasala et al. fabricated a new bioink based on alginate and acid soluble dentin matrix extract (10, and 100 μg/mL). After optimizing the bioink, the researchers bioprinted SCAPs in alginate-dentin matrix bioink using a modified Hyrel 3D printer (extrusion printing) and placed the construct in odontogenic medium. They observed a high cell viability (>90%) after printing and an enhancement in ALP and RUNX2 gene expression at day 10 of culture (Athirasala et al., 2018).

3.3 Bioinks for periodontal ligament regeneration

Periodontal ligament (PDL) is a connective tissue that is mainly composed of collagen type I fibers and proteoglycans; PDL surrounds teeth roots and the interface between teeth and alveolar bones. The Young's modulus of PDL is 5×10^6 N/m^2. It is a specialized tissue that embeds blood vessels, nerves, and several cell types (e.g., fibroblasts, osteoblasts, osteoclasts, PDLSCs), which show viscoelastic properties, contain proprioceptive sensors, anchor teeth and are involved in tissue regeneration and homeostasis of alveolar bones. The cementum interfaces the PDL and the dentin of the roots and is a hard and thin avascular mineralized tissue composed of 45%–50% HA, 50% organic matrix (mainly collagen type I, and collagen types III and XII, proteoglycans, osteopontin, osteonectin, osteocalcin, and sialoporotein), and cells (cementoblasts, PDLSCs, cementocytes) (Goudouri et al., 2017). Moreover, gingiva is the oral mucosa that covers alveolar bones. It is a highly vascularized tissue composed of a stratified epithelium (keratinized layer, granular layer, spinous layer, and basal layer) and a fibrous connective tissue named the lamina propria. Gingiva thickness ranges from 0.3–6.7 mm, and its Young's modulus ranges from 1–5 MPa. Gingiva contains several cell types (mainly keratinocytes, Langerhan's cells, and Merkel cells) (Chen et al., 2015). Gingiva is a constituent of the periodontium.

Park et al. wrote an interesting review on periodontal complex regeneration. The periodontal complex consists of tooth supportive tissues and includes the cementum, the PDL, the gingiva, and the alveolar bone. They presented several advances techniques, such as scaffolding, cell sheet technology, and 3D printing, used in periodontal regeneration (Park et al., 2016). Thus, Dan et al. fabricated a calcium phosphate (CaP)-coated PCL for the transplantation of cell sheets to denuded root surfaces of an athymic rat periodontal defect model. Human periodontal ligament cells were cultured on thermosensitive poly (N-isoproplyacrylamide) (PiPAam) dishes. Several cell sheets (3 layers) were then harvested on CaP-PCL and transplanted onto the defect. Four weeks after transplantation, the results showed that CaP-PCL alone promoted bone formation, whereas cell sheets induced the formation of PDL (Dan et al., 2014). Furthermore, Reis et al. fabricated a PLGA/CaP bilayer scaffold with flat-smooth outer layer and a 1 mm thick rough macroporous inner layer, which was implanted in a dog model of a furcation defect. The results showed the formation of new cementum, bone, and periodontal ligament with Sharpey fiber insertions (Carlo Reis et al., 2011). Moreover, Lee et al. used 3D printed with a 3D-Bioplotter EnvisionTec (extrusion bioprinting) to 3D print a multiphasic scaffold of PCL-HA (90:10 wt%) with interlaid strands (diameter 100 μm) which defined interconnected microchannels with diameters of 100, 600, and 300 μm in phases A, B, and C, respectively. In addition, PLGA microspheres encapsulating recombinant human amelogenin, connective tissue growth factor (CTGF), and BMP-2 were tethered to phases A, B, and C, respectively. The results after 4 weeks of culture in defined medium or implanted *in vivo* subcutaneously in immunodeficient mice showed that hDPSCs seeded on this scaffold differentiated into dentin/cementum, PDL, and alveolar bone (Lee et al., 2014). Periodontal regeneration implies the restoration of multiple tissue types, spatial fibrous tissue organization, and functional restoration. To overcome this structural complexity, Park et al. 3D printed a wax mold with a Solidscape printer Model Maker II (extrusion printing) to cast biomimetic hybrid scaffolds with specific polymer areas to engineer bone in the PCL compartment and PDL in the PGA

compartment. Primary human gingival fibroblasts (hGF) and hPDLCs in fibrinogen solution were seeded in the PCL and PDL compartments, respectively. After achieving gelation with thrombin, human dentin slices with exposed dentinal tubules were used to cap the constructs. The whole constructs were then transplanted subcutaneously into the dorsa of an immunodeficient mouse model for 6 weeks. The results showed that ligament and bone tissues were generated with specific localization and organization (Park et al., 2010). In another study, Rasperini et al. reported on a customized scaffold clinically transplanted in a periodontal defect. Patient with periodontal defect underwent a CT scan and a biodegradable PCL scaffold containing 4% HA was 3D printed with a selective laser sintering EOS Formiga P100 System, sterilized by ethylene oxide, immersed in recombinant human PDGF (0.3 mg/mL) for 15 min, and transplanted on the defect. The scaffold remained in place for 1 year without signs of inflammation or dehiscence. However, at 13 months postoperation the site showed dehiscence and wound failure, and the scaffold was removed and analyzed. The researchers concluded that the choice of PCL biomaterial was not ideal and that another biomaterial with a highly porous structure and a faster resorption time would be better (Rasperini et al., 2015). After optimizing the conditions of printing, Raveendran et al. bioprinted primary hPDLCs with a Gesim Bioscaffolder 3.1 (inkjet printing) in 12.5% GelMA at 11 mm/s, 135 kPa, and a 25 G needle. The cells proliferated well in the construct and colonized it within 2 weeks (Raveendran et al., 2019).

GMSCs have been differentiated into neural cells, endothelial cells, osteoblasts, adipocytes, chondrocytes, and myocytes and are often used for bone and neural regeneration (Grawish, 2018). Sun et al. have injected GMSCs into the tail vein of mice with periodontitis. They observed that GMSCs could target the periodontal injury site and promote periodontal ligament and alveolar bone tissue regeneration (Sun et al., 2019). Although many publications have used GMSCs, within the field of bone and neural regeneration, there are usually less discussion on gingiva regeneration, especially regeneration through bioprinting. An analogy is sometimes made between skin regeneration and gingival regeneration. Nesic et al. wrote an interesting review on 3D bioprinting for oral soft tissues (Nesic et al., 2020b). In a recent study, Yi et al. fabricated a bioink of injectable platelet-rich fibrin (iPRF)-alginate-gelatin. Six milliliters of human whole blood without anticoagulant was centrifuged at 700 rpm at room temperature (RT). The plasma liquid was harvested and mixed at 10%, 30%, and 50% volume ratios with 4% sodium alginate-8% gelatin-α-MEM culture medium bioink. Primary hGFs (1×10^6 cells/mL) were loaded in the bioink and bioprinted with a Medprin bioprinter 2.0 (extrusion bioprinting) at 10 °C, 30 mm/s, and a nozzle diameter of 260 μm. The results showed a sustained release of growth factors over 2 weeks, excellent cell attachment, and promotion of hGF cell proliferation. At 4 weeks post-implantation in nude mice, a 20% increase in new blood vessels was observed in the scaffold (Yi et al., 2022).

3.4 Bioinks for alveolar bone regeneration

Alveolar bones are the parts of the mandible and maxilla that anchor the teeth in tooth sockets (Goudouri et al., 2017). They are mainly trabecular bone, composed of 65% mineralized tissue (calcium deficient HA), 30% organic matrix (mainly collagen type I and noncollagenous proteins such as osteopontin, osteonectin, sialoporotein), water 15%, and cells (~5%) which are mainly osteoclasts, osteoblasts, and osteocytes. Their Young's modulus ranges between 0.9×10^9–13.7×10^9 N/m^2. Alveolar bones are covered by a membrane (periosteum). When designing a bioink for alveolar bone regeneration the load (while chewing), Young's modulus, porosity, and bioactivity of different cell types must be considered.

Leyendecker Junior et al. performed an interesting analysis of the literature from 1984 to 2017 concerning the use of DPSCs and SHED for bone tissue engineering and wrote a review (Leyendecker Junior et al., 2018). Furthermore, Duarte Campos et al. used a custom-made inkjet bioprinter to fabricate agarose-collagen type I hydrogel constructs and studied the effect of their stiffness (low, medium, high) on MSC osteogenic differentiation (Table 1). The results showed that the viscosity of the hydrogels increased with the agarose concentration, whereas the high stiffness blended hydrogel was 3 times greater than that of pure agarose hydrogels. Furthermore, higher osteogenic differentiation was observed when cells were encapsulated in lower stiffness agarose-collagen hydrogel, which allowed the spreading and branching of cells (Duarte Campos et al., 2016). However, the compressive modulus of these hydrogels ranged from 18.1 kPa to 89.1 kPa, which is very low compared to the 110 MPa of bone. In another study, Park et al. evaluated the cell viability and differentiation of hDPSCs encapsulated in a BMP-2-conjugated GelMA bioink. They used a synthetic BMP-2 mimetic peptide (KIPKASSVPTELSAISTLYL) and checked the rheological property of this new bioink. They observed high cell viability (>90%) after bioprinting with the integrated organ printing system (ITOP system, extrusion bioprinting) and cell proliferation. After 4 weeks in osteogenic differentiation medium, calcium deposition was evaluated by alizarin red S staining and showed that 55% of the construct was calcified. Furthermore, high expression of DSPP and OCN genes was observed in the construct (Park et al., 2020). To increase mineralization, Kim et al. mixed collagen type I (5%), and bone-dECM (5%) with β-TCP (0, 10, 20, 30, 40% fraction weights) to obtain different bioinks; then, they encapsulated 1×10^7 hDPSCs/mL into these bioinks that were bioprinted with a three-axis robot system DTR3-2210-T-SG (DASA Robot, extrusion printing). They selected the bioink containing 20% wt of β-TCP on the basis of high cell viability (>95%) and placed the bioprinted constructs in osteogenic differentiation medium. After 21 days in culture, they evaluated osteogenic (ALP, OCN, OPN) and odontogenic (DSPP, DMP-1) differentiation and observed significant enhancement in both differentiation (Kim et al., 2022). Similarly, Yang et al. fabricated a bioink of GelMA-methacrylated hyaluronic acid with or without collagen type I, in which they encapsulated osteocytes (IDG-SW3, 1×10^7 cells/mL) that were printed with a 3D-Bioplotter EnvisionTec (extrusion bioprinting). After 28 days of culture in mineralization medium, the results showed high DMP-1 and calcium deposition, whereas cells exhibited a typical dendritic morphology with aligned and dense dendrites and were characterized as mature osteocytes by the high expression of SOST protein (Yang et al., 2020). In another study, Son et al. examined the differences between primary mouse alveolar bone-derived cells (mABDCs) and primary mouse long

TABLE 1 Overview of bioinks used for dental alveolar tissue regeneration with their effects.

Tissue	Matrix	Cell source	Construct type	Printer and printing type	Effects	References
Dental pulp	Alginate/GelMA	hDPSCs (Cells seeded)	-Printed constructs	-Bioplotter Envision Tec	Printed constructs > hydrogel scaffolds. Higher cell attachment, and proliferation. Higher mineralization (Calcium up/ ALP up)	Yu et al. (2019)
	Alginate/GelMA		-Hydrogel scaffolds	-Extrusion printing		
Dental pulp	GelMA-MTA	hDPSCs (Cells seeded)	Printed construct	-Rokit Healthcare *IN VIVO* printer	GelMA-MTA increases mineralization ALP, DSPP, DMP-1 up	Choi et al. (2022)
	GelMA			-extrusion printing		
Dental pulp	fibrinogen/gelatin/ hyaluronic acid/glycerol with [fibrinogen] 5–20 mg/mL	hDPSCs (Cells encapsulated)	Bioprinted constructs	-ITOP system	Spatial differentiation (undifferentiated in central pulp area and dentin deposition in outer area)	Han et al. (2018)
				-extrusion bioprinting		
Dental pulp	–0.2% Collagen type I/ 0.5% agarose	hDPSCs/HUVECs (Cells encapsulated)	Bioprinted constructs in bovine root canal (hand-held bioprinter)	-DropGun Black Drop Biodrucker	Vascularized dental pulp with the three bioinks. (Collagen/agarose bioink has better mechanical properties)	Duarte Campos et al. (2020)
	–0.5% fibrin –0.3% Collagen type I			-inkjet bioprinting		
Dentin	PCL/45S5 bioglass	hDPSCs (Cells seeded)	Printed constructs	-3DPL bioprinter N2	PCL/bioglass induced dentin formation DSPP, OCN, DMP-1 up	Mousavi Nejad et al. (2021)
	PCL/Hyaluronic acid			-extrusion printing	PCL/Hyaluronic acid induced dental pulp formation	
Dentin	Collagen type I/ hydroxyapatite/alginate	hMSCs (Cells seeded)	Printed constructs	-CELLINK bioprinter Biox	Constructs mimic natural dentin. Pores size 2–4 μm. Good cell attachment and proliferation	Naseri et al. (2021)
				-extrusion printing		
Dentin	Fibrinogen/gelatin/10% DDM particles	hDPSCs (Cells encapsulated)	Bioprinted constructs	-ITOP system	Mineralization increases with increase [DDM] DSPP, DMP-1 up	Han et al. (2021)
				-extrusion bioprinting		
Dentin	Alginate/dentin matrix extract (10 and 100 mg/mL)	SCAPs (Cells encapsulated)	Bioprinted constructs	-Hyrel 3D printer	Optimized printing parameters. Good cell viability. ALP, RUNX2 up	Athirasala et al. (2018)
				-extrusion bioprinting		
Periodontal ligament	PCL/Hydroxyapatite (+ PLGA microspheres with amelogenin or CTGF or BMP2)	hDPSCs (Cells seeded)	Multi-phasic scaffolds (with A, B, C areas)	-Bioplotter Envision Tec	Spatial cell differentiation. Formation of dentin-cementum, PDL, and alveolar bone	Lee et al. (2014)
				-Extrusion printing		
Periodontal ligament	PCL/PGA	hGFs, hPDLSCs (Cells seeded in A, B areas, respectively)	Multi-phasic scaffolds (with A, B areas)	-SolidScape printer Model Maker II	Spatial cell differentiation. Formation of cementum, ligament (with oriented fibers), and bone	Park et al. (2010)
				-Extrusion printing		
Periodontal ligament	PCL/4% hydroxyapatite	No cells, but PDGF	Printed scaffold implanted in human	-Formiga P100	No inflammation, no problem for 1 year. At 13 months, dehiscence and wound failure. Scaffold was removed	Rasperini et al. (2015)
				-selective laser sintering		
Periodontal ligament	GelMA 12.5%	hPDLSCs (Cells encapsulated)	Bioprinted constructs	-Gesim Bioscaffolder 3.1	Optimized printing parameters. Good cell viability and proliferation	Raveendran et al. (2019)
				-inkjet bioprinting		
Gingiva	4% alginate/8% gelatin/ (10, 30, 50%) platelet rich fibrin	hGFs	Bioprinted constructs	-Medprin bioprinter 2.0	Optimized printing parameters. Good cell viability and proliferation	Yi et al. (2022)

(Continued on following page)

TABLE 1 (*Continued*) Overview of bioinks used for dental alveolar tissue regeneration with their effects.

Tissue	Matrix	Cell source	Construct type	Printer and printing type	Effects	References
		(Cells encapsulated)	Implanted 4, 8 Wks in nude mice subcutaneously	-Extrusion bioprinting	Host cell infiltration Neovascularization	
Alveolar bone	Agarose/Collagen type I (with low, medium, high stiffness)	hMSCs (Cells encapsulated)	Bioprinted constructs	-custom-made bioprinter -Inkjet bioprinting	Higher osteogenic differentiation in low stiffness bioink Alizarin red staining, ALP, COL1, RUNX2 up	Duarte Campos et al. (2016)
Alveolar bone	BMP2 peptide-conjugated GelMA	hDPSCs (Cells encapsulated)	Bioprinted constructs	-ITOP system -extrusion bioprinting	Good cell viability and proliferation. High calcification. DSPP, OCN up	Park et al. (2020)
Alveolar bone	Collagen type I 5%/bone dECM 5%/β-TCP 20%	hDPSCs (Cells encapsulated)	Bioprinted constructs	-three axis DASA Robot system -Extrusion bioprinting	Osteogenic and odontogenic differentiation. ALP, OCN, OPN up DSPP, DMP-1 up	Kim et al. (2022)
Alveolar bone	GelMA/HAMA GelMA/HAMA/Collagen type I	IDG-SW3 (Cells encapsulated)	Bioprinted constructs	-Bioplotter Envision Tec -Extrusion printing	After 28 days culture, high DMP-1 and calcium deposition. Cx43, Sost, Phex up, high dendrite density	Yang et al. (2020)
Alveolar bone	SrCS (strontium calcium silicate)	hMSCs (Cells seeded)	Printed constructs	-Gesim Bioscasffolder 3.1 -inkjet bioprinting	Higher cell attachment, proliferation, differentiation with Sr. ALP, BSP, OPG, OC up	Chiu et al. (2019)
Alveolar bone	Collagen/SrCS (bilayers) SrCS (single layer)	hGFs (Cells encapsulated)	Bioprinted constructs Implanted 12 Wks in rabbit subcutaneously	-Gesim Bioscasffolder 3.1 -inkjet bioprinting	Promotes FGF2, BMP2, VEGF secretion. Bone formation around and in the construct (bilayers), around only (single layer)	Chen-Ying Wang et al. (2021)
Alveolar bone	Octapeptide/amorphous Mg phosphate	hDPSCs (Cells encapsulated)	Bioprinted constructs Implanted 4, 8 Wks in rats calvarial defects	-RegenHU printer -inkjet bioprinting	Promotes osteogenic differentiation. High mineralization. Increases bone formation and bone density	Dubey et al. (2020)

bone-derived cells (mLBDCs). They observed that both exhibit similar osteoblastic characteristics, morphology, and proliferation rates, but show distinct expression of epithelial-mesenchymal interaction (EMI)-related genes. Thus, among these genes, BMP-4 has a critical effect on bone formation in mABDCs but not in mLBDCs (Son et al., 2020). Moreover, Chiu et al. fabricated a strontium-containing calcium silicate (SrCS) scaffold by 3D printing with a Gesim Bioscaffolder 3.1 (inkjet printing) and evaluated it relative to a CS scaffold for osteoinduction. Analysis showed that the SrCS scaffold exhibits macropores of 0.5 mm and a compressive modulus two times higher than that of the CS scaffold. Moreover, when placed in simulated body fluid (SBF) solution, SrCS released more Ca, Si, Sr, and P ions, whereas both scaffolds induced apatite formation. When MSCs were seeded on the scaffolds, compared to CS, SrCS more greatly stimulated cell attachment, proliferation, and osteogenic differentiation with higher levels of ALP, BSP, OPG, and OC. When implanted *in vivo* in a rabbit model, 2 times more new bone formed in SrCS than in CS at 4 weeks postsurgery (Chiu et al., 2019). Similarly, Wang et al. bioprinted with Gesim Bioscaffolder 3.1 (inkjet printing) a bilayer scaffold of collagen-SrCS with hGFs encapsulated in collagen as the top layer and SrCS as the bottom layer. The bilayer scaffold supports cell viability and proliferation, as observed over an 8-week period. Furthermore, the bilayer scaffold promoted the secretion of FGF-2, BMP-2, and VEGF by hGFs. After the scaffold was implanted in rabbits for 12 weeks, new bone formed around and in the bilayer scaffold, while it only formed around the single-layer SrCS scaffold used for comparison, as determined by μCT analysis and Von Kossa staining (Wang Z. et al., 2021b).

3.5 Bioinks for whole tooth engineering

An early attempt to regenerate a whole tooth was made by Kim et al., who printed a molar-shaped scaffold with a PCL (80%)/HA (20%) bioink (without cells) through 3D-Bioplotter EnvisionTec

(extrusion bioprinting); in addition, they used a cell-homing strategy to condense multiple cell lineages into the scaffold for the generation of multiple tissues. They coated the scaffold with a blend of stromal derived factor-1 (SDF1, 100 ng/mL) and bone morphogenic protein 7 (BMP-7, 100 ng/mL) in a collagen type I solution and implanted the scaffold subcutaneously in rats for 9 weeks. The results showed new alveolar bone formation, mineralization, PDL formation, and angiogenesis (Kim et al., 2010). Interestingly, it was determined that the epithelial/mesenchymal cell interface observed in the early stage of tooth formation was essential, and it was shown that the regeneration of a whole tooth was possible. Although these studies did not involve a printing technique, we present the results due to their importance. However, since cell localization is important in the process, with new developments, a printing technique may be useful for whole tooth regeneration. Thus, Nakano et al. fabricated a tooth germ by encapsulating compartmentalized epithelium- and mesenchymal-derived stem cells at a high density (5×10^8 cells/mL) in collagen hydrogel. The tooth germ generated the correct tooth structure in *vitro* cultures, as in *vivo* subcutaneous transplantation with penetration of blood vessels and nerves (Nakao et al., 2007; Ikeda et al., 2009). Similarly, Oshima et al. generated a tooth bud by compartmentalizing epithelium- and mesenchymal-derived stem cells. They placed this tooth bud in a plastic ring for size control and transplanted it into the mouse subrenal capsule for 2 months, which generated a tooth unit surrounded by alveolar bone. Then, the team investigated the potential engraftment of such a tooth unit into a defect in a mouse molar region of alveolar bone. Full bone integration was observed at 30 days post-surgery with regeneration of alveolar bone (Oshima et al., 2011). Oshima and Takuji wrote a review about the evolution of techniques used for whole tooth regeneration. They described the following methods: the scaffold method, the cell aggregation method, and the organ germ method (Oshima and Tsuji, 2014). In the scaffold method, epithelial and mesenchymal stem cells are seeded on biodegradable materials and the whole tooth is generated (Iwatsuki et al., 2006; Sumita et al., 2006; Yelick and Vacanti, 2006; Honda et al., 2007). The major drawbacks of this method are the irregularities in tooth production and in tissue structure full achievement. In the cell aggregation method, an aggregate of dental epithelial and mesenchymal cells is fabricated, and a tooth is generated by cell reorganization. However, the frequency of tooth formation and correct tissue formation are not secured (Yamamoto et al., 2003; Hu et al., 2006). In the organ germ method, epithelial and mesenchymal stem cells at high cell density are compartmentalized into a collagen gel. The tooth bud generates a whole tooth that is structurally correct *in vitro* and *in vivo* when transplanted into a jawbone (Oshima et al., 2011). Thus, Wen et al. fabricated a tooth germ by mixing hemisphere mouse iPS and mouse mesenchymal stem cells in a collagen type I. Then, they added epithelial cells to the adjacent area. The construct was placed in a 12-well insert culture plate in odontogenic induction medium for 5 days and then transplanted into the mouse subrenal capsule for 4 weeks. The results showed that the iPS alone group did not form tooth-like structures, epithelial cells with mesenchymal stem cells but without iPS cells formed irregular tooth-like structures, and only the 3 cell types together formed mature tooth-like structures similar to normal teeth (Wen et al., 2012). The organ germ method (or tooth bud model) has also been used by Smith et al., who encapsulated porcine dental epitaxial (pDE) progenitor cells, porcine dental mesenchymal (pDM) progenitor cells, and HUVECs in 3% and 5% GelMA hydrogels, which were cultured in osteogenic medium. After 3 and 6 weeks of culture *in vitro*, the results showed robust expression of DSPP, whereas the marker of bone differentiation was weak. Furthermore, after 6 weeks of subcutaneous implantation in rats, the explant analysis showed mineralized tissue formation, collagen type I and type III deposition, neovascularization, and bone formation (Smith et al., 2017). Furthermore, Zhang et al. used porcine decellularized tooth buds as a matrix, seeded them with porcine dental epithelial cells, human dental pulp cells, and HUVECs, and then implanted them in the mandible of mini-pigs for 3 and 6 months. The results showed successful whole tooth formation with enamel, pulp, dentin, periodontal ligament, and tooth roots. However, not all implants form mature teeth (Zhang et al., 2017).

4 Bioprinting regulations for dentistry

Since Charles Hull invented stereolithography in 1983, substantial progress and development have been achieved with 3D printing and bioprinting, and these technologies have been applied in various fields such as tissue engineering, regenerative medicine, personalized medicine, prostheses, implants, drug fabrication, and medical education (Ashammakhi et al., 2018; Ashammakhi et al., 2019; Cheng et al., 2021). Driven by the technological development of 3D bioprinters and biomaterials, numerous bioprinting companies have appeared on the market, among which 80% are established companies and 20% are start-ups (Santoni et al., 2022). In terms of business, the bioprinting market in the United States was evaluated in 2019 at $586.13 million and is expected to reach $1,949.94 million by 2025 (Santoni et al., 2022). As bioprinting is a new rising technology that is being dynamically developed there is also a strong need for regulation and standardization.

Different countries worldwide have established regulatory agencies to produce laws and regulations, which ensure the safety of new medicinal products and allow these products to enter clinical trials and the market. These agencies include the US Food and Drug Administration (FDA), the Central Drug Standards Control Organization (CDSCO) in India, the European Medicines Agency (EMA) in Europe, the Federal Service for Control over Healthcare and Social Development (Roszdravnadzor) in Russia, the Pharmaceutical and Medical Devices Agency (PMDA) in Japan, and the China Food and Drug Administration (CFDA) in China. 3D printed constructs, implants, and prostheses, without cellular components are usually regulated by these agencies as medical devices, whereas 3D bioprinted tissue engineered medical products (TEMPs) that contain cellular components are usually regulated as biologics or drugs (Sekar et al., 2021). For commercial purposes, 3D printed/bioprinted products should be fabricated under Good Manufacturing Practices (GMP) using clinical grade materials and be tested with Good Clinical Practice (GCP). The International Organization of Standards (ISO) and the American Society for Testing and Materials (ASTM) are the organizations internationally recognized for producing standardization guidelines for biomaterials and medical devices to ensure the product characteristics, their qualities, and the quality of

the fabrication process and product analysis (Simon et al., 2014). These two organizations have technical committees and subcommittees that regularly establish new standards or revise previous standards (for example, ISO/ASTM 52900 and ISO 17296 series on 3D printing, ISO/TS 22911:2016 on dentistry and the preclinical evaluation of dental implants, ISO 7405:20,018 on the evaluation of the biocompatibility of medical devices used in dentistry, and ISO 22803 on membrane materials for guided tissue regeneration in oral and maxillofacial surgery).

For example, the FDA regulates 3D printed products for dentistry as medical devices based on their risks to health and classifies them into classes I, II, and III (Schuh and Funk, 2019). Class I includes devices presenting low risk for health, such as toothbrushes, surgical guides, and custom trays, and manufacturers must show that their product is biocompatible and produce the mechanical performance data (for FDA Products Classification see: https://www.accessdata.fda.gov/scripts/cdrh/cfdocs/cfPCD/PCDSimpleSearch.cfm). The ISO 10993 series focuses on "Biological evaluation of medical devices", and these guidelines can be used for the preclinical evaluation of the biocompatibility of materials (Schuh and Funk, 2019). Class II includes devices that present moderate risk for health, such as dental implants, mouthguards, and aligners, and manufacturers must show that their product is biocompatible, that the contact between the device and the body does not induce complications and that the product is substantially equivalent to a product already on the market. When this equivalence is shown, a 510(k) clearance (premarket notification) is delivered (https://www.fda.gov/medical-devices/device-approvals-denials-and-clearances/510k-clearances). Class III includes devices with high risk for health, and the regulation is more severe, requiring higher safety assessment; usually 3D printed dental products fall into Class I and II. However, the product is sometimes not classified yet (e.g., plastic mouthguard fitted to the teeth, code OCO), and sometimes the product is exempted from the 510(k) clearance (e.g., additively manufactured preformed resin denture tooth, code PZY) despite being in Class II.

For the 3D bioprinted products with cellular components, the product combines a synthetic scaffold matrix and a cellular part qualifies in the United States as an HCT/Ps (human cell, tissues and cellular and tissues-based products, https://www.fda.gov/media/70689/download; and https://www.fda.gov/media/82724/download) as defined in the Code of Federal Regulation (21CFR Part 1271.3) based on the Public Health Service act (PHS Act). Since the cells have been mixed with the matrix (more than minimally manipulated), the product is then regulated as a biologic under Section 351 of the PHS Act, and a premarket notification, a new drug application (NDA), and a Biologics License Application (BLA) are necessary (Hourd et al., 2015; Ricles et al., 2018; Sekar et al., 2021).

Regulations between different countries may be similar but each country also has its own specificities; thus, clearance obtained in one country is not automatically recognized in another country. However, when a country does not have a regulatory agency, clearance might be first required from a country with an agency, before national regulation is considered. In Europe (EU), medical devices (no cellular component) are classified in Class I (low risk), Class IIa (low to medium risk), Class IIb (medium to high risk), and Class III (high risk), and products with cellular components are considered drugs or biologics. The regulation 2017/745 deals with medical devices, whereas the Directive 2004/23/EC covered transplants, tissues or cells of human origin, or their derivatives (https://op.europa.eu/en/publication-detail/-/publication/83bdc18f-315d-11e7-9412-01aa75ed71a1/language-en/format-PDF/source-58036705, https://eurlex.europa.eu/LexUriServ/LexUriServ.do?uri=OJ:L:2004:102:0048:0058:en:PDF).

5 Conclusion and perspective

Bioengineering is causing a major shift in the approach of dental treatments. Until now, traditional dental restoration techniques were the best possible with the technology available but were globally based on cleaning, inserting inert biomaterials for capping, protecting teeth and restoring a shape; thus, teeth would gradually lose parts of their functionalities and vitalities. In contrast, the aim of tissue engineering is to prevent the teeth from losing function and regenerate the damaged parts of tissue and functions. 3D bioprinting allows the precise deposition of cells, matrix, and signaling components to fabricate sophisticated constructs; these constructs show potential to revolutionize dental treatments and accelerate a rapid transition away from traditional restoration techniques toward bioengineered solutions. Currently, many efforts are being made to develop new bioinks that support cell proliferation and differentiation for dental alveolar tissue regeneration. Interestingly, papers have usually shown that bioprinted contructs are superior to hydrogel scaffolds (of the same material composition) in terms of cell support and cell differentiation. To provide additional guidance effects on cells and improve tissue regeneration, more complex bioinks may integrate signaling molecules, such as growth factors or peptides. For example, BMP-2 and BMP-7 have been approved by the FDA and may be used to induce tissue mineralization. The native protein may be replaced by a synthetic peptide, such as a haptamer, to reduce the cost, and its conjugation with the bioink leads to a long lasting effect rather than a short inducing effect and a faster clearance by proteases. Furthermore, due to the strong interrelations between dental alveolar tissues, multimaterial and multicellular bioprinting may often be needed. We have provided several examples of multiphasic constructs that have been fabricated, especially for periodontal complex regeneration, in which several tissues were generated simultaneously with proper orientation and integration. The developments of these bioprinting techniques should increase with the development of new multimaterial bioinks that support multicell types and compartmentalization. Moreover, stem cells are an inhexaustible source of cells for human organ regeneration that can differentiate into several tissue types. Different stem cells are available for dental regeneration, and among them, hDPSCs are frequently used, as shown by the literature. Another source of abundant and available stem cells could be adipose-derived stem cells (ASCs), which can differentiate into dental pulp, dentin, cementum, and periodontal ligament PDL. Due to the ability to reprogram adult cells into less differentiated cells, named induced pluripotent stem cells (iPSCs), ASCs are a very promising cell source of progenitors for dental regeneration. The technology to reprogram cells into iPSCs has progressed well; rather than using direct reprogramming with the insertion of transcription factors *via* lentivirus into cells, small

molecules are now used in culture medium to induce specific signaling and to prevent viral components (Ostrovidov et al., 2023). However, the use of undifferentiated cells (e.g., MSCs, iPSCs) for transplantation has raised several concerns due to potential tumorigenicity, unwanted immune response inducement, and transmission of adventitious agents (Medvedev et al., 2010; Herberts et al., 2011; Lukomska et al., 2019). Another axis of development is on whole tooth regeneration. The healing potential of the tooth organogenesis technique is impressing, and more developments may include the use of 3D printing, and perhaps of iPSCs cells for the regeneration of whole teeth. When a body part can be regenerated or replaced (e.g., nose, ear), it is a considerable success (Zhou et al., 2018). Therefore, the technical opportunity to fully regenerate teeth should be fully exploited, and further developments should be explored to apply the technology to the clinic. Moreover, 3D bioprinting technology needs further development to improve the resolution, printing speed and biocompatibility, as well as to scale up the technology. In bioprinting, the highest resolution is obtained for a continuous line up of cells, in which cells are printed individually at defined positions and are in contact with each other. Currently, only laser-assisted bioprinters have a high resolution (approximately 10 μm) depending on the bioink and the cell concentration. Increasing the speed of printing is also an important development that is beneficial for cell viability, complex structure fabrication, and cost. Furthermore, it would be good to scale up bioprinted tissue constructs for clinical applications. Interestingly, in recent developments, an emerging technique named volumetric bioprinting has overcome these limitations and significantly improved the printing velocity and size of constructs with high complexity, providing new opportunities (Bernal et al., 2019). Additionally, any technological developments in handheld bioprinters will be beneficial for dentistry.

Author contributions

All authors listed have made a substantial, direct and intellectual contribution to the work, and approved it for publication.

Funding

This work was supported by the Japan Society for the Promotion of Science (JSPS) KAKENHI (Grant Numbers 22K18936 and 21K04852); AMED (Grant Number JP21gm1310001); The JST Adaptable and Seamless Technology Transfer Program through Target-driven R&D (Grant Number JPMJTM22BD), CASIO SCIENCE PROMOTION FOUNDATION, and by the Research Center for Biomedical Engineering at Tokyo Medical and Dental University, Japan.

Conflict of interest

The authors declare that the research was conducted in the absence of any commercial or financial relationships that could be construed as a potential conflict of interest.

Publisher's note

References

Abbass, M. M. S., El-Rashidy, A. A., Sadek, K. M., Moshy, S. E., Radwan, I. A., Rady, D., et al. (2020). Hydrogels and dentin–pulp complex regeneration: From the benchtop to clinical translation. *Polymers* 12, 2935. doi:10.3390/polym12122935

Amoli, S. M., EzEldeen, M., Jacobs, R., and Bloemen, V. (2022). Materials for dentoalveolar bioprinting: Current state of the art. *Biomedicines* 10, 71. doi:10.3390/biomedicines10010071

Ashammakhi, N., Ahadian, S., Pountos, I., Hu, S.-H., Telissi, N., Bandaru, P., et al. (2019). *In situ* three dimensional printing for reparative and regenerative therapy. *Biomed. Microdevices* 21, 42. doi:10.1007/s10544-019-0372-2

Ashammakhi, N., Ahadian, S., Zengjie, F., Suthiwanich, K., Lorestani, F., Orive, G., et al. (2018). Advances and future perspectives in 4D bioprinting. *Biotechnol. J.* 13, 1800148. doi:10.1002/biot.201800148

Athirasala, A., Lins, F., Tahayeri, A., Hinds, M., Smith, A. J., Sedgley, C., et al. (2017). A novel strategy to engineer pre-vascularized full-length dental pulp-like tissue constructs. *Sci. Rep.* 7, 3323. doi:10.1038/s41598-017-02532-3

Athirasala, A., Tahayeri, A., Thrivikraman, G., França, C. M., Monteiro, N., Tran, V., et al. (2018). A dentin-derived hydrogel bioink for 3D bioprinting of cell laden scaffolds for regenerative dentistry. *Biofabrication* 10, 024101. doi:10.1088/1758-5090/aa9b4e

Bernal, P. N., Delrot, P., Loterie, D., Li, Y., Malda, J., Moser, C., et al. (2019). Volumetric bioprinting of complex living-tissue constructs within seconds. *Adv. Mat.* 31, 1904209. doi:10.1002/adma.201904209

Cadena, M., Ning, L., King, A., Hwang, B., Jin, L., Serpooshan, V., et al. (2021). 3D Bioprinting of neural tissues. *Adv. Healthc. Mat.* 10, 2001600. doi:10.1002/adhm.202001600

Cai, J., Zhang, Y., Liu, P., Chen, S., Wu, X., Sun, Y., et al. (2013). Generation of tooth-like structures from integration-free human urine induced pluripotent stem cells. *Cell. Regen.* 2, 6. doi:10.1186/2045-9769-2-6

Carlo Reis, E. C., Borges, A. P. B., Araújo, M. V. F., Mendes, V. C., Guan, L., and Davies, J. E. (2011). Periodontal regeneration using a bilayered PLGA/calcium phosphate construct. *Biomaterials* 32, 9244–9253. doi:10.1016/j.biomaterials.2011.08.040

Chae, S., and Cho, D.-W. (2022). Three-dimensional bioprinting with decellularized extracellular matrix-based bioinks in translational regenerative medicine. *MRS Bull.* 47, 70–79. doi:10.1557/s43577-021-00260-8

Chen, F.-M., Zhang, J., Zhang, M., An, Y., Chen, F., and Wu, Z.-F. (2010). A review on endogenous regenerative technology in periodontal regenerative medicine. *Biomaterials* 31, 7892–7927. doi:10.1016/j.biomaterials.2010.07.019

Chen, J., Ahmad, R., Li, W., Swain, M., and Li, Q. (2015). Biomechanics of oral mucosa. *J. R. Soc. Interface* 12, 20150325. doi:10.1098/rsif.2015.0325

Chen, J., Cui, C., Qiao, X., Yang, B., Yu, M., Guo, W., et al. (2017). Treated dentin matrix paste as a novel pulp capping agent for dentin regeneration. *Tissue Eng. Regen. Med.* 11, 3428–3436. doi:10.1002/term.2256

Cheng, L., Suresh, K. S., He, H., Rajput, R. S., Feng, Q., Ramesh, S., et al. (2021). 3D printing of micro- and nanoscale bone substitutes: A review on technical and translational perspectives. *Int. J. Nanomed.* 16, 4289–4319. doi:10.2147/IJN.S311001

Chiu, Y.-C., Shie, M.-Y., Lin, Y.-H., Lee, A. K., and Chen, Y.-W. (2019). Effect of strontium substitution on the physicochemical properties and bone regeneration potential of 3D printed calcium silicate scaffolds. *Int. J. Mol. Sci.* 20, 2729. doi:10.3390/ijms20112729

Choi, D., Qiu, M., Hwang, Y.-C., Oh, W.-M., Koh, J.-T., Park, C., et al. (2022). The Effects of 3-dimensional bioprinting calcium silicate cement/methacrylated gelatin scaffold on the proliferation and differentiation of human dental pulp stem cells. *Materials* 15, 2170. doi:10.3390/ma15062170

Chung, J. H. Y., Naficy, S., Yue, Z., Kapsa, R., Quigley, A., Moulton, S. E., et al. (2013). Bio-ink properties and printability for extrusion printing living cells. *Biomater. Sci.* 1, 763. doi:10.1039/c3bm00012e

Cui, H., Nowicki, M., Fischer, J. P., and Zhang, L. G. (2017). 3D bioprinting for organ regeneration. *Adv. Healthc. Mat.* 6, 1601118. doi:10.1002/adhm.201601118

Dan, H., Vaquette, C., Fisher, A. G., Hamlet, S. M., Xiao, Y., Hutmacher, D. W., et al. (2014). The influence of cellular source on periodontal regeneration using calcium phosphate coated polycaprolactone scaffold supported cell sheets. *Biomaterials* 35, 113–122. doi:10.1016/j.biomaterials.2013.09.074

Duarte Campos, D. F., Blaeser, A., Buellesbach, K., Sen, K. S., Xun, W., Tillmann, W., et al. (2016). Bioprinting organotypic hydrogels with improved mesenchymal stem cell remodeling and mineralization properties for bone tissue engineering. *Adv. Health. Mat.* 5, 1336–1345. doi:10.1002/adhm.201501033

Duarte Campos, D. F., Zhang, S., Kreimendahl, F., Köpf, M., Fischer, H., Vogt, M., et al. (2020). Hand-held bioprinting for de novo vascular formation applicable to dental pulp regeneration. *Connect. Tissue Res.* 61, 205–215. doi:10.1080/03008207.2019.1640217

Dubey, N., Ferreira, J. A., Malda, J., Bhaduri, S. B., and Bottino, M. C. (2020). Extracellular matrix/amorphous magnesium phosphate bioink for 3D bioprinting of craniomaxillofacial bone tissue. *ACS Appl. Mat. Interfaces.* 12, 23752–23763. doi:10.1021/acsami.0c05311

Fatimi, A., Okoro, O. V., Podstawczyk, D., Siminska-Stanny, J., and Shavandi, A. (2022). Natural hydrogel-based bio-inks for 3D bioprinting in tissue engineering: A review. *Gels* 8, 179. doi:10.3390/gels8030179

Ferris, C. J., Gilmore, K. J., Beirne, S., McCallum, D., Wallace, G. G., and in het Panhuis, M. (2013). Bio-ink for on-demand printing of living cells. *Biomater. Sci.* 1, 224–230. doi:10.1039/c2bm00114d

Gao, X., Qin, W., Wang, P., Wang, L., Weir, M. D., Reynolds, M. A., et al. (2019). Nano-structured demineralized human dentin matrix to enhance bone and dental repair and regeneration. *Appl. Sci.* 9, 1013. doi:10.3390/app9051013

Goudouri, O.-M., Kontonasaki, E., and Boccaccini, A. R. (2017). "17 - layered scaffolds for periodontal regeneration," in *Biomaterials for oral and dental tissue engineering*. Editors L. Tayebi and K. Moharamzadeh (Sawston, United Kingdom: Woodhead Publishing), 279–295.

Grawish, M. E. (2018). Gingival-derived mesenchymal stem cells: An endless resource for regenerative dentistry. *World J. Stem Cells* 10, 116–118. doi:10.4252/wjsc.v10.i9.116

Grigoryan, B., Sazer, D. W., Avila, A., Albritton, J. L., Padhye, A., Ta, A. H., et al. (2021). Development, characterization, and applications of multi-material stereolithography bioprinting. *Sci. Rep.* 11, 3171. doi:10.1038/s41598-021-82102-w

Guo, W., Gong, K., Shi, H., Zhu, G., He, Y., Ding, B., et al. (2012). Dental follicle cells and treated dentin matrix scaffold for tissue engineering the tooth root. *Biomaterials* 33, 1291–1302. doi:10.1016/j.biomaterials.2011.09.068

Guzzi, E. A., and Tibbitt, M. W. (2019). Additive manufacturing of precision biomaterials. *Adv. Mat.* 32, 1901994. doi:10.1002/adma.201901994

Han, J., Jeong, W., Kim, M.-K., Nam, S.-H., Park, E.-K., and Kang, H.-W. (2021). Demineralized dentin matrix particle-based bio-ink for patient-specific shaped 3D dental tissue regeneration. *Polymers* 13, 1294. doi:10.3390/polym13081294

Han, J., Kim, D. S., Jang, H., Kim, H.-R., and Kang, H.-W. (2019). Bioprinting of three-dimensional dentin–pulp complex with local differentiation of human dental pulp stem cells. *J. Tissue Eng.* 10, 204173141984584. doi:10.1177/2041731419845849

Hass, R., Kasper, C., Bohm, S., and Jacobs, R. (2011). Different populations and sources of human mesenchymal stem cells (MSC): A comparison of adult and neonatal tissue-derived MSC. *Cell. Commun. Signal.* 9, 12. doi:10.1186/1478-811X-9-12

Herberts, C. A., Kwa, M. S. G., and Hermsen, H. P. H. (2011). Risk factors in the development of stem cell therapy. *J. Transl. Med.* 9, 29. doi:10.1186/1479-5876-9-29

Honda, M. J., Tsuchiya, S., Sumita, Y., Sagara, H., and Ueda, M. (2007). The sequential seeding of epithelial and mesenchymal cells for tissue-engineered tooth regeneration. *Biomaterials* 28, 680–689. doi:10.1016/j.biomaterials.2006.09.039

Hourd, P., Medcalf, N., Segal, J., and Williams, D. J. (2015). A 3D-bioprinting exemplar of the consequences of the regulatory requirements on customized processes. *Regen. Med.* 10, 863–883. doi:10.2217/rme.15.52

Hu, B., Nadiri, A., Kuchler-Bopp, S., Perrin-Schmitt, F., Peters, H., and Lesot, H. (2006). Tissue engineering of tooth crown, root, and periodontium. *Tissue Eng.* 12, 2069–2075. doi:10.1089/ten.2006.12.2069

Ikeda, E., Morita, R., Nakao, K., Ishida, K., Nakamura, T., Takano-Yamamoto, T., et al. (2009). Fully functional bioengineered tooth replacement as an organ replacement therapy. *Proc. Nati. Acad. Sci. U.S.A.* 106, 13475–13480. doi:10.1073/pnas.0902944106

Iwatsuki, S., Honda, M. J., Harada, H., and Ueda, M. (2006). Cell proliferation in teeth reconstructed from dispersed cells of embryonic tooth germs in a three-dimensional scaffold. *Eur. J. Oral Sci.* 114, 310–317. doi:10.1111/j.1600-0722.2006.00385.x

Jain, P., Kathuria, H., and Dubey, N. (2022). Advances in 3D bioprinting of tissues/organs for regenerative medicine and *in-vitro* models. *Biomaterials* 287, 121639. doi:10.1016/j.biomaterials.2022.121639

Khayat, A., Monteiro, N., Smith, E. E., Pagni, S., Zhang, W., Khademhosseini, A., et al. (2016). GelMA-encapsulated hDPSCs and HUVECs for dental pulp regeneration. *J. Dent. Res.* 96, 192–199. doi:10.1177/0022034516682005

Khorsandi, D., Fahimipour, A., Abasian, P., Saber, S. S., Seyedi, S., Ahmad, A., et al. (2021). 3D and 4D printing in dentistry and maxillofacial surgery: Printing techniques, materials, and applications. *Acta Biomater.* 122, 26–49. doi:10.1016/j.actbio.2020.12.044

Kim, D., Lee, H., Lee, G.-H., Hoang, T.-H., Kim, H.-R., and Kim, G. H. (2022). Fabrication of bone-derived decellularized extracellular matrix/ceramic-based biocomposites and their osteo/odontogenic differentiation ability for dentin regeneration. *Bioeng. Transl. Med.* 7, e10317. doi:10.1002/btm2.10317

Kim, K., Lee, C. H., Kim, B. K., and Mao, J. J. (2010). Anatomically shaped tooth and periodontal regeneration by cell homing. *J. Dent. Res.* 89, 842–847. doi:10.1177/0022034510370803

Kim, N. R., Lee, D. H., Chung, P.-H., and Yang, H.-C. (2009). Distinct differentiation properties of human dental pulp cells on collagen, gelatin, and chitosan scaffolds. *Oral Surg. Oral Med. Oral Pathol. Oral Radiol. Endod.* 108, e94–e100. doi:10.1016/j.tripleo.2009.07.031

Lee, C. H., Hajibandeh, J., Suzuki, T., Fan, A., Shang, P., and Mao, J. J. (2014). Three-dimensional printed multiphase scaffolds for regeneration of periodontium complex. *Tissue Eng. Part A* 20, 1342–1351. doi:10.1089/ten.tea.2013.0386

Leyendecker Junior, A., Gomes Pinheiro, C. C., Lazzaretti Fernandes, T., and Franco Bueno, D. (2018). The use of human dental pulp stem cells for *in vivo* bone tissue engineering: A systematic review. *J. Tissue Eng.* 9, 204173141775276. doi:10.1177/2041731417752766

Li, R., Guo, W., Yang, B., Guo, L., Sheng, L., Chen, G., et al. (2011). Human treated dentin matrix as a natural scaffold for complete human dentin tissue regeneration. *Biomaterials* 32, 4525–4538. doi:10.1016/j.biomaterials.2011.03.008

Lukomska, B., Stanaszek, L., Zuba-Surma, E., Legosz, P., Sarzynska, S., and Drela, K. (2019). Challenges and controversies in human mesenchymal stem cell therapy. *Stem Cells Int.* 2019, 1–10. doi:10.1155/2019/9628536

Ma, Y., Xie, L., Yang, B., and Tian, W. (2019). Three-dimensional printing biotechnology for the regeneration of the tooth and tooth-supporting tissues. *Biotechnol. Bioeng.* 116, 452–468. doi:10.1002/bit.26882

Madduma-Bandarage, U. S. K., and Madihally, S. V. (2021). Synthetic hydrogels: Synthesis, novel trends, and applications. *J. Appl. Polym. Sci.* 138, e50376. doi:10.1002/app.50376

Mandrycky, C., Wang, Z., Kim, K., and Kim, D.-H. (2016). 3D bioprinting for engineering complex tissues. *Biotechnol. Adv.* 34, 422–434. doi:10.1016/j.biotechadv.2015.12.011

Medvedev, S. P., Shevchenko, A. I., and Zakian, S. M. (2010). Induced pluripotent stem cells: Problems and advantages when applying them in regenerative medicine. *Acta Naturae* 2, 18–27. doi:10.32607/20758251-2010-2-2-18-27

Morrison, D. G., and Tomlinson, R. E. (2021). Leveraging advancements in tissue engineering for bioprinting dental tissues. *Bioprinting* 23, e00153. doi:10.1016/j.bprint.2021.e00153

Mosaddad, S. A., Rasoolzade, B., Namanloo, R. A., Azarpira, N., and Dortaj, H. (2022). Stem cells and common biomaterials in dentistry: A review study. *J. Mat. Sci. Mat. Med.* 33, 55. doi:10.1007/s10856-022-06676-1

Mousavi Nejad, Z., Zamanian, A., Saeidifar, M., Vanaei, H. R., and Salar Amoli, M. (2021). 3D bioprinting of polycaprolactone-based scaffolds for pulp-dentin regeneration: Investigation of physicochemical and biological behavior. *Polymers* 13, 4442. doi:10.3390/polym13244442

Nakao, K., Morita, R., Saji, Y., Ishida, K., Tomita, Y., Ogawa, M., et al. (2007). The development of a bioengineered organ germ method. *Nat. Methods* 4, 227–230. doi:10.1038/nmeth1012

Naseri, S., Cooke, M. E., Rosenzweig, D. H., and Tabrizian, M. (2021). 3D printed *in vitro* dentin model to investigate occlusive agents against tooth sensitivity. *Materials* 14, 7255. doi:10.3390/ma14237255

Nesic, D., Durual, S., Marger, L., Mekki, M., Sailer, I., and Scherrer, S. S. (2020b). Could 3D printing be the future for oral soft tissue regeneration? *Bioprinting* 20, e00100. doi:10.1016/j.bprint.2020.e00100

Nesic, D., Schaefer, B. M., Sun, Y., Saulacic, N., and Sailer, I. (2020a). 3D printing approach in dentistry: The future for personalized oral soft tissue regeneration. *J. Clin. Med.* 9, 2238. doi:10.3390/jcm9072238

Oshima, M., Mizuno, M., Imamura, A., Ogawa, M., Yasukawa, M., Yamazaki, H., et al. (2011). Functional tooth regeneration using a bioengineered tooth unit as a mature organ replacement regenerative therapy. *PLOS ONE* 6, e21531. doi:10.1371/journal.pone.0021531

Oshima, M., and Tsuji, T. (2014). Functional tooth regenerative therapy: Tooth tissue regeneration and whole-tooth replacement. *Odontology* 102, 123–136. doi:10.1007/s10266-014-0168-z

Ostrovidov, S., Ramalingam, M., Bae, H., Orive, G., Fujie, T., Shi, X., et al. (2023). Latest developments in engineered skeletal muscle tissues for drug discovery and development. *Expert Opin. Drug Discov.* 18, 47–63. doi:10.1080/17460441.2023.2160438

Ostrovidov, S., Salehi, S., Costantini, M., Suthiwanich, K., Ebrahimi, M., Sadeghian, R. B., et al. (2019). 3D bioprinting in skeletal muscle tissue engineering. *Small* 15, 1805530. doi:10.1002/smll.201805530

Ostrovidov, S., Shi, X., Sadeghian, R. B., Salehi, S., Fujie, T., Bae, H., et al. (2015). Stem cell differentiation toward the myogenic lineage for muscle tissue regeneration: A focus on muscular dystrophy. *Stem Cell. Rev.* 11, 866–884. doi:10.1007/s12015-015-9618-4

Park, C. H., Kim, K.-H., Lee, Y.-M., and Seol, Y.-J. (2016). Advanced engineering strategies for periodontal complex regeneration. *Materials* 9, 57. doi:10.3390/ma9010057

Park, C. H., Rios, H. F., Jin, Q., Bland, M. E., Flanagan, C. L., Hollister, S. J., et al. (2010). Biomimetic hybrid scaffolds for engineering human tooth-ligament interfaces. *Biomaterials* 31, 5945–5952. doi:10.1016/j.biomaterials.2010.04.027

Park, J. H., Gillispie, G. J., Copus, J. S., Zhang, W., Atala, A., Yoo, J. J., et al. (2020). The effect of BMP-mimetic peptide tethering bioinks on the differentiation of dental pulp stem cells (DPSCs) in 3D bioprinted dental constructs. *Biofabrication* 12, 035029. doi:10.1088/1758-5090/ab9492

Peters, J. T., Wechsler, M. E., and Peppas, N. A. (2021). Advanced biomedical hydrogels: Molecular architecture and its impact on medical applications. *Regen. Biomater.* 8, rbab060–21. doi:10.1093/rb/rbab060

Radwan, I. A., Rady, D., Abbass, M. M. S., El Moshy, S., AbuBakr, N., Dörfer, C. E., et al. (2020). Induced pluripotent stem cells in dental and nondental tissue regeneration: A review of an unexploited potential. *Stem Cells Int.* 2020, 1–24. doi:10.1155/2020/1941629

Rana, D., Kumar, T. S. S., and Ramalingan, M. (2014). Cell-laden hydrogels for tissue engineering. *J. Biomater. Tissue Eng.* 4, 507–535. doi:10.1166/jbt.2014.1206

Rasperini, G., Pilipchuk, S. P., Flanagan, C. L., Park, C. H., Pagni, G., Hollister, S. J., et al. (2015). 3D-printed bioresorbable scaffold for periodontal repair. *J. Dent. Res.* 94, 153S–157S. doi:10.1177/0022034515588303

Raveendran, N. T., Vaquette, C., Meinert, C., Samuel Ipe, D., and Ivanovski, S. (2019). Optimization of 3D bioprinting of periodontal ligament cells. *Dent. Mat.* 35, 1683–1694. doi:10.1016/j.dental.2019.08.114

Ricles, L. M., Coburn, J. C., Di Prima, M., and Oh, S. (2018). Regulating 3D-printed medical products. *Sci. Transl. Med.* 10, eaan6521. doi:10.1126/scitranslmed.aan6521

Rosa, V., Sriram, G., McDonald, N., and Cavalcanti, B. N. (2022). A critical analysis of research methods and biological experimental models to study pulp regeneration. *Int. Endod. J.* 55, 446–455. doi:10.1111/iej.13712

Samandari, M., Quint, J., Rodriguez-delaRosa, A., Sinha, I., Pourquie, O., and Tamayol, A. (2022). Bioinks and bioprinting strategies for skeletal muscle tissue engineering. *Adv. Mat.* 34, 2105883. doi:10.1002/adma.202105883

Santoni, S., Gugliandolo, S. G., Sponchioni, M., Moscatelli, D., and Colosimo, B. M. (2022). 3D bioprinting: Current status and trends-a guide to the literature and industrial practice. *BIO-DES Manuf.* 5, 14–42. doi:10.1007/s42242-021-00165-0

Santos, J. M., Coelho, C. M., Sequeira, D. B., Marques, J. A., Pereira, J. F., Sousa, V., et al. (2021). Subcutaneous implantation assessment of new calcium-silicate based sealer for warm obturation. *Biomedicines* 9, 24. doi:10.3390/biomedicines9010024

Schuh, J. C. L., and Funk, K. A. (2019). Compilation of international standards and regulatory guidance documents for evaluation of biomaterials, medical devices, and 3-D printed and regenerative medicine products. *Toxicol. Pathol.* 47, 344–357. doi:10.1177/0192623318804121

Sekar, M. P., Budharaju, H., Zennifer, A., Sethuraman, S., Vermeulen, N., Sundaramurthi, D., et al. (2021). Current standards and ethical landscape of engineered tissues-3D bioprinting perspective. *J. Tissue Eng.* 6, 204173142110276–33. doi:10.1177/20417314211027677

Simon, C. G., Yaszemski, M. J., Ratcliffe, A., Tomlins, P., Luginbuehl, R., and Tesk, J. A. (2014). ASTM international workshop on standards and measurements for tissue engineering scaffolds: ASTM international scaffolds workshop report. *Biomed. Mat. Res. Part B* 103, 949–959. doi:10.1002/jbm.b.33286

Smith, E. E., Zhang, W., Schiele, N. R., Khademhosseini, A., Kuo, C. K., and Yelic, P. C. (2017). Developing a biomimetic tooth bud model. *Tissue Eng. Regen. Med.* 11, 3326–3336. doi:10.1002/term.2246

Son, C., Choi, M. S., and Park, J.-C. (2020). Different responsiveness of alveolar bone and long bone to epithelial-mesenchymal interaction-related factor. *JBMR Plus* 4, e10382. doi:10.1002/jbm4.10382

Stefańska, K., Mehr, K., Wieczorkiewicz, M., Kulus, M., Angelova Volponi, A., Shibli, J. A., et al. (2020). Stemness potency of human gingival cells-Application in anticancer therapies and clinical trials. *Cells* 9, 1916. doi:10.3390/cells9081916

Sumita, Y., Honda, M. J., Ohara, T., Tsuchiya, S., Sagara, H., Kagami, H., et al. (2006). Performance of collagen sponge as a 3-D scaffold for tooth-tissue engineering. *Biomaterials* 27, 3238–3248. doi:10.1016/j.biomaterials.2006.01.055

Sun, W., Starly, B., Daly, A. C., Burdick, J. A., Groll, J., Skeldon, G., et al. (2020). The bioprinting roadmap. *Biofabrication* 12, 022002. doi:10.1088/1758-5090/ab5158

Sun, W., Wang, Z., Xu, Q., Sun, H., Liu, X., Yang, J., et al. (2019). The treatment of systematically transplanted gingival mesenchymal stem cells in periodontitis in mice. *Exp. Ther. Med.* 17, 2199–2205. doi:10.3892/etm.2019.7165

Vijayavenkataraman, S., Yan, W.-C., Lu, W. F., Wang, C.-H., and Fuh, J. Y. H. (2018). 3D bioprinting of tissues and organs for regenerative medicine. *Adv. Drug Deliv. Rev.* 132, 296–332. doi:10.1016/j.addr.2018.07.004

Wang, C.-Y., Chiu, Y.-C., Lee, A. K., Lin, Y.-A., Lin, P.-Y., and Shie, M.-Y. (2021). Biofabrication of gingival fibroblast cell-laden collagen/strontium-doped calcium silicate 3D-printed bi-layered scaffold for osteoporotic periodontal regeneration. *Biomedicines* 9, 431. doi:10.3390/biomedicines9040431

Wang, Z., Kapadia, W., Li, C., Lin, F., Pereira, R. F., Granja, P. L., et al. (2021a). Tissue-specific engineering: 3D bioprinting in regenerative medicine. *J. Control. Release* 329, 237–256. doi:10.1016/j.jconrel.2020.11.044

Wang., Z., Wang, L., Li, T., Liu, S., Guo, B., Huang, W., et al. (2021b). 3D bioprinting in cardiac tissue engineering. *Theranostics* 11, 7948–7969. doi:10.7150/thno.61621

Wen, Y., Wang, F., Zhang, W., Li, Y., Yu, M., Nan, X., et al. (2012). Application of induced pluripotent stem cells in generation of a tissue-engineered tooth-like structure. *Tissue Eng. Part A* 18, 1677–1685. doi:10.1089/ten.tea.2011.0220

Weng, T., Zhang, W., Xia, Y., Wu, P., Yang, M., Jin, R., et al. (2021). 3D bioprinting for skin tissue engineering: Current status and perspectives. *J. Tissue Eng.* 12, 204173142110285–28. doi:10.1177/20417314211028574

Wu, Y., Azmi, D. F. B., Rosa, V., Fawzy, A. S., Fuh, J. Y. H., Wong, Y. S., et al. (2016). Fabrication of dentin-like scaffolds through combined 3D printing and bio-mineralisation. *Cogent Eng.* 3, 1222777. doi:10.1080/23311916.2016.1222777

Xie, M., Yu, K., Sun, Y., Shao, L., Nie, J., Gao, Q., et al. (2019). Protocols of 3D bioprinting of gelatin methacryloyl hydrogel based bioinks. *J. Vis. Exp.* 154, e60545. doi:10.3791/60545

Yamamoto, H., Kim, E., Cho, S., and Jung, H. (2003). Analysis of tooth formation by reaggregated dental mesenchyme from mouse embryo. *Microscopy* 52, 559–566. doi:10.1093/jmicro/52.6.559

Yang, B., Chen, G., Li, J., Zou, Q., Xie, D., Chen, Y., et al. (2012). Tooth root regeneration using dental follicle cell sheets in combination with a dentin matrix - based scaffold. *Biomaterials* 33, 2449–2461. doi:10.1016/j.biomaterials.2011.11.074

Yang, Y., Wang, M., Yang, S., Lin, Y., Zhou, Q., Li, H., et al. (2020). Bioprinting of an osteocyte network for biomimetic mineralization. *Biofabrication* 12, 045013. doi:10.1088/1758-5090/aba1d0

Yelick, P. C., and Vacanti, J. P. (2006). Bioengineered teeth from tooth bud cells. *Dent. Clin. N. Am.* 50, 191–203. doi:10.1016/j.cden.2005.11.005

Yi, K., Li, Q., Lian, X., Wang, Y., and Tang, Z. (2022). Utilizing 3D bioprinted platelet-rich fibrin-based materials to promote the regeneration of oral soft tissue. *Regen. Biomater.* 9, rbac021. doi:10.1093/rb/rbac021

Yu, H., Zhang, X., Song, W., Pan, T., Wang, H., Ning, T., et al. (2019). Effects of 3-dimensional bioprinting alginate/gelatin hydrogel scaffold extract on proliferation and differentiation of human dental pulp stem cells. *J. Endod.* 45, 706–715. doi:10.1016/j.joen.2019.03.004

Zennifer, A., Subramanian, A., and Sethuraman, S. (2022). Design considerations of bioinks for laser bioprinting technique towards tissue regenerative applications. *Bioprinting* 27, e00205. doi:10.1016/j.bprint.2022.e00205

Zhang, H., Liu, S., Zhou, Y., Tan, J., Che, H., Ning, F., et al. (2011). Natural mineralized scaffolds promote the dentinogenic potential of dental pulp stem cells via the mitogen-activated protein kinase signaling pathway. *Tissue Eng. Part A* 18, 677–691. doi:10.1089/ten.tea.2011.0269

Zhang, W., Vazquez, B., Oreadi, D., and Yelick, P. C. (2017). Decellularized tooth bud scaffolds for tooth regeneration. *J. Dent. Res.* 96, 516–523. doi:10.1177/0022034516689082

Zhang, Y.-R., Du, W., Zhou, X.-D., and Yu, H.-Y. (2014). Review of research on the mechanical properties of the human tooth. *Int. J. Oral Sci.* 6, 61–69. doi:10.1038/ijos.2014.21

Zhou, G., Jiang, H., Yin, Z., Liu, Y., Zhang, Q., Zhang, C., et al. (2018). *In vitro* regeneration of patient-specific ear-shaped cartilage and its first clinical application for auricular reconstruction. *EBioMedicine* 28, 287–302. doi:10.1016/j.ebiom.2018.01.011

Zhou, Q., Cheng, Y., Sun, F., Shen, J., Nasser, M. I., Zhu, P., et al. (2021). A comprehensive review of the therapeutic value of urine-derived stem cells. *Front. Genet.* 12, 781597. doi:10.3389/fgene.2021.781597

Frontiers in
Bioengineering and Biotechnology

Accelerates the development of therapies, devices, and technologies to improve our lives

A multidisciplinary journal that accelerates the development of biological therapies, devices, processes and technologies to improve our lives by bridging the gap between discoveries and their application.

Discover the latest Research Topics

See more →

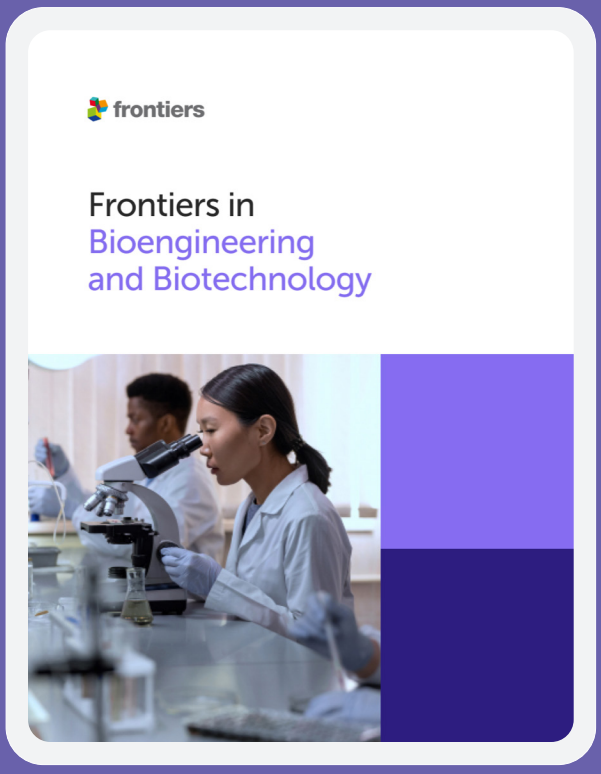

Frontiers

Avenue du Tribunal-Fédéral 34
1005 Lausanne, Switzerland
frontiersin.org

Contact us

+41 (0)21 510 17 00
frontiersin.org/about/contact